CONVECTIVE INSTABILITY OF OSCILLATORY FLOW IN PULSE TUBE CRYOCOOLERS DUE TO ASYMMETRIC GRAVITATIONAL BODY FORCE

A Dissertation
Presented to
The Academic Faculty

by

Thomas Ian Mulcahey

In Partial Fulfillment
of the Requirements for the Degree
Doctor of Philosophy in the
School of Mechanical Engineering

Georgia Institute of Technology
May, 2014

CONVECTIVE INSTABILITY OF OSCILLATORY FLOW IN PULSE TUBE CRYOCOOLERS DUE TO ASYMMETRIC GRAVITATIONAL BODY FORCE

Approved by:

Dr. S. Mostafa Ghiaasiaan, Advisor
School of Mechanical Engineering
Georgia Institute of Technology

Dr. Prateen V. Desai
School of Mechanical Engineering
Georgia Institute of Technology

Dr. Sheldon M. Jeter
School of Mechanical Engineering
Georgia Institute of Technology

Dr. Mitchell L. R. Walker, II
School of Aerospace Engineering
Georgia Institute of Technology

Dr. Bart L. Lipkens
School of Mechanical Engineering
Western New England University

Dr. Carl S. Kirkconnell
Chief Technology Officer
Iris Technology Corporation

Date Approved: January 6, 2014

To my grandfather James A. Mulcahey, Jr. (April 29, 1918 - April 13, 2013)

ACKNOWLEDGEMENTS

There are many people who deserve my gratitude for enabling me to complete my doctoral research. First, my advisor Dr. S. Mostafa Ghiaasiaan for his unwavering support and encouragement during the more difficult times of my career at Georgia Tech. I am forever grateful for the opportunities that I have been given as a result of our relationship.

A special thanks is owed to Carl Kirkconnell for his mentorship, patience, and guidance through the years. I have learned significantly more valuable skills from my experience working with Carl than through any other single graduate school experience. I would also like to thank Dr. Prateen Desai for helpful discussions on convection and for keeping me up to date on publications. Thanks are also due to Dr. Mitchell Walker for encouraging the pursuit of a thesis I can be proud of and for agreeing to serve on my committee. Dr. Sheldon Jeter is also acknowledged for his support as part of my dissertation committee. Dr. Bart Lipkens was my undergraduate advisor and encouraged me to pursue graduate education. His encouragement and support for the last decade have significantly impacted my ability to get to where I am today and inspired me to be a meticulous engineer.

Former Cryo Lab student and current Raytheon engineer Dr. Ted Conrad deserves my deepest gratitude for his guidance and tutelage in all things cryo, including CFD and Sage modeling. Without Ted's support on this dissertation work, I would not have been able to obtain the data needed to validate the models. Also crucial to my success was Dr. Vishal Acharya, a Research Scientist who took the time to help me learn how to effectively manage supercomputing resources. I owe a great debt of gratitude to Dr. Ryan Taylor at VMI for serving as a collaborator and advisor on

this research work. I am grateful to have had the fortune of working with one of the foremost experts in the field of pulse tube simulation.

Dr. Mihir Pathak, NASA employee and Cryo Lab alumnus, has been my inspiration and support group throughout my entire experience at Georgia Tech. His leadership and hard work have helped catapult the Georgia Tech Cryo Lab to new heights, allowing me to come along for the ride. Without Mihir I would not have joined the Cryo Lab, and consequently would not be completing this dissertation today. I will sincerely miss our whiteboard problem-solving strategy sessions and meetings at Rocky Mountan Pizza Co.

The greatest appreciation is due to my family. It would not have been possible to manage the doctoral workload without their love and support. Brittany White has been my biggest champion and supporter over the past five and a half years. It is impossible to overstate the value of clean laundry and packed lunches during the sprints of 20 hour workdays. I must acknowledge my daughter Rayleigh Danielle Mulcahey who arrived during my final year of graduate school for helping me realize just how much responsibility I can actually handle. I would like to thank Erika and Neale White, and László and Irén Szegedi, for taking care of Rayleigh so that I could finish my dissertation; I know it would not have been possible otherwise. To my parents Debbie Watland and Michael Mulcahey, for giving me life and for always nurturing my intellectual curiousity. To my brothers Christopher, Patrick, Peter, and Morgan, and to my sister Corrie for being proud of me and motivating me to pursue my dreams.

Finally, thanks are due to my grandfather James A. Mulcahey, Jr., to whom this dissertation is dedicated. His lifelong passion for education inspired me to continue to completion. I owe much of who I am today to him.

TABLE OF CONTENTS

DEDICATION . . . . . **iii**

ACKNOWLEDGEMENTS . . . . . **iv**

LIST OF TABLES . . . . . **x**

LIST OF FIGURES . . . . . **xi**

0.1 Greek Symbols xvii

0.2 English Symbols and Abbreviations xviii

0.3 Subscripts and Indices xx

0.4 Superscripts xxii

0.5 Common Notations xxii

SUMMARY . . . . . **xxiii**

I INTRODUCTION **1**

1.1 Executive Research Summary 2

1.2 Thesis Overview and Outline 4

1.3 The Stirling Cycle and Pulse Tube Cryocooler Operation 7

1.3.1 The Stirling Cycle for Refrigeration 7

1.3.2 Pulse Tube Refrigerator Operating Principles 11

1.3.3 Historical Development of Pulse Tube Refrigerators 13

1.3.4 Pulse Tube Cryocooler Configurations 18

II PULSE TUBE BACKGROUND AND THEORY **22**

2.1 Pulse Tube Thermodynamics and Hydrodynamics 22

2.1.1 Pulse Tube Refrigerator Control Volume Analysis and Energy Flows 25

2.1.2 Pulse Tube Loss Mechanisms 31

2.1.3 Boundary Layers and Turbulence Effects 36

2.2 Fluid Mechanics of Oscillating Flow in Inclined Cylinders 38

2.2.1 Rayleigh-Bénard Convection 41

2.2.2 Convective Instability Theory 43
2.2.3 Method of Analogous Dynamic systems 43
2.3 Previous Work (Literature Review) 47
2.3.1 Empirical Studies 48
2.3.2 Visualization Studies 50
2.3.3 Computational PTR Studies 52
2.3.4 Experimental Flow Straightening Approaches 54
III MODELING METHODOLOGY AND THEORY 56
3.1 First-Order System-Level Modeling Methods 57
3.1.1 REGEN 3.3 57
3.1.2 Overview of Sage Simulation Environment 59
3.1.3 DeltaEC 61
3.2 Multidimensional Computational Fluid Dynamics 62
3.3 Governing Equations for Computational Fluid Dynamics 64
3.3.1 Fluid Zone Finite Volume Governing Equations 65
3.3.2 Energy Equation in Solid Domains 67
3.3.3 Porous Media Theory and Numerical Treatment 68
3.4 Pulse Tube Modeling Methods - Open and Closed System Modeling 72
3.4.1 Boundary Conditions 74
3.4.2 Operating Conditions 75
3.4.3 Initial Conditions 77
3.4.4 Solver Settings 78
3.4.5 Discretization Schemes 80
3.4.6 Meshing Schemes 81
3.5 Material Properties 81
3.5.1 Working Gas Properties 81
3.5.2 Solid Material Property Treatment 83
3.5.3 Porous Material Property Treatment 83

IV 3-D SYSTEM-LEVEL CFD MODELING 87

4.1 System-Level Modeling Scope and Study Geometries 88

4.2 Computational Domain and Mesh Discretization Scheme 94

4.2.1 Initialization and Convergence 97

4.3 System-level Flow and Temperature Fields 101

4.4 System-level Energy Flow Effects 113

4.5 Conclusions 115

V PULSE TUBE COMPONENT-LEVEL CFD SIMULATION AND PARAMETRIC STUDY 116

5.1 Overview 116

5.2 Computational Domain, Grid Independence, and Time Step Convergence 116

5.2.1 Computational Domain 116

5.2.2 Time Step and Grid Independence 118

5.3 Computational Parametric Study Results 123

5.3.1 Parameters Investigated 123

5.3.2 Stability Results for Simulated Pulse Tubes 126

VI MODEL VALIDATION AND ANALYSIS OF COMBINED RESULTS 168

6.1 Introduction 168

6.2 Measurement Methodology 172

6.3 Reference Cryocooler Data and Sage Model Correlation 175

6.4 Data Comparison and Error Analysis 178

6.5 Analysis of combined experimental and simulated results 181

6.6 Conclusion 187

VII CONCLUSIONS AND FUTURE WORK 189

7.1 Summary 189

7.2 Contributions 191

7.3 Future Work 191

7.3.1 Separate Effects Testing of Inclined Pulse Tubes 191

7.3.2 Exploration of Dynamic Gravitational Body Forces in Pulse Tubes 192

APPENDIX A — DEVELOPMENT OF A ROTATING CRYOGENIC TEST FACILITY 194

APPENDIX B — FLUENT CODE 223

APPENDIX C — MATLAB PROCESSING CODES 242

REFERENCES 260

VITA 269

LIST OF TABLES

3.1 CFD Solver Settings 79

3.2 CFD Convergence Criteria 80

3.3 CFD discretization schemes 80

3.4 Wire cloth porous material hydrodynamic parameters 86

4.1 Operating conditions for system-level model PTRs. 94

4.2 Component geometries for system-level model PTRs. 95

4.3 Dynamic mesh control parameters. 96

4.4 Meshing statistics for system-level half-symmetry model using swept meshing with biased boundary layers. 97

5.1 Dimensions for component-level pulse tube models incorporating CHX, PT, PT wall, and WHX. 119

5.2 Grid parameters 123

5.3 Ranges for parametric study variables 125

A.1 Separate effects component dimensions. 217

LIST OF FIGURES

1.1 Comparison of pulse tube temperature contours as inclination angle varies from vertical cold end down to horizontal 3

1.2 Stirling refrigeration cycle *P-v* and *T-s* diagrams 7

1.3 Pictorial representation of the Stirling cycle 8

1.4 Linear Pulse Tube Cryocooler Schematic 12

1.5 Historical Evolution of PTRs from BPTR to ITPTR 14

1.6 Micro-scale PTC Prototype 18

1.7 Alternative PTR configurations 20

1.8 Cascaded PTR arrangements: fluid- and thermally-coupled systems . 21

2.1 PTR system control volume 26

2.2 Pulse tube control volume 28

2.3 Cold heat exchanger control volume 30

2.4 Graphical description of shuttle heat transfer and surface heat pumping effect 33

2.5 Illustration of the acoustic streaming phenomenon 34

2.6 Four flow regimes for oscillatory pipe flow outlining the transition to turbulence 38

2.7 Domain introducing the transition angle which marks the onset of free convection 39

2.8 Transition angle as a function of length-to-diameter aspect ratio . . . 40

2.9 Overview of Rayleigh-Bénard convective cells 42

2.10 Pulse tube inverted pendulum analogy from [3] 45

2.11 Smoke-wire visualization of velocity profiles at varied angles of inclination [51] 51

2.12 Flow partitioning technique applied by Zhang et al. [53] resulting in reduced orientation sensitivity, but also reduced overall performance. 52

2.13 muticellular convection regime suggested by Kasthurirengan [68] . . . 54

3.1 Flow chart of PTR modeling applied to the design process 58

3.2 Overview of Sage simulation environment 60

3.3 CFD mesh cell types 63
3.4 Comparison of closed-system and open-system modeling methods in CFD 73
3.5 Helium density as a function of temperature and pressure 82
3.6 Solid material specific heat capacity as a function of temperature . . 83
3.7 Solid material thermal conductivity as a function of temperature . . . 84
3.8 Porous screen material overview 85
4.1 REGEN 3.3 sizing of system-level simulated regenerator 90
4.2 System-level PTR model computational domain schematic 95
4.3 System-level 3-D mesh for aspect ratio L/D=8 98
4.4 Isometric L/D=4 system-level temperature contours at 0° and at 91° 102
4.5 Isometric L/D=4 system-level temperature contours at 135° 103
4.6 L/D=4 system-level symmetry plane temperature contours and velocity vectors 104
4.7 Isometric L/D=8 system-level symmetry plane temperature contours and velocity vectors 105
4.8 Isometric L/D=4 system-level symmetry plane velocity contours . . . 108
4.9 L/D=4 system-level 135° time sequence of symmetry plane temperature contours 109
4.10 L/D=4 system-level 135° time sequence of velocity contours 110
4.11 L/D=4 system-level 135° time sequence of wall temperature contours 111
4.12 Comparison of temperature initialization profile with final cycle temperature profile as a function of inclination angle 112
4.13 Comparison of net energy flows in the pulse tube and regenerator as a function of inclination angle 114
5.1 Schematic of the computational domain for isolated pulse tube CFD models 117
5.2 Component-level model grid independence study meshes 122
5.3 L/D=4, 60 Hz, 300-60 K, 4 g/s convergence history 128
5.4 L/D=4, 60 Hz, 300-60 K, 2.5 g/s convergence history 128
5.5 L/D=4, 60 Hz, 300-60 K, 1 g/s convergence history 129

5.6 Comparison of simulated cold end mass flow and dynamic pressure for an $L/D = 8$ pulse tube operating between 300 K and 60 K with mass flow amplitude of 1 g/s and pressure ratio of 1.2 for a charge pressure of 2 MPa at different orientation angles. The phase angle between mass flow and pressure is $\varphi_{m-p} = +30°$. 131

5.7 Comparison of simulated cold end mass flow and dynamic pressure for an $L/D = 8$ pulse tube operating between 300 K and 60 K with mass flow amplitude of 2.5 g/s and pressure ratio of 1.2 for a charge pressure of 2 MPa at two orientation angles. The phase angle between mass flow and pressure is $\varphi_{m-p} = +30°$ 132

5.8 Comparison of simulated cold end mass flow and dynamic pressure for an $L/D = 8$ pulse tube operating between 300 K and 60 K with mass flow amplitude of 4 g/s and pressure ratio of 1.2 for a charge pressure of 2 MPa at different orientation angles. The phase angle between mass flow and pressure is $\varphi_{m-p} = +30°$. 133

5.9 Comparison of simulated energy flows for an $L/D = 8$ pulse tube operating between 300 K and 60 K with mass flow amplitude of 1 g/s as a function of orientation angle 135

5.10 Comparison of simulated energy flows for an $L/D = 8$ pulse tube operating between 300 K and 60 K with mass flow amplitude of 2.5 g/s as a function of orientation angle 136

5.11 Comparison of simulated energy flows for an $L/D = 8$ pulse tube operating between 300 K and 60 K with mass flow amplitude of 4 g/s as a function of orientation angle 137

5.12 Net Cycle-averaged energy flow $\langle \dot{E} \rangle$ for 40 Hz simulations with 60 K cold end and 300 K warm end for an aspect ratio (L/D) of 8. The phase angle between mass flow and pressure is $\varphi_{m-p} = +30°$ 138

5.13 Normalized energy flow loss for 40 Hz simulations with 60 K cold end and 300 K warm end for an aspect ratio (L/D) of 8 139

5.14 Net Cycle-averaged energy flow $\langle \dot{E} \rangle$ for 60 Hz simulations with 60 K cold end and 300 K warm end for an aspect ratio (L/D) of 8. The phase angle between mass flow and pressure is $\varphi_{m-p} = +30°$ 141

5.15 Normalized energy flow loss for 60 Hz simulations with 60 K cold end and 300 K warm end for an aspect ratio (L/D) of 8. The phase angle between mass flow and pressure is $\varphi_{m-p} = +30°$ 142

5.16 Net Cycle-averaged energy flow $\langle \dot{E} \rangle$ for 60 Hz simulations with 80 K cold end and 300 K warm end for an aspect ratio (L/D) of 8. The phase angle between mass flow and pressure is $\varphi_{m-p} = +30°$ 143

5.17 Normalized energy flow loss for 60 Hz simulations with 80 K cold end and 300 K warm end for an aspect ratio (L/D) of 8. The phase angle between mass flow and pressure is $\varphi_{m-p} = +30°$ 144

5.18 Maximum cooling loss as a function of cold end Reynolds number for all $\varphi_{m-p} = +30°$ cases 145

5.19 Comparison of cold end mass flow and dynamic pressure for an $L/D = 8$ pulse tube operating between 300 K and 60 K with mass flow amplitude of 1 g/s and pressure ratio of 1.2 for a charge pressure of 2 MPa as a function of orientation angle. The phase angle between mass flow and pressure is $\varphi_{m-p} = -30°$ 147

5.20 Comparison of simulated cold end mass flow and dynamic pressure for an $L/D = 8$ pulse tube operating between 300 K and 60 K with mass flow amplitude of 2.5 g/s and pressure ratio of 1.2 for a charge pressure of 2 MPa as a function of orientation angle. The phase angle between mass flow and pressure is $\varphi_{m-p} = -30°$. 148

5.21 Comparison of simulated cold end mass flow and dynamic pressure for an $L/D = 8$ pulse tube operating between 300 K and 60 K with mass flow amplitude of 4 g/s and pressure ratio of 1.2 for a charge pressure of 2 MPa as a function of orientation angle. The phase angle between mass flow and pressure is $\varphi_{m-p} = -30°$. 149

5.22 Comparison of simulated energy flows for an $L/D = 8$ pulse tube operating between 300 K and 60 K with mass flow amplitude of 1 g/s as a function of orientation angle 150

5.23 Comparison of simulated energy flows for an $L/D = 8$ pulse tube operating between 300 K and 60 K with mass flow amplitude of 2.5 g/s as a function of orientation angle 151

5.24 Comparison of simulated energy flows for an $L/D = 8$ pulse tube operating between 300 K and 60 K with mass flow amplitude of 4 g/s as a function of orientation angle 152

5.25 Net Cycle-averaged energy flow $\langle \dot{E} \rangle$ for 60 Hz simulations with 60 K cold end and 300 K warm end for an aspect ratio (L/D) of 8. The phase angle between mass flow and pressure is $\varphi_{m-p} = -30°$ 154

5.26 Normalized energy flow loss for 60 Hz simulations with 60 K cold end and 300 K warm end for an aspect ratio (L/D) of 8. The phase angle between mass flow and pressure is $\varphi_{m-p} = -30°$ 155

5.27 Net Cycle-averaged energy flow $\langle \dot{E} \rangle$ for 60 Hz simulations with 60 K cold end and 300 K warm end for an aspect ratio (L/D) of 4. The phase angle between mass flow and pressure is $\varphi_{m-p} = -30°$ 156

5.28 Normalized energy flow loss for 60 Hz simulations with 60 K cold end and 300 K warm end for an aspect ratio (L/D) of 4. The phase angle between mass flow and pressure is $\varphi_{m-p} = -30°$ 157

5.29 Net Cycle-averaged energy flow $\langle \dot{E} \rangle$ for 40 Hz simulations with 20 K cold end and 80 K warm end for an aspect ratio (L/D) of 8. The phase angle between mass flow and pressure is $\varphi_{m-p} = -30°$ 159

5.30 Normalized energy flow loss for 40 Hz simulations with 20 K cold end and 80 K warm end for an aspect ratio (L/D) of 8. The phase angle between mass flow and pressure is $\varphi_{m-p} = -30°$ 160

5.31 Contours of temperature and velocity vectors on the symmetry plane for an L/D=8, 80 K to 20 K pulse tube with 2.5 g/s mass flow amplitude 161

5.32 Contours of temperature pulse tube wall an L/D=8, 80 K to 20 K pulse tube with 2.5 g/s mass flow amplitude 162

5.33 Contours of temperature and velocity vectors on radial slices at the cold end and center of the pulse tube for an L/D=8, 80 K to 20 K pulse tube with 2.5 g/s mass flow amplitude 163

5.34 Net Cycle-averaged energy flow $\langle \dot{E} \rangle$ for 25 Hz simulations with 4 K cold end and 20 K warm end for an aspect ratio (L/D) of 8. The phase angle between mass flow and pressure is $\varphi_{m-p} = -30°$ 165

5.35 Normalized energy flow loss for 25 Hz simulations with 4 K cold end and 20 K warm end for an aspect ratio (L/D) of 8. The phase angle between mass flow and pressure is $\varphi_{m-p} = -30°$ 166

6.1 Coaxial validation cooler schematic and computational domain 170

6.2 Computational mesh used to simulate the coaxial PTR for CFD model validation 171

6.3 Images of the experimental coaxial cooler used to collect data for CFD model validation 173

6.4 Comparison of measured net cooling capacity at 0° to the correlated Sage model of the experimental coaxial PTR 176

6.5 Measured loss in net cooling capacity between 0° and 90° for the Raytheon Dual Use Cooler 178

6.6 Normalized energy flow loss as a function of pulse tube convection number for experimental data recorded from the Raytheon Dual Use Cooler at 90° angle of inclination 179

6.7 Comparison of normalized energy flow loss data experimentally measured and predicted by 3-D CFD 180

6.8 Normalized energy flow loss as a function of pulse tube convection number for experimental data recorded from Cooler A at 90° angle of inclination 182

6.9 Cooler B normalized energy flow loss data 183

6.10 Normalized energy flow loss as a function of cold end pulse tube convection number N_{PTC} 185

6.11 Logarithmic plot of normalized energy flow loss as a function of cold end pulse tube convection number N_{PTC} 186

A.1 Photograph of the rotating cryogenic test facility 195

A.2 Two-stage turbomolecular pump system 197

A.3 Conflat all-metal vacuum seals 198

A.4 O-ring sealing features in the GTCL test facility 199

A.5 Sensor and liquid coolant feedthroughs used in the rotating cryogenic vacuum test facility. 200

A.6 Sumitomo RDK-408D2 load map 202

A.7 Thermal bus bar design predictions of temperature difference as a function of thermal load and temperature 204

A.8 Thermal bus apparatus and calibration curves 207

A.9 Cross-section view of the oscillatory mass flow sensor 209

A.10 Phasor diagram relating mass flow to measured pressures across a heat exchanger 211

A.11 Mass flow calibration curve for 180 K operation and mass flow and pressure ratio as a function of compressor input power. 213

A.12 Mass flow calibration during calibration testing at 180 K 214

A.13 PWG mounted with custom stainless steel KF40 adapter 215

A.14 Schematic renderings of the pulse tube tilt test section assembly . . . 216

A.15 Experimental pulse tubes 217

A.16 Warm heat exchanger with liquid coolant loop 217

A.17 Indium seal in an O-ring groove 219

LIST OF SYMBOLS

0.1 Greek Symbols

α	Thermal diffusivity, m^2/s
α_S	Empirical fitting parameter used in N_{PTC}
β	Thermal expansion coefficient, K^{-1}
$\delta_{subscript}$	Boundary layer penetration depth, m
ε	Matrix material porosity
Γ	Argument of a trigonometric function, radians
γ	Ratio of specific heats
μ	Dynamic viscosity, kg/(m-s)
ν	Kinematic viscosity, m^2/s
φ	Phase angle, radians or $^\circ$
Φ	An arbitrary property
Ψ	Representative cell dimension, m
ψ	Angle $\pi/2 - \theta$, degrees
ρ	Density, kg/m^3
σ	Standard deviation used in error propagation
τ	Period of oscillation, s
$\bar{\bar{\tau}}$	Viscous stress tensor, N/m^2
θ	Angle of inclination, degrees
ω	Radian Angular Frequency, s^{-1}
ξ	Relative difference in primary variable between grids

0.2 English Symbols and Abbreviations

A	Cross-sectional area, m^2
AC	Aftercooler heat exchanger
AR	Aspect ratio, L/D
a	Amplitude of oscillating displacement, m
C	Sutherland's constant, K
$\bar{\bar{C}}$	Inertial resistance tensor, m^{-1}
C_P	Specific heat at constant pressure J/(kg-K)
CHX	Cold heat exchanger
c	Compliance, m/N
c_f	Forchheimer's inertial coefficient
D	Diameter, m
$\bar{\bar{D}}$	Viscous resistance tensor, m^{-2}
E	Energy, J
$\mathbf{E}$	Exergy, J
e	Relative error
F	External body force in momentum equation, N
FOM	Pulse tube figure of merit
f	Frequency, Hz
f_r	Fanning friction factor
$func$	Signum of relative error in mesh convergence
G	Gibbs Free Energy, J
GCI	Grid convergence index
g	Gravitational acceleration constant, m/s^2
Gr	Grashof number
H	Enthalpy, J
h	Specific enthalpy, J/kg

I	Identity matrix
J_n	Diffusion flux associated with species n, mol/(m^2-s)
K	Darcy Permeability, m^2
k	(real) Thermal conductivity, W/(m-K)
k	(complex) Spatial wave number, m^{-1}
L	Length (streamwise), m
$L(\theta)$	Normalized loss as a function of angle
l	Inertance, Pa-s^2/m^{-3}
$\dot{M}$	Mass flow amplitude in series expansion, kg/s
m	Mass, kg
N	Total number of elements in a computational mesh
N_{PTC}	Pulse tube convection number
n	Unit normal
P	Pressure, Pa
PR	Pressure ratio, peak to average
Pr	Prandtl number
p	Pressure, Pa
Q	Heat flow, W
q	Function used to compute grid convergence
R	Radius, m (except in ideal gas law and Ohm's law)
R	Ideal gas constant, J/(mol-K)
$R_{subscript}$	Resistance, Ω
Ra	Rayleigh number
Re	Reynolds number
r	Resistance, Ω
$r_{subscript}$	Grid refinement factor
S	Entropy, J/K

$S_{subscript}$	Source term in conservation equations
s	Specific entropy, J/(kg-K)
T	Temperature, K
t	Time, s
u	Specific internal energy (Section 2.1), J/kg
u	Velocity (Remaining sections), m/s
WHX	Warm heat exchanger
V	Volume, m^3
$\mathcal{V}$	Volume, m^3
w	Solenoidal portion of oscillating temperature field, K
X	Apparent model order
x	Cartesian ordinate direction x
Y	Species mass fraction in multiphase flows
y	Cartesian ordinate direction y
Z	Impedance, N-s/m
z	Cartesian ordinate direction z

0.3 Subscripts and Indices

avg	Average value of a property
C	Cold end property
c	Cold end property
$char$	Characteristic, as in characteristic length
cr	Critical value of a dimensionless number
d	Peak dynamic amplitude of a harmonic signal
e	Effective property
ext	Extrapolated

f	Indicates a fluid property
$fine$	Referring to the fineness of a computational grid
g	Referring to a gas property, used interchangeably with f
gci	Grid convergence index
H	Hot end property
h	Enthalpy, in the energy source term
i	Indicial notation denoting directions. $x = 1$, $y = 2$, $z = 3$
j	Indicial notation denoting directions. $x = 1$, $y = 2$, $z = 3$
k	Thermal
m	Matrix typically, as in a porous structure. Mass in Equation 3.1
n	Species index for multiphase flow
net	Referring to a net value
$open$	Open volume of enclosed fluid
osc	Oscillating
PT	Pulse tube
p	Particle, in packed beds
R	Regenerator
r	Reservoir, surge volume
ref	Reference
s	Referring to a solid material property
sup	Superficial, as in superficial velocity
$surf$	A property evaluated along a surface
T	Transition
v	Viscous
vib	Vibrational
w	Wall
0	Reference value of a property

0.4 Superscripts

δ	Referenced to Stokes boundary layer thickness
T	Transpose of a vector or matrix

0.5 Common Notations

$\langle\Phi\rangle$	A cycle-averaged property
$\dot{\Phi}$	The flow rate of a property
$\widetilde{\Phi}$	Time-varying portion of a property
$\overline{\Phi}$	Steady, or time-invariant portion of a property
$\lvert\widetilde{\Phi}\rvert$	Amplitude of a harmonically oscillating property
$\vec{\Phi}$	Vector in Cartesian coordinates
$\hat{\Phi}$	Unit direction vector

SUMMARY

Pulse tube cryocoolers (PTC) are among the most attractive choices of refrigerators for applications requiring up to 1 kW of cooling in the temperature range of 4-123 K as a result of the high relative efficiency of the Stirling cycle, the reliability of linear compressors, and the lack of cryogenic moving parts resulting in long life and low vibration signature [1]. Recently, PTCs have been successfully used in applications in the 150 K range, extending the useful range of the device beyond the traditional cryogenic regime. A carefully designed cylindrical cavity referred to as the pulse tube replaces the mechanical expander piston found in a Stirling machine. A network consisting of the pulse tube, inertance tube, and surge volume invoke out-of-phase pressure and mass flow oscillations while eliminating all moving parts in the cold region of the device, significantly improving reliability over Stirling cryocoolers.

Terrestrial applications of PTCs expose a fundamental flaw. Many PTCs only function properly in a narrow range of orientations, with the cold end of the device pointed downward with respect to gravity. Unfavorable orientation of the cold head often leads to a catastrophic loss of cooling, rendering the entire cryocooler system inoperable. Previous research indicates that cooling loss is most likely attributed to secondary flow patterns in the pulse tube caused by free convection. Convective instability is initiated as a result of non-uniform density gradients within the pulse tube. The ensuing secondary flow mixes the cryogen and causes enhanced thermal transport between the warm and cold heat exchangers of the cryocooler.

This study investigates the nonlinear stabilizing effect of fluid oscillation on Rayleigh-Bénard instability in a cryogenic gas subject to misalignment between gravitational body force and the primary flow direction. The results are directly applicable to the

flow conditions frequently experienced in pulse tube refrigerators (PTRs). Research has shown that the convective component can be partially or completely supressed by parametrically-driven fluid oscillation as a result of sinusoidal pressure excitation; however, a reliable method of predicting the influence of operating parameters has not been reported.

In this dissertation, the entire PTR domain is first fully simulated in three-dimensions at various angles of inclination using a hybrid method of finite volume and finite element techniques in order to incorporate conjugate heat transfer between fluid domains and their solid containment structures. The results of this method identify the pulse tube as the primary contributor to convective instability, and also illustrate the importance of pulse tube design by incorporating a comparison between two pulse tubes with constant volume but varied aspect ratio. A reduced domain that isolates the pulse tube and its adjacent components is then developed and simulated to improve computational efficiency, facilitating the model's use for parametric study of the driving variables. A parametric computational study is then carried out and analyzed for pulse tubes with cold end temperatures ranging from 4 K to 80 K, frequencies between 25-60 Hz, mass flow - pressure phase relationships of -30° (mass lags pressure) and +30° (mass leads pressure), and Stokes thickness-based Reynolds numbers in the range of 43-350, where the turbulent transition occurs at 500.

In order to validate the computational models reported and therefore justify their suitability to perform parametric exploration, the CFD codes are applied to a commercially developed single stage PTR design. The results of the CFD model are compared to laboratory-measured values of refrigeration power at temperatures ranging from 60 K to 120 K at inclination angles of 0° and 91°. The modeled results are shown to agree with experimental values within 8.5% of net pulse tube energy flow with simulation times of approximately six days using high performance computing (HPC) resources through Georgia Tech's Partnership for Advanced Computing (PACE) cluster, and

10 days on a common quad-core desktop computer.

The results of the computational parametric study as well as the commercial cryocooler data sets are compiled in a common analysis of the body of data as a whole. The results are compared to the current leading pulse tube convective stability model to improve the reliability of the predictions and bracket the range of losses expected as a function of pulse tube convection number. Results can be used to bracket the normalized cooling loss as a function of the pulse tube convection number N_{PTC}. Experimental data and simulated results indicate that a value of N_{PTC} greater than 10 will yield a loss no greater than 10% of the net pulse tube energy flow at any angle. A value of N_{PTC} greater than 40 is shown to yield a loss no greater than 1% of the net pulse tube energy flow at all angles investigated.

The computational and experimental study completed in this dissertation addresses static angles of inclination. Recent interest in the application of PTRs to mobile terrestrial platforms such as ships, aircraft, and military vehicles introduces a separate regime wherein the angle of inclination is dynamically varying. To address this research need, the development of a single axis rotating cryogenic vacuum facility is documented. A separate effects apparatus with interchangeable pulse tube components has also been built in a modular fashion to accommodate future research needs.

CHAPTER I

INTRODUCTION

Cryogenics is the study of low temperature phenomena below 123 K, the temperature below which most commonly occuring gases liquefy. The term cryogenics is derived from the Greek words "kryos" meaning frost and "genic", meaning to produce; therefore, cryogenics can be thought of as the science of producing extreme cold. While a number of unsustainable methods are used to achieve this temperature regime including boiling of liquified gases such as nitrogen (LN2) or helium (LHe), cryocoolers provide continuous cooling capacity at cryogenic temperatures for extended periods of time. Cryocoolers can be broken down into a number of basic types including Joule-Thompson, reverse turbo-Brayton, Stirling, Gifford-McMahon (G-M), and Stirling-type pulse tube. This dissertation study focuses on thermal-fluid phenomena that occur during prototypical conditions present in Stirling-type pulse tube cryocoolers.

Cryocoolers are commonly used to cool high performance devices such as infrared focal plane arrays, and enable the practical use of superconducting materials like Niobium in superconducting quantum interference devices (SQUIDs) and superconducting quantum interference filters (SQIFs), high-power magnets used in particle accelerators and laboratory studies, magnetic shields, and electrical transmission lines. Cryocoolers are considered an enabling technology in the future of space exploration as well as the field of quantum computing. Cryocoolers are also used in industrial applications including the liquefaction of gases, vacuum chamber cryopumps, and magnetic resonance imaging (MRI) magnets.

Stirling-type pulse tube cryocoolers (PTCs) are particularly attractive for many

applications owing to their inherent simplicity and robust nature, requiring no moving parts in the expander. The lack of moving parts also yields a low vibration signature, providing an additional advantage over many other cryocooler types. While PTCs have numerous advantages over competing technologies, many current pulse tube implementations have a fundamental disadvantage when used in the presence of gravity: most PTCs only function properly in a limited range of stable orientations within about 45° of the optimal orientation in which the cold end is directed downward with respect to gravity. Changing the orientation of the cold head often leads to a catastrophic loss of cooling, rendering the entire cryocooler system inoperable. The purpose of the current research effort is to identify the drivers of instability through an experimentally-validated computational fluid dynamics (CFD) approach and to develop a prediction methodology to aid designers in minimizing orientation sensitivity prior to building hardware.

1.1 Executive Research Summary

A pulse tube replaces the expander piston in a traditional Stirling cooler via a carefully designed unfilled tube and an impedance network consisting of an inertance tube and surge volume, which provides the required phase relationship between mass flow and pressure perturbations. The key responsibilities of the pulse tube are given below as a prelude to the detailed thermal and hydrodynamic analysis that follows in Chapter 2. The ideal pulse tube:

- provides a thermal buffer between the cold and warm heat exchangers
- transmits acoustic power and enthalpy flow across a temperature gradient (from cold to hot) with minimized entropy generation rate
- creates a thermally stratified, oscillating slug of gas that acts as a hydrodynamic piston

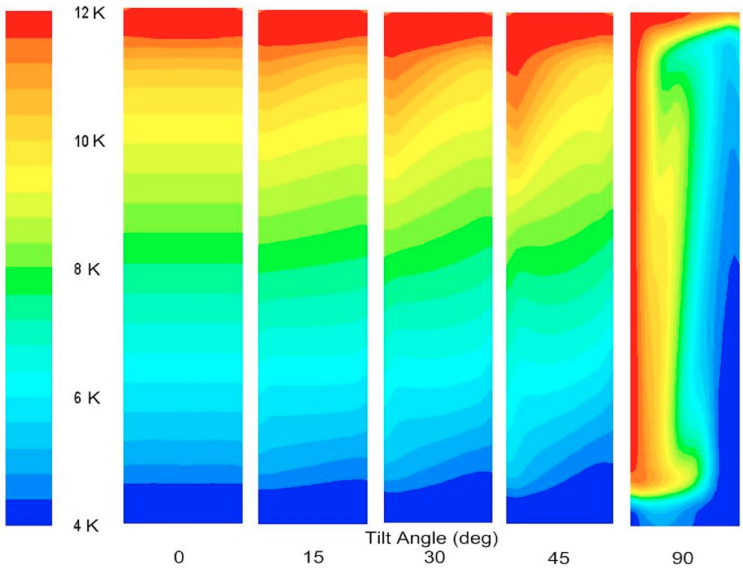

Figure 1.1: Temperature contours of the pulse tube component in increasing orientation angles compared to the vertical 0° orientation with the cold end pointed down.

If any of the critical operating parameters of the pulse tube are not fulfilled, the cooler will not operate optimally. As the pulse tube is an open cylindrical flow channel and experiences a thermal gradient by design, it is prone to instability in any orientation where the denser cold gas is situated at a higher potential then the hot gas at the opposing end. As the pulse tube is tilted with respect to the gravitational vector and approaches a critical angle, buoyancy forces increase in magnitude and free convection can ensue. The temperature along the symmetry plane of an example pulse tube is shown in Figure 1.1 as an illustration.

The flow scenario present within inclined pulse tubes is a nonlinear interaction between the intended pure oscillating flow experienced in correctly oriented pulse tubes, and a convective cell (or cells) resulting from a net moment about the centerline of the tube caused by asymmetry of the gravitational body force. The literature on tilted pulse tubes commonly refers to the convective phenomenon as Rayleigh-Bénard convection [2] since the scenario is equivalent to a layer of fluid heated from below. The difference in this case is that the heat flows from cold to hot by design; however,

from a buoyancy perspective the two cases are analogous. Free convection can be dynamically stabilized if the inertial forces related to the flow oscillation are sufficient to suppress the asymmetric gravitational body force [3] as a result of an opposing net torque created by a nonlinear inertial effect of the vibrating gas. Currently there is no analytical model that reliably predicts the degree of convective stability of pulse tubes, and none of the previously reported models are capable of predicting the magnitude of the cooling loss associated with the adverse gravitational effect.

1.2 Thesis Overview and Outline

This section outlines the essential goals of this dissertation work and gives a general outline of the organization of the thesis document. The investigation relies on a simulation-based approach to elucidating the fundamental physical mechanisms driving the stabilization of Rayleigh-Bénard convection in inclined pulse tubes. The resulting analysis is a combination of an approach using computational fluid dynamics (CFD) simulation validated against measured data from operating PTRs, and a computational study used to parametrically isolate the contribution of each affecting operating condition determined to carry importance.The goals of the dissertation were to:

1. Experimentally measure and characterize the off-axis performance of commercial cryocoolers for which all critical operating conditions and component geometries are known and quantified.

2. Develop a one-dimensional system level model that replicates the performance of the commercial cryocoolers studied in a vertical, cold end down orientation.

3. Develop and execute a comprehensive three-dimensional PTR system computational fluid dynamics (CFD) model (a system-level model) that identifies the system components that experience orientation sensitivity. This system-level

model requires significant solution time.

4. Develop a reduced three-dimensional CFD model (a component-level model) capable of replicating the off-axis performance measured in goal 1, informed by boundary conditions determined by the model developed in goal 2. The purpose is to facilitate an expedient method of predicting losses within some tolerable level of error.

5. Validate the component-level modeling using experimental cryocooler data. Perform a parametric analysis on the correlated CFD model to separate the effects of the key variables that characterize pulse tube operation.

6. Develop an experimental facility to perform separate effects tests on pulse tubes operated in any orientation, both static and time varying.

The outline of this dissertation is as follows:

Chapter 1: In the remainder of this chapter the basic operating principles through which a pulse tube refrigerator (PTR) functions will be presented, followed by an account of the historical development of these devices, giving examples of the architectures and staging configurations commonly encountered.

Chapter 2: After briefly describing the essential background of PTRs, the thermodynamics and gas dynamics critical to the understanding of pulse tube operation as well as the influence of misaligned gravitational body forces is presented in Chapter 2. The concept of Rayleigh-Bénard instability and the influence of parametrically driven excitation are developed, and a literature survey of the past efforts to identify and quantify these effects is given.

Chapter 3: In Chapter 3 an in-depth description of the numerical modeling methodologies used in this study is presented along with the solution theory. This includes one-dimensional system-level models based on thermoacoustic principles, as well as

the three-dimensional half-symmetric models used to characterize gravitational effects.

Chapter 4: Chapter 4 presents the method and resuts of a full PTR system simulation set in 3-D half-symmetry at various inclination angles. The basic methodology used to thermodynamically design a PTR is described in detail. Two model sets with identical volume but varied pulse tube aspect ratio are investigated. The results isolate orientation sensitivity predominantly to the pulse tube, motivating the development of a more nimble pulse tube model that isolates the sensitive region of the domain.

Chapter5: In this chapter, a methodology is presented for reduced domain simultaion of the pulse tube and neighboring heat exchangers. A parametric evaluation study is performed to yield stability data for pulse tubes operating with cold end temperatures as low as 4 K and as high as 80 K. An in depth analysis of the flow fields and trends observed during simulation is included.

Chapter 6: This chapter presents the experimental methodology used by the manufacturer to collect data from commercial cryocoolers used to validate the component-level CFD model developed in Chapter 5. Once the models and experimental facilities are well-defined, a set of results for commercial cooler testing are presented and analyzed. Finally, all results obtained through simulation and experimental data collection are combined on common axes and compared to the pulse tube convection number to identify trends and develop design criteria.

Chapter 7: The closing chapter summarizes the key findings of this investigation. Additionally it suggests a means to extend the utility of this study in future work to develop a more comprehensive body of results beyond what can be practically achieved through computational modeling.

Appendix A: Development of a separate effects testing facility capable of providing an environment as low as 4.2 K. The facility can also provide cooling at up to two

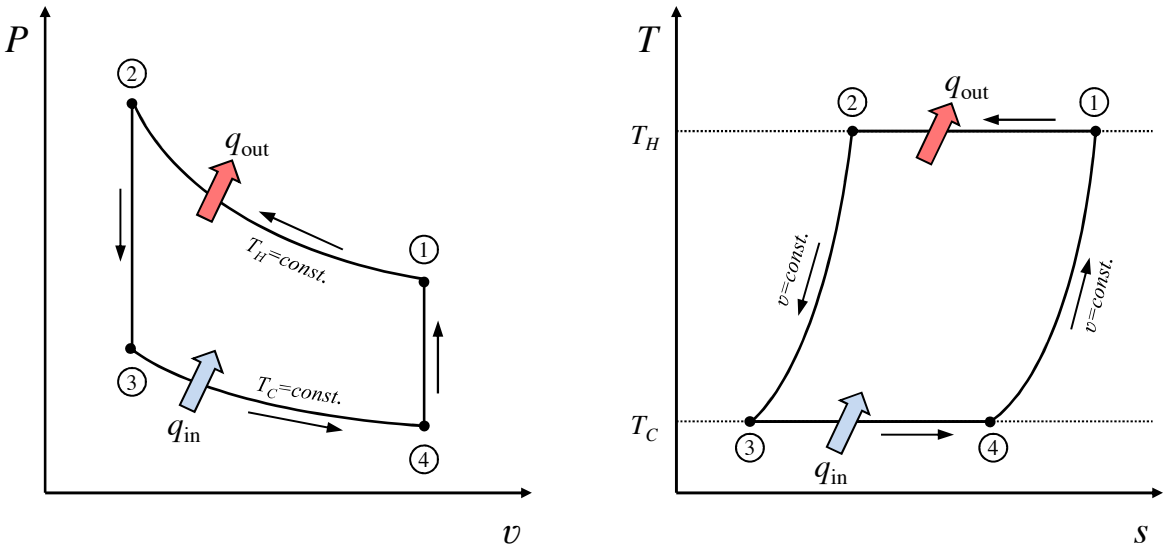

Figure 1.2: The ideal Stirling cycle thermodynamic processes for refrigeration. **(a.)** P-v diagram. **(b.)** T-s diagram.

other controllable temperatures using G-M coolers. Rotation of the entire chamber facilitates measurement of off-axis performance for pulse tube cryocoolers and components. The facility is also well suited to perform low temperature regenerator testing in any orientation.

Appendices B and C: These appendices contain useful information regarding the exact setup and post-processing methods used to generate the data contained in this report. Appendix B presents all code associated with the CFD modeling performed in ANSYS FLUENT. Appendix C presents the various MATLAB codes used to design and post-process the simulations performed.

1.3 The Stirling Cycle and Pulse Tube Cryocooler Operation

1.3.1 The Stirling Cycle for Refrigeration

PTC operation is based on the Stirling thermodynamic cycle. The cycle was patented by Robert Stirling in 1816 as a means for producing mechanical motion from a source of thermal energy [4]. As with many thermodynamic power cycles, the Stirling cycle

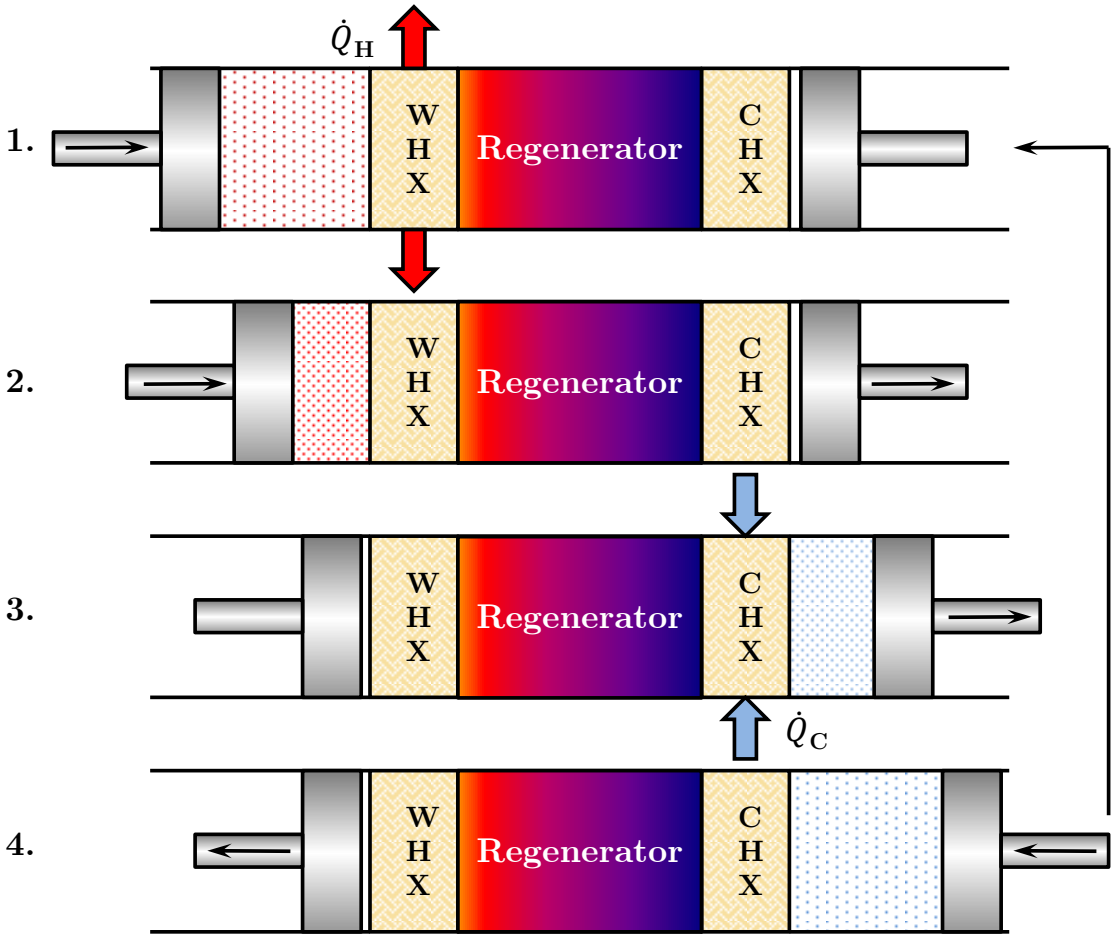

Figure 1.3: Pictorial representation of the four parts of the Stirling cycle. A detailed explanation of each process 1-4 is outlined in the text.

can be driven in reverse to convert a mechanical input source into useful refrigeration. In 1834, John Herschel proposed the idea of reversing the Stirling cycle to produce ice [5], but it was not until 1861 that the idea was successfully implemented by Alexander Kirk [6]. Cryogenic temperatures were not produced using the Stirling cycle until 1946 when a Dutch company drove a Stirling engine in reverse using a motor with helium as the working fluid instead of air. The device was able to liquefy air on the thermal intercept [7]. Currently, the most common working gas is ^{4}He due to its high heat capacity and thermal conductivity relative to other gases at cryogenic temperatures as well as its extremely low condensation point, allowing it to remain gaseous at temperatures below 4 K when pressurized. The helium-3 isotope (^{3}He) is also used in high performance applications due its thermodynamic advantages which improve efficiency and its lower liquefaction point near 2 K; however, the rarity (only 1 molecule per 1000 helium molecules) and prohibitive cost associated with isolating ^{3}He prohibit its widespread use.

Idealized *P-v* and *T-s* diagrams of the Stirling cycle are shown in Figure 1.2, where the numerical labels correspond to the graphics shown in Figure 1.3. A Stirling refrigerator consists of a sinusoidally driven compressor piston, a warm heat exchanger that rejects heat to the surroundings, a regenerative heat exchanger matrix which holds and releases thermal energy during various portions of the cycle, a cold heat exchanger which accepts a thermal load from the object or space to be cooled, and an expander piston which oscillates in a controlled phase relationship relative to the compressor piston. The heat exchangers and regenerator are typically composed of a porous material such as diffusion bonded screen packs or epoxyset packed sphere beds, though heat exchangers are also frequently made by cutting radial slots in a copper block. The regenerator matrix material is chosen for maximum volumetric heat capacity over the temperature range of interest. For clarity, the Stirling cycle is broken into four simplified processes as illustrated in Figure 1.3, though in practice

the processes are not discrete due to the sinusoidal motions of the pistons. These processes are summarized as follows:

1-2: The compressor piston advances toward the expander piston. As the volume of the working gas space decreases, the temperature of the working fluid rises. Since the compression space gas temperature is higher than the surroundings, the heat of compression is rejected via the warm heat exchanger.

2-3: The compressor and expander piston move in phase toward the cold end of the refrigerator. The gas temperature is locally greater than that of the porous matrix material, therefore the regenerator accepts heat as the fluid advances toward the cold end. The result is a pre-cooling effect where the gas entering the expansion space is nearly at the cold temperature of the device.

3-4: As the compressor piston bottoms in its forward stroke, the expander piston continues to advance. The result is a net increase in the volume of the working fluid, decreasing the temperature of the working fluid everywhere in the cooler as the pressure drops and the gas expands. The cold fluid is then at a lower potential than the cold heat exchanger, and thus accepts a thermal load at low temperature.

4-1: Both pistons move in tandem toward the warm end of the system, driving the working fluid from cold to hot. The fluid, now having accepted the applied thermal load from the refrigerated space, moves through the regenerator picking up the heat deposited in the matrix material during process 2-3 and moving it toward the warm compression space. The heat is subsequently rejected when process 1-2 resumes.

The Stirling cycle is of interest because the ideal cycle is perfectly reversible; therefore in the absence of losses, the Stirling cycle approaches the Carnot cycle, which represents the optimum efficiency achievable for a heat engine operating between two fixed temperature reservoirs. In reality, irreversibilities in the system such as conduction losses, real gas effects, pressure drop through the regenerator, and imperfect heat transfer in the hot and cold heat exchangers drive the efficiency of practical Stirling machines well below Carnot.

Maximum cooling power is achieved when the pistons in a Stirling machine are driven 90° degrees out of phase, where the expander motion lags the compressor. In practice, the expander piston phasing is often controlled and adjusted to optimize the cooling power. A common mode of failure for Stirling cryocoolers is at the seal between the expander piston and the housing cylinder. Failure can occur for a number of reasons including wear caused by thermal cycling that results in unequal contraction and expansion between the piston and the housing cylinder, as well as wear caused by contaminants in the working fluid which migrate to the seal gap. Unit failure also commonly occurs in the mechanical balancers used to mitigate piston-induced vibration, which can include tuned spring-mass passive absorbers in low-cost tactical coolers or actively driven flexure spring assemblies for more expensive space-qualified versions. These failure modes significantly decrease the life expectancy of Stirling coolers and served as the motivation for the pulse tube cryocooler (PTC).

1.3.2 Pulse Tube Refrigerator Operating Principles

The PTR illustrated in Figure 1.4 operates through a set of of principles identical to the Stirling cooler. The critical difference is that the PTR replaces the active expander piston with a passive network consisting of a hollow tube, often referred to as a pulse tube, a buffer tube, or a compliance tube depending on the temperature range, as well as an impedance network including an inertance tube and surge volume.

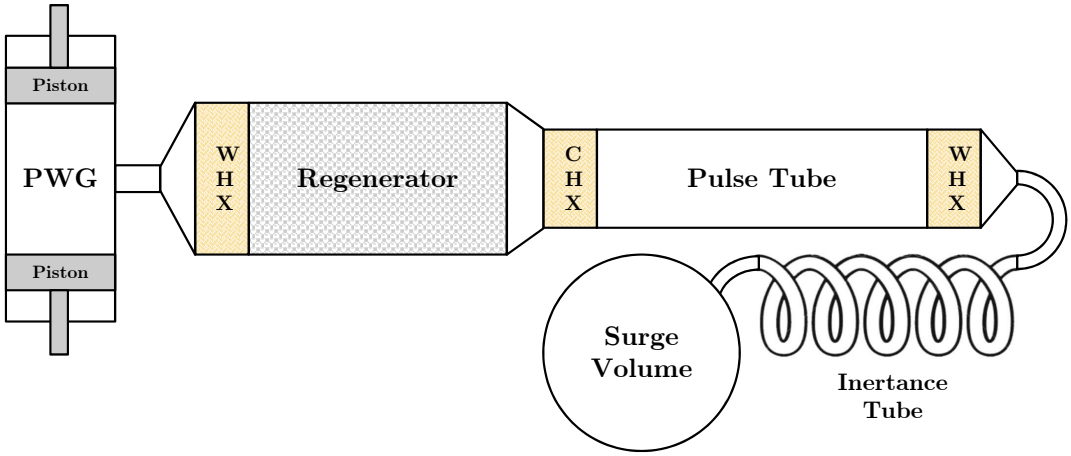

Figure 1.4: The linear inertance tube pulse tube refrigerator (ITPTR). PWG is a dual opposed piston pressure wave generator (*"compressor"*), WHX are warm heat exchangers, and CHX is the cold heat exchanger.

These components can be tuned to yield the proper relationships between mass flow and pressure to provide a net transport of enthalpy across the pulse tube, from cold to hot. One can imagine that the ideal pulse tube creates a unique hydrodynamic "virtual piston" effect wherein a thermally stratified slug of laminar (non-mixing) flow oscillates within the pulse tube domain. Pulse tubes are typically designed such that >80% of the fluid remains within the tube over the course of a cycle (*the piston*) while the gas at the extreme ends pass through either porous or slotted heat exchangers, which also serve as flow straighteners.

Confusion commonly arises when trying to rectify the Stirling cycle principles with pulse tube operation due to the misunderstanding of the oscillatory flow regime itself. While it is convenient to illustrate the working fluid having large net displacements which take the hot fluid all the way to the cold end in back, in reality each parcel of gas has a very small oscillation amplitude and only traverses a small fraction of the length of the cooler during its excursion. To be thorough, the *P-v* and *T-s* diagrams presented Figure 1.2 only accurately represent the thermodynamic cycle seen by each local parcel of gas, and each parcel sees a different cycle. In reality, the proper operation of the PTR as a refrigerator requires that the system does not operate

as an ideal Stirling cycle [8]. In fact, if the processes undergone by each gas parcel were ideal the parcel would oscillate back and forth with oscillating temperature as a function of the pressure field, but no net work would be done and no refrigeration would occur.

1.3.3 Historical Development of Pulse Tube Refrigerators

Pulse tube refrigerators are not a new development. The concept was first proposed by Gifford and Longsworth in the 1960's [9, 10]. The initial device they developed is now referred to as the basic pulse tube refrigerator (BPTR) as shown in Figure 1.5(a). The original design had no phase shifting device on the warm end of the pulse tube to control the phase relationship between mass flow and pressure oscillation in the cooler. As a result of the lack of phase shifter, the only heat pumping effect observed was due to shuttle heat transfer between the fluid and the pulse tube wall [11]. The reader is urged to read more on shuttle heat transfer in Chapter 2. Using helium as the working gas and a driving frequency of approximately 1 Hz, Gifford and Longsworth were able to achieve a temperature of 124 K in a single stage BPTR.

Little work was done to improve the performance of PTCs until the early 1980's. Mikulin, Tarasov and Shkrbyonock were able to reach 105 K using air as the working gas by adding a sharp-edged orifice and surge volume to the warm end of the pulse tube, which is now referred to as the orifice-type pulse tube refrigerator (OPTR) [12]. The surge volume was designed to have significantly larger volume compared to other components in the system, such that the pressure in the reservoir remained relatively constant over the course of the cycle. The OPTR operated on a fundamentally different heat transfer process compared to the BPTR as the orifice allowed control over the phase relationship between mass flow and oscillating pressure, resulting in the pumping of heat from cold to hot via a net flow of enthalpy across the pulse tube. At low frequency ($\sim$1 Hz) the surface heat pumping effect present in the

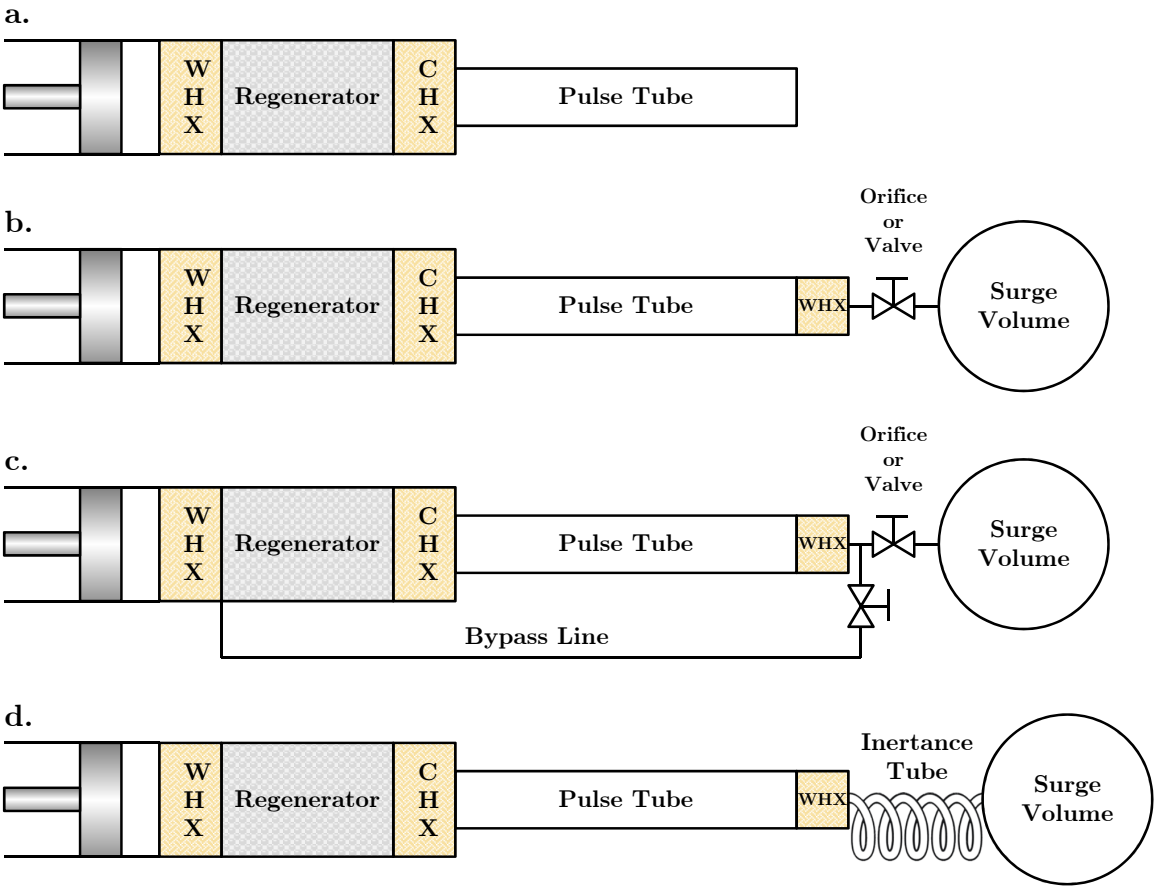

Figure 1.5: Schematic representation of PTR evolution from 1964-present. **(a)** Basic pulse tube refrigerator (BPTR). **(b)** Orifice pulse tube refrigerator (OPTR). **(c)** Double orifice pulse tube refrigerator (DIPTR). **(d)** Inertance tube pulse tube refrigerator (ITPTR).

BPTR actually becomes a loss for the OPTR. At the relatively higher frequencies (∼5-10 Hz) that OPTR's were initially operated, the shuttle loss is minimized as the period of oscillation becomes increasingly small compared to the thermal time constant of the wall.

Maturation of the OPTR resulted in the replacement of the fixed orifice with a needle valve by Radebaugh, Zimmerman, Smith and Louie at NIST in 1981 [13]. The needle valve allowed for easy optimization of the flow impedance. Using helium as the working fluid, the NIST research group was able to reach a temperature of 60 K. The extension of pulse tube applications to a temperature range useful for cooling detectors drove interest in development of the pulse tube refrigerator to achieve higher efficiency.

In 1990 Zhu, Wu and Chen [14] introduced the concept of adding a secondary orifice after the primary orifice which allows approximately 10% of the gas from the compressor to bypass the regenerator and other porous components, aiding the compression of the gas in the warm end of the pulse tube. This configuration is referred to as the double-inlet pulse tube refrigerator (DIPTR). The result of this configuration was improved efficiency, as the bypass gas no longer had to sustain losses through the porous components. A negative effect of the new configuration was later uncovered and termed DC streaming, a result of the line connecting the warm end to the compressor creating a possible flow loop driven by asymmetric impedance of the secondary orifice [15]. The result of this small secondary flow is a relatively large enthalpy flow from the hot end to the cold end. When properly mitigated either by the appropriate choice of valves or orifices, or by using a tapered pulse tube [16], DIPTRs have reached temperatures lower than 35 K [17].

A result of years of development showed that pulse tube performance could be optimized when a phase angle of -30° between mass flow and pressure is achieved at the cold end of the pulse tube, where the negative sense indicates that mass flow lags

pressure. This regime has been shown to minimize the flow losses in the regenerator as it requires the minimum mass flow to achieve the required acoustic power flow, and hence minimizes pressure drop across the regenerator. OPTRs and DIPTRs were only able to achieve a positive phase relationship which severely limited the theoretical maximum efficiency that could be achieved. The need for a more effective means of phase shift sparked much of the development in the late 1990's.

In 1996 Godshalk et al. reported the beneficial effect of inertance on pulse tube performance [18]. In 1997 Zhu, Zhou, Yoshimura and Matsubara [19] and Gardner and Swift [20] reported the phase shifting effects of adding a long, narrow tube between the pulse tube and the surge volume. The inertance effect caused by the momentum of the high velocity gas in the narrow tube is analogous to the inductance effect observed in electrical systems. The orifice was eventually removed altogether, resulting in all of the flow from the pulse tube going first through the warm heat exchanger, then directly into the inertance tube. This configuration, dubbed the inertance tube pulse tube refrigerator (ITPTR) improved efficiency significantly while also eliminating the circulation loop that causes DC streaming. Currently, most meso-scale ($\geq$10 cc total cooler volume) pulse tube cryocoolers produced are ITPTR configurations.

In order to provide an appropriate phase shift, the length and diameter of the inertance tube must be optimized as the configuration can actually provide too much shifting in certain situations. In other cases, additional phase shifting has been achieved by adding a second inertance tube of a different diameter [17]. The inertance effect only appears when frequency is sufficient, resulting in the gradual increase in operating frequency over the years. Current coolers typically operate at frequencies of 40-60 Hz, though cascaded low-temperature coolers pushing toward 4 K tend to operate at frequencies of 20-40 Hz. Various form-factors of the ITPTR are used in practice, and it is common for a two to four stage cascaded arrangement of ITPTRs to be used in order to reach temperatures as low as 2 K. These arrangements will be

discussed in Section 1.3.4.

In addition to efficiency improvements, in recent years much effort has been directed at reducing the physical size of PTRs owing to more rigorous mass and volume constraints on tactical and space payloads. In 2008, Garaway and Grossman [21] published a report on a miniature pulse tube cooler with total volume (less the compressor) of 2.3 cc that reached a temperature of 146 K. A review of additional micro-scale developments is given by Conrad [22, 23] and an example cold head is shown in Figure 1.6. One consideration that affects the design of these meso- and micro-scale cryocoolers is the relative thickness of the boundary layers compared to the overall dimensions. The boundary layers are characterized in terms of the thermal penetration depth given in Equation 1.1, and the viscous penetration depth shown in Equation 1.2 [24].

$$\delta_k = \sqrt{\frac{2k_f}{\omega \rho_f C_{P,f}}} = \sqrt{\frac{2\alpha_f}{\omega}} \tag{1.1}$$

where the subscript f denotes properties of the working fluid. k is the thermal conductivity, ω is the radian angular frequency of oscillation, ρ is the fluid density, C_P is the specific heat capacity, and α is the thermal diffusivity.

$$\delta_v = \sqrt{\frac{2\mu}{\omega \rho_f}} = \sqrt{\frac{2\nu}{\omega \rho_f}} \tag{1.2}$$

where μ and ν are the dynamic and kinematic viscosities of the fluid, respectively. These representative length scales become important in both the regenerator, where good thermal contact is necessary for performance and therefore the characteristic pore size must be on the order of the thermal penetration depth, as well as in the pulse tube, where viscous losses need to be minimized and the viscous penetration must be significantly smaller than the hydraulic diameter. The remedy in the regenerator component is to scale the dimensions of the regenerator material. The requirement for significantly reduced pore sizes typically dictates the use of finely woven meshes on the order of #635 or finer. In order to reduce the viscous penetration, the fill pressure

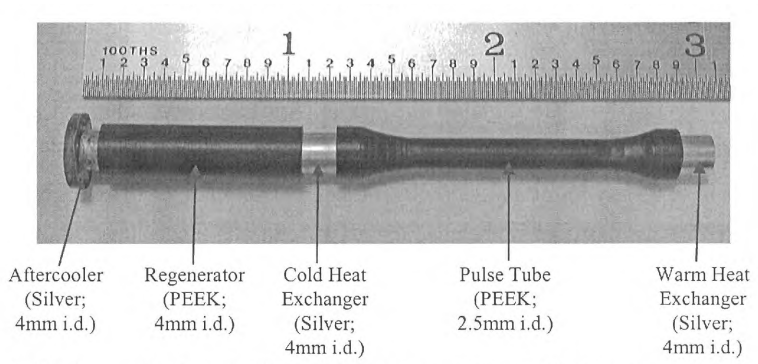

Figure 1.6: A micro-scale PTC prototype with total volume of approximately 4cc designed by Georgia Tech Cryo Lab (GTCL) and Virtual Aerosurface Technologies (VAST).

and operating frequencies significantly increase. Micro-scale coolers typically operate in the range of 150-350 Hz and utilize fill pressures up to 5 MPa [25].

1.3.4 Pulse Tube Cryocooler Configurations

A wide variety of PTR configurations are used in practice as shown in Figure 1.7. PTRs were originally designed in the linear configurations depicted in Figures 1.4, 1.5, and 1.7 due to the mechanical simplicity of the linear architecture. Although this configuration imposes minimal design constraints based on manufacturability, the absence of a salient cold tip is often inconvenient in terms of applying a thermal load, while also requiring two separate locations where ambient heat rejection must occur. To address these deficiencies, the U-tube and coaxial configurations shown in Figure 1.7 were developed. The advantages of these configurations are three-fold: easy access to a cold tip, a shorter form factor, and the ability to orient the temperature gradients of all components in the same direction, stabilizing the density gradients in all components. The difficulty in implementing these alternative configurations arises due to real engineering constraints resulting from the required geometric relationships between parts that must insert into a common cold block. Often the relative lengths between the pulse tube and regenerator impose a maximum mismatch. Performance is often compromised to some extent for ease of manufacture.

The coaxial configuration requires the most stringent set of constraints to properly implement. Nesting the pulse tube component within an annular regenerator can either be a benefit or a detriment depending on the relative temperature profiles. Since the two components are in thermal contact, a mismatch of the temperature gradients can lead to unwanted heat transfer; however, the configuration can effectively eliminate radiation heat transfer between the pulse tube wall and the surroundings and provides an efficiency improvement if the components are designed with closely matching temperature profiles. An additional benefit to this concentric arrangement is that the pulse tube is no longer a pressure vessel as it is contained within the regenerator, therefore the wall thickness can be significantly reduced allowing for a reduction in parasitic conduction within the pulse tube wall.

In order to reach temperatures lower than approximately 30 K, a cascaded arrangement of PTRs is typically employed, although hybrid architectures are common as well where each stage is selected for the temperature range for which it is particularly well suited. An example of a commercially successful hybrid configurations is the combination of Stirling and PTR stages patented by Raytheon. which have reached temperatures as low as 5 K [26]. Cascaded PTRs are also frequently used to pre-cool adiabatic demagnetization refrigerators (ADRs) or dilution refrigerators to reach temperatures in the 50 mK range and lower.

Cascaded multi-stage PTRs can take on any combination of the form factors illustrated in Figure 1.7 and have been successfully developed in 2, 3, and 4 stage implementations. The staging can be accomplished in either a fluidically-coupled or a thermally-coupled arrangement as shown in Figure 1.8. In a fluidically-coupled arrangement, the stages all share a common compressor and flow is split at the cold heat exchangers (CHX) of each stage, where a portion of the flow is expanded in the pulse tube of the current stage and a portion is siphoned off to the next stage to reach a lower temperature prior to expansion.

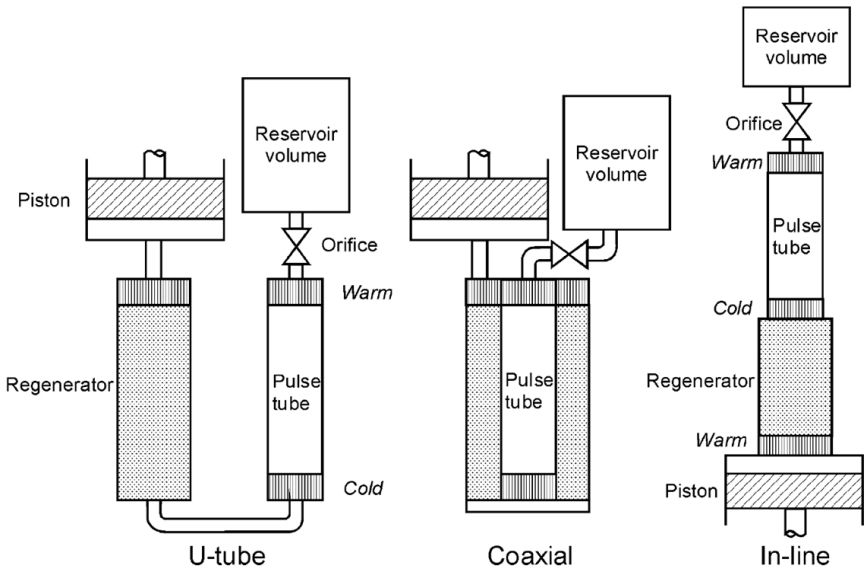

Figure 1.7: Commonly used form factors for PTRs, reproduced from [17]. Configurations shown are for OPTRs; however, the same principles can be applied to any variant including ITPTRs

In a thermally-coupled arrangement, the working gas is split directly downstream of the compressor with a portion of the gas directly accessing each stage. The stages are thermally linked, typically using an OFHC copper thermal bus linking the CHX of the first stage to a thermal anchoring point in the following stage regenerator. In a thermally-coupled system, the earlier stages can be thought of as precoolers for the lower stages. In addition, there is a new part called the precooling regenerator that is required to support the temperature gradient between the ambient temperature gas exiting the compressor and the gas temperature at the entrance to the second stage. The precooling regenerator is designed to maximize the acoustic power flow while simultaneously minimizing the enthalpy flow from hot to cold.

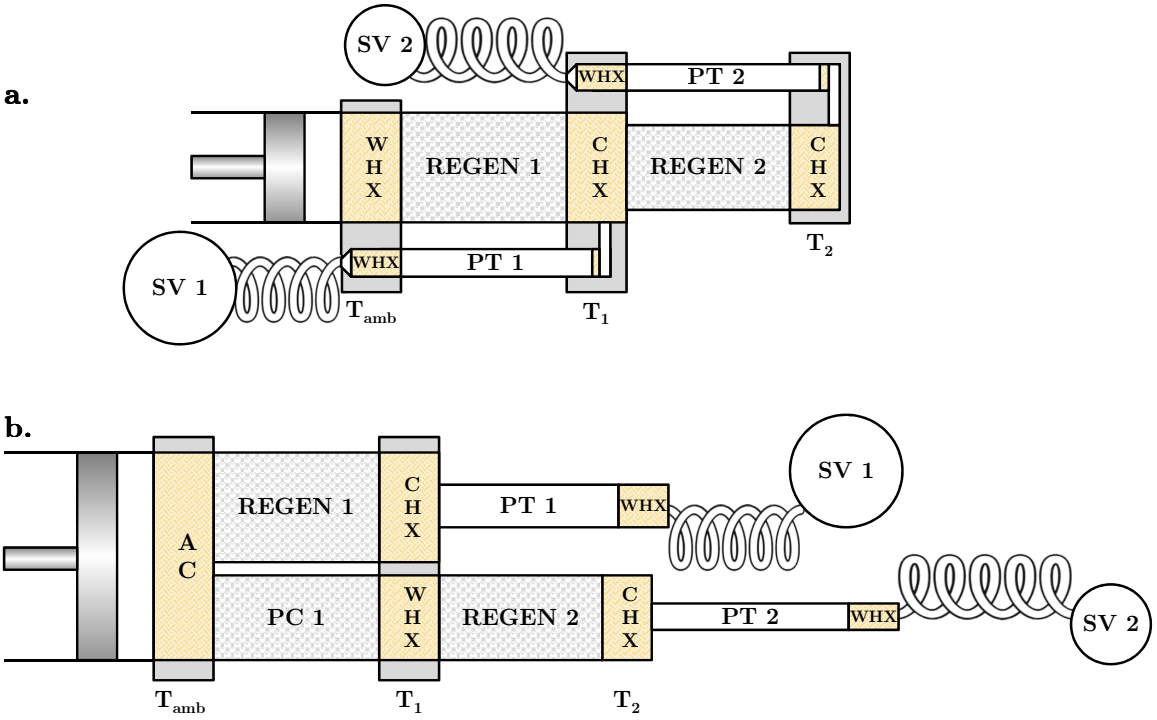

Figure 1.8: Comparison of cascaded multi-stage PTR arrangements. Two stage systems are shown for illustration purposes, though up to five have been used in practice. CHX denotes a cold heat exchanger, WHX is a "warm" heat exchanger, PC is a precooling regenerator, REGEN is a regenerator, PT is a pulse tube, SV is a surge volume, and AC represents an ambient temperature aftercooler. The variables T_{amb}, T_1, and T_2 are the staging temperatures in order of decreasing magnitude. **(a)** Fluidically-coupled arrangement. **(b)** Thermally-coupled arrangement.

CHAPTER II

PULSE TUBE BACKGROUND AND THEORY

2.1 Pulse Tube Thermodynamics and Hydrodynamics

In the current section, the key thermodynamic aspects of pulse tube operation will be developed and presented as they pertain to the pulse tube itself and its neighboring components. These thermodynamic principles introduce the energy flows of interest in the pulse tube, regenerator, and heat exchangers. The expressions derived are used to post-process numerical simulations using monitored properties of the system to isolate the energy flows and compare the changes in each as a function of gravitational body force. For a more complete analysis of the system-level thermodynamics, the reader is urged to review the thorough developments given by Kittel [27], Kittel, Kashani, Lee, and Roach [28] and de Waele, Steijaert, and Gijzen [29]. Much of the notation that will be used in the following sections is consistent with the referenced literature, but the conventions will be presented here as an introduction.

Due to the oscillatory nature of the flow field characteristic of PTRs, it is often more convenient or intuitive to discuss items such as physical properties or transient flow rates in terms of the net cycle-averaged value or cyclic integral of that item. We denote the cycle average of some property Φ or a flow rate $\dot{\Phi}$ using angled brackets as follows:

$$\begin{aligned} \langle \dot{\Phi} \rangle &= \frac{1}{\tau} \int_0^\tau \dot{\Phi}(t) dt \\ &= \frac{1}{\tau} \int_0^\tau \dot{m}(t) \Phi(t) dt \end{aligned} \tag{2.1}$$

Many of the terms of interest in pulse tube cryocoolers can also be expressed as the superposition of a time varying component denoted by $\widetilde{\Phi}$ and a steady or "DC"

component denoted by $\overline{\Phi}$ as described in Equation 2.2.

$$\Phi(t) = \widetilde{\Phi}(t) + \overline{\Phi} \tag{2.2}$$

$$\widetilde{\Phi}(t) = \Phi_d \sin(\omega t + \varphi) \tag{2.3}$$

where the subscript d denotes the peak dynamic amplitude of the time-varying property of interest. The period of oscillation τ is related to the driving frequency f and the angular frequency ω as follows:

$$\tau = \frac{1}{f} = \frac{2\pi}{\omega} \tag{2.4}$$

In a number of instances, the magnitude of a harmonic term is needed. The notation that will be consistently used for magnitude is $|\widetilde{\Phi}|$.

$$|\widetilde{\Phi}| = \Phi_d \tag{2.5}$$

where in this definition, Φ_d incorporates any leading coefficients before a harmonic term that contribute to the amplitude of the dynamic property.

Often the phase angles φ are relative phase angles between two harmonically varying properties. The notation for relative phase angles is given in Equation 2.6.

$$\varphi_{1-2} = \varphi_1 - \varphi_2 \tag{2.6}$$

The development of a control-volume-type analysis describing the essential physics in the pulse tube refrigerator relies on a few basic thermodynamic concepts developed in an introductory-level thermodynamics text [4]. In the following discussion, lower case terms are specific, ie. per unit mass, while upper case terms are total quantities. The enthalpy of a fluid is given by Equation 2.7.

$$h = u + Pv \tag{2.7}$$

$$TdS = dU + PdV \tag{2.8}$$

$$g = h + T_0 s \tag{2.9}$$

where u is the specific internal energy, P is the pressure, and v is the specific volume. The enthalpy is a property which incorporates both the internal energy contained in a fluid and the flow work needed to bring the fluid in or out of a control volume. Enthalpy is needed to perform a first law analysis (energy balance) of the system. Equation 2.8 gives the expression for entropy, an extensive property used in second law analysis (entropy balance) to determine the degree of irreversibility present in a process, where V is the total volume.

Enthalpy and entropy can be combined to form the Gibbs free energy, g, which is useful in developing a third law expression (exergy balance) of the system of interest. By cycle-averaging Equation 2.9, we can obtain an expression of Gibbs free energy useful for exergy analysis of the pulse tube as shown in Equation 2.10.

$$\langle \dot{G} \rangle = \langle \dot{H} \rangle - T_d \langle \dot{S} \rangle \tag{2.10}$$

By rigorously developing the terms $\langle \dot{H} \rangle$ and $\langle \dot{S} \rangle$ in terms of their total derivative definitions and applying the definition of the cycle average using Equation 2.1, one can derive an alternative expression for the Gibbs function. This derived expression assumes that all properties vary harmonically with time at the same fundamental frequency.

$$\begin{aligned} \langle \dot{G} \rangle = \langle P_d \dot{V} \rangle &= \frac{1}{2} P_d \frac{\dot{m}_d}{\rho} \cos(\varphi_{m-p}) \\ &= \frac{1}{2} P_d \dot{V} \cos(\varphi_{m-p}) \end{aligned} \tag{2.11}$$

The expression in Equation 2.11 is commonly referred to as acoustic power or "PV" power. PV power is not an energy flow that would be applied to a control volume energy balance, but represents the flow of work that could be extracted if the working fluid were reversibly expanded against an ideal piston. If dynamic pressure and volumetric flow rate data is accessible, as in the case of a CFD simulation or an instrumented assembly, the PV power can be directly computed using Equation 2.12

without any simplifying assumptions, and therefore should be used whenever practical.

$$\langle P\dot{V} \rangle = \frac{1}{\tau} \int_{1}^{\tau} \widetilde{P} \cdot \frac{\widetilde{\dot{m}}}{\rho} dt \tag{2.12}$$

2.1.1 Pulse Tube Refrigerator Control Volume Analysis and Energy Flows

Figure 2.2 displays a control volume representation of a single stage pulse tube cryocooler. At the full system level, there are only four main contributing energy flows in or out of the system. Mechanical energy is input to the compressor piston in the form of PV work $\langle \dot{W}_{comp} \rangle$. The heat of compression $\langle \dot{Q}_{comp} \rangle$ is rejected to the ambient in the aftercooler (AC) immediately downstream of the compressor. The thermal load from the object or space being cooled, $\langle \dot{Q}_{net} \rangle$ is accepted at the cold heat exchanger (CHX). The thermal load and any regenerator losses, which will be discussed in greater detail, are transported across the pulse tube via enthalpy flow $\langle \dot{H}_{PT} \rangle$ and rejected as heat $\langle \dot{Q}_{rej} \rangle$ in the warm heat exchanger to the ambient.

A first law energy balance of the closed PTR system results in Equation 2.13, where the typical conventions for control volumes are adopted such that positive heat flows add heat to the system, and positive work flows are done by the system. As previously mentioned, thermodynamic analysis will be performed using cycle-averaged quantities in place of instantaneous values.

$$\Delta \langle E_{PTR} \rangle = \langle \dot{Q}_{net} \rangle - \langle \dot{Q}_{comp} \rangle - \langle \dot{Q}_{rej} \rangle + \langle \dot{W}_{comp} \rangle \tag{2.13}$$

Rearranging and solving for the net cooling capacity the system-level energy balance at periodic steady-state, where $\Delta \langle E_{PTR} \rangle = 0$ is,

$$\langle \dot{Q}_{net} \rangle = \langle \dot{Q}_{comp} \rangle + \langle \dot{Q}_{rej} \rangle - \langle \dot{W}_{comp} \rangle \tag{2.14}$$

The second law of thermodynamics is then applied the system to balance the entropy flows resulting from heat transfer at the heat exchangers and the rate of entropy

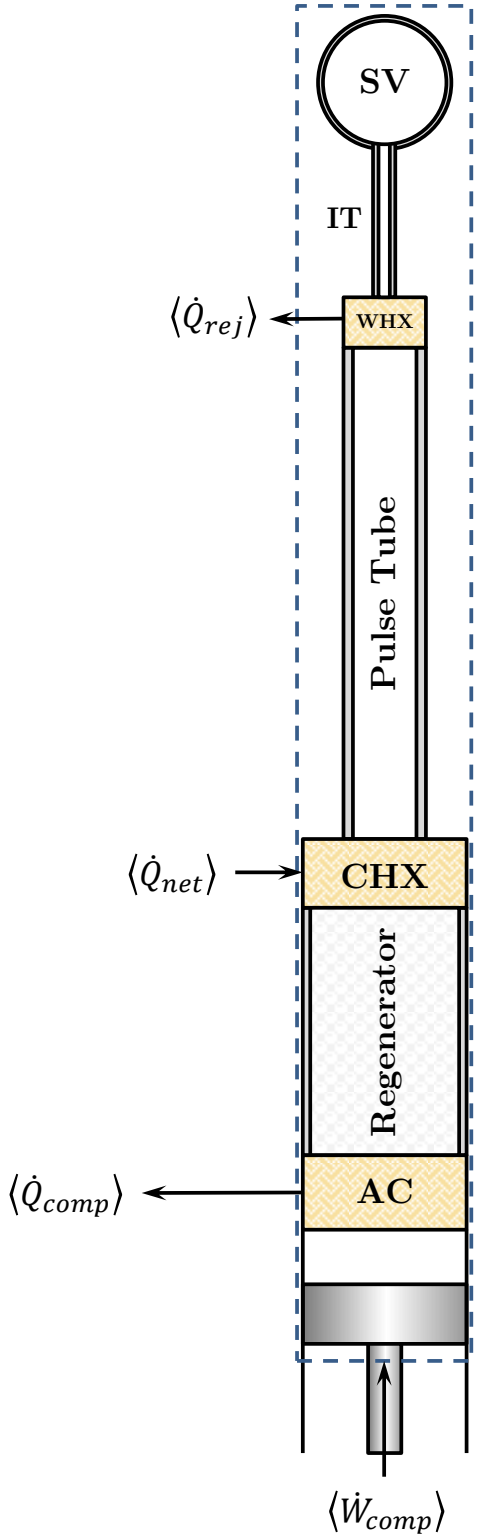

Figure 2.1: Control volume representataion of a full PTR system. Piston work is input at the compressor, the heat of compression is removed at the aftercooler (AC), the thermal load to be cooled is accepted at the cold heat exchanger (CHX), and the thermal load and regenerator losses are rejected at the warm heat exchanger (WHX).

production within the system caused by irreversibilities. The generic statement of the second law applied in cycle-averaged form to a closed system is as follows:

$$\frac{d\langle S_{PTR}\rangle}{dt} = \sum_j \frac{\langle Q_j\rangle}{T_j} + \langle\dot{\sigma}\rangle \tag{2.15}$$

where j is an index denoting the various heat transfer surfaces and $\dot{\sigma}$ is the rate of entropy generation. At periodic steady-state the rate of entropy accumulation is zero. Heat is rejected from the PTR to the rejection temperature T_{rej} and cooling power is provided at temperature T_C. Plugging in the various heat flows in the system, a second law expression for the PTR system is then:

$$0 = \frac{\langle\dot{Q}_{net}\rangle}{T_C} - \frac{\langle\dot{Q}_{comp}\rangle}{T_{rej}} - \frac{\langle\dot{Q}_{rej}\rangle}{T_{rej}} + \langle\dot{\sigma}_{PTR}\rangle \tag{2.16}$$

The first and second law statements can then be used in an exergy analysis of the full system. The exergy $\mathbf{E}$ is a measure of the energy available for useful work relative to the surroundings, in this case the thermal rejection reservoir (usually ambient). The generic form of the exergy balance for a closed system is given in Equation 2.17

$$\frac{d\langle\mathbf{E}_{PTR}\rangle}{dt} = \sum_j \left(1 - \frac{T_0}{T_j}\right)\langle\dot{Q}_j\rangle - \left(\langle\dot{W}\rangle - \langle P_0\dot{V}\rangle\right) - \langle\dot{\mathbf{E}}_d\rangle \tag{2.17}$$

where the reference temperature T_0 is in fact the rejection temperature T_{rej}; therefore, there is no exergy transfer at the warm heat exchangers. Exergy is not a conserved property and the rate of destruction is given by $\langle\dot{\mathbf{E}}_d\rangle$. Substituting the terms from the PTR system control volume, the exergy balance at periodic steady-state (where there is no exergy accumulation) is as follows:

$$0 = \left(1 - \frac{T_{rej}}{T_C}\right)\langle\dot{Q}_{net}\rangle + \langle P_d\dot{V}_{comp}\rangle - \langle\dot{\mathbf{E}}_{d,PTR}\rangle \tag{2.18}$$

For the ideal pulse tube cryocooler, no exergy would be destroyed and Equation 2.18 could be rearranged to yield the ratio of cooling power to input power, i.e., the ideal PTR Carnot efficiency.

$$\frac{\langle\dot{Q}_{net}\rangle}{\langle P_d\dot{V}_{comp}\rangle} = \frac{T_C}{T_{rej} - T_C} \tag{2.19}$$

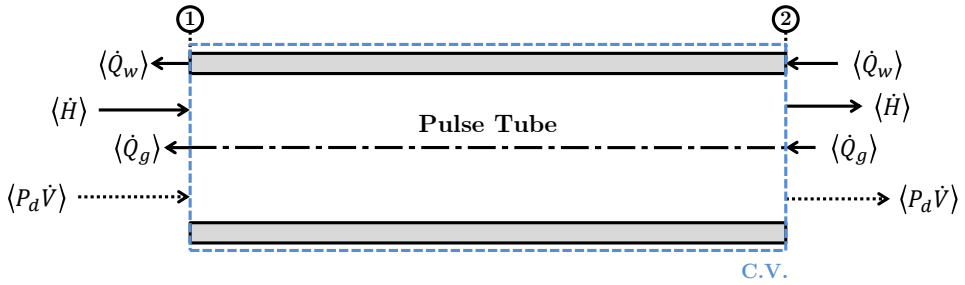

Figure 2.2: Control volume representataion of a section of the pulse tube component. Temperature increases from left to right where Location 1 is at T_C. Subscript w refers to the wall. Subscript g refers to the gas.

The efficiency of a real PTR is less than Carnot primarily because the work of expansion is not recovered, resulting in the following expression for PTR efficiency [27].

$$\frac{\langle \dot{Q}_{net} \rangle}{\langle P_d \dot{V}_{comp} \rangle} = \frac{T_C}{T_{rej}} \tag{2.20}$$

In a real pulse tube cooler, there are irreversibilities present in nearly all components. Let us first look at a reduced control volume of the pulse tube component to identify the real energy flows present that will be quantified in the current study. A second isolated control volume centered on the cold heat exchanger will then be presented to illustrate how the real energy flows affect the net refrigeration capacity of the pulse tube refrigerator. The pulse tube is presented first as it is the primary component of interest in this study of pulse tube convective stability.

As shown in Figure 2.2, there are a number of energy flows of importance to the pulse tube component in addition to the enthalpy flow. While the dominant flow of energy in a properly designed pulse tube is the enthalpy flow, thermal conduction also plays an important role, both in the gas and in the solid wall material. This conduction manifests itself as a loss, decreasing the net amount of energy available for the gas to do work. These losses are represented mathematically as follows, based on Fourier's law of conduction, where the subscript s refers to properties of the solid medium:

$$\dot{Q}_w = \iint_{A_w} -k_s A_w \frac{dT_s}{dz} dA_w \tag{2.21}$$

$$\dot{Q}_g = \iint_{A_{PT}} -k_g A_{PT} \frac{dT_g}{dz} dA_{PT} \tag{2.22}$$

assuming that the z-direction is pointing to the right of the page, along the pulse tube centerline. A key term of interest is the net energy transport at a given cross-section along the pulse tube, e.g., locations 1 and 2 as noted on Figure 2.2, given by Equation 2.23.

$$\langle \dot{E}_{PT,net} \rangle = \langle \dot{H}_{PT} \rangle - \langle \dot{Q}_g \rangle - \langle \dot{Q}_w \rangle \tag{2.23}$$

In terms of relative magnitude, the enthalpy flow term typically dwarfs the conduction terms. In capturing the effects of inclination angle on pulse tube performance, Equation 2.23 will be applied to the cold end of the pulse tube when post-processing simulations. This allows the performance to be quantified without requiring the regenerator energy flows that will be presented next.

Let us now examine the control volume shown in Figure 2.3 centered on the cold heat exchanger to look at the interplay between the real energy flows in the regenerator, the energy flows in the pulse tube, and the externally applied load. The purpose of the regenerator is to minimize the enthalpy and heat flow into the cold heat exchanger while also minimizing pressure drop and therefore delivering the maximum acoustic power to the pulse tube. If a perfect regenerator existed, the net pulse tube energy flow defined by Equation 2.23 would be equal to the useful cooling capacity of the cooler, $\langle \dot{Q}_{net} \rangle$. In reality, the regenerator introduces an enthalpy flow into the cold heat exchanger (CHX) as a result of the losses associated with friction and bulk matrix conduction within the porous filler material. In addition, there is a conduction loss associated with the wall material that contains the regenerator. These regenerator parasitic energy flows are introduced to the cold heat exchanger (CHX) in the form

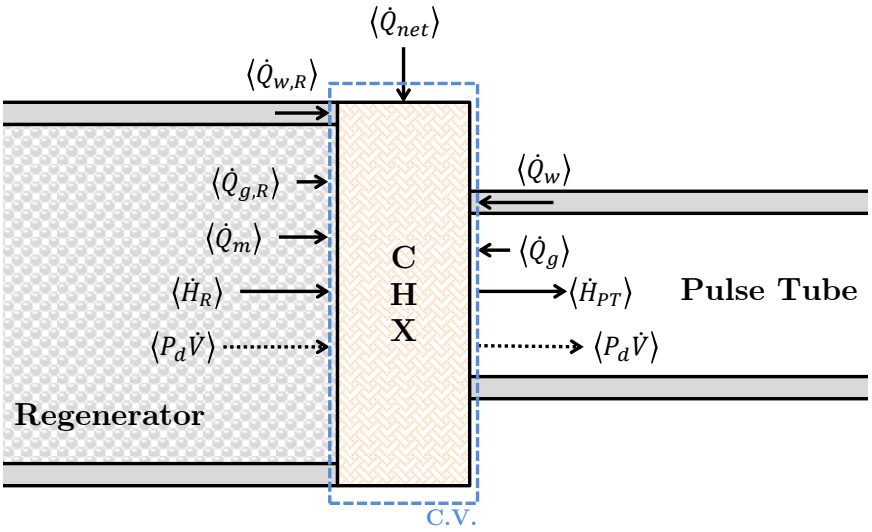

Figure 2.3: Control volume representation of the cold heat exchanger indicating both real (solid arrow) and free energy (dashed arrow) flows.

of enthalpy flow $\langle \dot{H}_{regen} \rangle$ in addition to the matrix, gas, and wall conduction. The net energy flow through the regenerator is expressed in Equation 2.24, where the subscript R refers to regenerator flows and m refers to the porous matrix material.

$$\langle \dot{E}_{R,net} \rangle = \langle \dot{H}_R \rangle + \langle \dot{Q}_m \rangle + \langle \dot{Q}_{w,R} \rangle + \langle \dot{Q}_{g,R} \rangle \tag{2.24}$$

where the regenerator enthalpy flow is given by:

$$\langle \dot{H}_R \rangle = \frac{1}{\tau} \int_0^\tau \left\{ \iint_{A_R} \varepsilon \rho_g u_z c_{p,g} T_g dA_R \right\} dt \tag{2.25}$$

where A_R is the regenerator cross sectional area. The net conduction in the regenerator is given by:

$$\langle \dot{Q}_R \rangle = \frac{1}{\tau} \int_0^\tau \left\{ \iint_{A_R} - \left(k_w \frac{dT_w}{dz} \right) - \left(\varepsilon k_g \frac{dT_g}{dz} \right) - \left((1-\varepsilon) k_m \frac{dT_m}{dz} \right) dA_R \right\} dt \tag{2.26}$$

A first law energy balance of the control volume shown in Figure 2.3 is determines the net cooling capacity of the pulse tube refrigerator at periodic steady-state.

$$\begin{aligned} \langle \dot{Q}_{net} \rangle &= \langle \dot{H}_{PT} \rangle - \langle \dot{Q}_{w,PT} \rangle - \langle \dot{Q}_{g,PT} \rangle - \langle \dot{E}_{R,net} \rangle \\ &= \langle \dot{E}_{PT,net} \rangle - \langle \dot{E}_{R,net} \rangle \end{aligned} \tag{2.27}$$

The critical function of a pulse tube is to convert acoustic energy to enthalpy flow. In an ideal pulse tube, compression and expansion would be adiabatic and perfect heat transfer would occur in the two adjacent heat exchangers. The pulse tube enthalpy flow itself is a function of the acoustic power and the relative losses due to irreversibilities in the pulse tube which generate entropy.

$$\langle \dot{H}_{PT} \rangle = \langle P\dot{V} \rangle - T_0 \langle \dot{S} \rangle \tag{2.28}$$

In an ideal pulse tube no entropy is generated and as a result there would be no net transport of entropy across the pulse tube, i.e., $\langle \dot{S} \rangle = 0$. As a result of an exergy analysis of a perfect, reversible PTC it has been shown in published literature that the net cooling power would be equal to the acoustic power in the pulse tube [30]. A gross figure of merit (FOM) for the pulse tube is typically defined as the ratio of enthalpy flow to available acoustic energy as an indicator of the degree of pulse tube efficiency in converting PV power to enthalpy flow.

$$FOM = \frac{\langle \dot{H}_{PT} \rangle}{\langle P\dot{V} \rangle} \tag{2.29}$$

FOM is also referred to as the pulse tube efficiency or the pulse tube effectiveness. For an ideal, adiabatic pulse tube, FOM would equal 1. In Section 2.1.2 the pulse tube phenomena that contribute to entropy generation will be described in detail, causing the real pulse tube efficiency to decrease.

2.1.2 Pulse Tube Loss Mechanisms

The preceding thermodynamic analysis of the pulse tube component is an oversimplified model of the true energy and mass transport processes that take place and significantly affect the performance of the design. In order to fully quantify the performance of a pulse tube design, real loss mechanisms must be taken into account which contribute to the production of entropy and therefore decrease the pulse tube's ability to efficiently convert acoustic energy to thermal energy.

2.1.2.1 Boundary Phenomena

There are a number of phenomena which occur within the boundary layer of the pulse tube that can either reduce or enhance pulse tube performance, depending on the operating conditions and architecture. These effects include:

- surface heat pumping and shuttle heat transfer
- acoustic streaming (Rayleigh Streaming)
- DC streaming (Gedeon Streaming)

The subsequently described effects involve transport phenomena that originate in the wall-adjacent gas domain.

Surface Heat Pumping/Shuttle Heat Transfer

Over the course of a typical expansion and rarefaction process, the gas directly adjacent to the pulse tube wall exchanges heat with the adjacent solid. During the compression half of the cycle, the gas is moving toward the hot end of the tube while pressure, and therefore temperature increase. During this portion the gas will be locally hotter than the wall, and will transfer heat to the solid. During the reverse portion of the cycle as the gas is traveling toward the cold end of the device, pressure and temperature will decrease, leaving the fluid locally cooler than the wall material. As the fluid moves toward the cold end, it picks up heat from the wall material and then rejects it on the subsequent cycle when it moves back toward the hot end, providing a small heat pumping effect. This effect is graphically represented in Figure 2.4(a). In early BPTRs this effect was the only contributor to useful cooling, hence the lack of efficiency in early PTCs.

In modern pulse tubes, the temperature gradients are much steeper than those experienced in the early BPTR devices. As a result, the surface heat pumping effect actually reverses direction and shuttles heat toward the cold end causing a parasitic

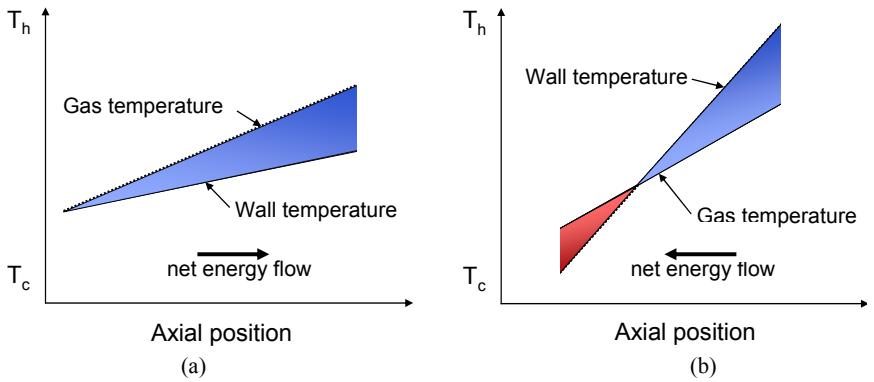

Figure 2.4: A graphical depiction of the **(a)** surface heat pumping, and **(b)** shuttle heat transfer phenomena within a pulse tube. Reproduced from [31] with the author's permission.

loss. This transition occurs when the gas temperature no longer exceeds the local wall temperature during the compression process, which causes it to accept energy as it moves toward the hot end and carry it back toward the cold end on the reverse portion of the process. Similarly, the gas temperature will exceed the wall temperature during the expansion process causing it to reject heat to the wall material as it moves toward the cold end. In this description, the shuttle heat transfer causes a decrease in the available net cooling power. The previously described phenomena are depicted in Figure 2.4.

Acoustic Streaming

Acoustic streaming, also referred to as Rayleigh streaming, is another boundary layer phenomenon that occurs due to the oscillatory nature of the flow field. The flow adjacent to the wall tends to lag behind the flow in the central core due to viscosity effects. The gas temperature varies during the expansion and rarefaction portion of the cycle, and since the viscosity of the gas is dependent on temperature, the gas parcels near the walls experience a different level of shear during the forward and reverse portions of the cycle. Acoustic streaming manifests itself as a DC flow directed from the cold end of the pulse tube to the hot end within the boundary layer.

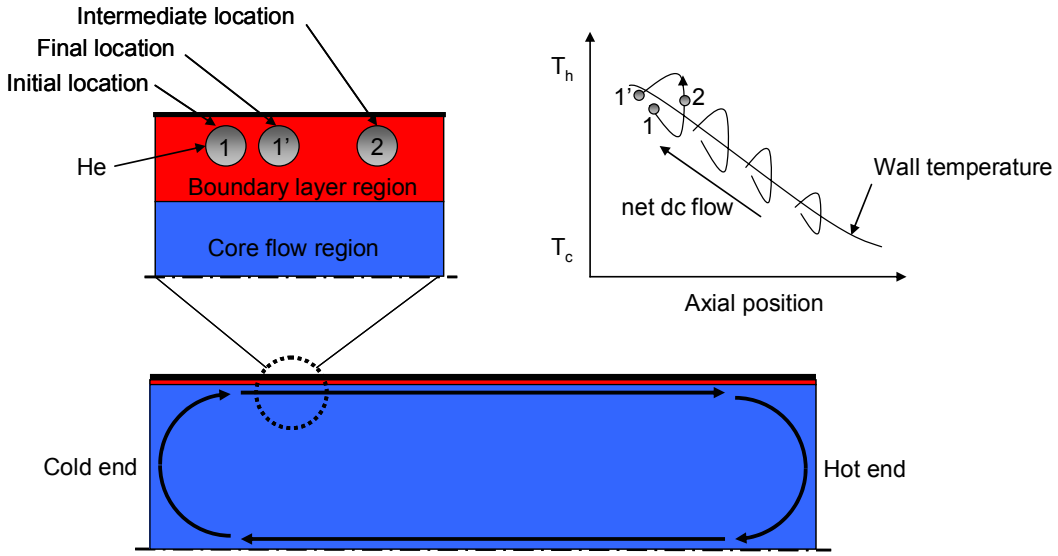

Figure 2.5: Illustration of the acoustic streaming effect driven by uneven temperature-dependent viscosity in the boundary layer during the forward and reverse portion of the cycle [31].

An opposing DC flow along the centerline of the duct allows the system to conserve mass, thus a convective flow loop is generated as illustrated in Figure 2.5.

The secondary streaming flow of gas within the pulse tube carries enthalpy with it from the hot end to the cold end, and can often significantly hinder the cooling performance of pulse tubes. Analytical prediction methods have been investigated since the 1970's [32] and development of this theory is out of the scope of this thesis. The effect of Rayleigh streaming has been shown to be minimized by implementing a properly designed tapered (conical, with very small included angle) tube as published and patented by Olsen and Swift [16].

Gedeon Streaming Whereas temperature-dependent viscosity is primarily responsible for Rayleigh streaming, Gedeon derived an expression that proved that DC streaming can occur even for an inviscid fluid, with magnitude proportional to acoustic intensity [15]. This phenomenon is driven largely by the phase difference between acoustic velocity and density perturbations.

2.1.2.2 Convective Losses

In the preceding sections we showed that net DC mass transport can occur due to phenomena that occur within the viscous and thermal boundary layers adjacent to the compliance tube wall. There are other sources of convection originating from the bulk flow region including natural convection, the subject of this thesis study. Bulk flow convective phenomena can be classified as follows:

- Jet-driven streaming
- Turbulent mixing
- Free convection

As with the boundary layer streaming phenomena, convective effects can have a catastrophic effect on the refrigeration performance of PTCs.

Jet-Driven Streaming

Convection within the compliance tube domain is often driven by flow maldistribution due to insufficient flow straightening at component junctions where large changes in cross sectional area occur, for instance the transition between the pulse tube and the inertance tube. During the reverse portion of the cycle, high velocity gas from the inertance tube is ejected into the pulse tube domain and often does not diffuse quickly enough to avoid a flow disturbance. The jetting effect disturbs the compliant piston portion of the pulse tube, thereby reducing the conversion efficiency between acoustic power and thermal energy.

Turbulent Mixing

Section 2.1.3 will formally introduce the concept of turbulence in oscillatory flow and what that entails relative to the concept normally understood in traditional

unidirectional flow regimes. In the context of a pulse tube, the component is purposely designed to remain within the laminar flow regime at all times throughout the cycle. Significant parasitic energy transport occurs when turbulence is present within the pulse tube, and concept of a virtual gas piston no longer holds.

Free Convection

Free convection in the pulse tube is driven by gravitational body force when the pulse tube is oriented in such a way that the gravity vector is not aligned in the primary flow direction pointing from the hot end to the cold end. Pulse tubes inherently support a temperature gradient and therefore significant variations in density occur throughout the pulse tube domain. In an otherwise quiescent container of fluid, the presence of unbalanced buoyancy forces initiates convective roll, for which there is extensive literature for common configurations including inclined cylinders. The concept becomes more complicated in the case of cryogenic inclined cylinders due to both the nonlinear behavior of the fluid properties and the presence of the imposed oscillating inertial flow regime that transforms the problem into nonlinear mixed convection. This concept is the basis of this dissertation study and will be discussed in greater detail throughout the entirety of this document. Theory on convective instability will be discussed later in this chapter.

2.1.3 Boundary Layers and Turbulence Effects

As introduced in Section 2.1.2.2, turbulence can have a devastating effect on the efficacy of a pulse tube. While the transition between laminar and turbulent unidirectional flow in pipes is well documented and quantified for many geometries, oscillatory flow in pipes still is not well understood. Many studies have been carried out on fully reciprocating flow over the past 50 years, but no universal agreement has been found that identifies the exact transition to turbulence. A relevant review of the

history of research in oscillatory flow turbulence is given by Brereton [33]. The oscillating nature of the flow is characterized by high velocity peak portions of the cycle, as well as portions of zero velocity as the flow reverses. As such, steady turbulence cannot form due to the constantly changing flow regime in the boundary layer. The complexity is exacerbated by the phase relationship between the boundary and the bulk flow region.

Ohmi and Iguchi [34] suggested that the mechanism for the generation of turbulence must be the same for both DC and oscillating flow, based on agreement between experimental data and the well-known 1/7 power law. They also describe the turbulence process in oscillatory flow as turbulent bursts. In an effort to quantify the transition region, they developed an expression for the critical ocillating Reynolds number $Re_{osc,cr}$ based on the dimensionless frequency of oscillation.

$$Re_{osc,cr} = 800\sqrt{\frac{R^2\omega}{\nu}} \tag{2.30}$$

The expression derived by Ohmi and Iguchi is seldom used in practice. Some researchers [35] have suggested that the most accurate representation is given by Akhavan, Kamm, and Shapiro [36,37]. The Akhavan study involved an experimental study using a laser-Doppler anemometer as well as a numerical simulation component to identify the transition region. They presented an alternative Reynolds number based on the Stokes oscillatory boundary layer thickness, Re^{δ}:

$$Re^{\delta} = \frac{\widetilde{U}_0\delta}{\nu} \tag{2.31}$$

where δ is the Stokes layer thickness given by:

$$\delta = \sqrt{\frac{2\nu}{\omega}} \tag{2.32}$$

and $\widetilde{U}_0$ is the cross-sectional mean velocity amplitude, denoted u_d in this dissertation. Akhavan determined that the flow transitioned from laminar to intermittently turbulent in the range of $500 < Re^{\delta} < 550$.

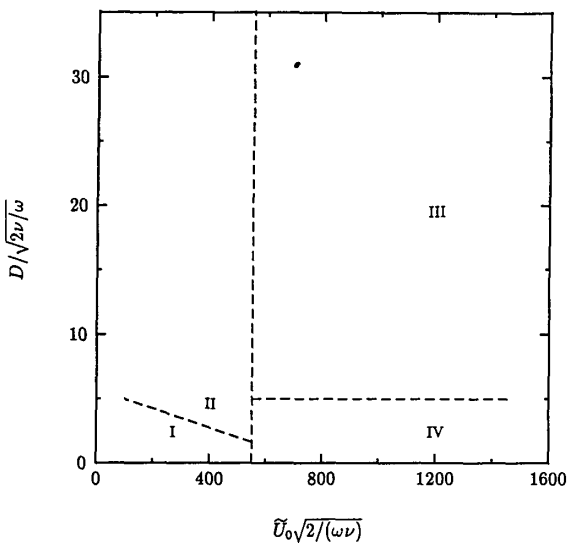

Figure 2.6: Flow regime map reproduced from [33] outlining the four regimes as follows: I. laminar flow, II. perturbed laminar flow, III. intermittently turbulent flow, and IV. fully turbulent flow.

In the thorough review of oscillatory turbulence by Brereton, a figure (reproduced here as Figure 2.6) breaks the flow regime into four distinct quadrants as a function of both the Stokes Reynolds number and a length scale relating the pipe diameter to the boundary layer thickness. For the remainder of this document, we will adopt Re^{δ} as the relevant dimensionless number and adopt a critical transition value of 500. Pulse tube designs may operate in either the I. laminar or II. perturbed laminar regimes in order to avoid loss and instability resulting from turbulent energy transport.

2.2 Fluid Mechanics of Oscillating Flow in Inclined Cylinders

The previous sections described the entropy generation mechanisms that are detrimental to pulse tube operation. In this section the fluid mechanics that characterize oscillatory flow in inclined tubes with an applied temperature gradient will be introduced. Current theories which attempt to quantify the issue at hand will then be presented and discussed in terms of their relationship to this study.

The pulse tube is essentially a hollow cylinder with smooth walls and no flow

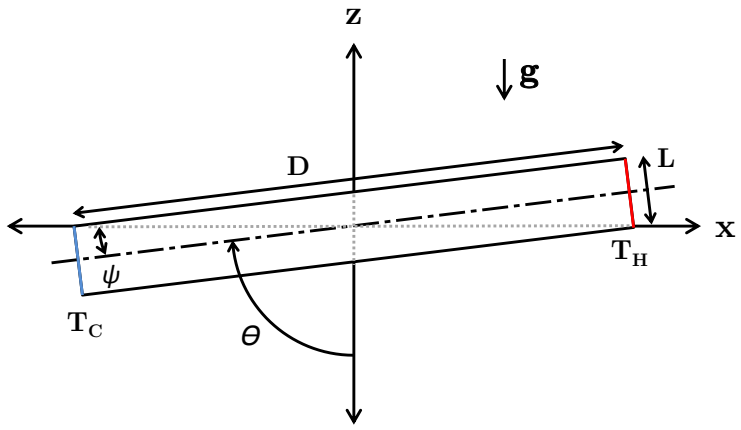

Figure 2.7: Domain introducing the transition angle which marks the onset of free convection

impedances. By nature of its operating conditions, the fluid field develops a thermal gradient from the cold end at the objective temperature of the cooler to the warm end where enthalpy flow is rejected either to ambient or to an upper stage. In the absence of the characteristic oscillatory motion driven by sinusoidal pressure perturbations, a one-dimensional temperature gradient along the centerline of the tube can only exist in a single stable orientation; the case where the local acceleration vector field is aligned with the temperature gradient. This orientation is referred to as "cold end down" and is the most common condition for permanently installed terrestrial PTRs. When the orientation deviates from the cold end down position, up to a critical angle, the fluid contained within the quiescent pulse tube tends to realign its thermal gradient with the local acceleration. The result is an asymmetric, but stable, temperature profile about the centerline. This regime exists for angles up to the transition angle θ_T when cold fluid reaches a higher gravitational potential than the warm fluid elsewhere in the cylinder.

Figure 2.7 illustrates the domain and the variables used to determine the transition point in terms of the pulse tube aspect ratio AR which will be used as a description for pulse tubes throughout the remainder of this document. The following equations utilize basic trigonometry to determine the critical angle at which the cold fluid

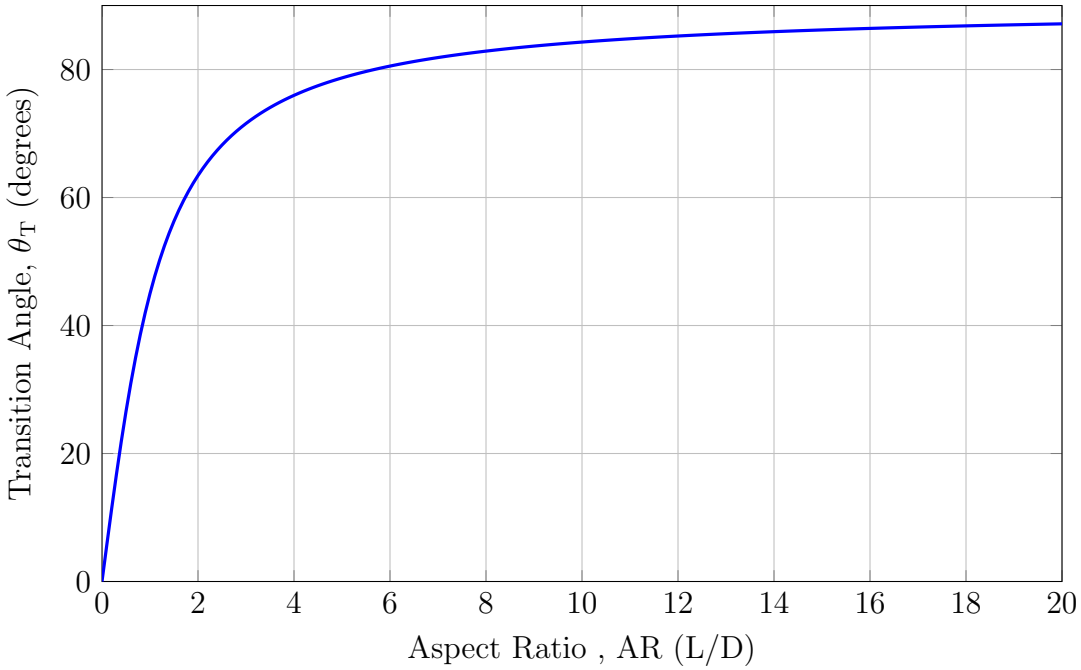

Figure 2.8: Transition angle as a function of the aspect ratio L/D of the inclined cylindrical enclosure.

reaches the same gravitational potential as the warm fluid.

$$\psi = \pi/2 - \theta \tag{2.33a}$$

$$AR = L/D \tag{2.33b}$$

$$\tan\psi = D/L \tag{2.33c}$$

$$\theta_T = \pi/2 - \tan^{-1}\left(\frac{1}{AR}\right) \tag{2.34}$$

By computing the transition angle as a function of pulse tube aspect ratio as shown in Figure 2.8, the functional relationship is clarified. As the aspect ratio decreases and the tube becomes more stout, the transition occurs at much lower angles of inclination. This creates an opportunity for natural convection to occur at angles less than 90°.

When the orientation of the inclined cylinder exceeds the transition point, convection ensues as a result of the unbalanced buoyancy forces within the field. In a typical pulse tube with objective temperature of 77 K and a thermal rejection temperature of

293 K, the cold gas density exceeds the warm gas density by a factor of 3.7 assuming a charge (mean) pressure of 3.0 MPa. This imbalance is further exacerbated at lower temperatures, for instance a 20 K pulse tube with 80 K heat rejection temperature where the density ratio is 3.95. The result of this force imbalance within the fluid domain is the formation of a convective cell, whose geometry is driven by the form of the container, and whose rotation rate is driven by the magnitude of the body force imbalance.

The name Rayleigh-Bénard convection (RB Convection) has been historically applied to the case of a fluid layer heated from below and cooled from above, which has been shown to produce hexagonal roll cells with alternating roll direction. The term has been extended in literature to include convection within enclosures experiencing heating from below and cooling from above, including those at an angle, as in the case of the tilted pulse tube. Although Bènard's problem never incorporated a harmonic disturbance in the flow field, various researchers have applied the same title to the case of convection in inclined pulse tubes, a convention we have chosen to adopt here as well.

2.2.1 Rayleigh-Bénard Convection

RB convection is a phenomenon that occurs when a fluid continuum is simultaneously heated and cooled at separate locations and subjected to a gravitational field or body force, where the refrigerated surface is situated above the heated surface. Instability forms as a result of density imbalances within the fluid. As the fluid is heated from below, the density decreases and the fluid experiences a buoyancy force which results in upward motion of the particle. As the particle rises in the domain, it exchanges heat with adjacent particles and eventually approaches the cooled surface. As the fluid cools on its upward path, the density once again increases and a net downward force is experienced. The result is a continuous cycle of particle motion.

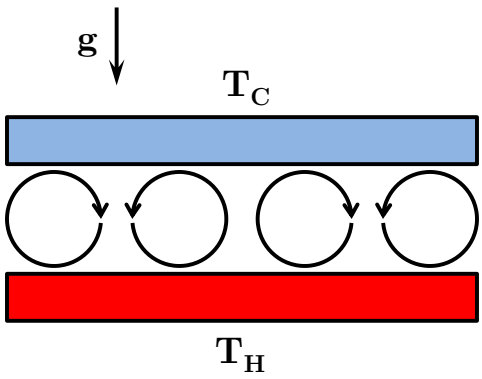

(a) Schematic of Bénard's problem (side view).

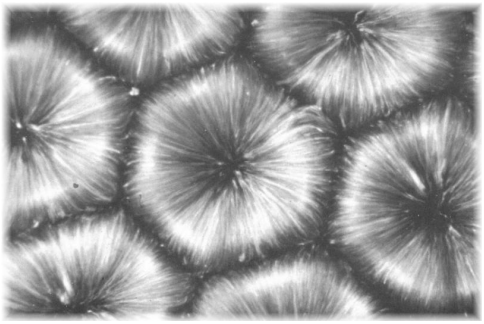

(b) Characteristic hexagonal roll cells (top view) [38].

Figure 2.9: Bénard cell images. **a.** Schematic representation. **b.** Time lapse image of Rayleigh-Bénard convective cells during a 10 second window using aluminum tracer particles reproduced from [38].

In the context of RB convection, stability is governed by the Rayleigh number, Ra, and the Prandtl number, Pr.

$$Ra = \frac{g\beta\Delta T l^3}{\nu\alpha} \tag{2.35}$$

$$Pr = \frac{\nu}{\alpha} \tag{2.36}$$

where β is the thermal expansivity, α is the thermal diffusivity, ν is the kinematic viscosity of the fluid, and l is a relevant characteristic length for the problem at hand.

When the critical value of the Rayleigh number is exceeded, the convection becomes unstable and cells form as shown in Figure 2.9. Critical values are only characterized for select cases in the open literature, and depend strongly on the boundary conditions containing the fluid field.

The formulation of Rayleigh number in Equation 2.35 is made in the framework of the Boussinesq approximation, which states that the fluid density is not a stong function of pressure, and depends linearly on temperature according to:

$$\rho - \rho_0 = -\rho_0\beta(T - T_0) \tag{2.37}$$

where ρ_0 is the fluid density evaluated at a suitable reference temperature. The Boussinesq assumption has been shown to be unsupported for the case of pulse tubes,

where the density is a strong function of both pressure and temperature, and variations in both field variables are time variant. The analysis is further complicated by the oscillation of the flow in pulse tubes, where Ra is time-variant.

2.2.2 Convective Instability Theory

Complete convective stability is classified as a continuum where the only mode of heat transfer is conduction. In the context of pulse tubes, partial suppression of instability can lead to a quasi-stable configuration where some convection occurs in addition to gas conduction. The third classification of flow is convectively unstable, where the dominant mode of heat transfer is convection. In both quasi-stable and fully unstable flow fields, the convection, although small compared to the oscillating amplitude of enthalpy flow, can have a very significant effect compared to the net refrigeration capacity of the pulse tube. Various methods have been published in an attempt to quantify instability within the pulse tube domain through a linearized method of analogous systems, and via traditional stability analysis techniques applied to simplified. The nonlinearities present in the interaction between the oscillating flow field and the free convection field preclude the pursuit of accurate closed form solutions using superposition methods as explained in the following sections. The most effective and accurate, but certainly not the most time efficient, methods applicable to solve the nonlinear partial differential equations that govern the flow of interest are numerical techniques such as finite difference or finite volume methods.

2.2.3 Method of Analogous Dynamic systems

In the field of heat transfer, it is common to use the method of analogous systems to derive semi-empirical solutions. In this method, a dynamically similar problem for which the solution is well known is identified. The relevant variables that are analogous in the two similar problems are equated to derive the same functional relationships.

2.2.3.1 Inverted Pendulum Analogy

Perhaps the most relevant analysis on the topic of convection in pulse tubes is provided by Swift and Backhaus [3, 39], who equated the problem of thermoconvective instability to that of an inverted pendulum, where the density imbalance resulting from the cold, dense gas in the cold end being situated above the warm end is equated to the net moment created by the off-center mass of the pendulum. This analogy is illustrated in Figure 2.10 reproduced from [3]. The analogy is interesting because a statically imbalanced inverted pendulum can be dynamically stabilized if the base is subjected to oscillation with sufficient magnitude and velocity. The result is that the pendulum aligns with the axis of oscillation due to the time-averaged torque created by the base motion opposing the net moment created by the mass imbalance. If such an analogy holds true, it implies that the unstable static temperature field in an inclined pulse tube with denser gas situated above the warm gas could be perfectly stabilized, i.e., no convective motion, in the presence of the correct set of driving parameters of the oscillatory flow.

Swift and Backhaus develop a stability criterion by applying a force balance between the gravitational body forces and inertial forces generated by the oscillating (vibrating) fluid. Stability is assumed to occur when the inertial forces are greater than or equal to the gravitational body forces. Vibrating (Ra_{vib}) and steady (Ra) Rayleigh numbers are developed for the analysis that adress the previously mentioned concern that Rayleigh number becomes time variant in pulse tubes. The vibrating Rayleigh number is given by:

$$Ra_{vib} = \frac{(\omega a l \Delta T)^2}{2\nu\alpha T_{avg}^2} \tag{2.38}$$

The ordinary Rayleigh number is given by:

$$Ra = \frac{g\Delta T l^3}{\nu\alpha T_{avg}} \tag{2.39}$$

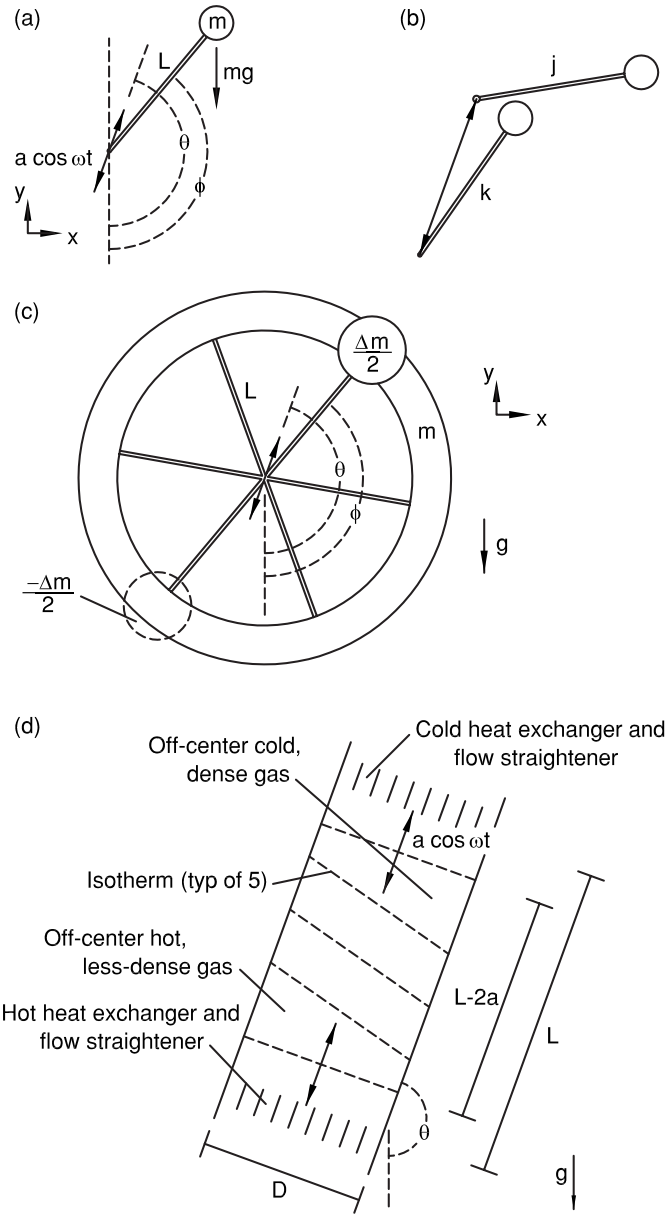

Figure 2.10: Pulse tube inverted pendulum analogy from [3].

where the thermal expansion coefficient β has been replaced by the expression $1/T$ in accordance with the Boussinesq approximation, which holds loosely for ideal gases such as helium at temperatures above roughly 60 K.

The force balance between gravitational and vibrational forces is given by:

$$Ra\vec{\nabla}T \times \hat{g} + Ra_{vib}\vec{\nabla}(\vec{w} \cdot \hat{z}) \times \vec{\nabla}T = 0 \tag{2.40a}$$

$$\vec{\nabla} \cdot \vec{w} = 0 \tag{2.40b}$$

$$\vec{\nabla} \times \vec{w} = \vec{\nabla}T \times \hat{z} \tag{2.40c}$$

assuming that the primary oscillatory flow (vibration) direction is in the $z-$axis. The notation $\hat{\Phi}$ indicates a unit vector in the direction of $\vec{\Phi}$. $\vec{w}$ is the solenoidal (divergence-free) part of the time averaged temperature field $T\hat{z}$. Implied by the previous equations is that temperature and vibration are only functions of $\vec{z}$, indicating that a 1-D approach is taken. The details of the remaining derivation are left to the reader to review in Ref. [3]. Based on the energy balance, equilibrium is achieved when the ratio of Ra_{vib} to Ra is greater than one. This leads to the dimensionless group in Equation 2.41, which is referred to as the pulse tube convection number.

$$N_{PTC} = \frac{\omega^2 a^2}{g(\alpha_S D \sin\theta - L\cos\theta)}\sqrt{\left(\frac{\Delta T}{T_{avg}}\right)} \tag{2.41}$$

where α_S is a fitting parameter, empirically determined to be 1.5.

The characteristic length $(\alpha_S D \sin\theta - L\cos\theta)$ was determined based on best fit to testing done on mock pulse tube experiments at elevated temperatures, where the "cold" end was at ambient temperature and the warm end was controlled with resistance heaters. Another critical concern with this formulation is the simplification of the density imbalance assuming temperature and density are linearly related, i.e.,

$$\frac{\Delta\rho}{\rho_{avg}} \approx \frac{\Delta T}{T_{avg}} \tag{2.42}$$

The pulse tube convection number N_{PTC} is only valid, as explained by the authors, to slender pulse tubes (large L/D) where angles of inclination $90° \leq \theta \leq 180°$,

and only for conditions where the particle velocity amplitude ωa is large enough to suppress convection such that large particle excursions are not present that would break down the baseline model in the derivation. With the significant number of simplifications and restrictions applied to this model, it is difficult to achieve agreement in practice between cryogenic PTR measurements and the expected critical value of $N_{PTC,cr} = 1$. Revisions to this model have suggested that better agreement is found if $N_{PTC,cr} = 2$, and later that designers should apply a value of $N_{PTC,cr} = 20$ to ensure orientation insensitivity. These claims will be investigated in Chapter 6, where the data generated in this dissertation study is compared to the predictions made by N_{PTC}.

2.3 Previous Work (Literature Review)

This dissertation effort is focused on elucidating the fundamental mechanisms by which gravity causes convective instability and loss of refrigeration in modern inertance tube pulse tube cryocoolers. In this section, the relevant published studies are reviewed which constitutes the foundation on which this study is built. The existing body of work establishes the heritage of modeling techniques applied to PTR systems in general, empirically reports orientation sensitivity in pulse tubes, and attempts to visualize and suggest solutions to the problem at hand. Interest in the study of mixed convection in pulse tubes was motivated in a research note by Scurlock and Beduz in 1998 [40], spawning a decade and a half of inquiry into the complex phenomenon by various researchers. The suggestions in Scurlock's research note included traditional convective suppression techniques such as compartmentalizing or partitioning the flow, introducing an elliptical cross section to the pulse tube, increasing the length to diameter ratio, and bending the pulse tube into a helical coil.

2.3.1 Empirical Studies

In 1997, Thummes, Schreiber, Landgraf and Heiden [41] reported convective instability for low frequency PTRs. In 2005 Yang and Thummes [42] followed up with a paper on higher frequency pulse tubes in the 40 Hz range, and reported that orientation sensitivity was significantly reduced by the increase in operating frequency. These articles posit that natural convection is responsible for the orientation-dependent losses.

In 2002, Wang and Gifford [43] reported orientation sensitivity for a 2-stage low frequency (2 Hz) G-M-type 4 K pulse tube cryocooler developed at Cryomech. This study was limited to observation of the observation of sensitivity but identified that the desired 4.2 K no-load temperature could no longer be sustained at angles of orientation in excess of 45°. It also identified enhanced internal convective loading at angles as low as 20° by monitoring the upper stage temperature which rose steadily for increasing angles, a symptom of added thermal loading on the lower stage.

Ross and Johnson reported results in 2004 [44] on a number of observed data sets for both linear and coaxial Stirling-type PTRs at the NASA Jet Propulsion Lab operating at frequencies of approximately 40 Hz. Their observations quantified no-load temperature as a function of both orientation angle and input power to the refrigerator, i.e., compressor piston stroke. The resulting no-load temperatures were then correlated to load curves measured with the cooler in the vertical, cold end down orientation in order to estimate the net convective load caused by orientation. The results reported that orientation sensitivity decreased with increasing input power, and that linear PTR configurations were more significantly stabilized by increasing input power in comparison to U-tube configurations. A key result of this study was the motivation to further study the driving parameters of convective instability in order to apply better design techniques to pulse tubes. Kasthurirengan et al. [45] published a study in 2004 on single stage PTRs with similar conclusions, a follow up

study to their previous work experimentally measuring the performance of elliptical pulse tubes [46].

In 2004, Trollier et al. [47] introduced experimental mini-parametric studies that attempted to isolate variables of interest in orientation sensitivity. Both the cold tip and the heat rejection temperature were varied in addition to varying to orientation angle and input power levels. In 2007, Hou, Wang, and Liang [48] reported orientation sensitivity for a coaxial PTR operating between 40-57 Hz, achieving a no load temperature of 42 K. This empirical study expanded the scope in a moderate parametric study including the effects of charge pressure variation and driving frequency. The lack of linearity in the system made is difficult to directly separate the influences of each parameter, as the cooler performance is altered as it operates away from its intended design point.

In 2006, James, Corey, and Spoor [49] reported convective losses for two small CFIC/QDrive 77 K PTRs operating in the 50-60 Hz range. The conclusion was that their higher frequency cryocoolers experienced minimal orientation sensitivity at all angles. The maximum reported loss in cooling capacity was less than 20% of the measured vertical cooling capacity.

In 2008 and 2009, Swift and Backhaus [3, 39] published the first coherent theory based on the method of analogous solutions described in the previous section. The result was a semi-empirical pulse tube convection number indicative of the stability of the design. They later modified the claims of that solution slightly based on additional experimental data. In both reported studies, data used to inform the calibration constants and characteristic length were taken for pulse tubes at temperatures in the range of 300-400 K. Berryhill and Spoor [50] later refuted the accuracy of this model based on elevated temperatures by comparing losses for four functioning PTRs as a function of pulse tube convection number. The discrepency between measured data and the analogous solution led the researchers to pose the question as to whether or

not there were system-level effects at work not captured by the pulse tube theory alone. The conclusion of this study was that a safe design should incorporate a pulse tube convection number of at least 20-30 to preserve at least 80% of the untilted cooling capacity.

2.3.2 Visualization Studies

Flow visualization is notoriously difficult to perform at cryogenic temperatures for a number of obvious reasons. Methods such as particle image velocimetry (PIV) require optical access to the flow, and additionally require the flow to be seeded with particles sufficiently large to resolve through cinematography. PIV is accomplished by illuminating a plane of the flow with a laser light sheet. That light sheet illuminates the seeding particles as they cross through that plane, and the particle motion is then captured through high speed cinematography. The primary difficulty in applying PIV techniques arises due to the cylindrical form factor of the pulse tube wall. Optical clarity determines the effective resolution of the boundary layer that is feasible with PIV, and producing perfectly cylindrical, optically clear tubes is difficult in practice. Additionally, the sealing of glass or quartz components at cryogenic temperatures to the adjoining copper parts is a practical challenge due to the vastly different coefficients of thermal expansion. Finally, the porous media used in the heat exchangers and flow straighteners adjacent to the pulse tube component can quickly become plugged with the seed particles, reducing the flow area.

For the reasons cited, few visualization studies have been attempted on pulse tubes. Shiraishi, Murakami, Nakano, and Iida [51, 52] applied smoke wire techniques to a double inlet pulse tube refrigerator (DIPTR) to visualize velocity profiles for 6 Hz operation using air at 0.2 MPa as the working gas. The temperature range for the study was limited to a cold temperature of around 250 K. The results revealed the

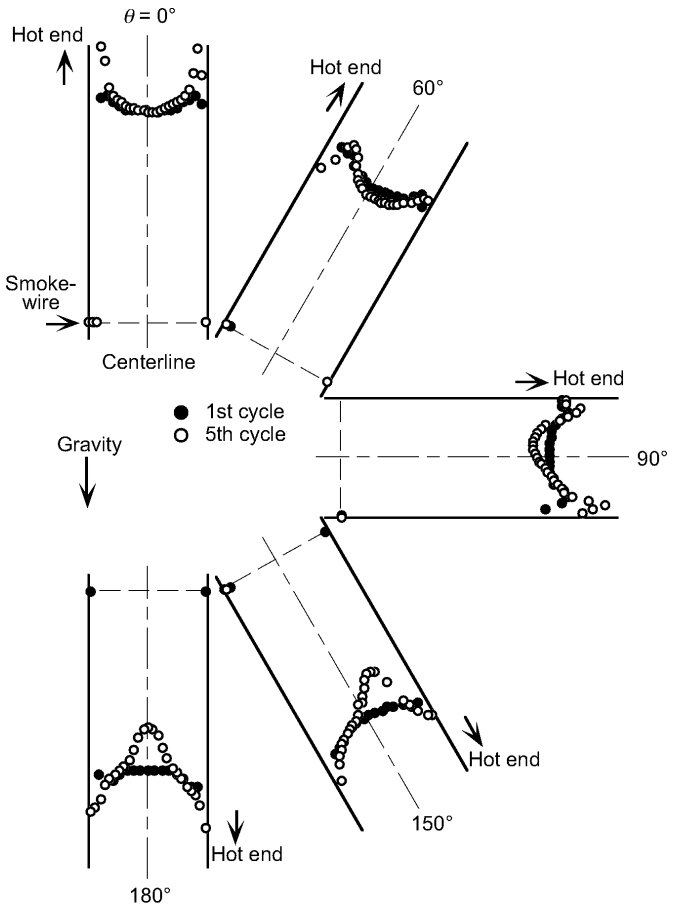

Figure 2.11: Smoke-wire visualization of velocity profiles at varied angles of inclination. Reproduced from [51].

transient particle excursions shown in Figure 2.11. These profiles indicate an asymmetric flow pattern where the flow along the upper wall (with respect to gravitational potential) experiences buoyancy at angles above 90° and is pulled downward along the bottom wall. Although this cooler type is not consistent with the ITPTR under investigation in this thesis, the results remain relevant.

Elevated temperature PIV measurements were performed by Matsumoto, Yasukawa, and Ohshima [54]. Similar to Shiraishi's study, the tests were performed at ambient temperature using air as the working fluid. The purpose of the flow visualization experiments was to inform better flow straightening techniques for U-tube PTRs. The results of this study are difficult to apply to pulse tube theory due to the

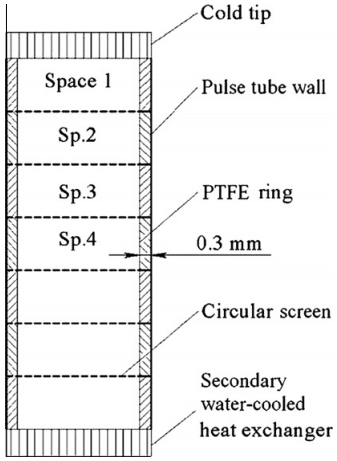

Figure 2.12: Flow partitioning technique applied by Zhang et al. [53] resulting in reduced orientation sensitivity, but also reduced overall performance.

lack of oscillatory flow in the measurements. Instead, steady air flow was introduced by applying vacuum to the warm end of the pulse tube, drawing the particle laden flow through the "cold" heat exchanger.

2.3.3 Computational PTR Studies

Over the past two decades. There has been significant advancement in the use of computational modeling to support efficiency improvements in PTRs, but on the system and component levels. Codes have advanced from one-dimensional finite difference codes to the currently reported three-dimensional hybrid finite volume / finite element simulations. Advancement has been largely driven by the improvement in computational resources available for simulation of comprehensive codes. In this section, a brief account of simulation history is given.

Significant efforts toward numerical analysis have been reported from the cryogenics research group at Georgia Tech. In 1996, Kirkconnell [55] performed 1-D numerical simulation of high frequency pulse tube flows reporting numerical parametric study results in 1998 [56]. In 2007, Cha [57, 58] reported 2-D axisymmetric CFD models of a full ITPTR system with various configurations of components to illustrate the importance of multi-dimensional effects not captured by 1-D codes. In

2008 and 2011 Conrad [22, 23] reported 2-D axisymmetric CFD studies applied to miniature and micro-scale PTR designs. CFD techniques for simulating pulsating and oscillatory flow have also been reported for investigations of pore-scale thermal and hydrodynamic analyses of flow in porous materials [59–63].

Taylor [31,64] reported the application of 2-D axisymmetric CFD modeling to the efficient design of flow transitions between the pulse tube and its adjacent components which have drastically different diameters. Taylor has reported the validated use of this methology to temperatures as low as 4 K with the use of appropriate real gas models.

Liang and de Waele [65] applied 3-D CFD simulation of the pulse tube component to a theoretical pulse tube design to reveal a convective loop caused by jetting. Hozumi et al. [66] also applied 3-D CFD simulation, this time to an orifice PTR. Hozumi was the first to investigate thermal convection in inclined pulse tubes, though the simulations performed were not carried longer than 0.1 seconds, which will be shown in later chapters to be insufficient for periodic steady-state flows to be developed.

In 2012 Carbo [67] approached the problem of instability in inclined pulse tubes using numerical methods applied to classical stability theories. The key simplification made in this work was that the pulse tube was square instead of cylindrical, allowing a 2-D domain to be simulated. Carbo applied his modeling methodology to the results reported by Swift and Backhaus, with the conclusion that their use of the Boussinesq approximation in deriving the pulse tube convection number N_{PTC} did not meet the requirements for such a simplification. Additionally, his work predicted that the functional dependence on temperature should have an exponent of 0.4 in place of the square-root relation used. This modified dependency is given in Equation 2.43.

$$N_{PTC} = \frac{\omega^2 a^2}{g l_{char}} (\beta \Delta T)^{0.4} \tag{2.43}$$

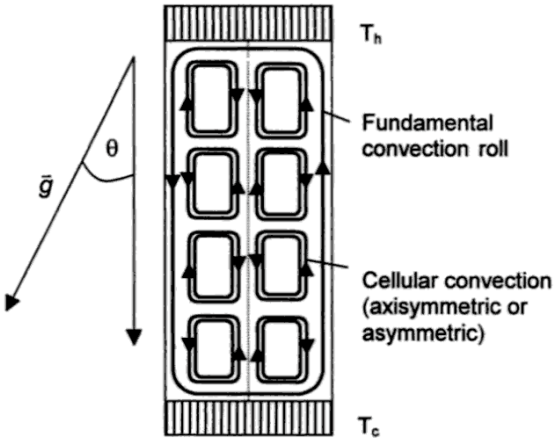

Figure 2.13: Hypothesized muticellular convection regime suggested by Kasthurirengan et al. [68].

2.3.4 Experimental Flow Straightening Approaches

In 2002 Kasthurirengan et al. [68] experimented with flow straightening in low frequency pulse tubes using various porous materials applied within the flow domain. Helical twists of various high and low conductivity screen materials (ranging from copper to nylon) with various mesh numbers were inserted in the pulse tube and the effects on cooling temperature were noted. Although convection was significantly suppressed, the cooling power also suffered in the vertical orientation. This work also suggested that the convection present in the pulse tube should be asymmetric and could possibly be muticellular as illustrated in Figure 2.13.

In 2011, Zhang, Hu, Luo, and Dai [53] reported a novel suppresion technique for reducing orientation sensitivity. Their approach involved partitioning the flow channel into seven axially spaced segments using high conductivity screens separated by low thermal conductivity PTFE rings. A schematic of their approach is included in Figure 2.12 extracted from [53]. The theoretical basis behind this approach was to reduce the effective length constant of each flow channel in order to decrease the Richardson number Ri, which indicates the importance of convection in a flow regime. As with the method reported by Kasthurirengan, the insertion of flow impedances

within the pulse tube reduced orientation sensitivity, but also reduced the cooling performance in the vertical orientation.

The apparent conclusion of the reported experimental methods for reducing convection instability in pulse tubes is that the addition of any impedance to the flow field within the pulse tube causes a reduction in performance across the operating range. It seems that the more sensible solution, if feasible, is to design the pulse tube in such a way as to avoid an unstable flow scenario. The approach taken in this dissertation favors intelligent design over added mechanical complexity.

CHAPTER III

MODELING METHODOLOGY AND THEORY

In order to design efficient refrigeration devices, including pulse tube refrigerators (PTR), it is necessary to first develop an understanding of the often nonlinear interplay between the design parameters that govern system dynamics. The general approach adopted by most engineers is to develop a simplified first-order model, build an apparatus based on this model, and then correct that model based on data gathered from the experimental apparatus. Another approach is to develop a higher order model, which although more computationally expensive, is likely to yield more precise results. The trade-off between a first order model and a higher order model is of course the time required to solve it. A first-order model can be used as a scoping tool to allow quick exploration of a broad design domain, but could result in an inaccurate solution. The higher order model approach inspires confidence in the results, but significantly limits the scope of investigation and may preclude the finding of true global optima.

A more sophisticated approach utilizes a combination of both modeling methods for the tasks that they are best suited. In the development of pulse tube refrigerators, the method adopted by the author is to first determine the desired system architecture, build a one-dimensional semi-empirical model, then isolate the components for which the risk is highest that the model does not accurately capture its effects. The identified zones are then modeled with a higher order tool such as 2-D and 3-D computational models including finite element analysis (FEA) or finite volume methods. These often rely on commercially available computational fluid dynamics (CFD) tools which incorporate routines for most physical situations.

The results of a higher order CFD model are analyzed to determine whether: (a) the one-dimensional model was sufficiently accurate to move forward, or (b) the one-dimensional model needs modification and the design needs to be reworked. At this point the thermodynamic design either moves forward to mechanical development, or undergoes another iteration of modeling. Often times, the results of higher order models and resulting measurements from an experimental apparatus can be used to correlate a first-order model well enough that CFD models are no longer necessary to build enhanced confidence in the results.

In this chapter, we will discuss the modeling tools used within this computational and experimental investigation. Commercially available codes based on well-known computational methods are used whenever possible, and are modified with external routines when necessary to render the model relevant to the atypical flow regimes encountered in cryogenic oscillatory flow. The context of these models as they pertain to the design and development process is illustrated in Figure 3.1.

3.1 First-Order System-Level Modeling Methods

A number of codes are available to simulate the components of the pulse tube refrigerator (PTR) as well as packages which interface submodels to simulate system performance. These modeling methods will be addressed in the following sections.

3.1.1 REGEN 3.3

REGEN 3.3 [69] is a 1-D finite difference model used to simulate performance of cryocooler regenerators with various geometries. The regenerator is typically the first component designed in a cryocooler system due to the fact that it determines that maximum cooling capacity that the system could conceivably be achieved. The Fortran-based program REGEN 3.3 is an open-source model developed by the National Institute of Standards and Technology (NIST) that solves the equations of motion and heat transfer within a variety of matrix materials including parallel plates,

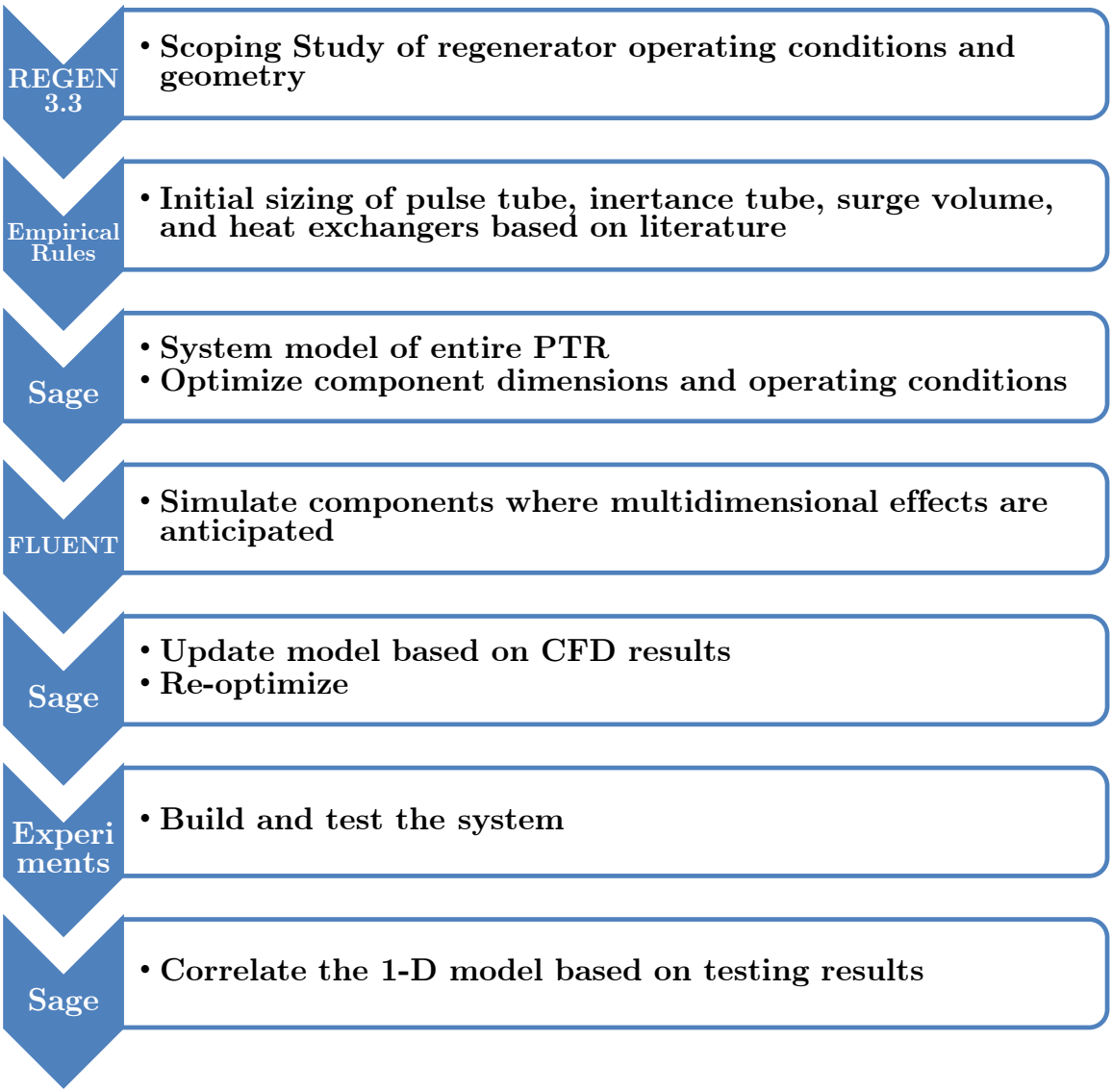

Figure 3.1: Flow chart of PTR modeling applied to the design process

stacked screens, and packed sphere beds. The program also includes real gas properties for both helium-3 and helium-4 as well as temperature-dependent property routines for 32 commonly used materials for design down to at least 4 K. REGEN utilizes an approach common to simulating oscillatory flow conditions where the solution is iteratively marched forward in time until the solution no longer changes with further iteration. REGEN is used as a result of its excellent accuracy and solution economy. A regenerator can be simulated with high confidence in approximately two minutes on current Intel i7-3770 3.4 GHz multicore workstations. This solution speed allows for thousands of designs to be iteratively solved and compared, identifying optima in a relatively short period of time.

3.1.2 Overview of Sage Simulation Environment

Sage [70] is an object-oriented program which integrates primitive submodels of each of the components found in typical cryogenic systems which operate based on acoustically driven flows. These primitive components called children can be interfaced to produce parent models that represent components such as pulse tubes, tube bundle heat exchangers, regenerators, pistons, and much more. These parent models are then interfaced with appropriate representations of fluid and energy flows to develop a fully-integrated global system model. The system model is iteratively solved using a looping time domain, referred to as a "time ring". Figure 3.2 illustrates the heirarchy between parent and child models and the global model.

Similar to REGEN, Sage has the advantage of incorporated property routines for common cryogenic materials as well as many cyrogenic gas property routines. Low-Temperature Sage v8.0 is the version utilized by the Georgia Tech Cryo Lab (GTCL) as it includes a routine to reference real gas properties from NIST's REFPROP database [71]. A key strength of the Sage software is that it incorporates nonlinear optimization procedures that allow for system-level optimization of one

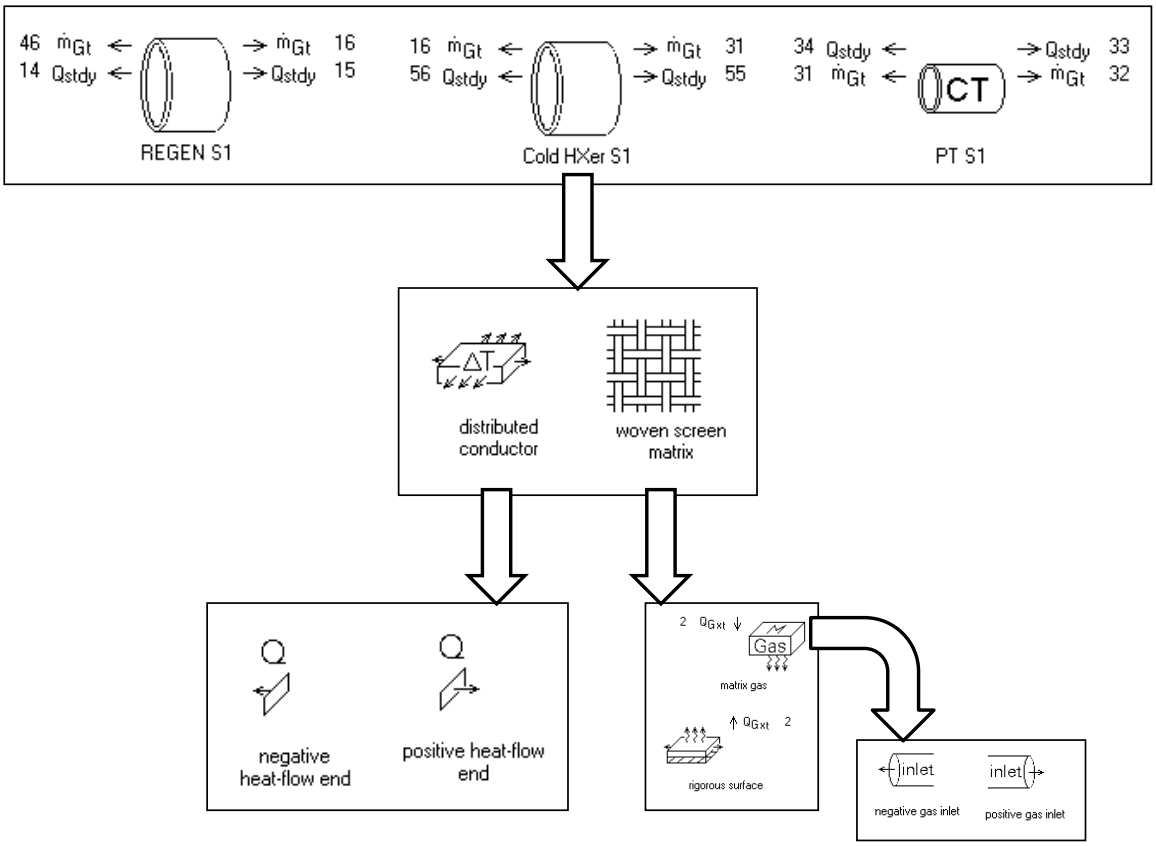

Figure 3.2: Example heirarchy illustration of the Sage simulation environment. Example is of a regenerator, cold heat exchanger, and pulse tube section. The submodels indicate the primitive components used to simulate a stacked screen heat exchanger.

or more of the system parameters simultaneously including component geometries and system operating conditions. When properly utilized, Sage is capable of finding globally optimal solutions of the design space.

The disadvantage of using system-level optimization programs such as Sage for design is that the solution time is inherently much longer than component models due to the complexity of the simulation. Another disadvantage is that the models are semi-empirical, meaning they are only as accurate as the underlying physics being represented, and system performance is often overpredicted when default values are used. The solution accuracy can be readily improved by correlating the models by incorporating adjusment factors in each submodel such that the results match experimentally measured values over a wide range of operating points.

Sage is used within this research project in order to derive flow conditions such as pressure amplitude and mass flow in locations where these values cannot be experimentally measured without severely impacting the performance of the component. Often the compact size of the components and the harsh conditions present preclude the use of most sensors. A well-correlated model can reliably reproduce those flow conditions within a small margin of error, comparable to the accuracy of the sensors that would be used to measure them.

3.1.3 DeltaEC

Design Environment for Low-amplitude ThermoAcoustic Energy Conversion (DeltaEC) [72] is an open-source program developed and distributed by Los Alamos National Lab. Similar to Sage, DeltaEC provides primitive objects that can be interconnected to simulate thermoacoustic systems. The decision between DeltaEC and Sage is based on preference and price. DeltaEC does not incorporate the optimization capability of the Sage distribution.

3.2 Multidimensional Computational Fluid Dynamics

The first order modeling methods presented in the previous sections rely on primitive models that contain mathematical representations of the physical phenomena that characterize the component they represent. Computational fluid dynamics (CFD) relies on a similar principle, in that models are composed of pieces for which the underlying physics they represent are well-known. The difference between first-order and CFD models is the flexibility to represent nearly any fluid and energy flow regime without prior knowledge of the physical principles unique to the system being simulated, creating a versatile and powerful tool. The primitive objects in the case of CFD are finite volumes which are interconnected via boundaries to form a network called a mesh in the form of the fluid continuum of interest. These finite volumes are small enough to obtain sufficient resolution of the flow field, but large enough that each volume contains a sufficient number of particles that the fluid can be characterized by its bulk properties, and not by its intermolecular physics. Mesh can be prismatic (structured) or unstructured as shown in Figure 3.3.

CFD simulations can be performed in two or three dimensions (2-D or 3-D) depending on the characteristics of the flow being studied. The solution time directly correlates to the number of dimensions simulated as the mesh size grows exponentially when transitioning from 2-D to 3-D simulation. Often the symmetry of a fluid domain can be exploited such as in the case of a non-rotating pipe flow. In such cases a 3-D flow can be represented by an axisymmetric 2-D domain. The caveat to this approach is that both the physical domain and the flow must be symmetric. Axisymmetry is often exploited when modeling linear PTRs as the computational time is significantly reduced.

Similar to the first-order models presented in the previous section, CFD models exist in various levels of complexity depending on the accuracy dictated by the problem statement and the computational economy required by the user. CFD is capable

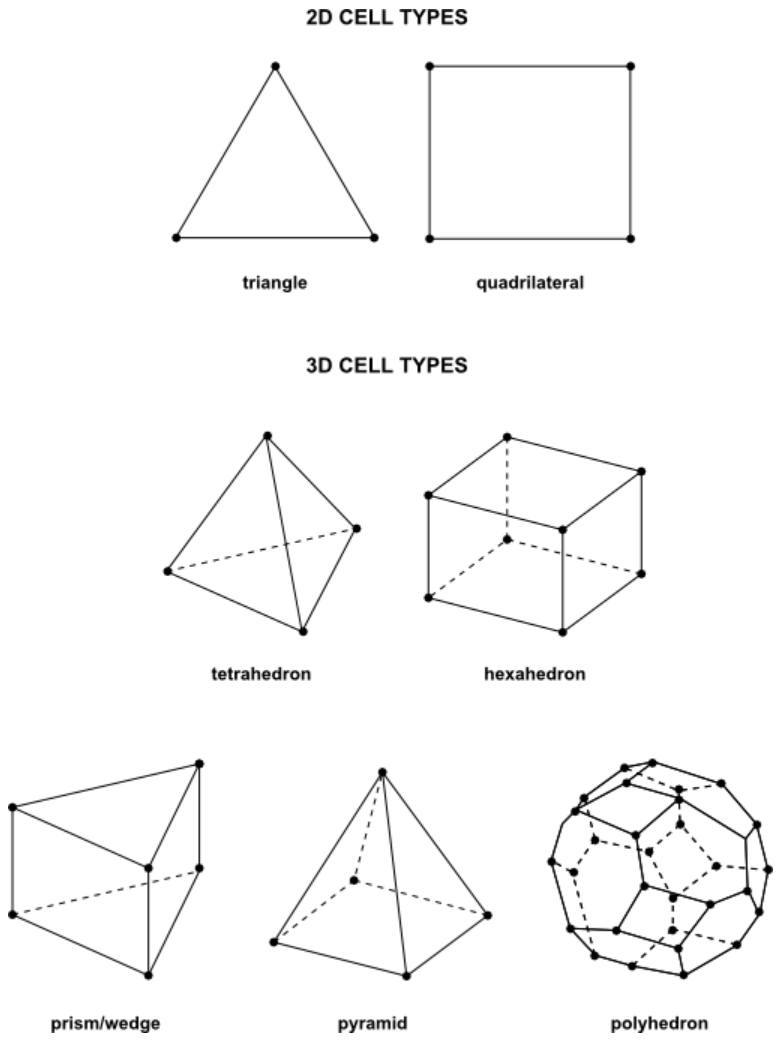

Figure 3.3: Examples of meshing elements that can be combined to represent 2-D and 3-D CFD domains. Reproduced from ANSYS FLUENT user's guide [73].

of simulating isolated sections of a flow field as well as full complex systems. Various levels of simplicity can be assigned by the user based on the flow field as well. In addition to fluid flow, most commercial packages are able to simulate fluid-solid interfaces as well as solve for energy transport via conduction and radiation heat transfer. At the extreme end, CFD simulations can be used to simulate multi-component mixtures of fluids which experience phase change, chemical reactions such as combustion, and turbulence within a complex structure. Multiphysics packages such as Comsol and ANSYS are capable of incorporating CFD models with fluid-structure interations as well as other physics models such as vibration, kinematics, and electromagnetics.

The approach utilized by the current PTR study was to modify the commercial CFD package ANSYS FLUENT 14.5.7 with user-defined functions (UDF) and materials to sufficiently model the oscillatory flow of a cryogen. 3-D modeling is dictated by the presence of the gravitational field which invalidates the simplifying assumption for the otherwise axisymmetric geometry. Applying an axisymmetry condition to the current problem would be akin to applying a gravitational vector rotated around the symmetry axis such that a conical vector is formed with an apex converging in the center of the flow field. This condition is obviously not physical. The following sections present the details of CFD simulation as they pertain to the current study of oscillatory flow in an inclined tube subject to a gravitational body force applied in a direction not parallel to the primary flow direction (off-axis).

3.3 Governing Equations for Computational Fluid Dynamics

Let us present the continuity equations for mass, momentum, and energy conservation as they apply to numerically simulated systems composed of mixed finite volumes and finite elements. The following sections develop and report the governing equations as they apply first to fluid zones, then to solid regions, and finally to porous media.

3.3.1 Fluid Zone Finite Volume Governing Equations

The following section discusses the generic expressions solved by each mesh cell within the fluid domain for the purposes of numerical solution in the commercial code ANSYS FLUENT [74]. The equations reference a fixed Cartesian xyz coordinate frame. In order to simulate the flow physics attributed to each mesh cell, the basic continuum conservation equations are solved for mass and momentum.

Conservation of mass is given by the expression displayed in Equation 3.1.

$$\frac{\partial \rho}{\partial t} + \nabla \cdot (\rho \vec{u}) = S_m \tag{3.1}$$

In Equation 3.1 ρ is the gas density, u is the fluid velocity, and S_m is a mass source term used to introduce or remove mass as in the case of reactions such as combustion. The mass source can also represent phase change phenomena where one phase must be removed for the secondary phase to be introduced, thus maintaining continuity. The source term can be controlled using user-defined functions (UDF) to model physical phenomena outside the scope of the FLUENT simulation package or introduced through specialized sub-models applied to the fluid domain. In all simulations undertaken in this body of work, the source term $S_m = 0$ as the flow under investigation consists of a pure single phase gas.

The conservation of momentum can be expressed as follows:

$$\frac{\partial \rho}{\partial t}(\rho \vec{u}) + \nabla \cdot (\rho \vec{u}\vec{u}) = -\nabla p + \nabla \cdot (\bar{\bar{\tau}}) + \rho \vec{g} + \vec{F} \tag{3.2}$$

where $\rho \vec{g}$ is the gravitational body force, which is critical in this study, and $\vec{F}$ is an external or user-defined body force. In Equation 3.2, $\bar{\bar{\tau}}$ is the viscous stress tensor given by:

$$\bar{\bar{\tau}} = \mu \left[\left(\nabla \vec{u} + \nabla \vec{u}^T \right) - \frac{2}{3} \nabla \cdot \vec{u} \bar{\bar{I}} \right] \tag{3.3}$$

where μ is the molecular or dynamic viscosity, and $\bar{\bar{I}}$ is the identity tensor.

The models solved in this thesis include internal heat transfer within the fluid as well as conjugate heat transfer between the fluid and the bounding walls. In

order to model heat transfer by conduction and convection, the energy equation is solved. The generic form of the energy equation solved in FLUENT is given by Equation 3.4, where they have chosen an enthalpy based formulation rather than the classical internal energy based method. The simplifications applied to the equation are then discussed, leading to a slightly simplified form of the energy equation as solved in the dissertation simulations.

$$\frac{\partial}{\partial t}(\rho E) + \nabla \cdot (\vec{u}\,(\rho E + p)) = \nabla \cdot \left[k_{eff} \nabla T - \sum_{n} h_n \vec{J}_n + (\bar{\bar{\tau}}_{eff} \cdot \vec{u}) \right] + S_h \qquad (3.4)$$

k_{eff} is the effective thermal conductivity of the fluid given by the sum of the fluid thermal conductivity and the turbulent thermal conductivity, which depends on the turbulence model utilized. S_h is an energy source term, which is not used in the reported simulation set. E is the total fluid energy given by Equation 3.5:

$$E = h + \frac{p}{\rho} + \frac{u^2}{2} \qquad (3.5)$$

The sensible enthalpy h in Equation 3.5 is typically defined for a gas mixture according to Equation 3.6:

$$h = \sum_{j} Y_n \int_{T_{ref}}^{T} c_{p,n} dT \qquad (3.6)$$

however, the gas properties in this study are extracted from an external routine which references the NIST REFPROP [71] database, therefore the enthalpy is called up according the temperature and density at each time step and at each location. As a result, Equation 3.6 can be replaced by its referenced value from REFPROP according to Equation 3.7.

$$h = h(T, \rho) \qquad (3.7)$$

The summation in the second term on the right hand side of Equation 3.4 represents the energy transported with diffusion flux J_n associated with species n, and since there is only a single species in the current mixed convection study, the summation can be eliminated altogether. Removing the species diffusion flux and the

energy source term, the simplified energy equation given by Equation 3.8 represents the expression solved in the open fluid domains for the pulse tube simulation set:

$$\frac{\partial}{\partial t}(\rho E) + \nabla \cdot (\vec{u}\,(\rho E + p)) = \nabla \cdot [k_{eff} \nabla T + (\bar{\bar{\tau}}_{eff} \cdot \vec{u})] \tag{3.8}$$

3.3.2 Energy Equation in Solid Domains

In both system-level and component-level modeling domains to be discussed in the following chapters, the role of solids strongly influence the simulation results in the pulse tube domain. The underlying physics incorporated in the solution of finite element discretized solid regions is limited to the energy equation for solid materials as given in Equation 3.9, where the subscript s represents properties of the solid material.

$$\frac{\partial}{\partial t}(\rho h_s) + \nabla \cdot (\vec{u} \rho_s h_s) = \nabla \cdot (k_s \nabla T) + S_h \tag{3.9}$$

The sensible enthalpy of the solid material, h_s is computed as:

$$h_s = \int_{T_{ref}}^{T} c_{p,s} dT \tag{3.10}$$

The second term on the left hand side of Equation 3.9 represents convective energy transfer due to motion of solid regions, which only applies in the cases of a moving reference frame or a solid particle-laden flow which physically transports mass. In the current simulations, this term drops out of the energy equation. The volumetric energy source term S_h is also not utilized in the current simulations, therefore the equation can be reduced further.

The material properties k_s and $c_{p,s}$ are computed based on user-defined property routines for the various materials used in the studied PTR domains. The details of the solid property routines are explained in depth in Section 3.5.2 to follow. These properties can be applied directionally to allow for material property anisotropy, as in the case of composite bulk materials such as stacks of micromachined plates or screens as would be encountered in regenerators or heat exchangers, or in layered

composites like fiberglass or G10/FR4 epoxy. When anisotropic properties are applied to the computational domain and the unused convective and energy source terms are neglected, the modified energy equation in solids becomes:

$$\frac{\partial}{\partial t}(\rho_s h_s) = \nabla \cdot (k_{ij} \nabla T) \tag{3.11}$$

where k_{ij} is a 3×3 matrix of directional material thermal conductivity properties.

Structural stress-strain relationships which would result in a full fluid-structure interaction (FSI) model are not included in the forthcoming models because they are assumed to have negligible effect on the flow field. The incurred computational expense would not be justified by the marginal increase in solution accuracy. To the author's knowledge, FSI models have not been applied to PTRs in published literature.

3.3.3 Porous Media Theory and Numerical Treatment

Porous media play an important role in PTR systems as well as the simulations performed in this study. Porous treatment is applied in modeling heat exchangers as well as regenerators, both of which consist of individual woven wire screens stacked in the flow direction to form an anisotropic bulk porous material. The inclusion of porous media affects both the momentum of the fluid, resulting in a pressure drop, as well as the desired effect of facilitating effective heat transfer.

Porous media are modeled in FLUENT using superficial velocity based on volumetric flow rate rather than physical velocity, such that the velocity vectors maintain continuity across boundary regions between open flow channels and porous zones. As a result, the physical velocity $\vec{u}$ is replaced by the expression for the superficial velocity $\vec{u}_{sup}$ in the standard conservation equations.

$$\vec{u}_{sup} = \varepsilon \vec{u} \tag{3.12}$$

where the porosity of the medium ε is introduced to account for the fixed volume of solid matrix material in the porous structure. The notation implies homogeneous

porosity throughout the material, though porosity can also be specified as a function of space and time using UDF codes.

$$\varepsilon = \frac{V_{open}}{V_{open} + V_m} \tag{3.13}$$

Equations that govern porous media theory are volume-averaged, such that the pore-level physical phenomena are not resolved but the bulk effects in terms of pressure drop and heat transfer are represented. The conservation of mass is given by a modified form of Equation 3.1

$$\frac{\partial(\varepsilon\rho)}{\partial t} + \nabla \cdot (\varepsilon\rho\vec{u}) = 0 \tag{3.14}$$

The momentum equation (3.2) is modified to include the pressure drop caused by viscous and inertial effects within the porous structure. A second-order viscous resistance tensor, $\bar{\bar{D}}$ (m^{-2}) which is the inverse of the permeability tensor, and and an inertial resistance tensor, $\bar{\bar{C}}$ characterize the key properties of the porous medium under investigation in addition to the base matrix material conductivity and specific heat. The modified momentum conservation equation in porous media is thus:

$$\frac{\partial\left(\varepsilon\rho\vec{u}\right)}{\partial t} + \nabla \cdot (\varepsilon\rho\vec{u}\vec{u}) + \varepsilon\nabla P + \nabla \cdot (\varepsilon\bar{\bar{\tau}} \cdot \vec{u}) - \varepsilon\vec{F}_{bf} + \mu\bar{\bar{D}} \cdot \vec{u} + \frac{\bar{\bar{C}}\rho}{2} \cdot |\vec{u}|\,\vec{u} = 0 \tag{3.15}$$

The inclusion of viscous and inertial resistance as tensors implies the ability to handle anisotropy in the porous domain properties. The porous materials of interest to cryocooler simulation are homogeneous stacks of layered wire screens commonly used in heat exchangers and regenerators, and packed beds of spherical particles which are either constrained with screens or permanently set with dilute epoxy. Only packed screen configurations are considered in this study. Packed screens are transverse anisotropic materials, meaning that the resistance properties are constant along the orthogonal directions, but are direction-dependent.

In practice, FLUENT applies the same mass and momentum conservation equations in both the open and porous domains. Corrections are made for the pressure

drop and associated energy dissipation through appropriately defined source terms. The FLUENT momentum sink in porous media is described by Equation 3.16:

$$S_i = -\left(\sum_{j=1}^{3} D_{ij}\mu u_j + \sum_{j=1}^{3} C_{ij}\frac{1}{2}\rho|u|u_j\right) \tag{3.16}$$

where the indices i and j represent the coordinate directions x, y, and z. Three momentum equations results, each in a principle direction of the porous medium. For isotropic porous components such as packed beds, or for flow through stacked screens in a principal direction (axial or radial), it is often more convenient to define the coefficients in terms of values that are available in open literature, namely the Darcy permeability K and Forchheimer's inertial coefficient c_f. The formulation for pressure drop given by Darcy's law, assuming flow is in a principle direction of the porous medium such as axial or radial in the case of screens, can be written as follows:

$$-\frac{\partial p}{\partial j} = \frac{\varepsilon\mu}{K_j}u_j + \frac{c_{f,j}\varepsilon^2\rho}{\sqrt{K_j}} \cdot |\vec{u}|u_j \tag{3.17}$$

where j is a principal direction of the porous structure. By direct term-by-term comparison of the momentum equation including the porous sink terms and 3.17, the following set of conversions facilitate the use of Darcy permeability (Equation 3.18) and Forchheimer's inertial coefficient (Equation 3.19) for isotropic or transverse anisotropic materials.

$$K_j = \frac{\varepsilon^2}{D_j} \tag{3.18}$$

$$c_{f,j} = \frac{C_j\sqrt{K_j}}{2\varepsilon^3} \tag{3.19}$$

A number of publications investigating oscillatory flow by Cha, Conrad, Clearman, Harvey, Landrum, and Pathak [22, 57, 75–81] give experimentally measured and CFD validated axial and radial coefficient values for screen meshes typically encountered in PTR heat exchangers and regenerators. These publications evaluated the coefficients for both unidirectional (DC) and oscillating (AC) flow regimes and determined that

DC values should be only be applied to oscillating flows with great caution, and there is often significant error associated with this simplification.

In the case of packed sphere beds, the coefficients can be computed directly based on the characteristic particle or pore size and the bulk porosity. In order to apply the appropriate treatment, the following equations can be used to determine the Darcy and Forchheimer coefficients based on Ergun's equations [82]:

$$K = \frac{\varepsilon^3 D_p^2}{150(1-\varepsilon)^2} \tag{3.20}$$

$$c_f = \frac{1.75}{\sqrt{150\varepsilon^3}} \tag{3.21}$$

where D_p is the characteristic particle diameter of the packed bed. In the case of a mixed diameter packed sphere bed, D_p is the hydraulic diameter of a characteristic pore, and typically the smallest pore size is chosen for representation. Unlike stacked screens, packed sphere beds tend to exhibit isotropic hydrodynamic properties, therefore Equations 3.20 and 3.21 are not subscripted. Experimentally derived and CFD-validated values for typical regenerator packed beds are available for a select few geometries at room temperature in recent publications by Pathak, Mulcahey, and Ghiaasiaan [83–85]. Additionally, Cheadle, Nellis, and Klein published a CFD pore-level study of generic packed sphere beds [86].

The simulations performed assume solid-fluid thermal equilibrium within the porous media. The energy equation is the same energy equation used in open flow regions (Equation 3.4), with modifications to correct for the effective conductivity of the matrix and a transient term which accounts for the thermal inertia of the solid phase of the porous medium. The modified energy equation is given in Equation 3.22:

$$\begin{aligned} \frac{\partial}{\partial t}\left(\varepsilon\rho_f E_f + (1-\varepsilon)\rho_s E_s\right) + \nabla\cdot\left(\vec{u}\left(\rho_f E_f + p\right)\right) = \\ \nabla\cdot\left[k_{eff}\nabla T + \left(\bar{\bar{\tau}}\cdot\vec{u}\right)\right] \end{aligned} \tag{3.22}$$

where the subscripts f and s represent properties of the fluid and the solid matrix, respectively, and k_{eff} is the effective thermal conductivity given by the volumetric

average of fluid and solid conductivity as described by Equation 3.23.

$$k_{eff} = \varepsilon k_f + (1 - \varepsilon)\, k_s \tag{3.23}$$

Thermal equilibrium has been shown to be an appropriate assumption in prototypical cryocooler flow conditions in a recent pore-level study by Pathak, Mulcahey, and Ghiaasiaan [87] to be appropriate for the range of frequencies, amplitudes, and fill pressures studied here. A more computationally intensive thermal non-equilibrium model is provided in ANSYS FLUENT. Rather than solving a single equilibrium energy equation, two separate energy equations are solved, one for the fluid phase and another for the solid. Given the negligible error associated with the equilibrium model and the additional time required to solve an additional equation in the system over each grid point at each iteration of every time step, the non-equilibrium model was not considered here. More information on the thermal non-equilibrium model can be found in Section 6.2.3.3.2 of FLUENT's user's guide [73].

3.4 Pulse Tube Modeling Methods - Open and Closed System Modeling

The oscillatory nature of the flow domain in PTR systems currently requires the use of transient modeling techniques, as there are no multi-dimensional codes available to numerically study looped time domains, the method utilized by Sage. There are two approaches that have been experimentally validated and used successfully in 2-D axisymmetric studies in open literature: a closed system method and an open system method. These methods are illustrated in Figure 3.4. The closed system, as the name suggests, contains no inlets or outlets for mass to enter or exit the computational domain; however, energy source or sink terms can be used in either volumetric form within the fluid continuum or at the boundaries. Flow excitation is driven through the use of deforming or dynamic meshing schemes, where wall motion is accomplished by adding, subtracting, or deforming cells in the zone adjacent to the moving boundary.

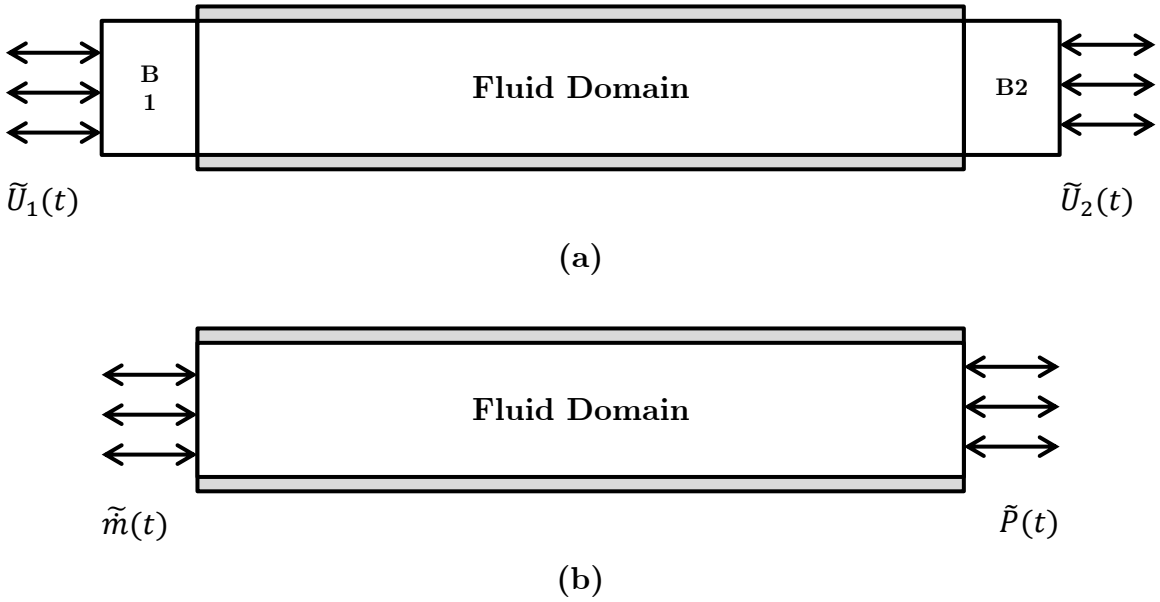

Figure 3.4: Comparison of **a.** closed-system and **b.** open-system modeling methods in CFD.

The advantage to this method is that the user does not need to know any details of the flow *a priori*. The disadvantage of the method is that the flow conditions desired are not easily controlled to meet exact specifications, with the exception of the case where an actual piston motion is being simulated. This method lends itself best to full system simulations.

The open system methodology requires knowledge of at least two key characteristics of the flow: boundaries consisting of either a known mass flow, velocity, and/or pressure as a function of time. The advantage of this modeling approach is the explicit control of specific flow features specified on a cross-section of the control surface, which is often the case when the pulse tube is the component of interest. This allows the simulation to focus explicitly on an isolated domain of interest, simplifying the meshing. During the design phase, pulse tube designers often know the cold end mass flow, mass-pressure phasing, and pressure ratio. Knowledge of these features allows the model to reduce mesh size by only meshing the flow domain of interest, whereas the closed system models often require the addition of purely computational buffer

zones which allow the moving mesh to be far enough removed from the flow features of interest that the flow is not affected by the moving zones. A difficulty with this simulation method is that it is often difficult for mass to be conserved within target convergence criteria in transient simulations. Another concern that must be considered when using this method for reversing flow fields is that any downstream effects in the reversed flow will be lost, as the fluid entering the domain will be uniform and conform (perhaps unphysically) to the user-specified temperature, pressure, and flow-profile. If there are no adjacent geometries that would introduce a non-uniform flow profile into the domain, the concern is alleviated.

3.4.1 Boundary Conditions

Boundary conditions vary based on the choice of an open- or closed-system modeling approach. Boundary Conditions (BCs) specific to each modeling method will be presented in the corresponding "computational domain" sections for the system-level and pulse tube component-level models. This section will cover the details of boundary conditions that are common to all approaches: isothermal wall conditions, adiabatic wall conditions, and symmetry conditions.

3.4.1.1 Isothermal Boundaries

Isothermal boundaries are commonly used throughout the forthcoming simulations in order to simulate a constant temperature load in locations such as heat exchanger walls, or ambient thermal rejection surfaces. Isothermal conditions allow energy to enter or exit the computational domain in real-time to facilitate heat transfer with the gas or solid boundary where it is applied. The amount of energy entering or exiting the domain at any time at an isothermal boundary is equal to the solid conduction, if the boundary is applied to a solid zone, or the combined gas conduction and convection, if applied as a boundary to a fluid zone. This expression is mathematically represented

as follows:

$$q_{surf} = -k_{s,f}\left(\frac{\partial T}{\partial \hat{n}}\right)_{surf} \tag{3.24}$$

where $k_{s,f}$ is the conductivity of the solid or fluid adjacent to the isothermal boundary, depending on application, and $\hat{n}$ is the unit vector normal to the isothermal surface.

3.4.1.2 Adiabatic Boundaries

Unlike isothermal boundary conditions, adiabatic boundaries do not allow any heat to enter or exit the domain, and are therefore perfectly insulated. This is accomplished numerically by setting the condition that the temperature gradient in the wall's inward normal direction must be zero at all times. This is mathematically stated in Equation 3.25.

$$\frac{\partial T}{\partial \hat{n}} = 0|_{wall} \forall t \tag{3.25}$$

3.4.1.3 Symmetry Boundaries

Symmetry boundaries represent a very powerful simplification when used appropriately. The conditions for the use of symmetry are both geometric symmetry and flow symmetry. One of the assumptions of the symmetry condition is that there is no mass flow through the symmetry boundary and therefore no component of any velocity vector orthogonal to the plane of symmetry. Additionally, there is no heat transfer across the symmetry plane; therefore as a condition of the symmetry boundary there must be no temperature gradient orthogonal to the plane of symmetry.

3.4.2 Operating Conditions

The main operating condition that must be defined is the system operating pressure $\bar{P}$. This term is important because it strongly affects the gas properties, which in turn affect all physical processes. The system operating pressure is akin to the charge pressure set in a cryocooler device prior to cooling that device down. Though the final operating pressure typically is reduced in a cryogenic system compared to the

fill pressure at ambient temperature, this effect is difficult to capture when specifying the operating pressure in a numerical simulation.

3.4.2.1 Buoyancy-Driven Flows

In order to simulate flows where buoyancy is important to the flow field, a number of settings must be properly configured in FLUENT in addition to using an appropriate fluid property package with temperature- and pressure-dependent properties. Determining the importance of buoyancy in a flow field in mixed convection is typically evaluated by computing the ratio of the Grashof and Reynolds numbers as shown in Equation 3.26.

$$\frac{Gr}{Re^2} = \frac{g\beta\Delta T L}{u^2} \tag{3.26}$$

where β is the thermal expansion coefficient given by Equation 3.27, ΔT is the characteristic temperature difference, and L is a relevant length scale, which varies according to the problem formulation. When value of the ratio exceeds 1, buoyancy is expected to have a large effect. Unfortunately this criterion was formulated for steady-flow behavior and has not been characterized for accuracy in oscillating flows. As a first-order approximation, the oscillatory velocity amplitude U_d can be substituted for u.

$$\beta = -\frac{1}{\rho}\left(\frac{\partial \rho}{\partial T}\right)_p \tag{3.27}$$

Once it is determined that buoyancy effects must be incorporated, the first key task is to specify the gravitational vector. In the context of the three-dimensional simulations undertaken in this dissertation, the z-axis is always oriented in the primary oscillating flow direction pointing from the warm end of the pulse tube to the cold end. The symmetry plane is always specified in the y-z plane, the plane in which the gravity vector is specified. The lack of an x-component in the gravity vector is the feature that allows the use of half-symmetry. Therefore, the gravity vector is

specified in the y- and z- directions according to Equation 3.28.

$$\vec{g} = 0\hat{i} - g\sin\theta\hat{j} + g\cos\theta\hat{k} \tag{3.28}$$

The gravitational vector can also optionally be controlled through a time-variant UDF function if one were interested in simulating the effects of a transient gravitational field such as the case of a rocking or pitching motion of the domain.

A subtle requirement to accurately model buoyancy driven cryogenic flows in FLUENT is that the system must be given a specified operating density of 0 kg/m^3 when an external property routine such as the *nist-real-gas* user-defined property package is used. If the default operating density is used, or the Boussinesq approximation is implemented, the temperature- and pressure-dependent properties will be overridden in the momentum equations using a redefinition of pressure as outlined in ref. [73].

Although solutions for steady mixed-convection problems can be found using the steady solver, the solution must utilize the Boussinesq approximation for density variations, and therefore accuracy is compromised. The preferred method of solution for mixed convection flows is a transient approach. Due to the oscillating nature of the flow field of interest, transient formulation must be used.

3.4.3 Initial Conditions

Initial conditions are critically important to the expedient and stable convergence of oscillating models to their final steady-state values. Initial conditions for the flow velocity field as well as the temperature field are specified as a starting point for the solver. The closer the initial conditions are to the final values, the faster the solution will converge. Velocity fields in inertial flows are complicated functions of both time and space, therefore it is difficult to accurately initialize the field to a meaningful set of values. Instead, the velocity fields are uniformly specified in $\vec{x}$, $\vec{y}$, and $\vec{z}$ to an arbitrary value of 0.001 m/s. Giving the field a small, non-zero value allows the solution to be initially more stable than initializing to either a quiescent field or to

an appreciable unidirectional flow velocity.

Temperature initial conditions are specified much more carefully than the velocity fields because they have a much more significant effect on the energy equation convergence. Many authors have reported using linear temperature field functions to initialize temperature in PTR domains [22, 31, 64] since there are large temperature gradients present. Initializing to a constant initial temperature near ambient temperature requires the simulation to carry out over the full time range required for the cooler to complete its cooldown procedure. A linear temperature profile in the form of Equation 3.29 is used to specify the initial temperature profile in porous zones experiencing temperature gradients such as the regenerator component.

$$T(z) = T_H - \frac{(T_H - T_C)}{L_{Regen}} \cdot z \tag{3.29}$$

Kashani et. al [28] suggest the use of a power-law relationship in the form of Equation 3.30, which better approximates the temperature profile in the central portion of the pulse tube component. The power law formulation is used as the initial temperature condition for all pulse tube sections simulated in the current study.

$$T(z) = T_C \cdot \left(\frac{T_H}{T_C}\right)^{\frac{z}{L_{PT}}} \tag{3.30}$$

Non-uniform temperature profiles are implemented as initial conditions using custom field functions in FLUENT. For examples of their implementation, the reader is encouraged to examine the sample journal files in Appendix B.1.

3.4.4 Solver Settings

The choice of solver type and settings strongly affects the stability, accuracy, and speed of a numerical solution. A thorough investigation of all of the available solver schemes was undertaken by the author to categorize these criteria as applied to the computational domains of interest in this study. It was found that of the three solver

options: pressure-based, density-based, and coupled, that a coupled solution methodology with a low Courant number provides the best trade between solution speed and stability. Higher Courant numbers of 200 and 1000000 have been successfully used in some of the simulations reported, but the solution stability suffered in some cases resulting in divergence of the energy and continuity residuals, which in turn caused the solutions to require excessive iteration to regain stability. For that reason, a very conservative value of 5 was used for all simulations that were performed using supercomputing resources with no graphical user interface (GUI). The solution settings used for all reported simulations are presented in Table 3.1.

Table 3.1: Solver settings for all CFD simulations reported.

Setting	**Value**
Solver Type	Coupled
Flow Courant Number	5
Momentum Relaxation Factor	0.75
Pressure Relaxation Factor	0.75
Density Under-Relaxation Factor	0.75
Body Forces Under-Relaxation Factor	0.75
Energy Under-Relaxation Factor	1.0

The under-relaxation factors (URF) used also strongly affect the solution speed and stability. Using lower under-relaxation factors typically improves solution speed, but decreases stability. Slightly reduced URFs are used for all equations with the exception of the energy equation. It is never recommended to relax the energy equation because large energy losses can quickly accumulate in transient simulations, degrading solution accuracy.

The convergence criteria are also important factors used to determine the solution speed and overall accuracy of the solution. The criteria used here are based on the

residuals of the solved system of equations for continuity, orthogonal velocities, and energy. Stringent convergence criteria were used to ensure that numerical drift is avoided in the transient simulations. The criteria used are displayed in Table 3.2.

Table 3.2: Residual convergence criteria settings for all CFD simulations reported.

Residual	**Absolute Criteria**	**Absolute or Relative**
Continuity	1×10^{-6}	absolute
X-Velocity	1×10^{-6}	absolute
Y-Velocity	1×10^{-6}	absolute
Z-Velocity	1×10^{-6}	absolute
Energy	1×10^{-8}	absolute

3.4.5 Discretization Schemes

The spatial and transient discretization schemes used for discretizing the terms in the underlying physical equations for solution and the formulation for marching the transient solution forward in time are summarized in Table 3.3.

Table 3.3: Discretization schemes used for all CFD simulations reported.

Term	**Type**	**Scheme**
Gradient	Spatial	Green-Gauss Cell Based
Pressure	Spatial	PRESTO!
Density	Spatial	Second Order Upwind
Momentum	Spatial	Second Order Upwind
Energy	Spatial	Second Order Upwind
Transient Formulation	Temporal	First-Order Implicit (system-level)
Transient Formulation	Temporal	Second Order Implicit (component-level)

3.4.6 Meshing Schemes

Meshing details for each of the computational domains in this study will be presented in Sections 4.2 and 5.2. In both cases, the domain is entirely composed of prismatic cells in order to ensure excellent orthogonal quality. Orthogonal quality is a critical metric because the higher the value, the more easily the the solver can converge to a solution. High aspect ratio meshes with low orthogonal quality such as those used in unstructured meshes typically required more iterations to solve each time step and lead to energy imbalances.

3.5 Material Properties

Within the cryogenic regime, both solid materials such as metals and composites, as well as gases exhibit interesting properties. Very few materials exhibit linear relationships between temperature and conductivity, specific heat capacity, viscosity, and density at cryogenic temperatures. From a numerical solution standpoint, this makes incorporation of temperature-dependent properties a challenge as nonlinear properties can cause solution instability. In this section we will discuss the treatment of the gas and solid properties pertinent to the simulation of inclined pulse tube systems.

3.5.1 Working Gas Properties

The working gas used in all simulations is research grade helium-4 (99.9999% ultra-pure). Near room temperature helium is well characterized by the ideal gas equations of state:

$$P = \rho RT \tag{3.31}$$

where R is the gas constant for helium. Viscosity is also well treated by traditional methods such as Sutherland's formula:

$$\mu = \mu_0 \frac{T_0 + C}{T + C} \left(\frac{T}{T_0} \right)^{3\backslash 2} \tag{3.32}$$

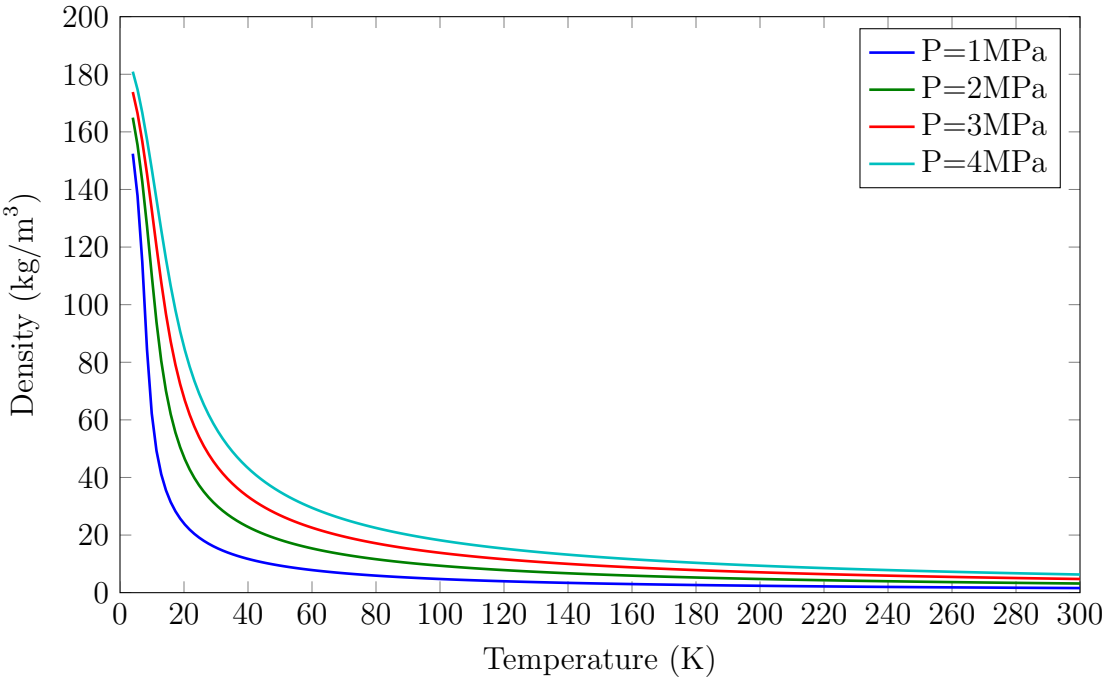

Figure 3.5: Helium density as a function of temperature and pressure [71].

where μ_0 is the reference viscosity of 19 $\mu Pa \cdot s$ for helium, T_0 is the reference temperature of 273 K, and C is Sutherland's constant for helium, which is 79.4 K.

The linear assumptions of the ideal gas law begin to break down as the temperature drops below approximately 80 K. At that point, the compressibilty of the gas deviates from 1.0 and the density becomes a non-linear function of temperature as illustrated in Figure 3.5.

The simulations carried out within the scope of this work cover a cold end range between 4 K and 80 K, therefore the use of a real gas property routine is incorporated into the models to ensure effective treatment of gas properties. The nist-real-gas routine is a user-defined property package within FLUENT's simulation environment that references NIST's REFPROP database of real gas properties. Although the routine increases computational complexity, the properties are accurate over the entire range of simulations. Although certain simulation sets encompass temperatures within the ideal gas regime and would typically justify its use, nist-real-gas is applied

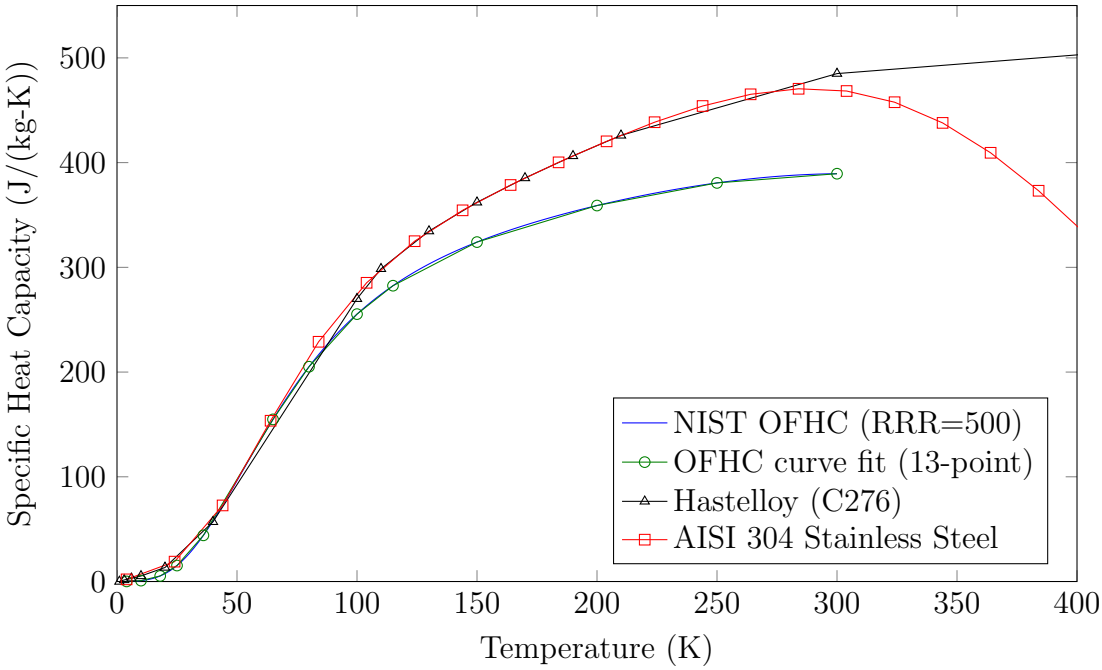

Figure 3.6: Solid material specific heat capacity as a function of temperature [88].

to all models to allow consistent processing of results.

3.5.2 Solid Material Property Treatment

The common solid materials used in both system-level and component-level CFD simulations are oxygen-free high-conductivity (OFHC) copper, AISI 304 Stainless steel, and Hastelloy (C276), a nickel-based superalloy used for pulse tube shells as a result of their extremely low thermal conductivity. Temperature-dependent properties are extracted from empirical data collected by the National Institute of Standards and Technology (NIST), which have been published in open literature [88]. These materials are represented by piecewise-linear curve fits of the NIST empirical curves and coded in a user-defined cryogenic material library. Plots of the specific heat capacity and thermal conductivity are shown in Figures 3.6 and 3.7.

3.5.3 Porous Material Property Treatment

Porous materials are widely used within the PTR domain. The regenerator and heat exchanger domains are composed of wire cloth screens punched into discs and

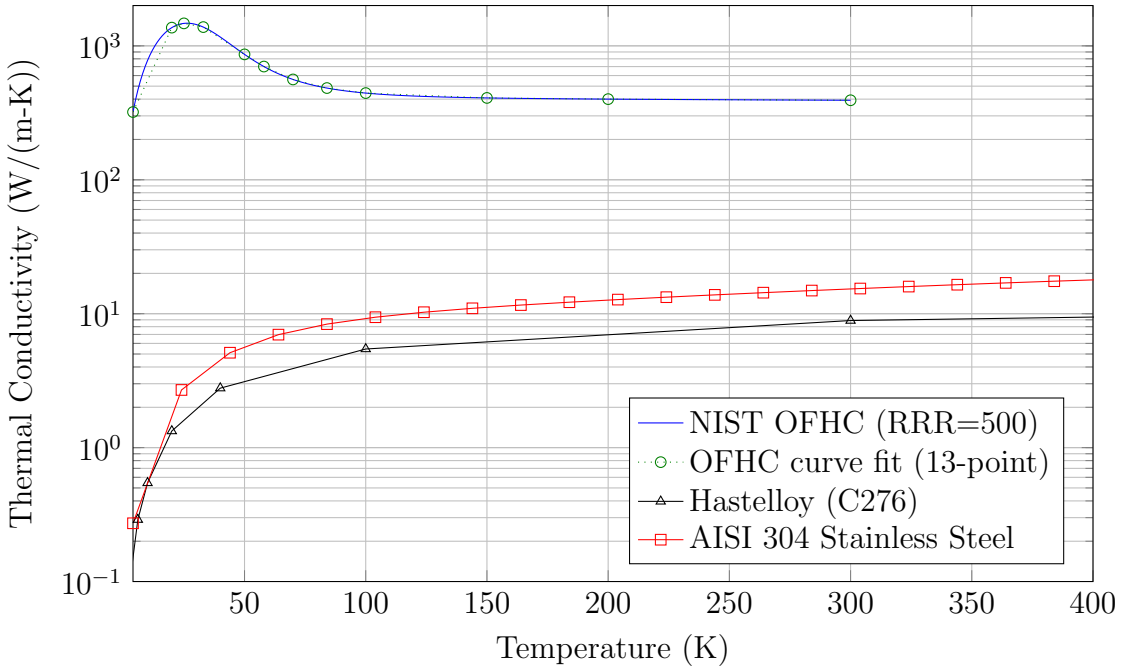

Figure 3.7: Solid material thermal conductivity as a function of temperature [88].

packed in the streamwise direction. The morphology of these screen packs causes the materials to exhibit anisotropic hydrodynamic and heat transfer properties in the flow and radial directions. Figure 3.8 illustrates front and side views of a punched mesh screen and clarifies the root of the hydrodynamic and thermal anisotropy. The packing factor for wires is significantly higher in the profile view, which corresponds to the radial flow direction since screens are packed in the axial flow direction. The actual flow path seen by the fluid in the axial direction depends on the directional alignment of the screens as they are packed, characterized by Moiré patterns. If they were perfectly aligned as shown in Figure 3.8c, there would be extremely low flow resistance. Optimal packing occurs when the screens are randomly aligned.

In order to model packed screens as a porous medium within a computational simulation, information must be specified about the hydrodynamic parameters such as the Darcy permeability and Forchheimer's inertial coefficient. Table 3.4 summarizes the directional hydrodynamic properties of the materials used within the simulations performed in this study. Note that the z-axis points in the flow direction for 3-D

a. Plain Weave

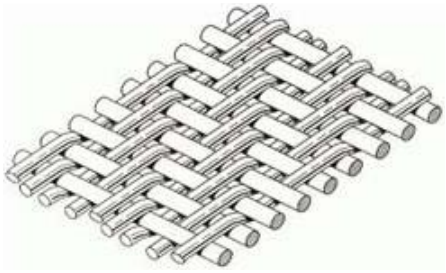

b. Twill Weave

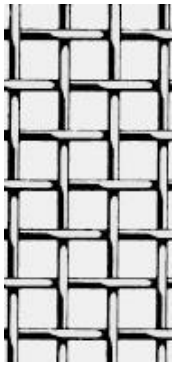

c. Front (axial flow) View

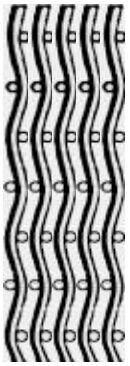

d. Side (radial flow) View

Figure 3.8: Overview of porous screen materials. Isometric views of **a.** the plain weave screens used in reegnerator simulations, and **b.** the twill mesh used in heat exchangers. **c.** Front and **d.** side view of screen materials used in regenerators and heat exchangers to show the variation in flow path in the streamwise and radial directions, respectively. Images extracted from manufacturer's sales materials [89].

Table 3.4: Hydrodynamic parameters for mire cloth materials used in PTR modeling.

Screen Type	ε	C_z	$C_{x,y}$	D_z	$D_{x,y}$
#325 304 SS [22]	0.6738	27,500	58,000	1.7×10^{10}	2.85×10^{10}
#100 Copper Twill	0.634	50,000	50,000	1.7×10^{10}	2.9×10^{10}

simulations, therefore the x and y directions represent radial or swirling flows.

CHAPTER IV

3-D SYSTEM-LEVEL CFD MODELING

Gravitational sensitivity in pulse tube cryocoolers has often been attributed in open literature exclusively to the pulse tube component, since it is the only component in the system which has an open flow channel subject to a temperature gradient; however, no previously reported model has attempted to validate this assertion. In order to definitively determine which components of the PTR system are sensitive to gravitational effects, a full system-level model was first designed using a combination of analytical, empirical, and numerical modeling modeling methods then constructed in 3-D half-symmetry using a closed system modeling approach. In the closed system approach, inlet and outlet boundary conditions are eliminated in favor of a dynamic meshing scheme used to simulate piston motion, which in turn drives the oscillatory flow of interest. The resulting simulations are used to analyze the net energy flows as well as qualitative flow and temperature profiles in three orientations: 0° (cold end down), 91° and 135°. In order to preliminarily classify the effect of pulse tube geometry on orientation dependence, two separate simulation domains were created with common volume but varied pulse tube aspect ratio. Due to the computational intensity required for these simulations, the scope of this study was limited to six simulated cases.

In the following sections, the methods used to thermodynamically design the simulated system will be presented first. The method used to translate this thermodynamic design into a CFD domain will then be disclosed. Finally the results of these transient simulations will be analyzed and compared to the initial design model used to size components. This iterative design and simulation method is not only useful

for identifying orientation sensitivity, but also in elucidating any three-dimensional effects not captured by the scoping models which significantly affect the predicted performance. This methodology has been successfully applied to the design of a number of multi-stage pulse tube cryocoolers in the Georgia Tech Cryo Lab (GTCL), reaching temperatures as low as 4 K.

4.1 System-Level Modeling Scope and Study Geometries

The initial design criteria for this design and development task was to incorporate two pulse tube aspect ratios (length-to-diameter) of 8 and 4. It is generally accepted that higher aspect ratios in the pulse tube component yield decreased orientation sensitivity; however, as the desired PTR cooling capacity increases the diameter typically scales, but not the length. The result is a more squat pulse tube. The designer cannot simply increase the length proportionally with the diameter without creating extraneous dead volume, which in turn degrades performance. In order to isolate the contribution of the pulse tube aspect ratio, all geometric features of the PTR with the exception of the pulse tube are identical in both permutations of the design.

A set of design constraints was first applied to the design, limiting the range of the scoping analysis to a manageable number of permutations. The study cooler was designed to operate at 60 Hz, with an objective temperature at the cold heat exchanger (CHX) of 60 K and a rejection temperature of 300 K at the aftercooler (AC) and the warm heat exchanger (WHX). The charge pressure was fixed at 2.0 MPa in all computational cases studied in this dissertation. Although the optimal fill pressure varies according to the frequency and temperature range desired for PTR operation, a fill pressure of 2.0 MPa is a versatile and neutral value that can be efficiently applied to 77 K stages as well as 4 K stages. The fill pressure is often a trade study for multiple stage PTRs due to the preference of each stage to perform optimally at a different pressure.

The pulse tube component was designed first as this study is primarily focused on pulse tube performance. The typical workflow dictates that the regenerator be designed first, as it determines the mass flow required to reach the desired cooling capacity; however, since this design is for illustrative purposes only there was no objective cooling capacity. It is sufficient in this case to obtain the optimum regenerator performance for the flow conditions dictated by the pulse tube flow. Both designs were chosen to give an oscillatory mass flow amplitude of 2.5 g/s at the cold end of the pulse tube with a pressure ratio of 1.2 and an objective phase shift of $\varphi_{m-p} = -30°$, for a pulse tube volume of 7.5 cc. This pulse tube volume is consistently used throughout this investigation and represents a typical volume in many small to moderate capacity commerial cooler designs. The volume was also chosen based on its ability to withstand the target mass flows for both aspect ratios without transition into a turbulent regime as described in Section 2.1.3.

Typically the pulse tube is designed with a volume of three to five times the cold end swept volume as computed with Equation 4.1, where the subscript c refers to properties evaluated at the cold end temperature. Other researchers have shown that this multiplicative empirical rule for volumetric scaling is not appropriate for all designs, with higher frequency systems requiring volumes as high as 13 times the swept volume [90]. Once the volume is determined, the minimum pulse tube diameter is then computed based on the minimum cross-sectional area that avoids turbulence according to Equation 4.2, where Re^{δ}_{crit} is 500. A factor of safety is typically placed on the critical Reynolds number to account for solution accuracy.

$$V_{c,PT} = \frac{2\dot{m}_c}{\omega \rho_{f,c}} \tag{4.1}$$

$$A_{min} = \frac{\dot{m}\delta}{Re^{\delta}_{cr}\mu} \tag{4.2}$$

$$\delta = \sqrt{\frac{2\nu}{\omega}} \tag{4.3}$$

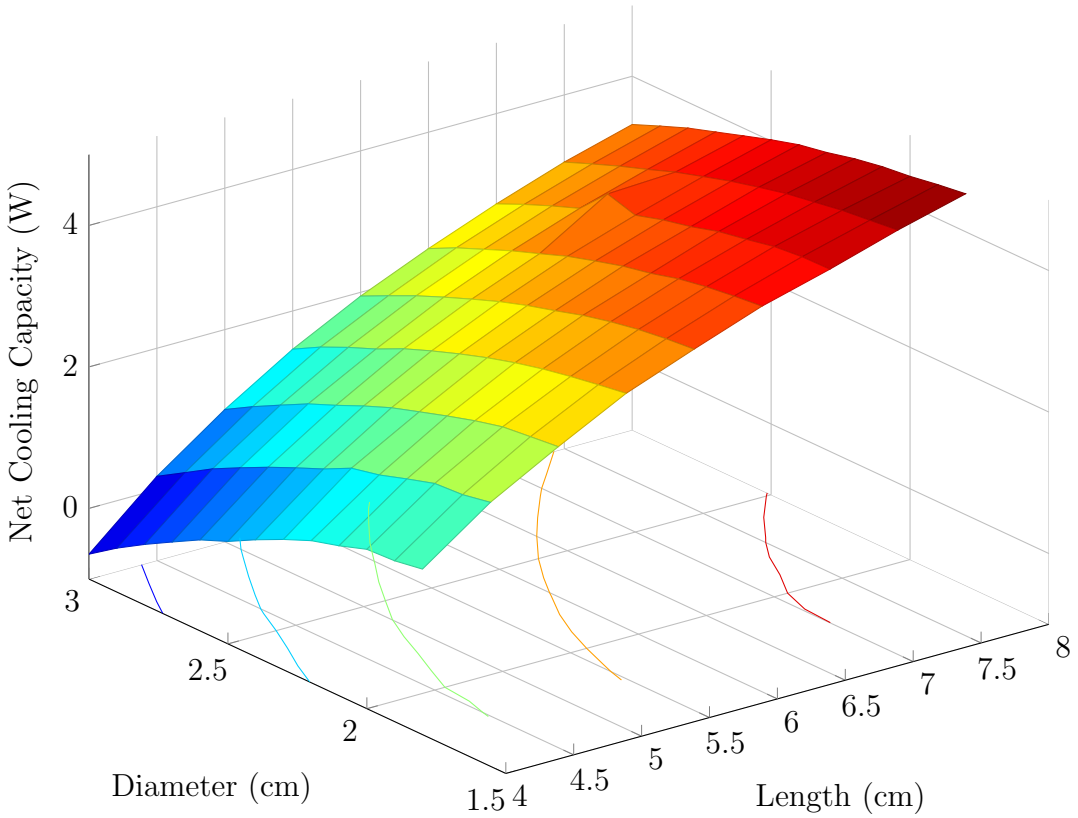

Figure 4.1: Color contour plot of regenerator performance for 2 MPa and 60 Hz operation between 300 K and 60 K as a function of geometry. A -30° phase difference between mass and pressure was used for all simulations, with a cold end mass flow of 2.5 g/s and pressure ratio of 1.2.

Following the pulse tube design, an optimal regenerator was designed using a filler of #325 stainless steel mesh. REGEN 3.3 was used to simulate regenerator performance to meet the objective pulse tube cold end boundary conditions while maximizing the net cooling capacity of the PTR. A nested loop of regenerator lengths and diameters was implemented to simulate a sweep of geometries using a MATLAB routine which controls Windows PowerShell in order to automate the REGEN 3.3 runs. Upon completion of the REGEN simulations, the data was post-processed to determine the regenerator geometry that yielded the highest COP, and therefore the largest net cooling capacity. The results of the REGEN 3.3 sweep are displayed in Figure 4.1.

As shown in Figure 4.1, the optimal design extends beyond the limits of the

scoping study range; however, the pressure drop incurred by a longer and more slender regenerator led to an unrealistic compressor sizing. As a result the valid design domain was constrained to the limits shown in the surface plot.

In order to provide the objective cold end phase shift of $\varphi_{m-p} = -30°$, the proper length and diameter for the inertance tube and the flow volume of the surge volume had to be designed. The tool used to perform this set of sizing computations was a MATLAB routine which solves the transmission line model published by Radebaugh et al. [91] and is reproduced in the following equations. The transmission line model analogously equates the dynamic response of the inertance tube - surge volume network to an equivalent series of resistors, inductors, and capacitors. In Equations 4.4-4.11, the characters r, l, and c represent the equivalent resistance, inertance, and compliance, respectively. Additionally, the subscript r refers to the reservoir, or surge volume.

The equivalent resistance, inertance, and compliance per unit length are given by Equations 4.4-4.6.

$$r(D) = \left(\frac{2}{\pi}\right) \frac{32 f_r |\dot{m}|}{\pi^2 \rho_0 D^5} \tag{4.4}$$

where f_r is the fanning friction factor, chosen appropriately for the flow regime and pipe wall smoothness from empirical charts such as a Moody diagram.

$$l(D) = \frac{4}{\pi D^2} \tag{4.5}$$

$$c(D) = \frac{\pi D^2}{4\gamma R T_0} \tag{4.6}$$

The existence of a surge volume at the end of the inertance tube produces a compliant load c_r with magnitude:

$$c_r = \frac{V_r}{\gamma R T_r} \tag{4.7}$$

The impedance in a fluid domain is the ratio of pressure to volumetric flow rate. The impedance of the surge volume's compliant load is:

$$Z_r = \frac{1}{i\omega c_r} \tag{4.8}$$

The complex impedance based on mass flow (denoted by subscript m) instead of volumetric flow at a location x along the pulse tube is expressed as:

$$Z_m(D,x) = Z_0(D)\left\{\frac{Z_r + Z_0(D)\tanh[k(D)(L-x)]}{Z_0(D) + Z_r\tanh[k(D)(L-x)]}\right\} \tag{4.9}$$

The characteristic impedance seen by the pulse tube at the entrance to the surge volume is given by:

$$Z_0(D) = \sqrt{\frac{r(D) + i\omega l(D)}{i\omega c(D)}} \tag{4.10}$$

In the above equations, the complex wave number k is equal to:

$$k(D) = \sqrt{[r(D) + i\omega l(D)]\, i\omega c(D)} \tag{4.11}$$

A sweeping methodology is used to solve over a range of dimensions until the optimum is found which matches the objective warm end phase shift for a given acoustic power. The above system of equations are solved for each inertance tube length L, diameter D, and surge volume V_r included in the sweep. The amplitude and phase are determined by finding the angle between the real and imaginary parts of Equation 4.9 evaluated at $x = 0$ (the inlet the inertance tube) as shown in Equation 4.12.

$$\theta_z = \tan^{-1}\left(\frac{\Re\{Z_m\}}{\Im\{Z_m\}}\right) \tag{4.12}$$

There are multiple points which yield the desired phase shift, but they occur for lengths that are integer multiples of the half-wavelength ($\lambda\backslash 2$) of the acoustic pressure wave. The optimal design occurs for the shortest tube that gives the desired phase shift, for which the dead volume is minimized.

Heat exchangers were sized based on best practice empirical rules, where the diameter of the CHX and WHX components are set to match the pulse tube inside diameter and the length is set to 5 mm in order to provide adequate flow straightening. The aftercooler was sized to match the regenerator diameter, using a length of 10 mm in order to sufficiently remove the heat of compression from the piston

component. The filler material for all heat exchangers is #100 mesh copper screen with a twill weave pattern. In a formal development effort where all cooler aspects are optimized, the heat exchangers would be simulated separately in ISOHX, a numerical finite-difference program developed by Ray Radebaugh and Vince Arp at NIST [92]. The purpose of this code is to determine the optimal filler and length for the heat exchanger which minimizes the pressure drop introduced by the porous section, while maintaining a nearly isothermal flow at the boundaries.

The driving piston used to excite the oscillatory flow in the system is controlled using a user-defined function (UDF) written in C++ that specifies the velocity amplitude of the piston face as a function of time. The sinusoidal piston motion is described by Equation 4.13 and the code used to enable this UDF is located in Appendix B.

$$\widetilde{U}_{piston}(t) = U_d \sin(\omega t + \varphi) \tag{4.13}$$

The velocity amplitude U_d was initially determined based on the warm end mass flow of the regenerator as determined by the REGEN 3.3 simulations, and adjusted after the first cycle in order to match the desired performance. A velocity amplitude of 3.41 m/s was determined to yield desired behavior. The phase angle φ in Equation 4.13 is arbitrary since the behavior in the rest of the system is relative to the time shift imposed by setting a non-zero phase angle at the piston face. A phase of π radians is set in order to allow the first stroke to be an expansion stroke whereby the buffer zone is remeshed during the first cycle to match the dynamic mesh settings chosen, which are described in the following section.

Solid features such as thin-walled tubes and thermal intercepts play an important role in pulse tube cryocoolers, especially in the pulse tube where shuttle heat transfer is driven by heat exchange with the wall. In order to capture correct flow phenomena in the pulse tube component, conjugate heat transfer with the wall material is modeled by explicitly meshing the 0.254 mm thick wall. The pulse tube material chosen for this simulation is Hastelloy, a nickel-based superalloy with exceptionally

low thermal conductivity at cryogenic temperatures and sufficient strength to allow for very thin pressure vessel walls. These features minimize system-level losses due to wall conduction.

The walls of the cold heat exchanger and warm heat exchanger are meshed and modeled using OFHC copper with temperature-dependent properties (Residual-resistivity ratio (RRR)=500) with an isothermal boundary condition applied to the outer-most radial surface. Additional information regarding the modeling of temperature-dependent properties is available in Section 3.5.2. While these heat exchanger wall features are not critical to the simulation, they allow for more realistic determination of the net thermal energy input and rejection at these components. Walls were not modeled for the remaining components as their effect is minimal and expected to yield no contribution to gravitational sensitivity.

Table 4.1 summarizes the key operating parameters of the simulated system-level models, which are common to both the L/D=8 and L/D=4 computational domains. The geometry of the simulated systems is presented in Table 4.2.

Table 4.1: Operating conditions for system-level model PTRs.

Operating Pressure	2 MPa
Working Fluid	REFPROP He-4
Drive Frequency	60 Hz
Piston Velocity Amplitude	3.41 m/s
Refrigeration Temperature (CHX)	60 K
Rejection Temperature (AC, WHX)	300 K

4.2 Computational Domain and Mesh Discretization Scheme

Figure 4.2 illustrates the application of boundary conditions used to model the full PTR system in 3-D half-symmetry using a piston motion UDF to drive flow in the

Table 4.2: Component geometries for system-level model PTRs.

Component Geometry	**L/D=8 (m)**	**L/D=4 (m)**
Piston Diameter	1.8×10^{-2}	1.8×10^{-2}
AC Diameter	1.8×10^{-2}	1.8×10^{-2}
Regenerator Diameter	1.8×10^{-2}	1.8×10^{-2}
Regenerator Length	8×10^{-2}	8×10^{-2}
CHX Diameter	1.0608×10^{-2}	1.3365×10^{-2}
CHX Length	5×10^{-3}	5×10^{-3}
Pulse Tube Diameter	1.0608×10^{-2}	1.3365×10^{-2}
Pulse Tube Length	8.4864×10^{-2}	5.3461×10^{-2}
Pulse Tube Wall Thickness	2.54×10^{-4}	2.54×10^{-4}
WHX Diameter	1.0608×10^{-2}	1.3365×10^{-2}
WHX Length	5×10^{-3}	5×10^{-3}
Inertance Tube Diameter	4×10^{-3}	4×10^{-3}
Inertance Tube Length	3.0408	3.0408
Surge Volume Length	3.3885×10^{-2}	3.3885×10^{-2}
Surge Volume Diameter	3.3885×10^{-2}	3.3885×10^{-2}
Surge Overall Volume	122 cc	122 cc

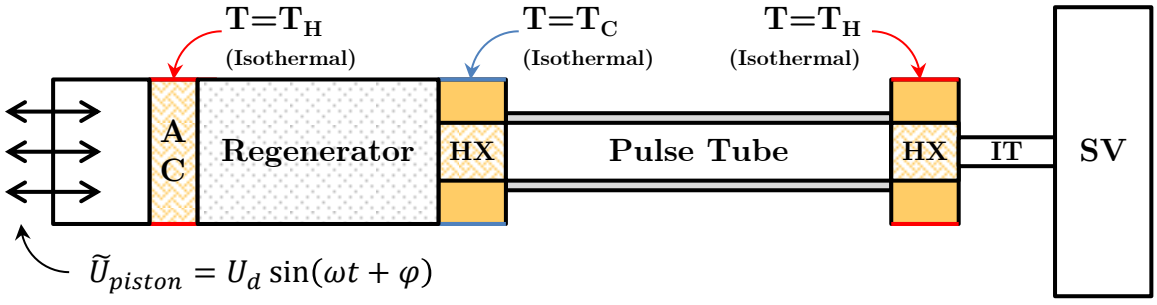

Figure 4.2: Schematic representation of the computational domain used to represent the full PTR system in 3-D half-symmetry. Dynamic meshing represented by oscillatory velocity on the left hand side. Isothermal surfaces are used to set temperatures on the heat exchanger components. Solid colors represent solid meshed domains. Pattern-filled zones represent porous domains of stacked screens.

Table 4.3: Dynamic mesh control parameters.

Layering?	No
Smoothing?	Yes
Collapse Factor	0.04
Split Factor	0.4
New Cell Height	0.005 m

system. In order to utilize the dynamic meshing scheme required to simulate piston motion, prismatic meshing was used in the z-direction in which the piston oscillates. Use of a non-orthogonal meshing scheme requires a higher-order mesh solution scheme such as spring-lattice, which is computationally intensive compared the the layering method used here. In this layering method, cells are added or subtracted once a threshold deformation has been reached, based on user settings. Once the threshold has been crossed, a new cell is introduced with user-specified height. The dynamic mesh settings used in the system-level models reported here are included in Table 4.3.

In order to provide a high quality mesh, a swept meshing scheme was used. In order to apply sweep meshing to a cylindrical domain, a central core is generated consisting of predominantly quadrilaterals which are extruded in the z-direction. The symmetry plane is pre-meshed by dividing the edges evenly in the z-direction, and using a bias in the y-direction in order to resolve the boundary layer effects in the pulse tube component. The boundary inflation is sized such that a minimum of five cells are applied within the Stokes boundary layer thickness. The pre-meshed symmetry plane is then swept around the central core over a specified number of angular increments to provide a radially symmetric mesh. A double-sided biasing scheme is also used in the inertance tube component along the z-direction due to the excessive length of the domain. The flow in the central region of the inertance tube is unimportant as the flow is essentially a 1-D plug flow at high velocity, therefore that region is quite

coarse to maximize computational efficiency as well as avoiding a situation where a flow particle would traverse a distance larger than the cell length over the course of a single time step.

The final mesh for a pulse tube aspect ratio of 8 is shown in Figure 4.3, where the $+z$-direction points along the central axis toward the compression space, and the $+y$-axis points vertically along the page. Table 4.4 summarizes the mesh statistics required to adequately mesh the computational domain. Grid independence will be demonstrated in Chapter 5 for the pulse tube and adjacent components, and the grid-independent domain was used as the basis for meshing the full system. Consistent body sizing was used throughout the domain to ensure uniform mesh density throughout the cooler.

Table 4.4: Meshing statistics for system-level half-symmetry model using swept meshing with biased boundary layers.

Mesh Statistic	**Aspect Ratio L/D=8**	**Aspect Ratio L/D=4**
Nodes	103,634	110,084
Elements	94,088	100,528
Min. Orthogonal Quality	0.51217	0.58814

4.2.1 Initialization and Convergence

The flow field in the domain is initialized to an essentially quiescent velocity field with nominal velocity of 0.001 m/s applied in the x and y directions, and 0.1 m/s in the z direction such that the solution does not begin at a stagnant initial condition, a condition which can cause slow solution convergence. The temperature field is initialized with a linear profile through the regenerator (Equation 3.29) and a power law formulation (Equation 3.30) in the pulse tube. The cold heat exchanger is initialized uniformly to 60 K, corresponding to the isothermal wall condition applied to its outermost radial surface. All other components are initialized with an isothermal profile

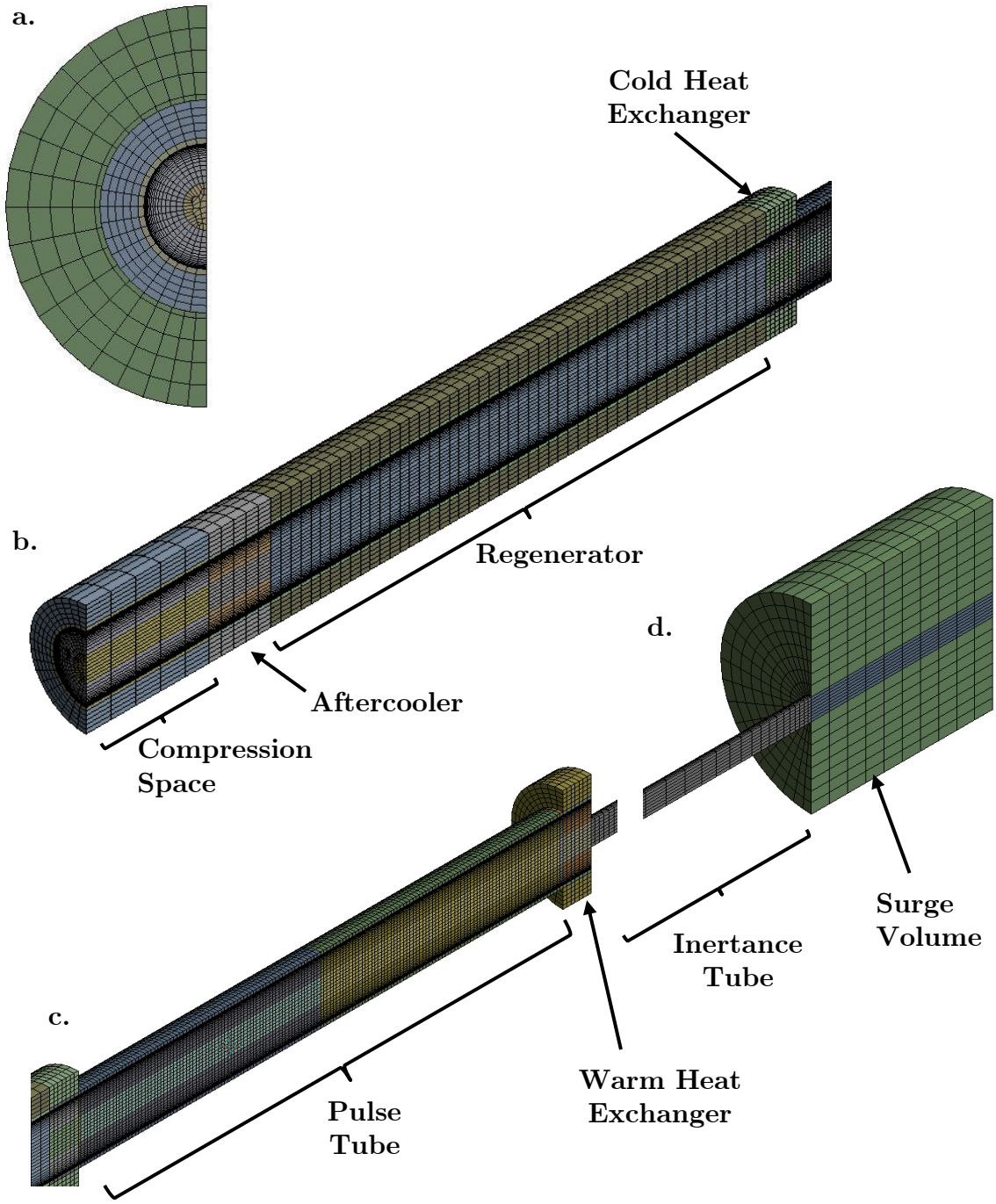

Figure 4.3: System-level 3-D meshing for an aspect ratio L/D=8. **a.** Cross-section. **b.** Piston through cold heat exchanger. **c.** pulse tube and warm heat exchanger. **d.** Inertance tube and surge volume.

corresponding to their nominal thermal rejection temperature of 300 K.

The time step chosen for the transient time progression was chosen based on a number of factors. The first influencing factor is the required number of steps for a period of oscillation. Previous work has shown that less critical simulations can be performed using as few as 200 steps/cycle [93] when flow field information is desired and up to 10% numerical error is tolerable in net energy terms, while others show that up to 400 steps/cycle [31] are required for accuracy in determining cycle-averaged energy flows, which are small in comparison to the transient energy flows.

The second factor that drives the time step selection is the requirement that the flow should not traverse a distance greater than the length of a single cell during the course of a time step; therefore, finer mesh grids require a small time step. Conversely, areas of high velocity either require coarse meshing or a fine time step. Given the size of the mesh used to represent the computational domains, a time step of 4.167×10^{-5} s was implemented, resulting in 400 time steps per cycle. First-order transient formulation was used since the 2nd order scheme is not compatible with the dynamic meshing formulation, which requires remeshing at each time step.

After solving of the intial cycle, monitors were implemented at each critical transition along the PTR domain. An initial iteration is required in order to set the expert functionality in FLUENT which includes post-processing of the temperature gradients required to compute gas and matrix conduction. The full set of monitors is described in the journal file found in Appendix B. A total of 52 monitors were implemented during the solution to report values at each time step allowing post-processing of flow and energy quantities. Because the pulse tube is the object of interest in this study, monitors were applied to each end of the pulse tube as well as three additional locations along the length, 0.5 mm from the cold end (L1), the center of the pulse tube (L2), and 0.5 mm from the warm end (L3). Location L1 is consistently used to evaluate cold end energy flow in this study due to inaccuracy in the formulation

of energy flows at the boundary between a porous section such as the CHX and an open flow domain. This inaccuracy at the interface leads to slight miscalculation of the local temperature gradient, therefore a distance was chosen which is equivalent to a single cell distance from the interface to evaluate energy flows.

The solution was iteratively time marched until model convergence was observed. At each time step, up to 120 iterations are performed until the specified residual convergence criteria are reached for the mass conservation, momentum in each ordinate direction, and energy conservation. When these criteria are met, the flow time is advanced, the dynamic mesh is recomputed, and the solution is iterated once again. The transient model has converged to periodic steady-state (PSS) when the cycle-averaged quantities do not change significantly between sequential time steps. For this study, PSS is defined as less than 0.1% change between cycles. Hydrodynamic convergence typically occurs quickly for periodic flow, within the first 10-20 cycles [62, 63]. The energy terms take significantly longer to converge fully, up to approximately 75 cycles.

Inclusion of the transfer tube assembly in the system-level model introduces a zone where the flow regime is most certainly turbulent. In order to account for the turbulence effects, an appropriate turbulence model is applied once the laminar model has converged. The k-ω SST model is applied to the inertance tube, warm heat exchanger, and pulse tube domains. This particular turbulence model was chosen due to its ability to handle low Re flows during portions of the cycle while using wall functions that do not require explicit grid resolution of the boundary layer, which would add an unmanageable number of cells in the inertance tube (not a specific area of interest). The solution is then iterated for an additional number of cycles until the energy flows once again converged.

Simulation of these extensive cases was enabled by the use of high performance computing (HPC). Supercomputing clusters are utilized at Georgia Tech through the Partnership for an Advanced Computing Environment (PACE). Performance was

optimized on the Linux cluster for maximum case throughput and each case was solved using 64 individual computing cores simulating in parallel. The computational domain is divided into 64 sub-domains and each subdomain is assigned to a single processor (CPU). The processors communicate through a high speed Infiniband ethernet connection to pass boundary conditions to the neighboring domains. Using this methodology, the simulation speed is able to scale in a nearly linear fashion compared to the use of a serial process. With 64 cores, the solution is advanced at an average rate of approximately 10 hours and 14 minutes per cycle. The total simulation time for each case to reach full PSS is therefore approximately 765 hours, or 32 days. In order to make efficient use of resources, the solutions reported in the following sections were carried out to 15,000 to 25,000 time steps. The total CPU time required to obtain the six simulated results reported is approximately 147,600 hours.

4.3 System-level Flow and Temperature Fields

A key benefit to utilizing computational fluid dynamics is the ability to post-process simulations to obtain enhanced vizualization of the flow field that would not be possible with experimental techniques. Figures 4.4 and 4.5 illustrate a three-dimensional isometric view of the temperature field on the symmetry plane as well as the external walls of the domain. All three isometric images were processed at the same time step, therefore they represent the same flow time.

In order to directly compare the flow field at the three simulated angles: 0°, 91°, and 135°, Figure 4.6 plots the temperature contours in a view orthogonal to the plane of symmetry for the case where the pulse tube aspect ratio is $L/D = 4$. Velocity vectors are overlaid on the symmetry plane to indicate the magnitude and direction of the flow field at the instant that the contour snapshot was processed. Symmetry plane temperature contours with velocity vectors are also plotted for the case where pulse tube aspect ratio is $L/D = 8$ at the same time step for comparison in Figure 4.7

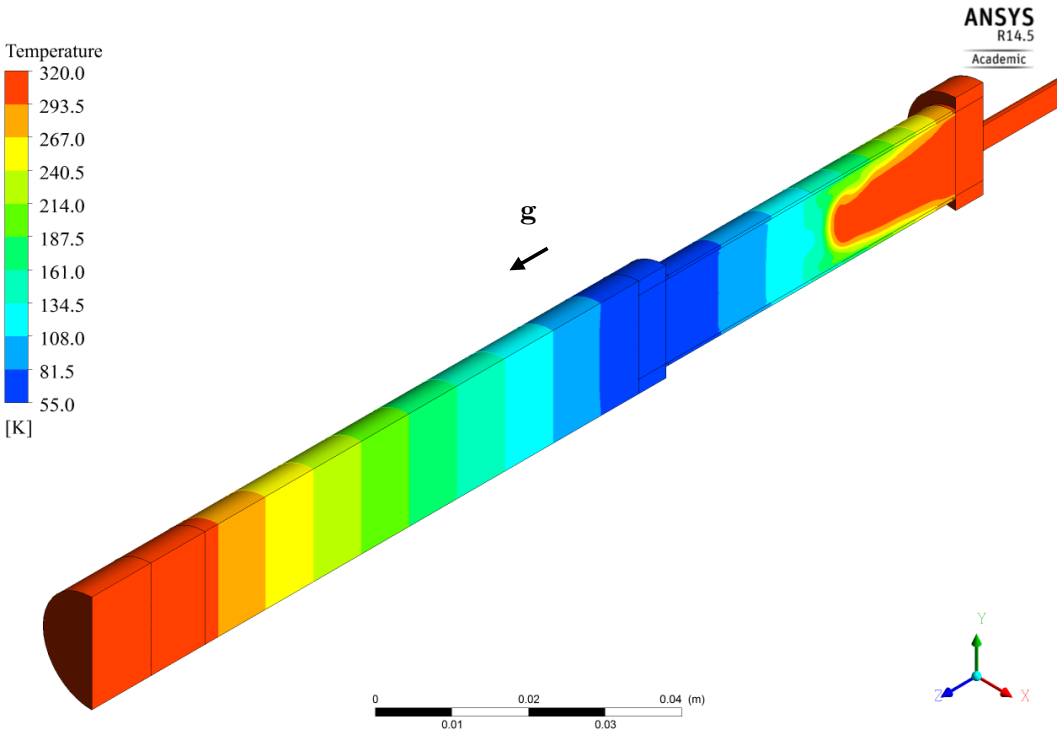

a. 0°, tstep=14,900

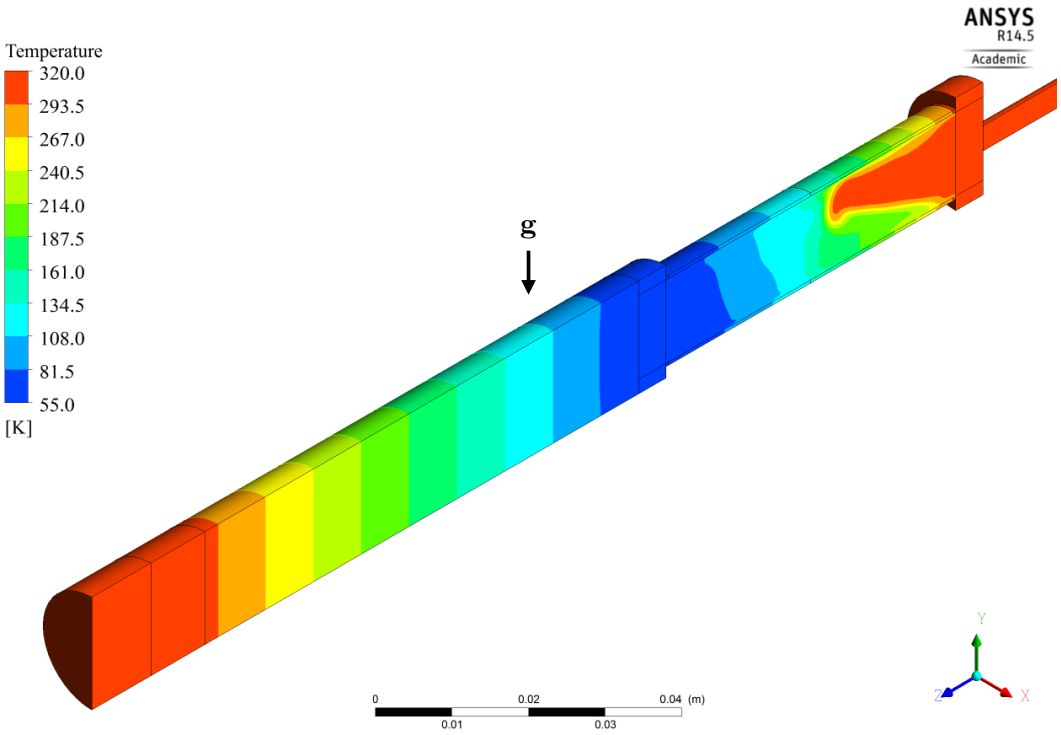

b. 91°, tstep=14,900

Figure 4.4: Instantaneous temperature contours for pulse tube aspect ratio L/D=4 at time step 14,900.

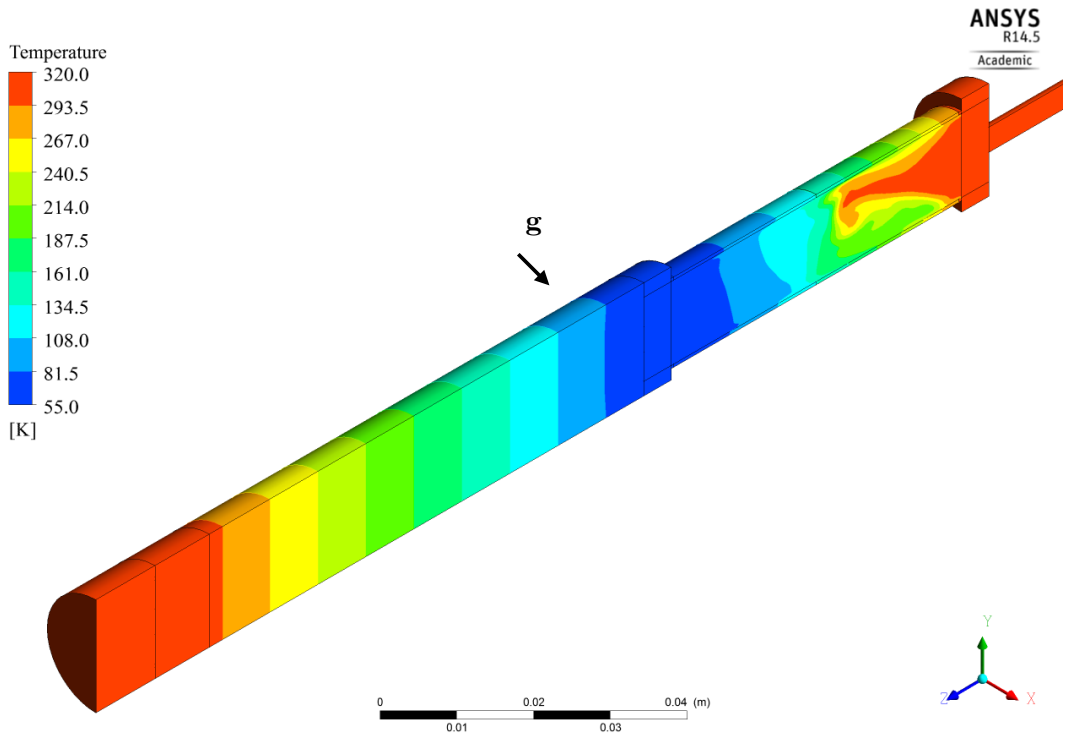

a. 135°, tstep=14,900

Figure 4.5: Instantaneous temperature contours for pulse tube aspect ratio L/D=4 at time step 14,900.

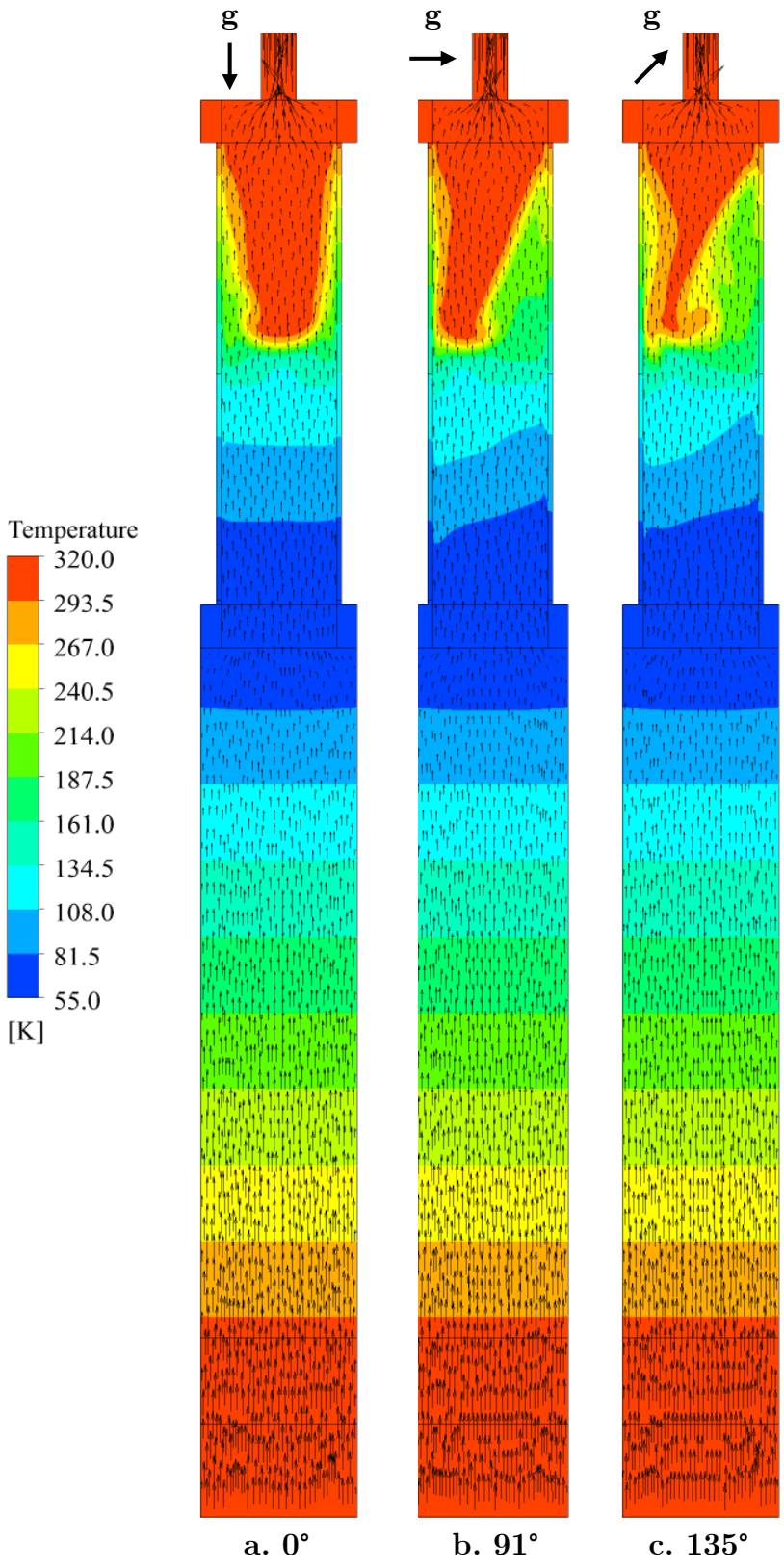

Figure 4.6: Instantaneous temperature contours with overlaid velocity vectors on the symmetry plane for pulse tubes with L/D=4 at time step 14,900.

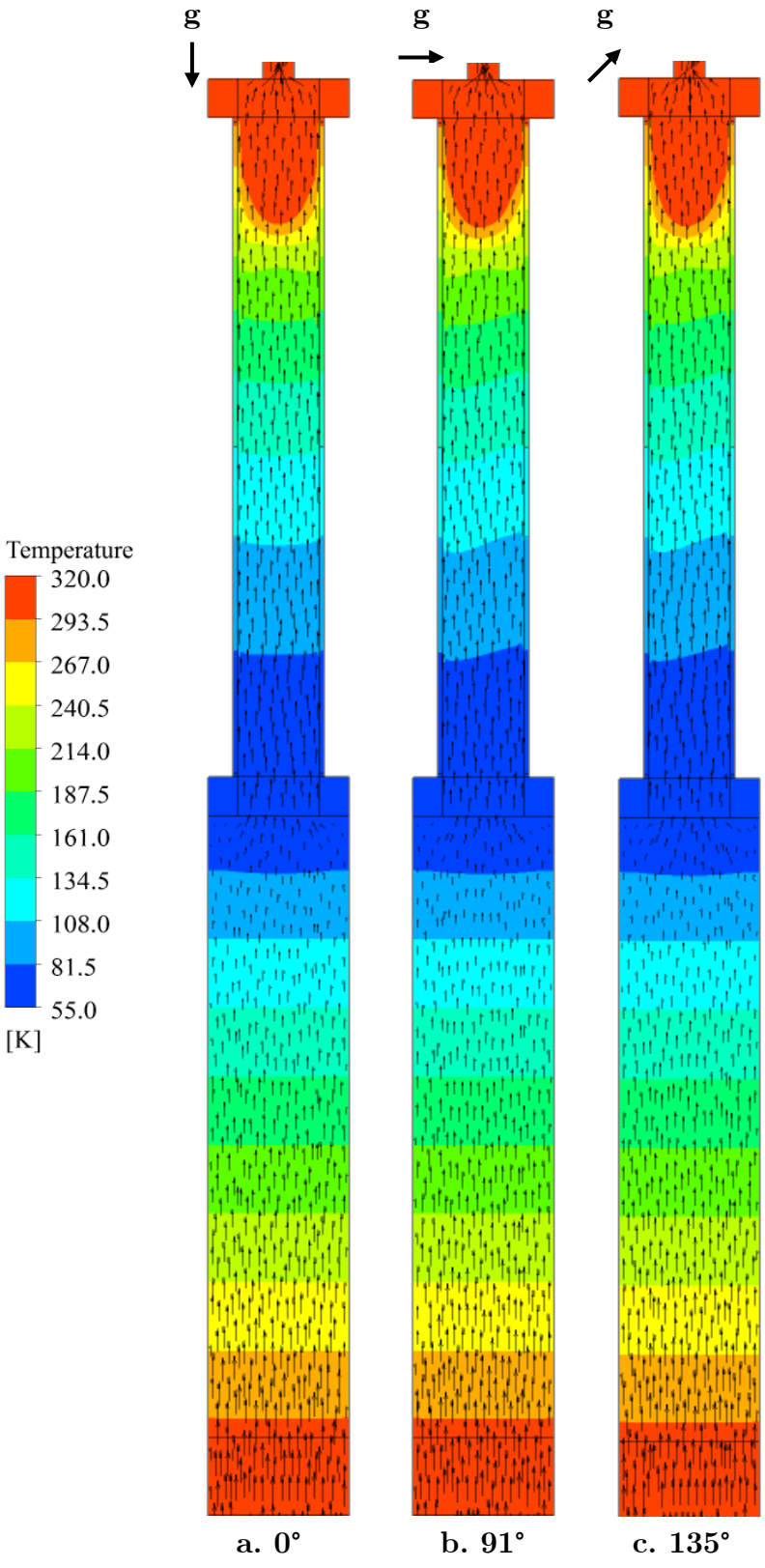

Figure 4.7: Instantaneous temperature contours with overlaid velocity vectors on the symmetry plane for pulse tubes with L/D=8 at time step 14,900.

Inspection of Figure 4.6a indicates the strong presence of jetting at the transition between the pulse tube and the inertance tube. This illustrates the need to incorporate appropriate flow straightening and diffusing techniques at the transition points. This is typically accomplished using a tapered conical section with coarse mesh screens at either end of the taper as described by Taylor et al. [31, 64]. Due to the required use of prismatic meshes for this simulation set (in order to utilize dynamic meshing), tapered sections could not be accommodated as they require tetrahedral elements. Comparison of Figure 4.6b and 4.6c with 4.6a shows that the pulse tube temperature field is significantly affected by the presence of the gravitational field. This gravitational effect is especially apparent as it perturbs the jet region at the entrance to the warm heat exchanger.

Comparison of the symmetry plane contours shown in Figures 4.6 and Figure 4.7 illustrates the impact of the choice of pulse tube aspect ratio. All other parameters are identical for the two domains aside from the pulse tube aspect ratio. Inspection of the figure clearly illustrates that the jetting phenomenon is not present in the design pulse tube aspect ratio 8. It is also apparent that the more slender pulse tube qualitatively does not experience the severity of convective mixing present in the shorter pulse tube.

The objective of developing a set of system-level models was to determine whether or not convective effects are isolated to the pulse tube component illustrated in the top half of Figures 4.6 and 4.7. The regenerator is the other major component within the PTR system that experiences a significant temperature gradient, and would therefore be subject to asymmetric buoyancy forces. Examining the lower portion of the temperature contours in Figures 4.6a, 4.6b and 4.6c indicates that the isotherms are sufficiently perpendicular to the flow direction to conclude that the temperature field within the regenerator is minimally, if at all, affected by the gravitational body forces. In order to further illustrate this, Figure 4.8 isolates velocity contours within

the simulated PTR domain for the case of a pulse tube aspect ratio of 4.

Whereas Figures 4.6 and 4.8 display contours and vectors at a single time step comparing the effect of inclination angle θ on the flow field, Figures 4.9 through 4.11 isolate a single inclination angle and display flow and temperature field information at sequential points through the oscillation cycle. The oscillation cycle is broken down into $\pi\backslash 2$ radian steps and referenced by the parameter Γ. $\Gamma = 0$ corresponds to the start of sinusoidal cycle.

$$\Gamma = \omega t + \varphi \tag{4.14}$$

In order to evaluate the effectiveness of the choice of initial temperature profile, which utilized a power law formulation for the pulse tube section and a linear temperature profile within the regenerator, axial temperature was plotted as a function of position along the pulse tube centerline on the symmetry plane after 15,000 time steps. This plot is shown in Figure 4.12. Inspection of the initial and final temperature profiles indicates that the linear approximation for the regenerator section is a very reasonable approximation as the final traces for all angles align well with the initial condition. The lack of deviation between the four plotted traces is also indicative of the lack of gravitational effect on regenerator performance.

The power law formulation used to initialize the pulse tube section appears well-suited in a small region between the cold end and the center, though the curve is offset by approximately 5 mm downstream. The final solution also deviates significantly over the warm half of the pulse tube. This deviation is a result of the unforeseen jetting problem that is apparent in this $L/D = 4$ pulse tube design. In spite of the obvious deviation from the initial conditions, the power law formulation is still more accurate than a linear approximation and supports its use.

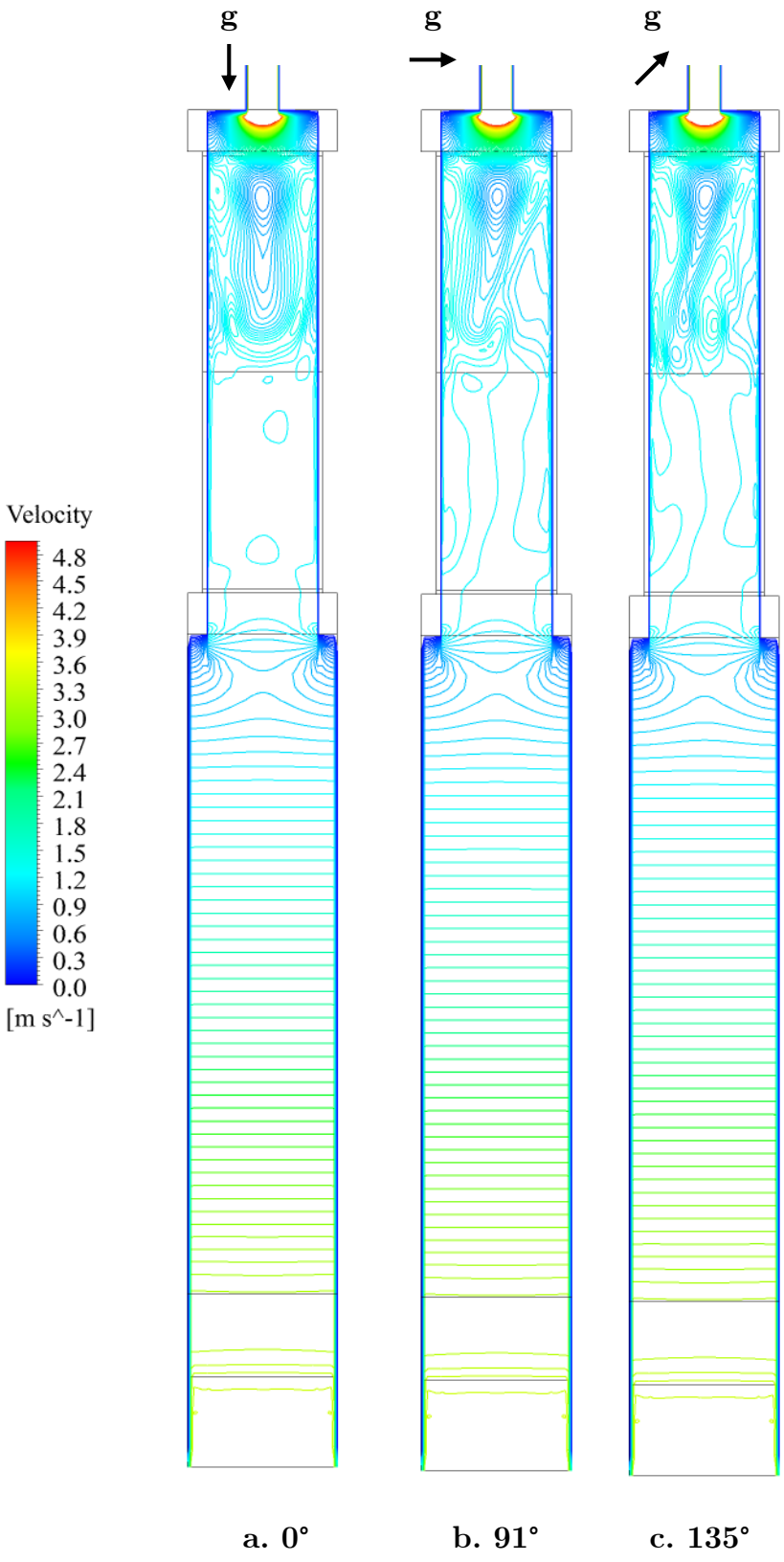

Figure 4.8: Instantaneous contours of velocity on the symmetry plane for pulse tubes with L/D=4 at time step 14,900.

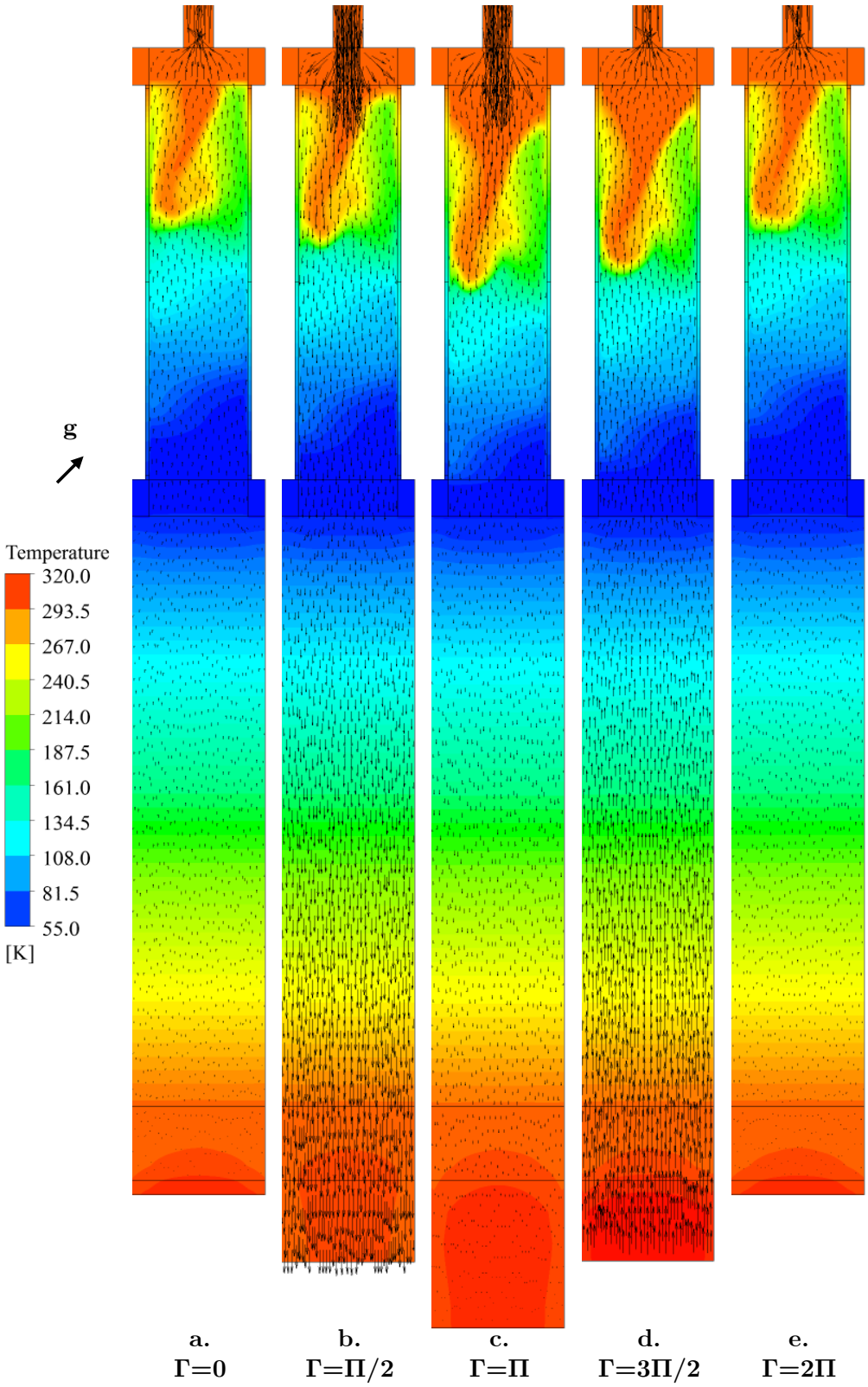

Figure 4.9: Time sequence of instantaneous temperature contours on the symmetry plane for a system-level model at 135° angle of inclination. Refence angle Γ is based on a single sinusoidal period of 2Π radians.

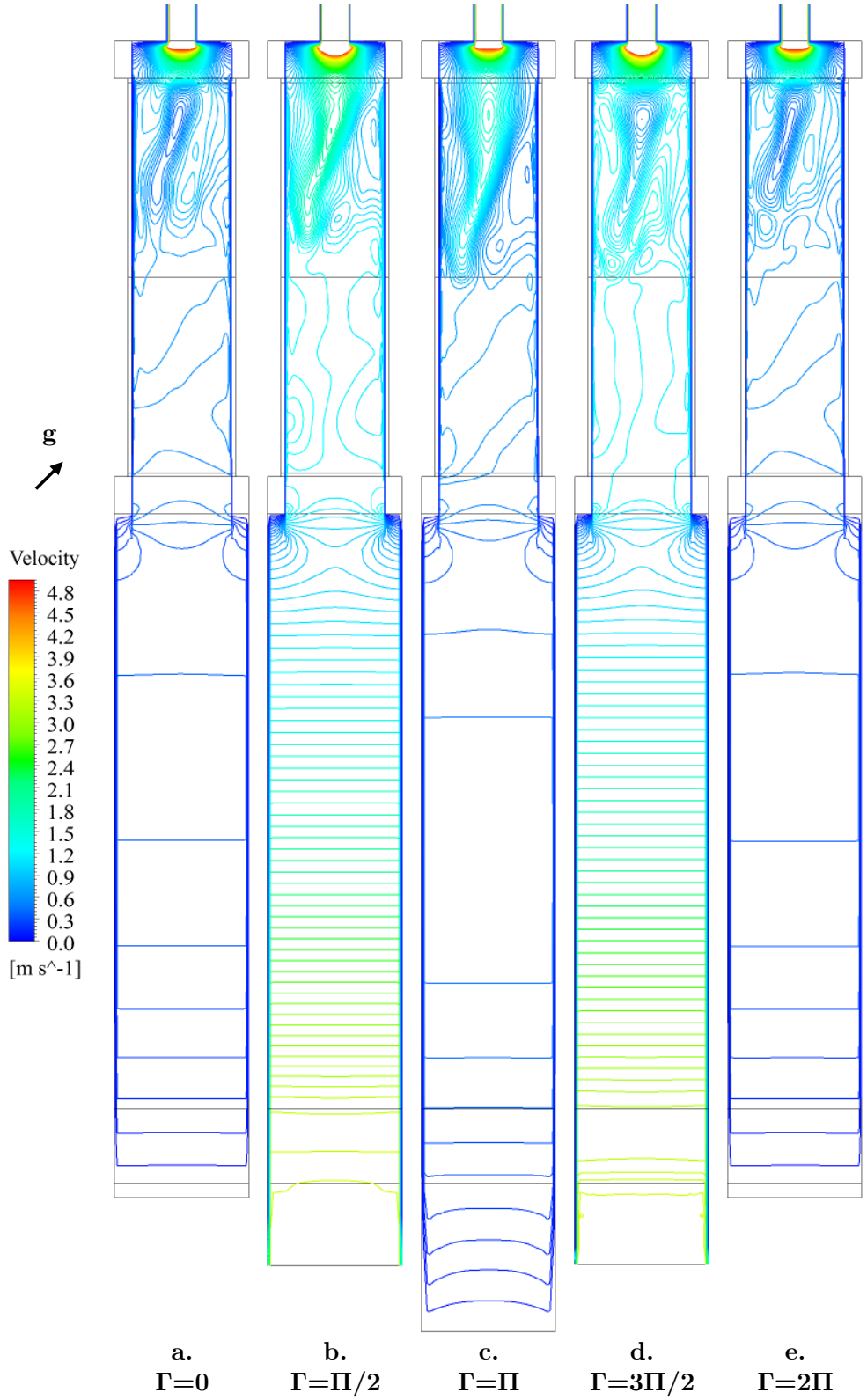

Figure 4.10: Time sequence of instantaneous contours of velocity on the symmetry plane for a system-level model at 135° angle of inclination. Refence angle Γ is based on a single sinusoidal period of 2Π radians.

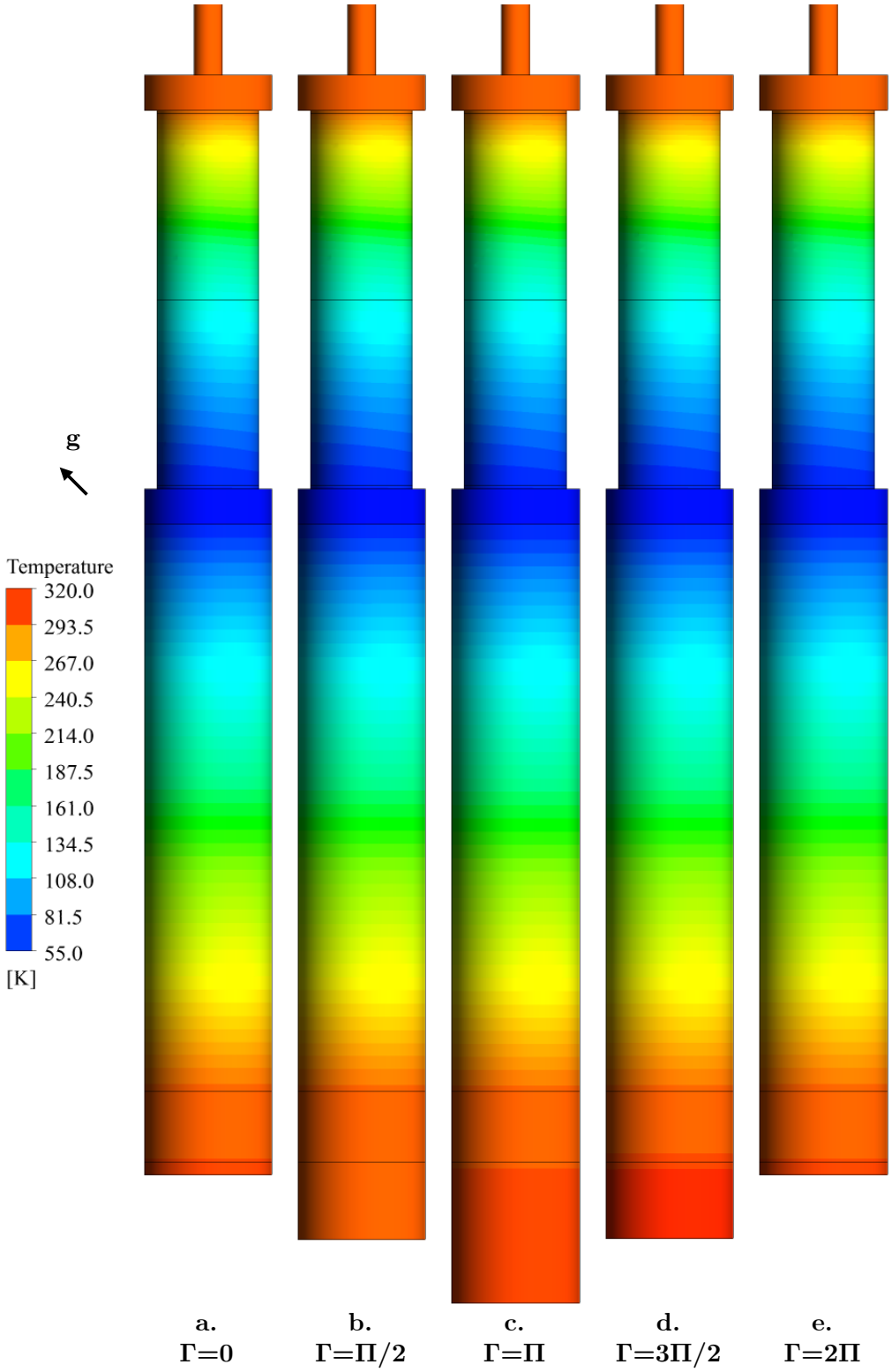

Figure 4.11: Time sequence of instantaneous wall temperature contours for a system-level model at 135° angle of inclination. Refence angle Γ is based on a single sinusoidal period of 2Π radians.

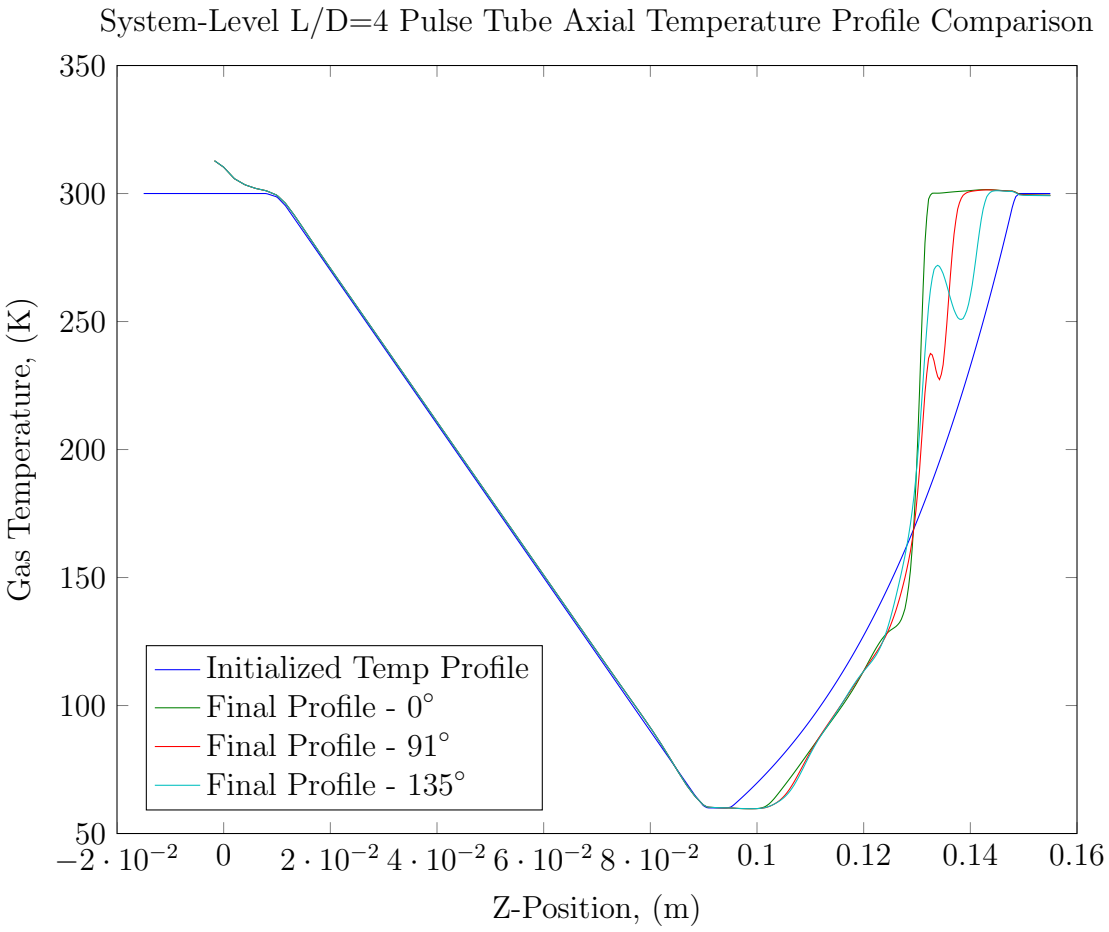

Figure 4.12: Comparison of temperature initialization profile with final cycle temperature profile as a function of inclination angle.

4.4 System-level Energy Flow Effects

Due to the immense computational resources required to reach periodic steady-state, only the models where pulse tube aspect ratio is 4 were carried out to full periodic steady-state (PSS). PSS was reached in approximately 25,000 time steps, corresponding to a flow time of 1.05 seconds. The L/D=8 cases were terminated after 15,000 time steps to conserve computational resources, as the results indicated that the design was not as convectively unstable as the L/D=4 cases. Since the purpose of the system-level models was to quantify the component contributions to orientation sensitivity, the objective is sufficiently satisfied by analyzing the L/D=4 cases alone. As a result of terminating the L/D=8 cases, 192 CPUs were freed for two weeks.

Upon completion, the L/D=4 models at 0°, 91°, and 135° were post-processed to determine the net energy flow in the pulse tube as well as the net enthalpy flow in the regenerator. A programmatic error in the output files for temperature gradients in the regenerator prevented the successful computation of conduction terms; however, by examination of the temperature contours shown in Figure 4.6, the change in conduction heat transfer must not vary significantly from case to case. As a result, the net energy flow in the regenator is dominated by the enthalpy flow and reported as such. Figure 4.13 compares the net energy flows in the regenerator and pulse tube as a function of angle of inclination.

The results of the energy comparison in the regenerator and pulse tube components are relatively straightforward. The maximum percent change of energy flow in the pulse tube is 41.23% between 0° and 135°. In contrast, the maximum percent change of energy flow in the regenerator is only 5.3% between 0° and 135°. This concludes that for the current cases, where the regenerator is composed of stacked wire mesh stainless steel screens, there is a small, but largely insignificant change in the energy flow across the regenerator as a function of orientation. By comparison, the change in energy flow across the pulse tube as a function of angle aptly characterizes the

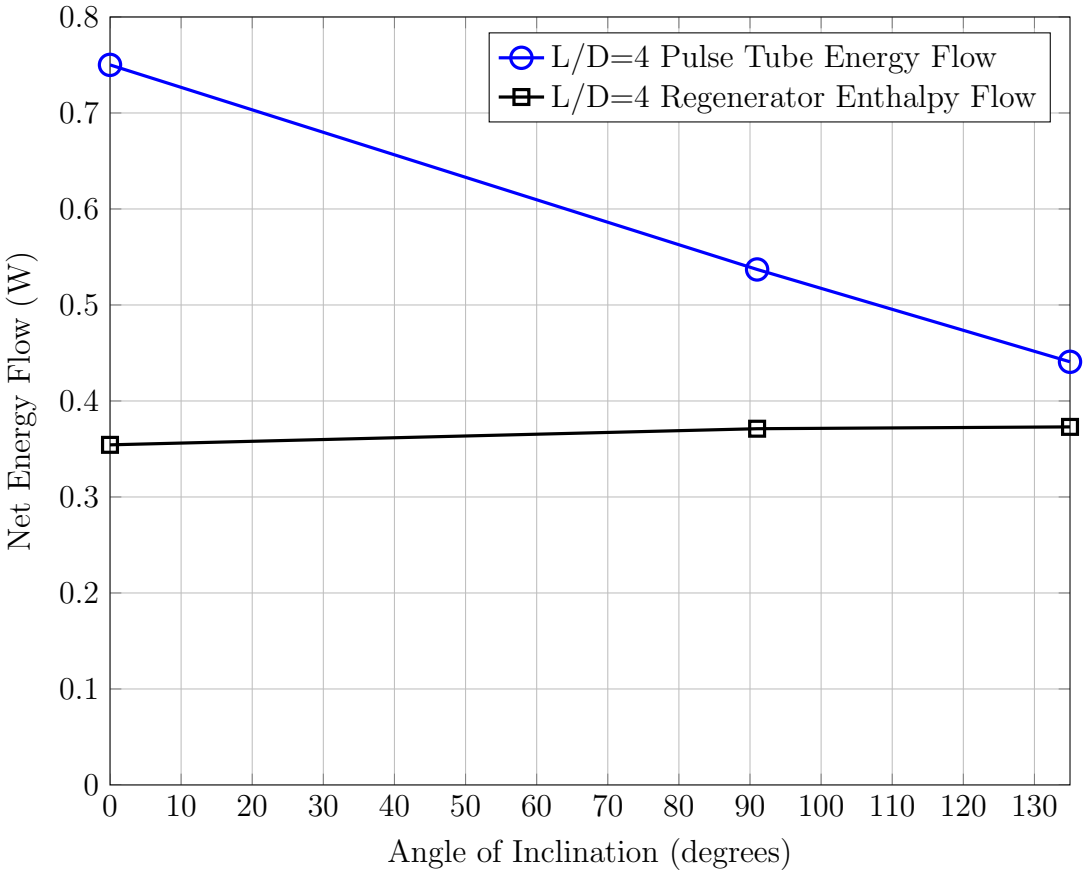

Figure 4.13: Comparison of net energy flows in the pulse tube and regenerator as a function of inclination angle for system-level L/D=4 models.

orientation-dependence of the cooler.

4.5 Conclusions

Using a closed system approach and modeling an entire PTR system in 3-D half-symmetry, there is now conclusive evidence that the pulse tube component is the dominant driver of flow instability due to the presence of gravitational body force. The existence of porous media within the remaining components which experience thermal gradients prevents the development of the convective cell that appears in the pulse tube domain. As a result, the impact on net cooling capacity is largely driven by the change in energy flow across the pulse tube. It was shown that for the stacked screen type of regenerator simulated here, only 18.7 mW of the total 309.3 mW cooling power loss at 135° could be attributed to the regenerator. According to this analysis, an error of approximately 6% of net cooling capacity loss can be expected when eliminating the regenerator from simulations investigating orientation sensitivity.

The qualitative results of this investigation and the immense computational resources required to solve system-level simulations justify and motivate the use of a reduced, isolated model of the pulse tube component to predict the orientation-dependent losses in PTR systems. In an industrial environment where computational resource utilization (especially HPC resources, which are typically outsourced) and engineering time are major cost drivers, 3-D system-level simulations are simply too cumbersome and expensive to incorporate into the design process in an optimization capacity. The following chapter introduces an expedited component-level pulse tube modeling methodology, which is validated with experimental data from commercial cryocoolers, then used to parametrically study the functional dependence of convective instability.

CHAPTER V

PULSE TUBE COMPONENT-LEVEL CFD SIMULATION AND PARAMETRIC STUDY

5.1 Overview

It was shown in Chapter 4 that orientation sensitivity effects in the PTR system are to first order isolated to the pulse tube component. Although other components may be affected, their contributions to the overall net energy flow loss are negligible in comparison to the model's precision. As mentioned in the conclusion of Chapter 4 the time required to converge a full 3-D system-level model to periodic steady state is prohibitive and precludes its use as a design tool. This motivated the need to develop a more nimble evaluation tool that trades reduced accuracy for speed of solution. This section introduces such a model, which has been applied to a wide range of conditions to investigate the fundamental parameters that contribute to convective instability within the pulse tube. These results will be utilized in Chapter 6 to evaluate the suitability of the pulse tube convection number N_{PTC} as a predictive tool for convective losses.

5.2 Computational Domain, Grid Independence, and Time Step Convergence

5.2.1 Computational Domain

The key criterion for creating an isolated component model of a fluid system is that the essential physics of the problem are not violated as a result of the simplifying assumptions of the model or the boundary conditions used to segregate the subdomain from the physical system. In order to ensure that this condition is met, the pulse tube component model incorporates the solid wall material as well as the adjacent cold

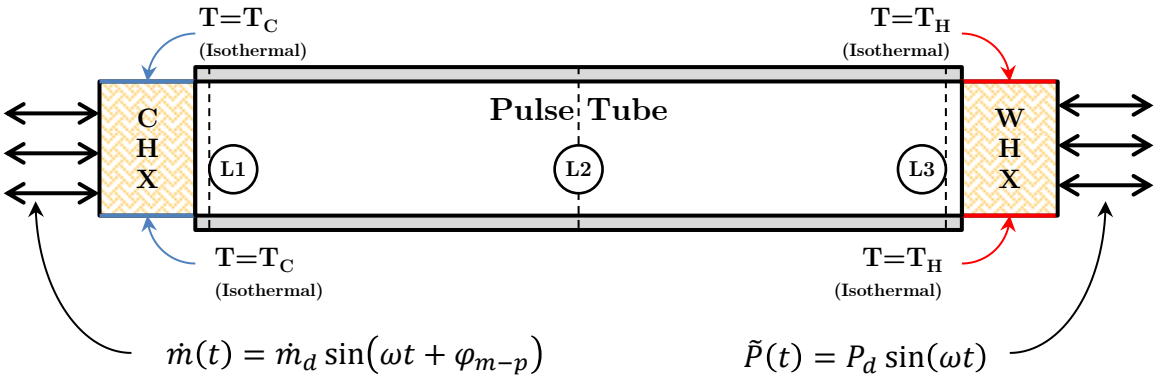

Figure 5.1: Schematic of computational domain for isolated pulse tube CFD models used in parametric study. Pattern filled areas represent porous zones, solid filled areas represent solid materials, and white zones indicate gas flow channels. Mass flow and pressure boundaries are implemented using UDF codes.

heat exchanger (CHX) and warm heat exchanger (WHX) as shown in Figure 5.1. The open system methodology described in Section 3.4 is used to represent the subsystem, where an oscillating mass flow inlet is applied to the cold heat exchanger inlet and an oscillating dynamic pressure outlet is applied to the warm heat exchanger boundary.

A significant assumption applied to this chosen computational domain is that the flow profile entering from the inertance tube does not significantly affect the flow within the pulse tube component. For this reason, the component-level methodology and parametric results presented in this chapter should only be applied to designs which incorporate sufficient flow straightening features that minimize jetting effects. For situations where the user is unsure whether or not proper flow straightening will be achieved, the computational domain can simply be extended to include any abnormal geometry that encompasses the transition region. Techniques for addressing inertance tubes which make a 90° turn at the exit of the WHX, such as those found in many coaxial cooler designs, will be presented in Chapter 6.

Isothermal boundaries are enforced on the outermost radial walls of the CHX and WHX which simulate perfect heat addition and rejection to the wall to maintain the isothermal condition. The solution is initialized with a temperature field consisting of uniform temperature T_C applied to the CHX porous zone, the power law formulation

described by Equation 3.30 applied to the pulse tube fluid domain and pulse tube wall, and uniform temperature T_H applied to the WHX porous zone. Unlike the constant velocity field initialization strategy applied to the closed-system models presented in the previous chapter, the velocity in the isolated pulse tube domain utilizes a hybrid initialization algorithm based on the flow conditions present at the boundaries. As a result, the initial velocity profile varies from case to case as determined by the algorithm.

The mass flow inlet condition is controlled by a UDF containing Equation 5.1. The full UDF is a C++ code and is located in Appendix B.4. The pressure outlet condition is also driven by a UDF containing Equation 5.2.

$$\dot{m}(t) = \dot{m}_d \sin(\omega t + \varphi_{m-p}) \tag{5.1}$$

$$P(t) = P_d \sin(\omega t) \tag{5.2}$$

The phase angle φ_{m-p} is arbitrarily applied to the mass flow condition due to the fact that the pressure oscillates almost entirely in phase throughout the PTR domain simulated here, which does not incorporate a long inertance tube or regenerator where appreciable pressure phase shifting can occur. The speed of sound c in helium at the operating temperature and pressure is high enough that the time required for a pressure wave to propagate from the cold exchanger to the opposing end of the warm heat exchanger and back is significantly smaller than the period of oscillation. The temperature of the flow coming in to the domain is uniformly set to T_C at the mass flow inlet and T_H at the pressure outlet. The dimensions of the two computational domains included in the computational parametric study are summarized in Table 5.1.

5.2.2 Time Step and Grid Independence

In order to ensure that the results of the component level models are numerically accurate, a sensitivity analysis was performed on the time step, the mesh density, and the meshing methodology prior to executing a full set of parametric simulations.

Table 5.1: Dimensions for component-level pulse tube models incorporating CHX, PT, PT wall, and WHX.

Component Geometry	**L/D=8 (m)**	**L/D=4 (m)**
CHX Diameter	1.0608×10^{-2}	1.3365×10^{-2}
CHX Length	5×10^{-3}	5×10^{-3}
Pulse Tube Diameter	1.0608×10^{-2}	1.3365×10^{-2}
Pulse Tube Length	8.4864×10^{-2}	5.3461×10^{-2}
Pulse Tube Wall Thickness	2.54×10^{-4}	2.54×10^{-4}
WHX Diameter	1.0608×10^{-2}	1.3365×10^{-2}
WHX Length	5×10^{-3}	5×10^{-3}

In this section we discuss the preliminary modeling results used to determine the final simulation methodology. As with the system level models previously presented, prismatic meshing schemes were applied in order to maximize the orthogonal quality of the computational mesh. Elimination of the tapered flow transitions from the larger diameter regenerator at the cold end and the slender inertance tube at the warm end allowed the use of a purely cylindrical domain which does not require tetrahedral mesh elements. Three successively denser meshes were generated with nominally 75,000, 150,000, and 300,000 elements in accordance with the Richardson extrapolation method adopted as a guideline by the Journal of Fluids Engineering [94, 95] as described in the following analysis. The three meshes described are shown in Figure 5.2.

For each mesh, a representative cell size Ψ is computed according to Equation 5.3, where subscripts $m = 1...3$ and i refer to the mesh identifier (in order of increasing density) and the cell idenfication number, N is the total number of cells for each mesh m, and V_i are the individual volumes of each element that makes up a given mesh.

$$\Psi_m = \sqrt[3]{\frac{1}{N}\sum_{i=1}^{N}\Delta V_i} \tag{5.3}$$

The resulting representative cell lengths are then used to compute the grid refinement factors $r_{(m)-(m-1)}$, which are the ratios of sequential values Ψ_m.

$$r_{21} = \frac{\Psi_2}{\Psi_1} \tag{5.4a}$$

$$r_{32} = \frac{\Psi_3}{\Psi_2} \tag{5.4b}$$

Given the transient formulation used, solution accuracy is estimated at the point in time where the model has reached periodic steady-state. The formal order of accuracy is estimated based on measured quantities of interest for the problem rather than based on residual convergence. In this case the critical information of interest is the pulse tube cold end net energy flow $\left\langle \dot{E}_{net} \right\rangle$ introduced in Equation 2.23. The relative differences in the key energy flow variable for sequential mesh densities are denoted as follows:

$$\xi_{21} = \left\langle \dot{E}_{net,2} \right\rangle - \left\langle \dot{E}_{net,1} \right\rangle \tag{5.5a}$$

$$\xi_{32} = \left\langle \dot{E}_{net,3} \right\rangle - \left\langle \dot{E}_{net,2} \right\rangle \tag{5.5b}$$

$$X = \frac{1}{\ln(r_{21})} \left[\ln \left| \frac{\xi_{32}}{\xi_{21}} \right| + q(func) \right] \tag{5.6a}$$

$$q(func) = \ln \left(\frac{r_{21} - func}{r_{32} - func} \right) \tag{5.6b}$$

$$func = \text{sgn} \left(\frac{\xi_{32}}{\xi_{21}} \right) \tag{5.6c}$$

The results are then used to compute the extrapolated exact solution ξ_{ext}^{21} that we assume would be computed by the ideal mesh.

$$\xi_{ext}^{21} = \frac{r_{21} - s}{r_{32} - s} \tag{5.7}$$

This extrapolated solution is then used to estimate the approximate extrapolated

relative error e_{ext}^{21}.

$$e_{ext}^{21} = \left| \frac{\xi_{ext}^{21} - \left\langle \dot{E}_{net,1} \right\rangle}{\xi_{ext}^{21}} \right| \tag{5.8}$$

Finally, the fine grid convergence index GCI_{fine}^{21} is computed based on the relative error between the solutions on grids 1 and 2 e_a^{21} as follows:

$$e_a^{21} = \left| \frac{\left\langle \dot{E}_{net,2} \right\rangle - \left\langle \dot{E}_{net,1} \right\rangle}{\left\langle \dot{E}_{net,2} \right\rangle} \right| \tag{5.9}$$

$$GCI_{fine}^{21} = \frac{1.25 e_a^{21}}{e_{ext}^{21}} \tag{5.10}$$

The mesh domains used in the evaluation of discretization uncertainty and model order are displayed in Figure 5.2, and the precise mesh statistics for each nominal mesh are presented in Table 5.2. The three meshes were used to simulate a 40 Hz pulse tube with a cold end temperature of 60 K, warm end temperature of 300 K, mean pressure of 2.0 MPa, pressure ratio of 1.2, and a mass flow rate amplitude of 1.081 g/s. Applying the resulting net energy flows from these three grids, evaluated at periodic steady-state, the apparent model order was computed as 8.35 and discretization error was estimated at 0.42% for use of the 75,000 element mesh domain. Simulation time scaled linearly with the total number of elements, with simulation times running from 12-30 days. Given the small 0.52% error associated with using the least refined mesh, the 75,000 element mesh was selected for all component level simulations.

In addition to spatial discretization error, error is introduced through the choice of time step in transient simulations. In this parametric study, time steps were chosen and analyzed that yielded 300 and 400 time steps per period of oscillation. The error associated with the coarser time step was determined to be as small as 0.06%; however, it was noted during testing of this parameter that the solution converged at a much more stable rate utilizing the finer time step, allowing the solution to converge at each time step in fewer iterations and with significantly improved consistency. The extra 25% total time steps required for the fine time steps was mitigated by the

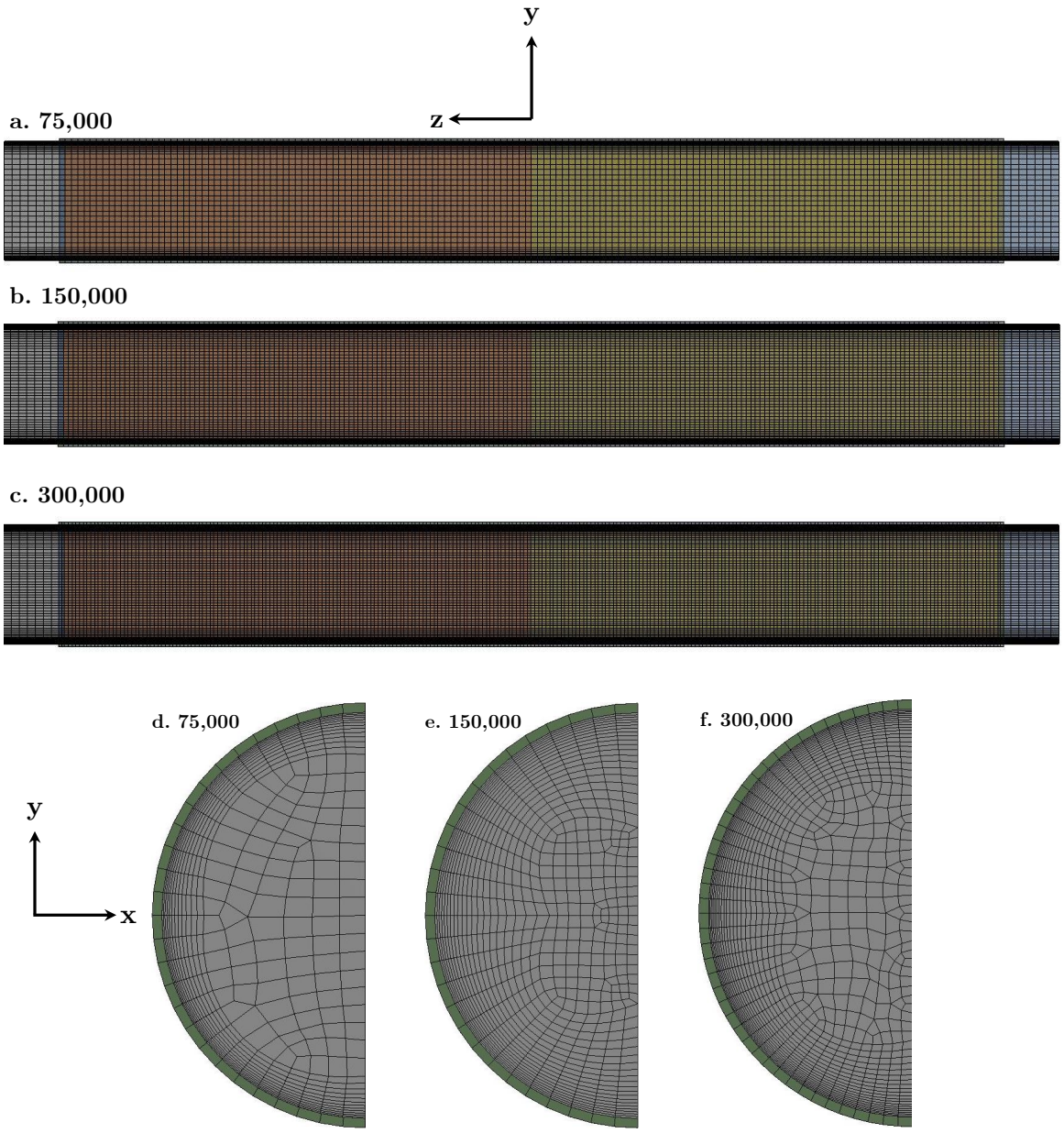

Figure 5.2: Meshes simulated in order to determine model order for grid independence for pulse tube aspect ratio $L/D = 8$

Table 5.2: Grid statistics for meshes used in component-level modeling and grid-independence testing results.

Mesh Statistic \ Nominal Size	**75,000**	**150,000**	**300,000**
Nodes	83,762	168,637	311,948
Elements	77,130	158,152	295,256
Boundary Inflation Layers	12	20	20
Min. Orthogonal Quality	0.7414	0.4075	0.6151
Body Sizing (m)	6.5×10^{-4}	6.0×10^{-4}	4.0×10^{-4}
Edge Sizing (# Divisions)	75	100	125
$\left\langle \dot{E}_{net,c} \right\rangle$	11.510 W	11.494 W	11.362 W
Apparent Model Order X	8.35	-	-
Extrapolated Rel. Error e_{ext}^{21}	0.42%	-	-
Fine Grid Index GCI	0.52%	-	-
Avg. Wall Time (8-12 cores)	285 h	509 h	733 h

expedited convergence such that the total case run time was actually reduced from 285 hours to 253 hours. For this reason, in addition to the added precision benefit, time steps were chosen to yield 400 time steps per cycle. Typical convergence was observed within 30 iterations at each time step.

5.3 Computational Parametric Study Results

5.3.1 Parameters Investigated

Once the most appropriate grid and time step resolution were identified, the resulting domain and settings were used to parametrically simulate a wide range of pulse tube operating conditions. The purpose of this study is to identify and to isolate the key driving parameters that affect pulse tube performance over a wide range of angles. The total number of permutations was limited by the immense computational resources required for simulation as reported in the previous section. A sensitivity

analysis of the simulation time to the number of parallel processes assigned to each case was performed and it was found that the simulation speed scaled inverse linearly with the number of parallel tasks. The supercomputing resources allotted to this investigation were limited by the number of HPC licenses available for simultaneous ANSYS simulations as well the total number of CPU hours (wall time $\times$ # parallel processes). A simple optimization study was done to determine the configuration that would yield the largest number of completed cases in the time allotted, and the result was that each case should utilize 24 CPU cores in parallel. Although total simulation time for each case varies based on both solution speed and percent utilization of the processor node handling the job, the average solution time with this configuration was approximately 6.5 days (155 hours).

Two computational domains were utilized with identical gas volume and pulse tube aspect ratios (L/D) of 4 and 8 such that the effect of aspect ratio could be quantified for select cases. The parameters of interest are presented in Table 5.3 and correspond primarily to those identified by the pulse tube convection number N_{PTC} [3]. The additional parameter which has not been previously included in analysis, presumably because it was assumed to have no effect, is the phase relationship between mass flow and pressure oscillation, which is known to vary widely by pulse tube type (BPTR, OPTR, ITPTR) as well as design.

Execution of a traditional parametric study where all permutations of all variables are pursued would require nearly 2,000 simulations when pressure ratio and average (charge) pressure are included. In order to reduce the number of cases to align with the available computational resources, a single charge pressure of 2.0 MPa was investigated, and a pressure ratio of 1.2 was applied to all cases studied. Analysis was carried out in a tree-branch methodology, where each branch of the tree isolates a particular variable of interest. In order to capture a wide range of cold and hot end temperatures, staged pulse tubes were modeled based on thermodynamically

Table 5.3: Ranges of values simulated for the parametric study of convective instability in pulse tubes.

Parameter	**Range Min.**	**Range Max.**	**# Permutations**
Driving Frequency f	25 Hz	60 Hz	3
Angle of Inclination θ	0°	180°	5-6
Cold End Temperature	4 K	80 K	4
Warm End Temperature	20 K	300 K	3
Phase Angle φ_{m-p}	$-30°$	$+30°$	2
Cold End Mass Flow $\dot{m}_d$	1 g/s	4 g/s	3
Cold End Reynolds Re_c^δ	43	350	18
Total Cases Simulated	-	-	119

optimal staging points at 300 K, 80 K, 20 K, and 4 K commonly used in three-stage PTRs. An additional set of runs between 300 K and 60 K were included which represent a common single stage cooler range. Three mass flows were simulated for each tempearture/geometry configuration in order to capture a reasonably wide range of Reynolds numbers varying from very laminar to approaching intermittently turbulent.

The angles θ investigated are 0°, 45°, 91°, 135°, and 180°. In some branches simulated early in the analysis, 60° inclination angles were simulated as well, but this angle was later eliminated since no interesting results were revealed in comparison to the neighboring angles. The 91° orientation was chosen such that the results could be included in an analysis of N_{ptc} as the formulation requires inclination angles $> 90°$. Angles $< 90°$ were included based on published literature [43,44,48,53] which indicates that orientation sensitivity is observed in some configurations at inclination angles deviating only slightly from the preferred cold end down 0° orientation.

The results of this parametric investigation cover a range wide enough to be generally applicable to any conceivable pulse tube design that falls within the frequency

and pressure range studied. Future work will be suggested in the final chapter of this dissertation to extend the study to incorporate a wider range of frequencies, charge pressures, and pressure ratios. Acquisition of this volume of data would be better suited to an experimental investigation where permutations can be performed much more readily. In spite of the limitations to the scope of study, the data represents a significant improvement in accuracy when compared to previous analyses based on ambient and elevated temperature testing. The models carried out in this parametric study incorporate three-dimensional and real gas effects, which are the primary differentiator assumed to invalidate elevated temperature results which tend to obey ideal gas relationships.

5.3.2 Stability Results for Simulated Pulse Tubes

As introduced in Section 5.3.1, two different mass flow - pressure phase relations were numerically modeled throughout the parametric study to determine whether the effects of orientation angle are phase dependent. The following sections will adress the results separately for cold end phase angles φ_{m-p} of $+30^\circ$ where mass flow leads pressure, and -30° where flow lags pressure. The general rule of thumb for most pulse tube designs is to come as close as possible to -30°, though especially for low PV power coolers it can be difficult to achieve this phase relationship.

5.3.2.1 Identifying Instability

In this section, transient traces of pulse tube energy flows will be investigated as the solution propagates from the specified initial conditions to the final cyclic steady-state solutions that will be reported in Sections 5.3.2.2 and 5.3.2.3. In general, for each configuration of end temperatures, geometry, and frequency, three sets of simulations were performed corresponding to mass flow rates of 1 g/s, 2.5 g/s, and 4 g/s. These mass flows were chosen based on their predicted Reynolds numbers which represent a wide variety of flow regimes including very laminar, intermediate, and approaching

intermittently turbulent. As will be shown in the following sections, lower Reynolds numbers yield a design that is more susceptible to convective instability and therefore loss.

Instability may be obvious to spot in some cases based on extreme losses of either cooling capacity or wide variation of the working temperature. In other cases it can be difficult to spot instability by inspection of cycle-averaged values at a snapshot in time. In very unstable cases, the cycle-averaged energy flows can jump by an order of magnitude or even reverse direction (complete loss of gross cooling capacity), making it difficult to evaluate instability losses on the bases of a final cycle-averaged value alone.

Figure 5.3 compares the cycle-averaged net energy flow rate as a function of time throughout the duration of the simulations for a slender ($L/D = 8$) pulse tube operating at 60 Hz with end temperatures of 300 K and 60 K for a mass flow amplitude of 4 g/s corresponding to $Re_c^\delta = 305$. As the figure shows, the cycle averages converge within 0.1% of the final periodic steady-state value in less than 1.25 seconds of simulated flow time. A simulation at 91° was carried out to a flow time of 2.5 seconds, ensuring that the behavior would remain consistent and therefore warranting the cutoff point of 1.25 seconds. Although there is characteristic numerical oscillation during the first 0.25 s of simulation, the solution quickly converges after and tracks toward a final value. The tight grouping of net energy flow traces indicates a very stable solution at all angles of inclination simulated.

Figure 5.4 illustrates the transition into an unstable regime. For the same 300-60 K temperature range, a reduced mass flow amplitude of 2.5 g/s corresponding to $Re_c^\delta = 197$ yields a significantly increase in temporal variation of the cold end net energy flow. While small angles of inclination have smoothly converging energy averages, the larger angles begin to oscillate with deviation as large as 8 W compared to the vertical solution after approximately 0.2 seconds. The final convergence history (Figure 5.5)

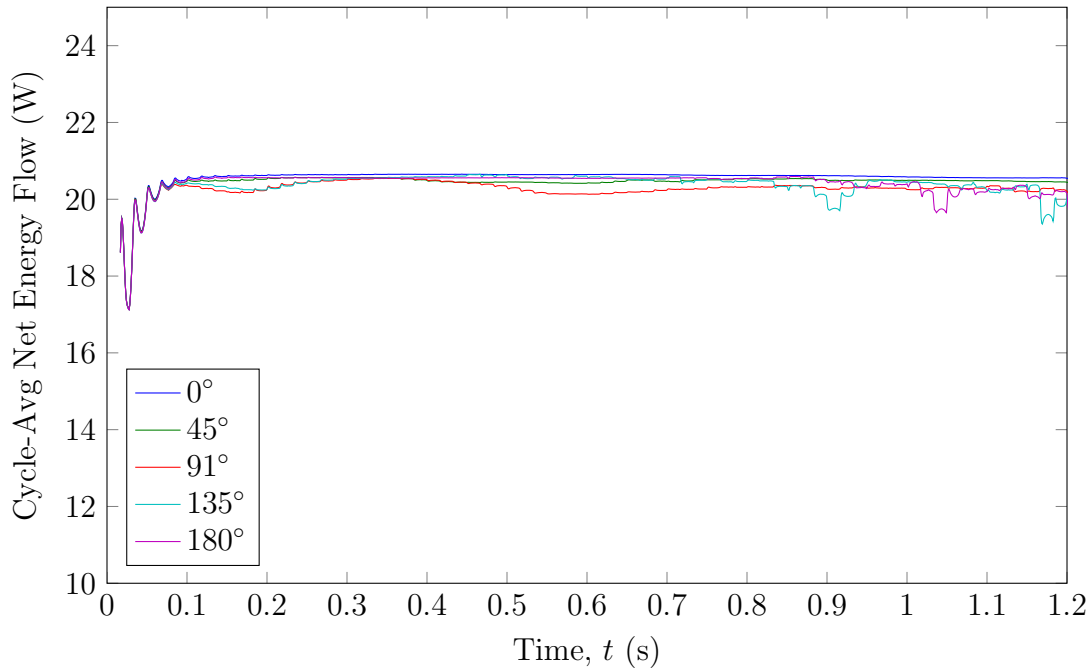

Figure 5.3: Convergence history for component-level model of a L/D=4, 60 Hz, 300-60 K pulse tube operating with a peak mass flow of **4 g/s.**

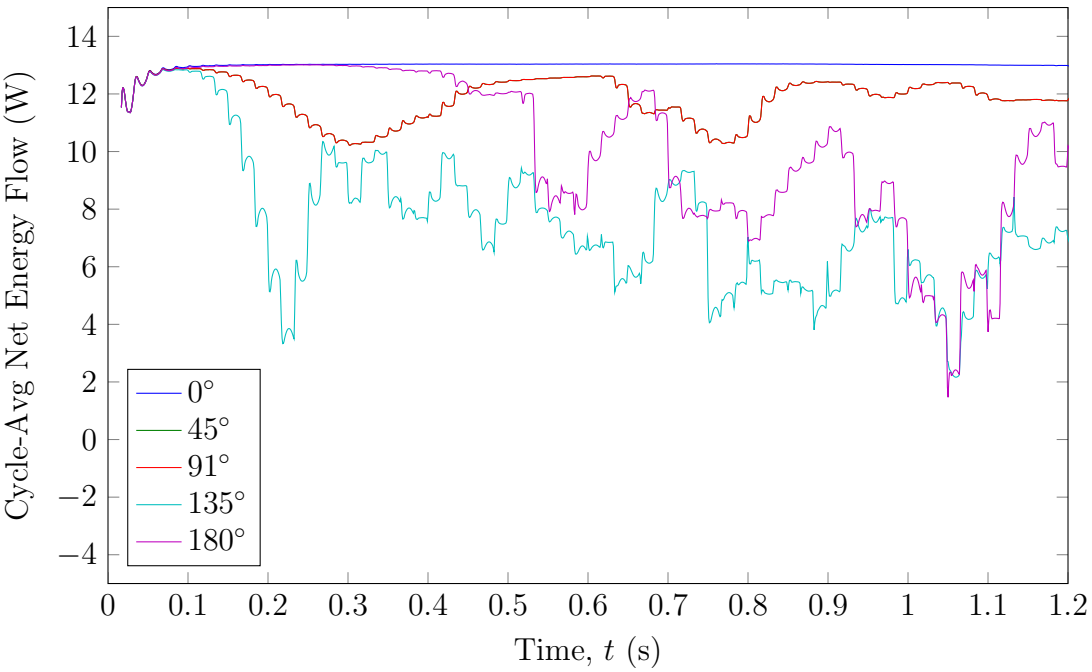

Figure 5.4: Convergence history for component-level model of a L/D=4, 60 Hz, 300-60 K pulse tube operating with a peak mass flow of **2.5 g/s**.

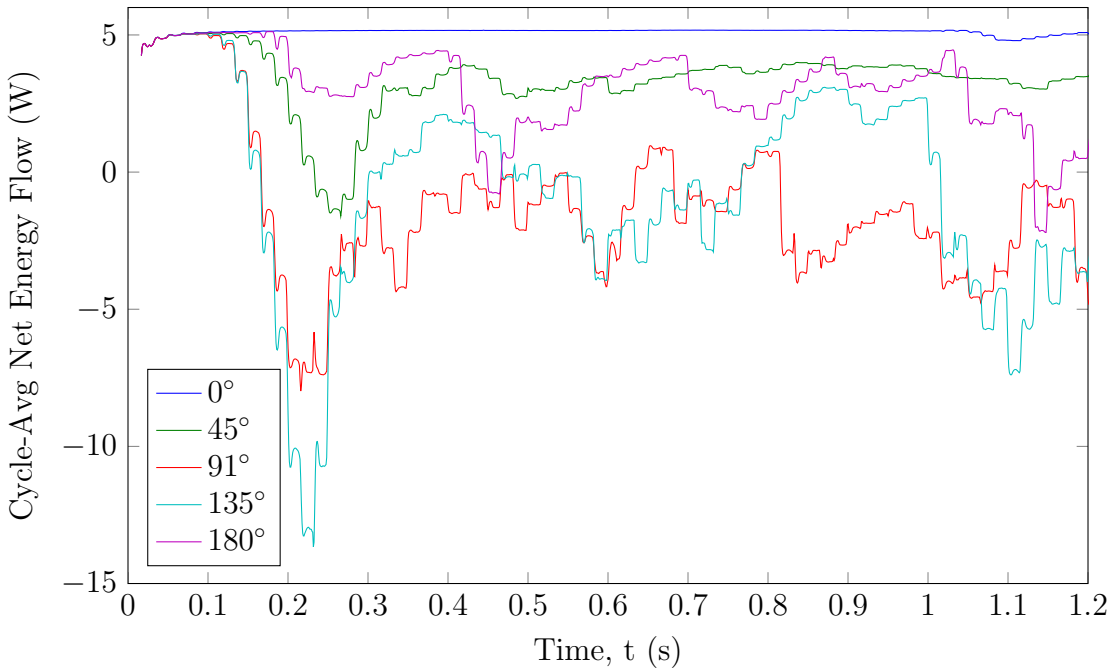

Figure 5.5: Convergence history for component-level model of a L/D=4, 60 Hz, 300-60 K pulse tube operating with a peak mass flow of **1 g/s**.

indicates a complete transition to instability for an identical set of operating conditions with mass flow of 1 g/s and $Re_c^\delta = 89$. Aside from the vertical (0°) case, the solutions oscillate dramatically. In many instances the average energy flow actually reverses, resulting in a negative net energy flow (from hot to cold, a parasitic loss). Reversed energy flows are permitted in the simulation as a result of the isothermal wall boundary condition applied to the heat exchangers. In practice this would be observed as a fluctuation of cold end temperature and a steady-state value is unlikely to ever be reached without active control of the driving parameters to modulate the fluctuation.

In order to capture the transient instability effects illustrated in Figures 5.4-5.5, the net energy flow values are reported with magnitude equal to the cycle-average of the final period of oscillation along with error bars representing the upper and lower bounds of the net energy flow throughout the last 0.25 seconds of simulated flow time. A larger error bar indicates a more unstable set of operating conditions. In the

following sections, results will be grouped by aspect ratio as well as temperature range and frequency. Evaluation of the quasi steady-state energy flows will be presented on a linear scale with instability-indicating error bars, as well as on a logarithmic scale which identifies losses that are not readily visible on a linear scale. Error bars are not included on the logarithmic plot to improve figure clarity. For select cases, the net energy term is delineated into its constituent components which include gas conduction, wall conduction, and enthalpy flow. The purpose of this analysis is to illustrate the relative contribution of each mode of thermal transport.

5.3.2.2 Condition 1: Cold End Mass Flow Leads Pressure by 30°

A positive phase relationship between mass flow and pressure where $\varphi_{m-p} \geq 0°$ is a condition predominantly found in orifice type pulse tube refrigerators (OPTR) [96], and therefore represents a condition worth exploring. Figure 5.6 illustrates the temporal relationship between mass flow and pressure perturbations for pulse tubes oriented vertically (cold end down, 0°) as well as marginally above the horizontal (91°). The plots illustrated are of low amplitude oscillation at 1 g/s mass flow amplitude. As the figure shows, the pressure oscillations are identical for both cases. For the tilted pulse tube, the mass flow trace experiences slight deviation from sinusoidal behavior near the peaks during periods of heavy acceleration. Vertical and horizontal mass flow rate and dynamic pressure traces are additionally compared for the remaining mass flows used in this parametric study in Figures 5.7 and 5.8. The mass flow phase lead of +30° is identified in the figures by locating the point where the blue and green traces cross the zero and observing the leftward shift in the mass flow trace. Note that the scales vary in Figures 5.6-5.8.

Figure 5.9 shows the comparison between the relevant energy flows in vertical and horizontal orientations. It is apparent from the figure that the gas conduction shows the most dominant change as a result of orientation angle. The wall conduction,

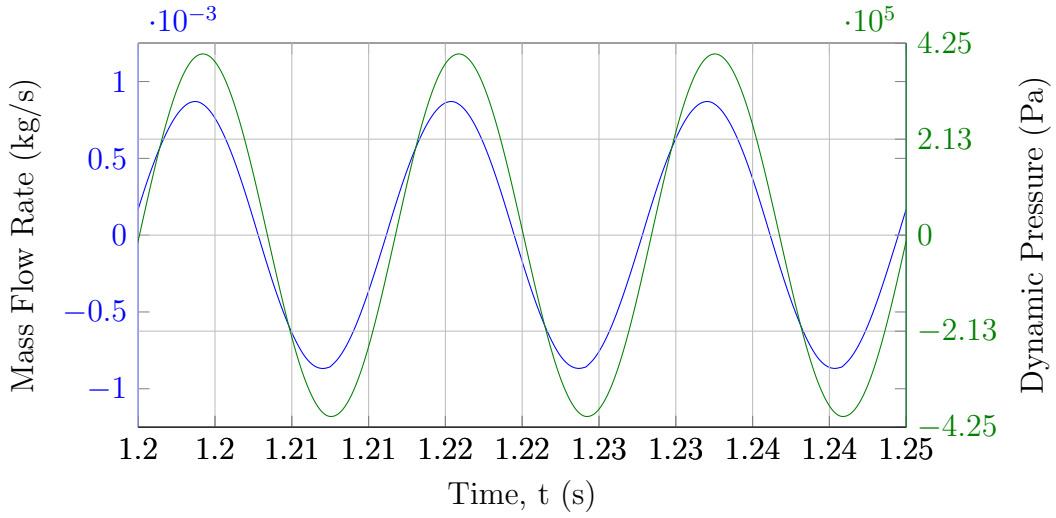

(a) Vertical (0°)

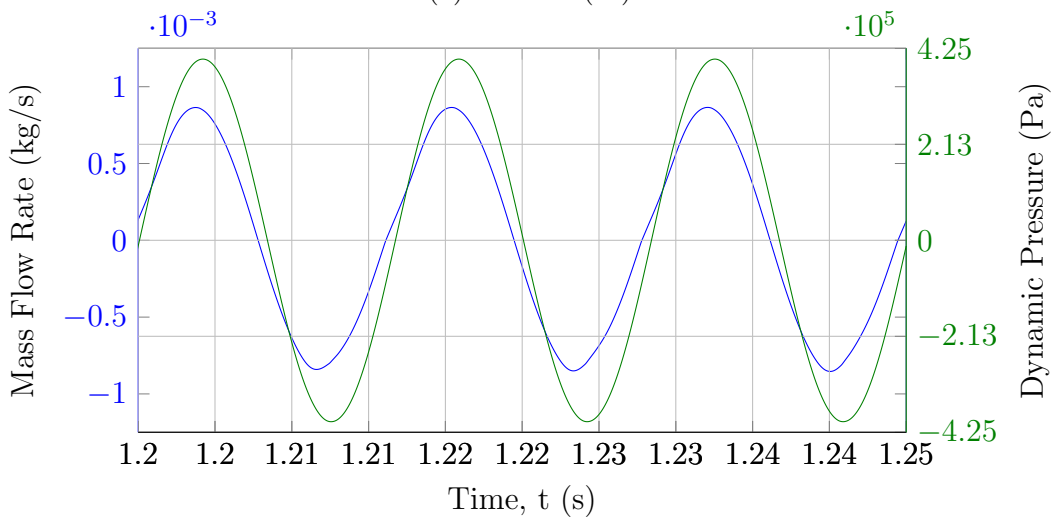

(b) Horizontal (91°)

Figure 5.6: Comparison of simulated cold end mass flow and dynamic pressure for an $L/D = 8$ pulse tube operating between 300 K and 60 K with mass flow amplitude of 1 g/s and pressure ratio of 1.2 for a charge pressure of 2 MPa at different orientation angles. The phase angle between mass flow and pressure is $\varphi_{m-p} = +30°$.

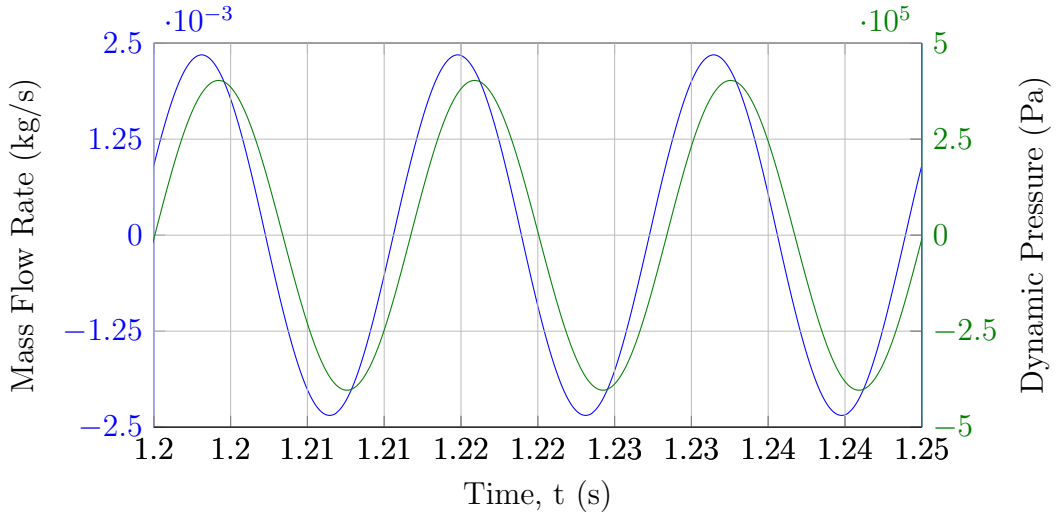

(a) Vertical (0°)

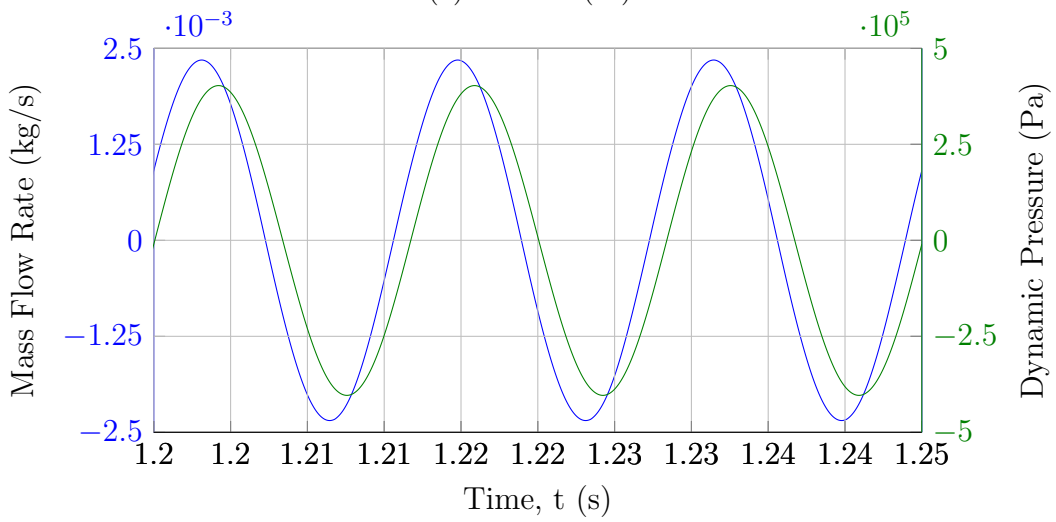

(b) Horizontal (91°)

Figure 5.7: Comparison of simulated cold end mass flow and dynamic pressure for an $L/D = 8$ pulse tube operating between 300 K and 60 K with mass flow amplitude of 2.5 g/s and pressure ratio of 1.2 for a charge pressure of 2 MPa at two orientation angles. The phase angle between mass flow and pressure is $\varphi_{m-p} = +30°$.

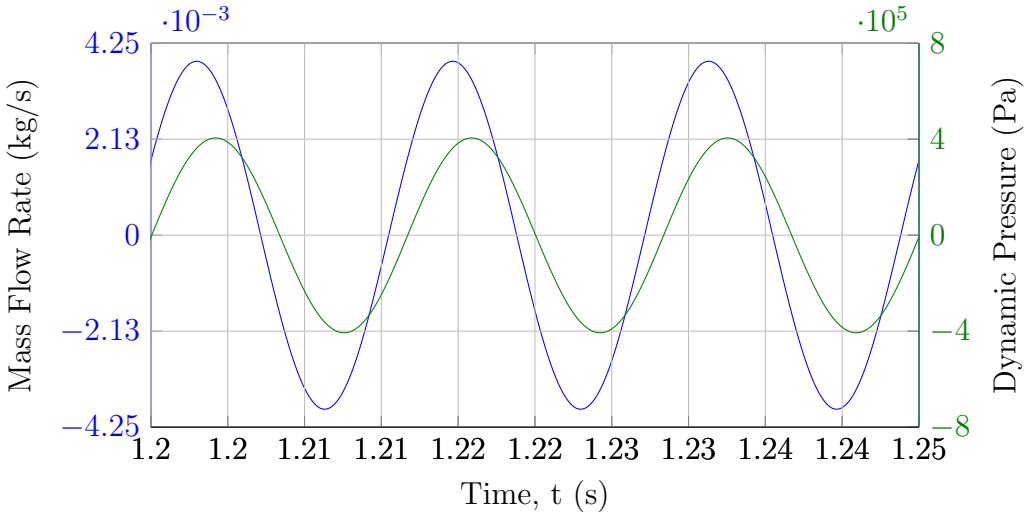

(a) Vertical (0°)

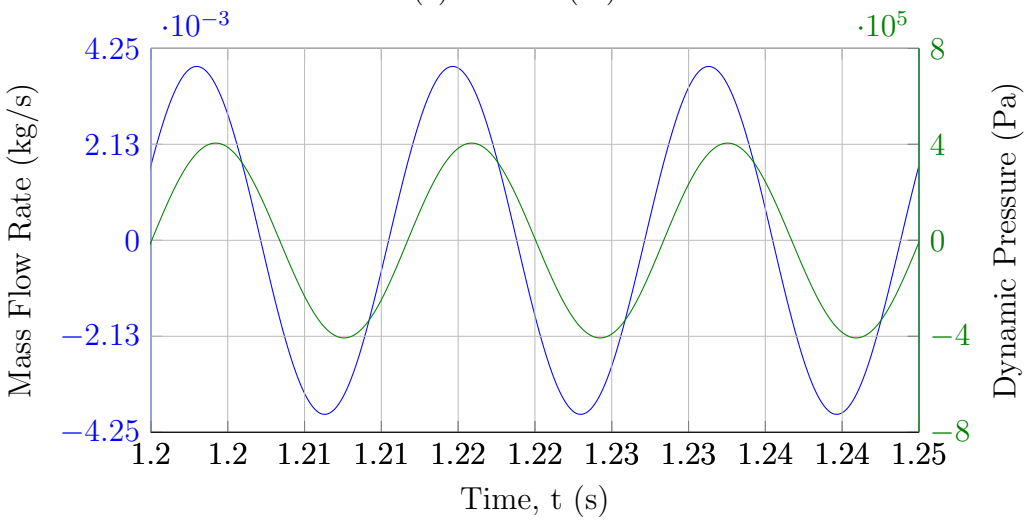

(b) Horizontal (91°)

Figure 5.8: Comparison of simulated cold end mass flow and dynamic pressure for an $L/D = 8$ pulse tube operating between 300 K and 60 K with mass flow amplitude of 4 g/s and pressure ratio of 1.2 for a charge pressure of 2 MPa at different orientation angles. The phase angle between mass flow and pressure is $\varphi_{m-p} = +30°$.

although changing, is a very small term compared to the magnitude of the other two energy flows, and therefore is nearly negligible. Due to the energy flows being plotted on different scales, the importance of the enthalpy flow is masked. The enthalpy flow term is two orders of magnitude larger than the other two terms, so small changes to the enthalpy flow that cause a loss on the order of Watts from the net energy flow appear small on the time traces of the data.

Figures 5.10 and 5.11 apply the same delineation of energy flows to the remaining mass flows of 2.5 g/s and 4 g/s, respectively, for the case of a 60 Hz pulse tube operating between 300 K and 60 K with +30° phase relationship. Inspection of the results reveals a tighter grouping of traces as a function of angle of inclination. In the cases with 4 g/s mass flow rate, there is nearly negligible variation in the enthalpy and gas conduction terms. The magnitude of the combined effects of the three modes of heat transfer are identified in the forthcoming analysis.

At the conclusion of each simulation, the final 0.25 s of data was post-processed to isolate the final cycle-averaged net energy flow at the pulse tube cold end (Location 1 on Figure 5.1) directly adjacent to the cold heat exchanger to pulse tube transition. The maximum and minimum cycle-averaged net energy flow over the final 0.25 s are also reported as upper and lower error bars. Therefore, the size of the error bar corresponds to the convective stability of the flow regime. Figure 5.12 reports the cycle-averaged net cold end energy flows for all simulated angles for the L/D=8 domain operating at 40 Hz over the range of 300 K to 60 K.

In Figure 5.13 the data presented in Figure 5.12 is normalized by the vertical (0°) net energy flow according to Equation 5.11 and plotted on logarithmic axes. This normalization method yields a non-dimensional energy flow loss that can be directly compared among all cases simulated. This normalized loss term $|L(\theta)|$ is indicative of the percentage of gross cooling capacity reduction caused by off-axis operation of the PTR.

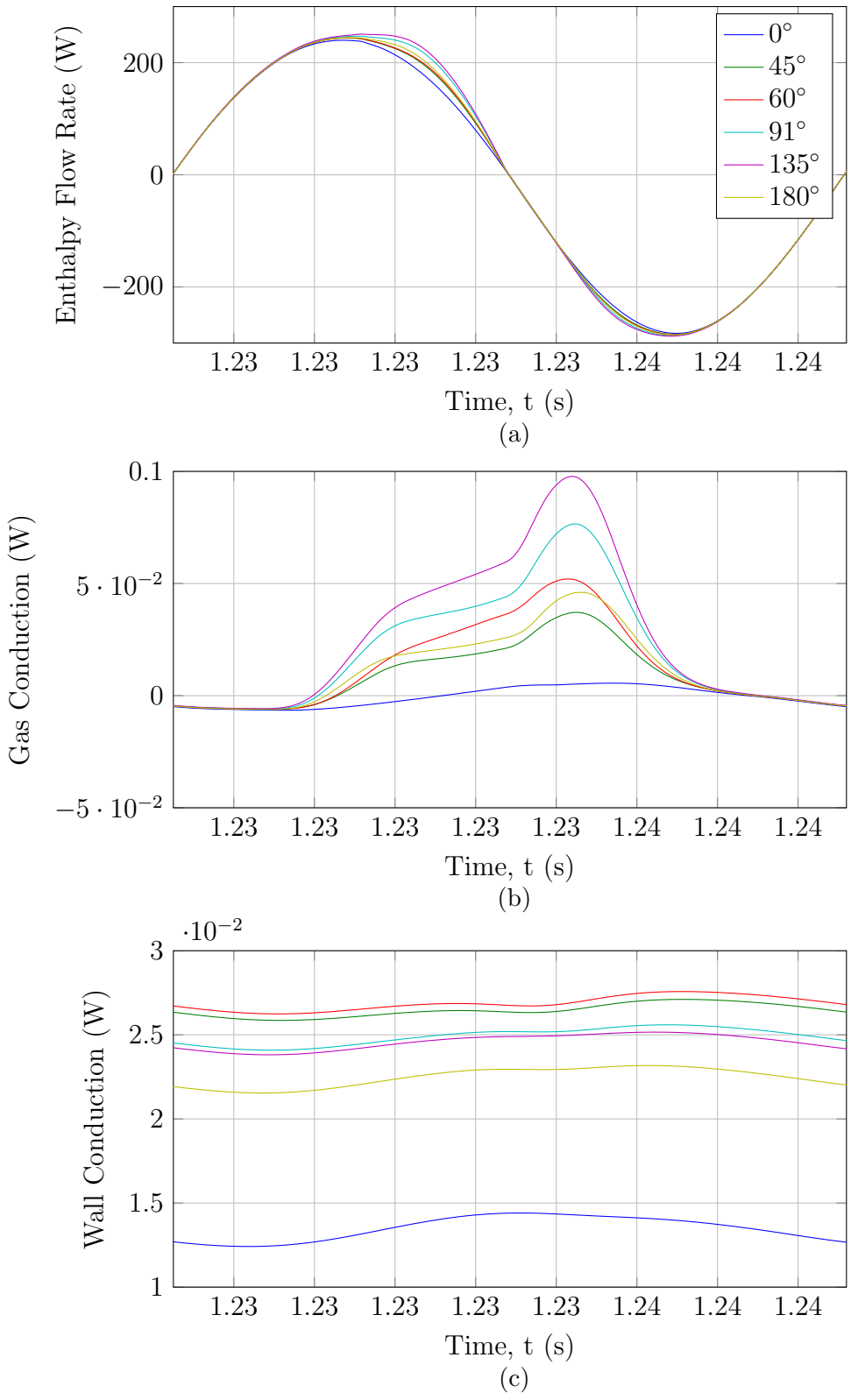

Figure 5.9: Comparison of simulated energy flows for an $L/D = 8$ pulse tube operating between 300 K and 60 K with mass flow amplitude of **1 g/s** as a function of orientation angle. Positive energy flow denotes parasitic flow from hot to cold. Note that the legend in (a) applies to (a)-(c).

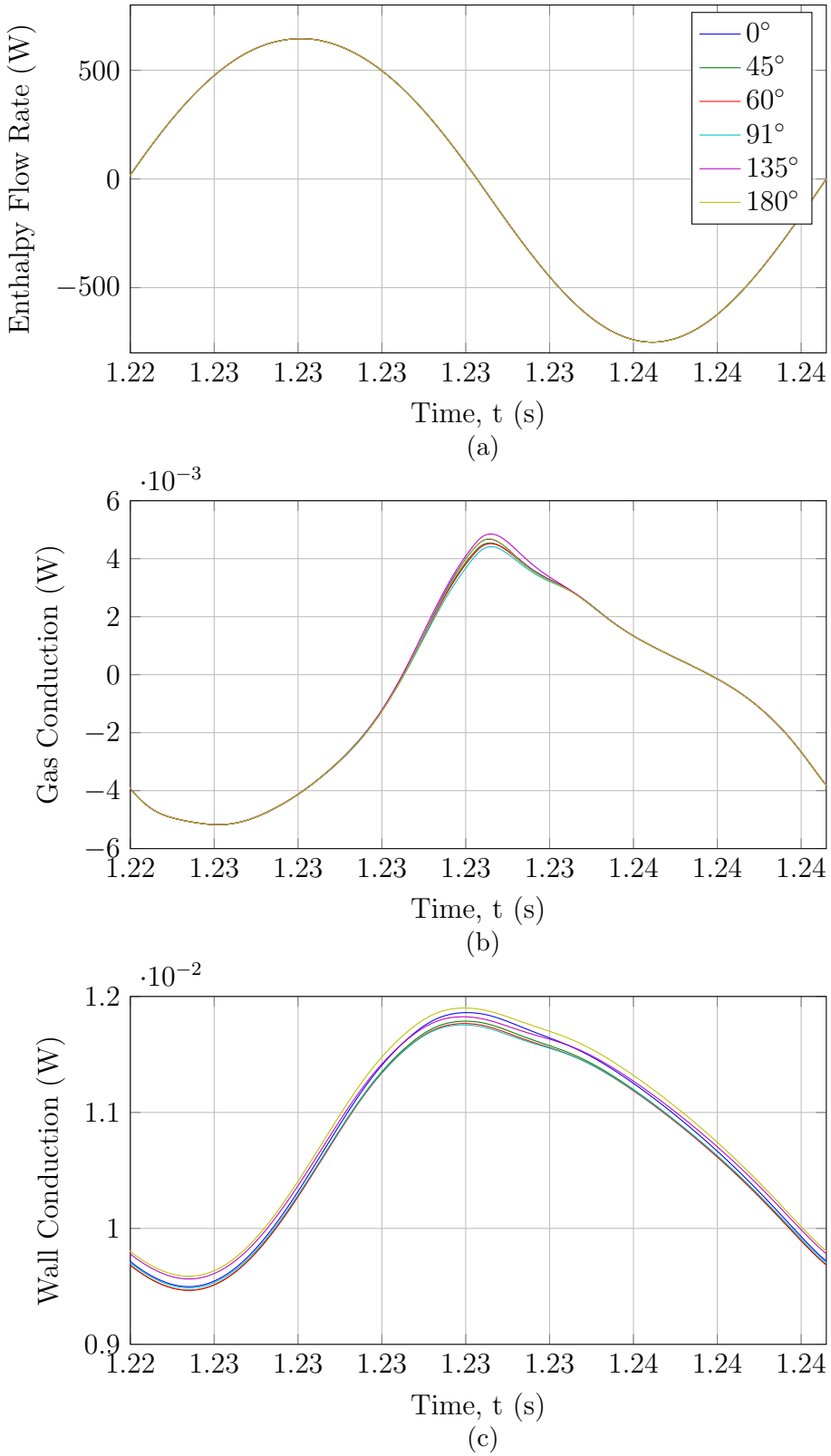

Figure 5.10: Comparison of simulated energy flows for an $L/D = 8$ pulse tube operating between 300 K and 60 K with mass flow amplitude of **2.5 g/s** as a function of orientation angle. Positive energy flow denotes parasitic flow from hot to cold. Note that the legend in (a) applies to (a)-(c).

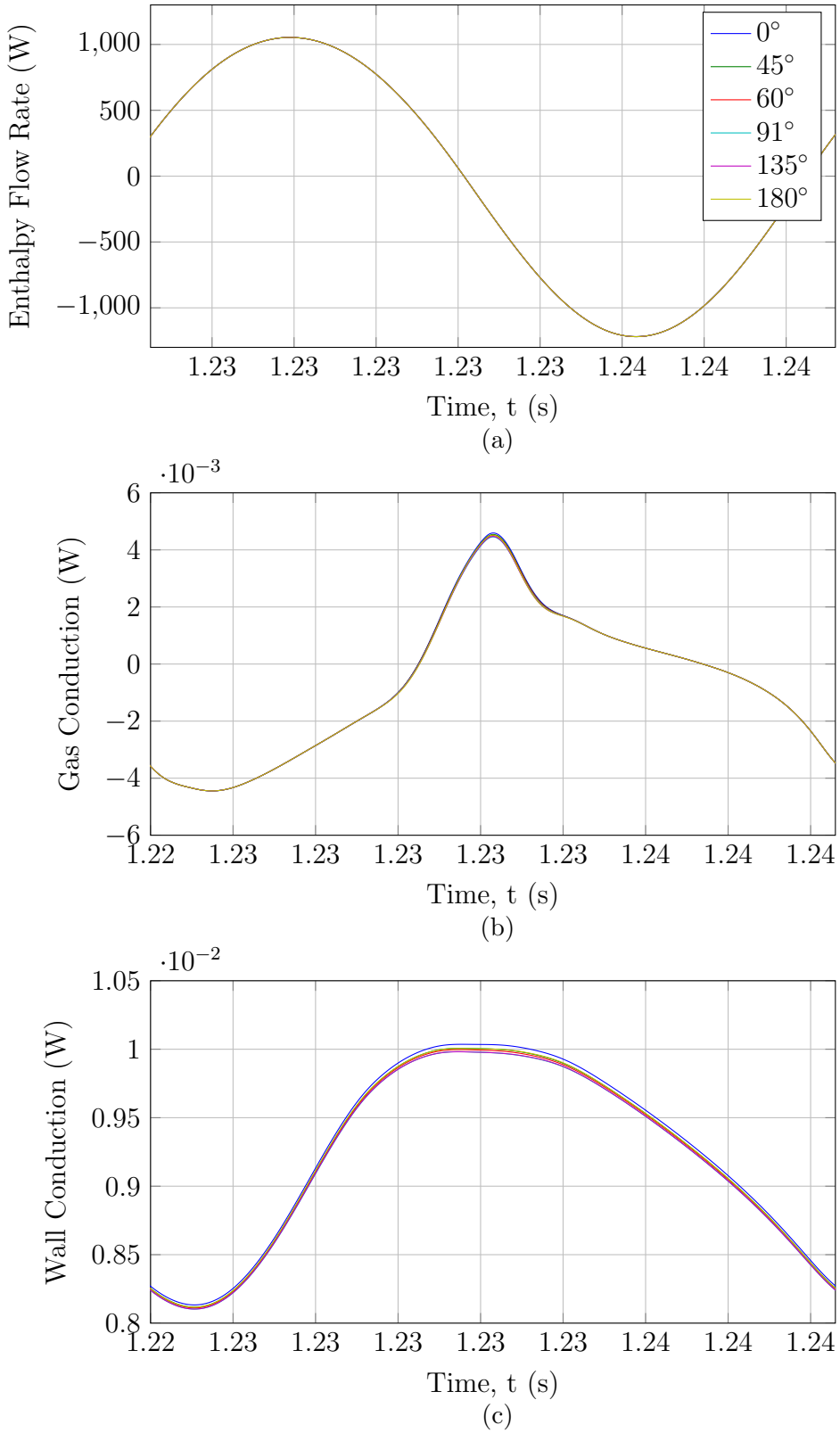

Figure 5.11: Comparison of simulated energy flows for an $L/D = 8$ pulse tube operating between 300 K and 60 K with mass flow amplitude of **4 g/s** as a function of orientation angle. Positive energy flow denotes parasitic flow from hot to cold. Note that the legend in (a) applies to (a)-(c).

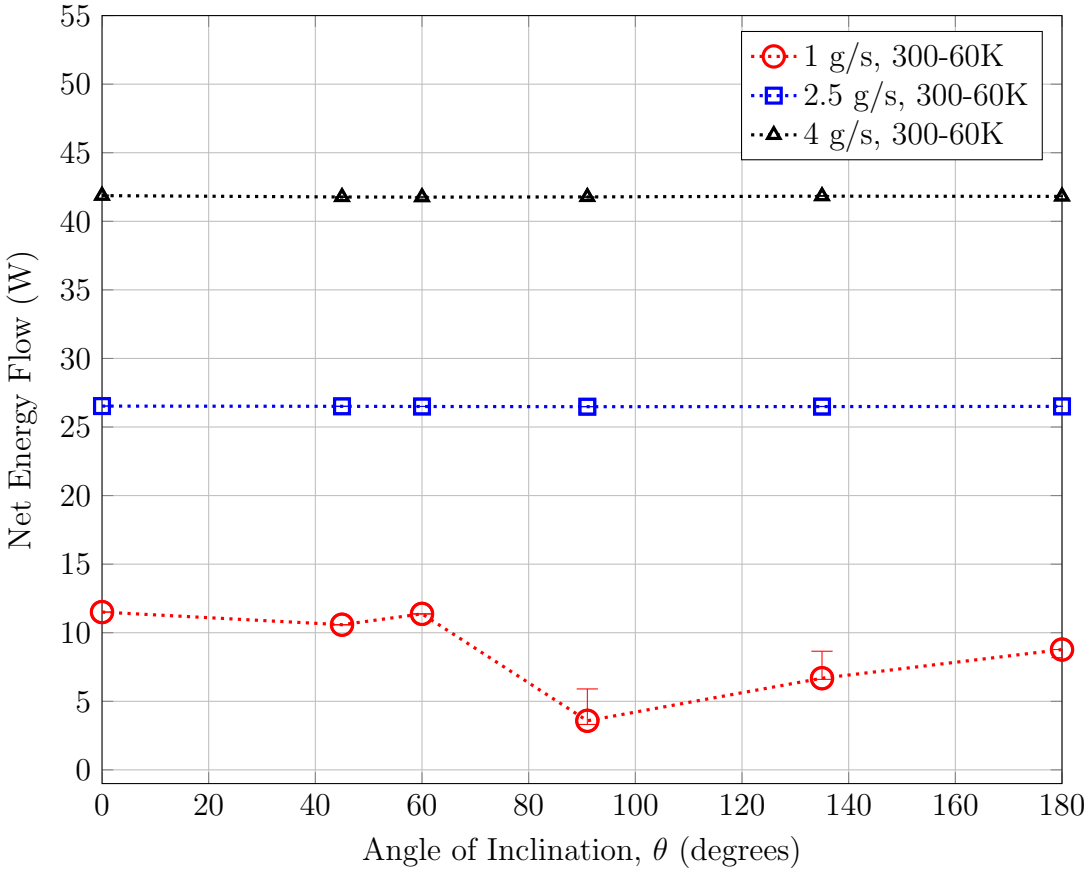

Figure 5.12: Net Cycle-averaged energy flow $\langle \dot{E} \rangle$ for 40 Hz simulations with 60 K cold end and 300 K warm end for an aspect ratio (L/D) of 8. The phase angle between mass flow and pressure is $\varphi_{m-p} = +30°$.

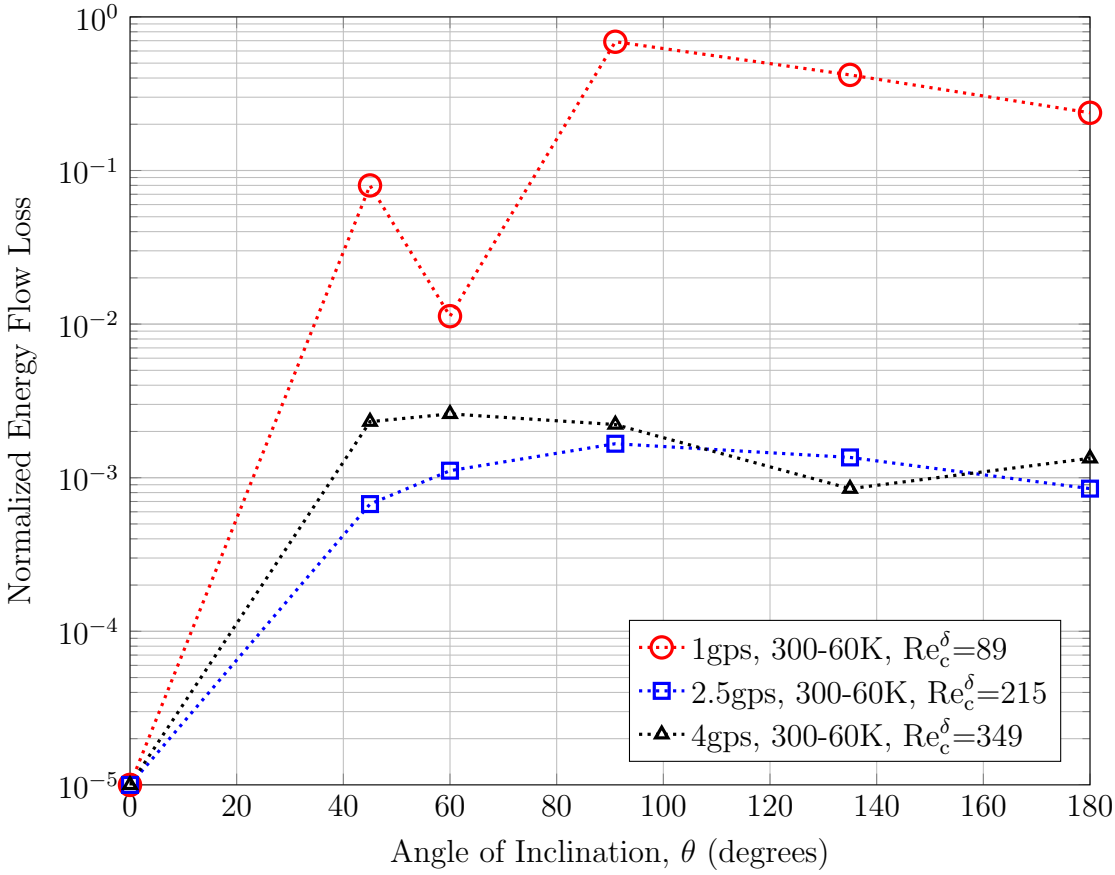

Figure 5.13: Normalized energy flow loss for 40 Hz simulations with 60 K cold end and 300 K warm end for an aspect ratio (L/D) of 8. The phase angle between mass flow and pressure is $\varphi_{m-p} = +30°$.

$$|L(\theta)| = \frac{\left\langle \dot{E}_{net,c}\left(0^\circ\right)\right\rangle - \left\langle \dot{E}_{net,c}(\theta)\right\rangle}{\left\langle \dot{E}_{net,c}\left(0^\circ\right)\right\rangle} \tag{5.11}$$

Figures 5.14 and 5.15 present the processed results for the same $L/D = 8$ computational domain with a driving frequency of 60 Hz. Direct comparison can be made to Figures 5.12 and 5.13, isolating the effect of driving frequency on the operational stability, as a result of all other operating parameters being identical for the two sets of cases. By inspection, the magnitude of the normalized energy flow loss is the same for 1 g/s and 2.5 g/s flow rates. The 4 g/s loss is reduced by an order of magnitude over the equivalent flow rate at 40 Hz. Additionally, the 4 g/s trace in Figure 5.13 reveals some peculiar behavior in relation to the 2.5 g/s results, wherein the 2.5 g/s case experiences less normalized loss.

Continuing with the tree-branch analysis, the $L/D = 8$ domain was simulated with end temperatures of 300 K and 80 K with 60 Hz driving frequency. All other parameters are identical to the previous 60 Hz, 300 K - 60 K branch. As a result of the commonality, the effect of temperature range alone can be isolated between the two sets of cases. By inspection, the sensitivity at 45° and 60° are reduced at 80 K. Additionally, the normalized loss is reduced for 2.5 g/s mass flow rate at 80 K. The highest mass flow cases show minimal differentiation between the two temperature fields.

In order to directly compare the effects of the three branches simulated for $\varphi_{m-p} = +30^\circ$, the loss at 135° from each flow rate is isolated for each set. The resulting maximum normalized flow losses are then plotted on common axes in Figure 5.18. The results indicated in this figure suggest that there is not a directly separable relationship between these variables isolated in the branch analysis. The general observation that can be made from the consolidated results is that tilt induced losses decrease rapidly as a function of the Reynolds number.

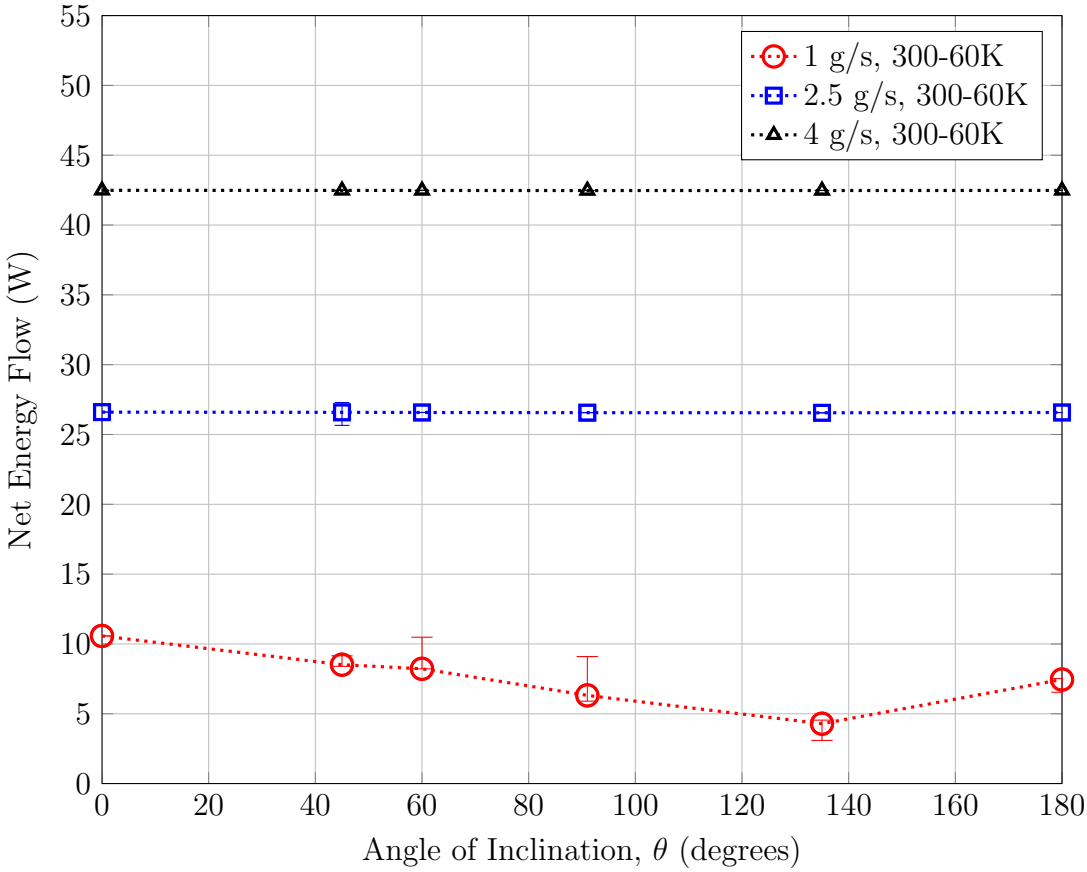

Figure 5.14: Net Cycle-averaged energy flow $\langle \dot{E} \rangle$ for 60 Hz simulations with 60 K cold end and 300 K warm end for an aspect ratio (L/D) of 8. The phase angle between mass flow and pressure is $\varphi_{m-p} = +30°$.

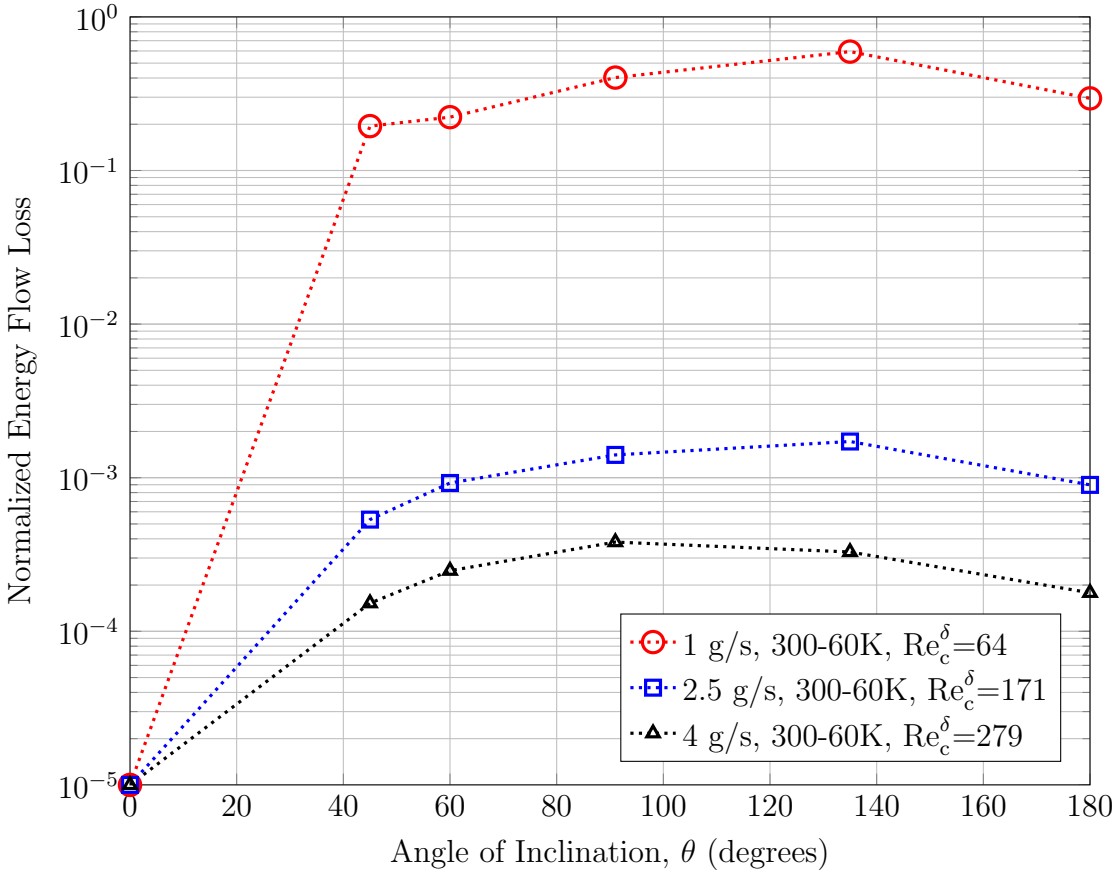

Figure 5.15: Normalized energy flow loss for 60 Hz simulations with 60 K cold end and 300 K warm end for an aspect ratio (L/D) of 8. The phase angle between mass flow and pressure is $\varphi_{m-p} = +30°$.

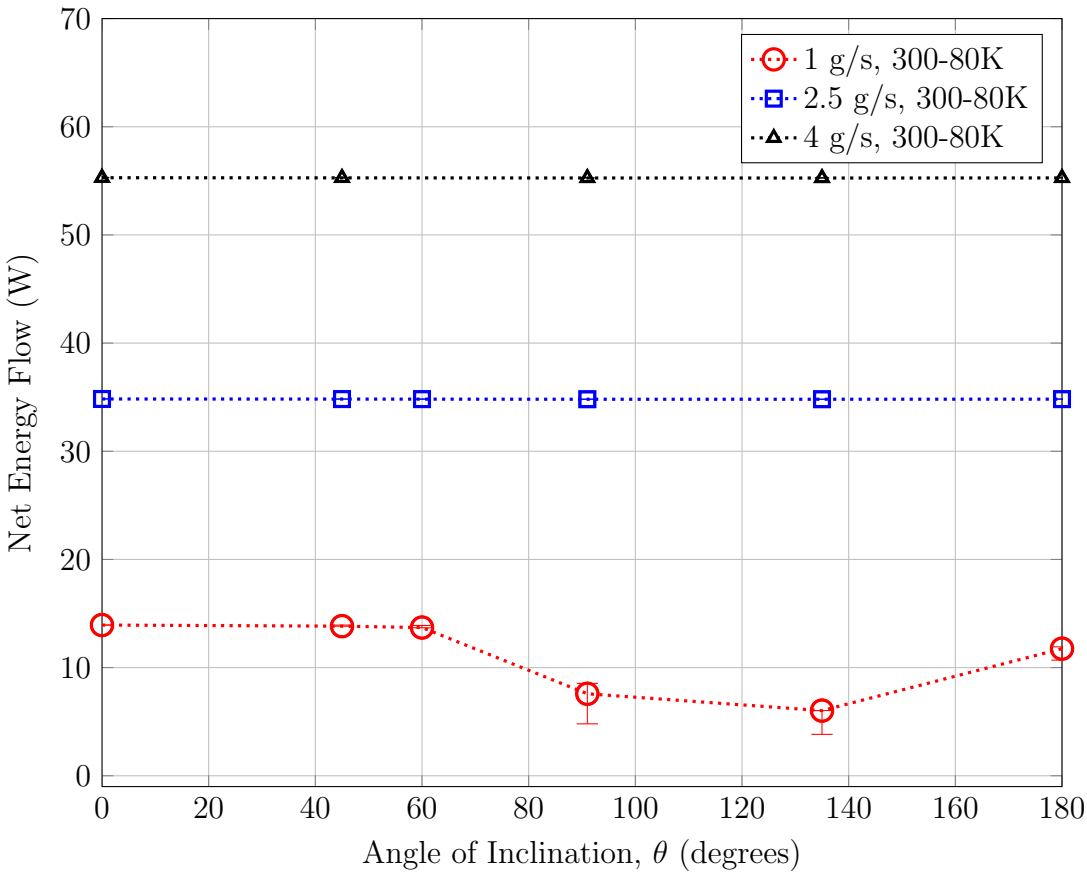

Figure 5.16: Net Cycle-averaged energy flow $\langle \dot{E} \rangle$ for 60 Hz simulations with 80 K cold end and 300 K warm end for an aspect ratio (L/D) of 8. The phase angle between mass flow and pressure is $\varphi_{m-p} = +30°$.

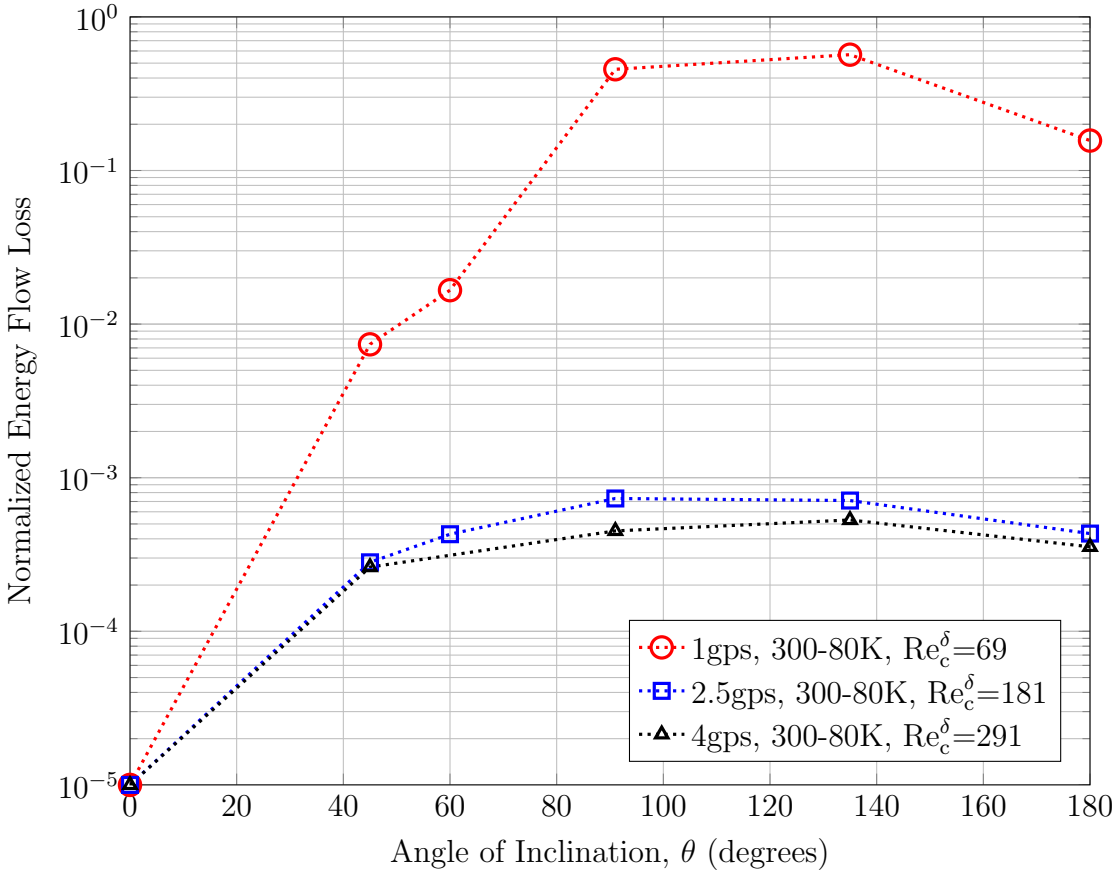

Figure 5.17: Normalized energy flow loss for 60 Hz simulations with 80 K cold end and 300 K warm end for an aspect ratio (L/D) of 8. The phase angle between mass flow and pressure is $\varphi_{m-p} = +30°$.

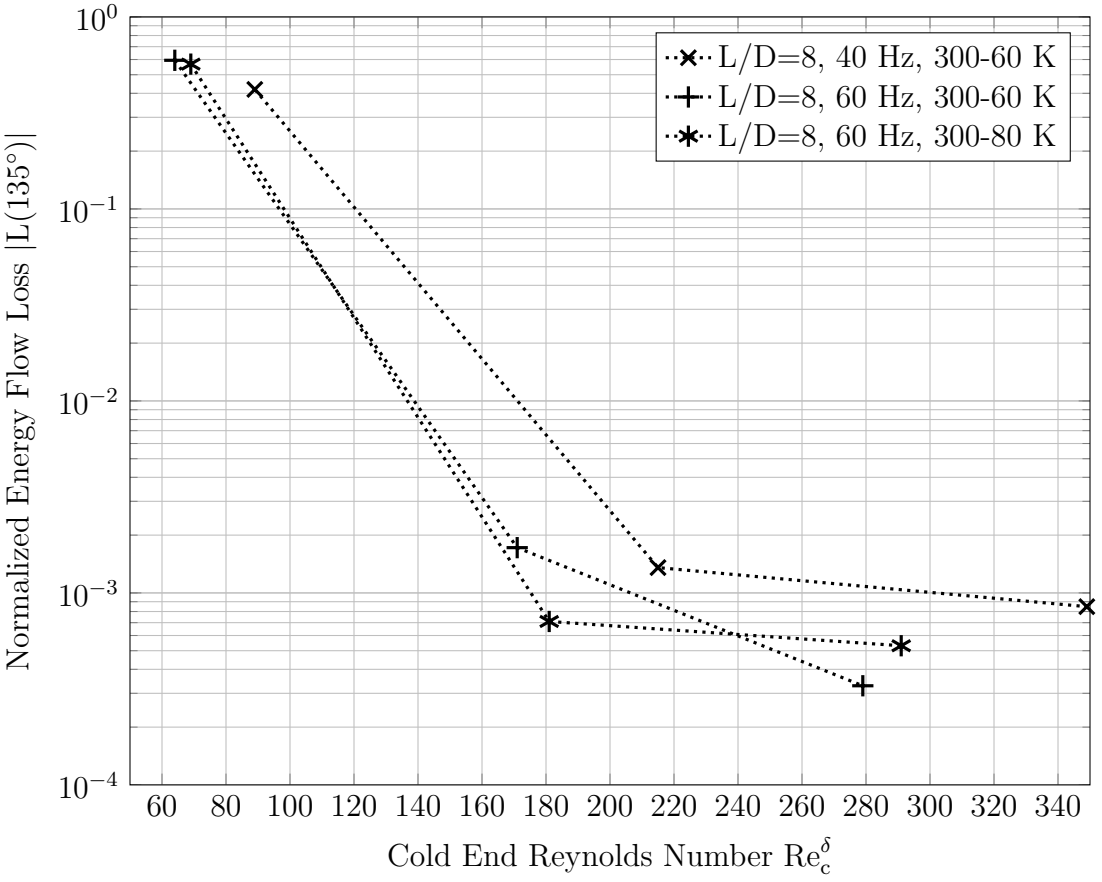

Figure 5.18: Compiled maximum losses for all simulated cases with phase relationship $\varphi_{m-p} = +30°$ plotted as a function of cold end Reynolds number Re_c^δ.

5.3.2.3 Condition 2: Cold End Mass Flow Lags Pressure by 30°

In this section, we present the results of the second portion of the parametric study where the mass-pressure phase relationship is changed to $\varphi_{m-p} = -30°$, which indicates that mass flow lags pressure. This condition is consistent with the well-known optimum design criterion for inertance tube pulse tube refrigerators, and therefore the results are most directly applicable to the design of modern pulse tubes. The relationships between mass flow and pressure are shown in Figures 5.19-5.21 for the three mass flow rate amplitudes studied for the case where the driving frequency is 60 Hz, the charge pressure is 2.0 MPa, and the pressure ratio is 1.2. Note that the scale magnitudes are different for all three figures. As indicated by the zero crossings of the two traces in each plot, the pressure crosses first indicating that mass flow lags pressure.

Following the flow of information from Section 5.3.2.3, the three components of heat transfer are delineated in Figures 5.22-5.24 for three example data sets as a function of angle with increasing mass flow rate amplitudes. The results are then grouped according their common frequency, temperature range, and pulse tube aspect ratio and plotted in terms of absolute net energy flow loss as well as the normalized angular loss coefficient. It is worth noting that the raw data presented in Figures 5.22-5.24 are directly processed from the simulation outputs, where the orientation of the z-axis in relation to the computational domain dictates that a negative energy flow is directed from the cold end to the hot end, the direction associated with positive gross cooling. In the post-processed figures that display calculated net energy flows and normalized losses, the data has been corrected such that a positive energy flow is aligned with positive gross cooling. In addition, the cycle-averaged gas conduction, wall conduction, and enthalpy flows have been corrected to account for the half-symmetry condition applied to the domain. For details, the reader is encouraged to inspect the post-processing algorithms presented in Appendix C.

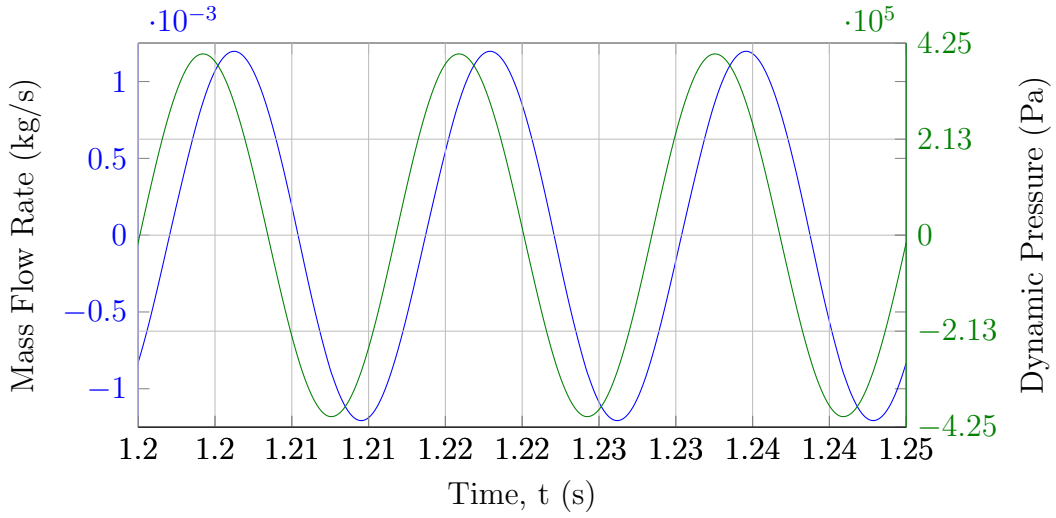

(a) Vertical (0°)

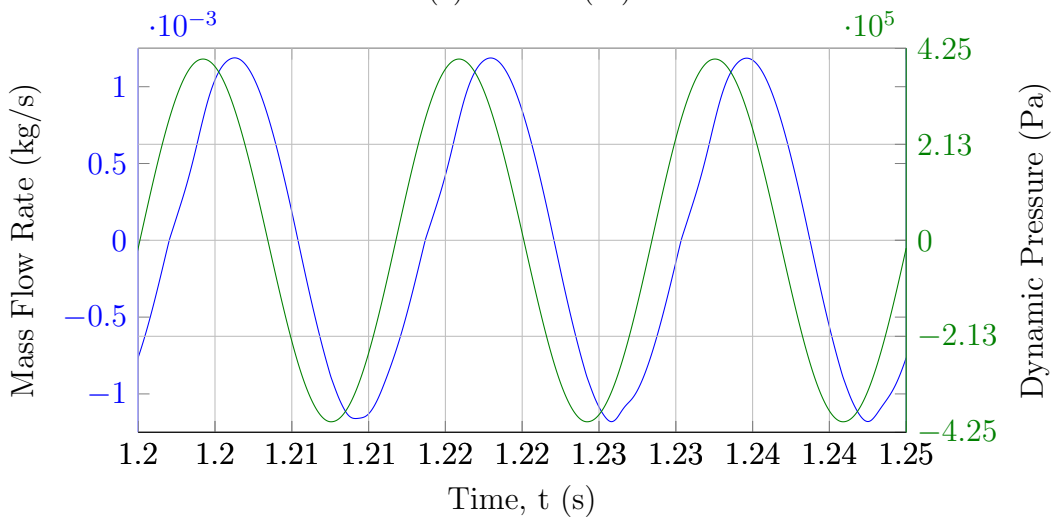

(b) Horizontal (91°)

Figure 5.19: Comparison of cold end mass flow and dynamic pressure for an $L/D = 8$ pulse tube operating between 300 K and 60 K with mass flow amplitude of 1 g/s and pressure ratio of 1.2 for a charge pressure of 2 MPa as a function of orientation angle. The phase angle between mass flow and pressure is $\varphi_{m-p} = -30°$.

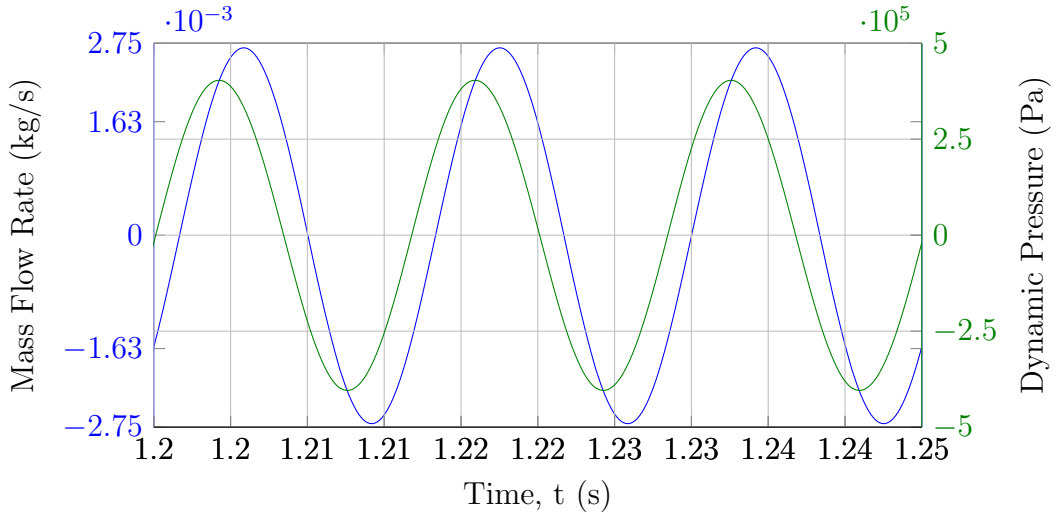

(a) Vertical (0°)

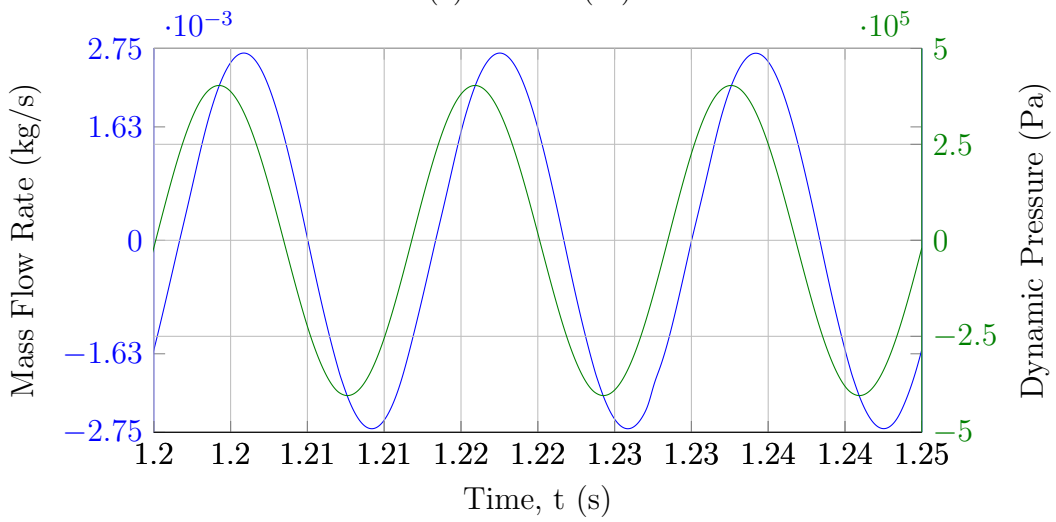

(b) Horizontal (91°)

Figure 5.20: Comparison of simulated cold end mass flow and dynamic pressure for an $L/D = 8$ pulse tube operating between 300 K and 60 K with mass flow amplitude of 2.5 g/s and pressure ratio of 1.2 for a charge pressure of 2 MPa as a function of orientation angle. The phase angle between mass flow and pressure is $\varphi_{m-p} = -30°$.

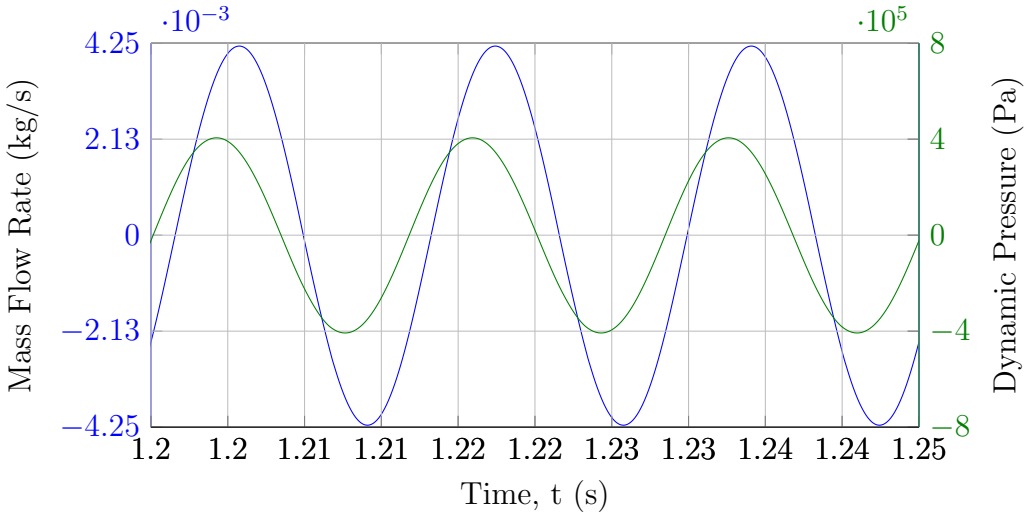

(a) Vertical (0°)

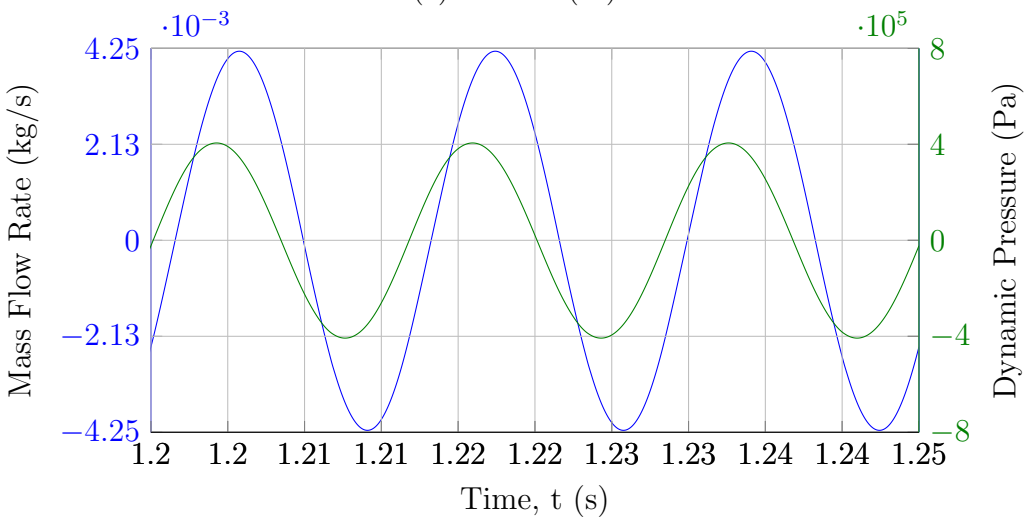

(b) Horizontal (91°)

Figure 5.21: Comparison of simulated cold end mass flow and dynamic pressure for an $L/D = 8$ pulse tube operating between 300 K and 60 K with mass flow amplitude of 4 g/s and pressure ratio of 1.2 for a charge pressure of 2 MPa as a function of orientation angle. The phase angle between mass flow and pressure is $\varphi_{m-p} = -30°$.

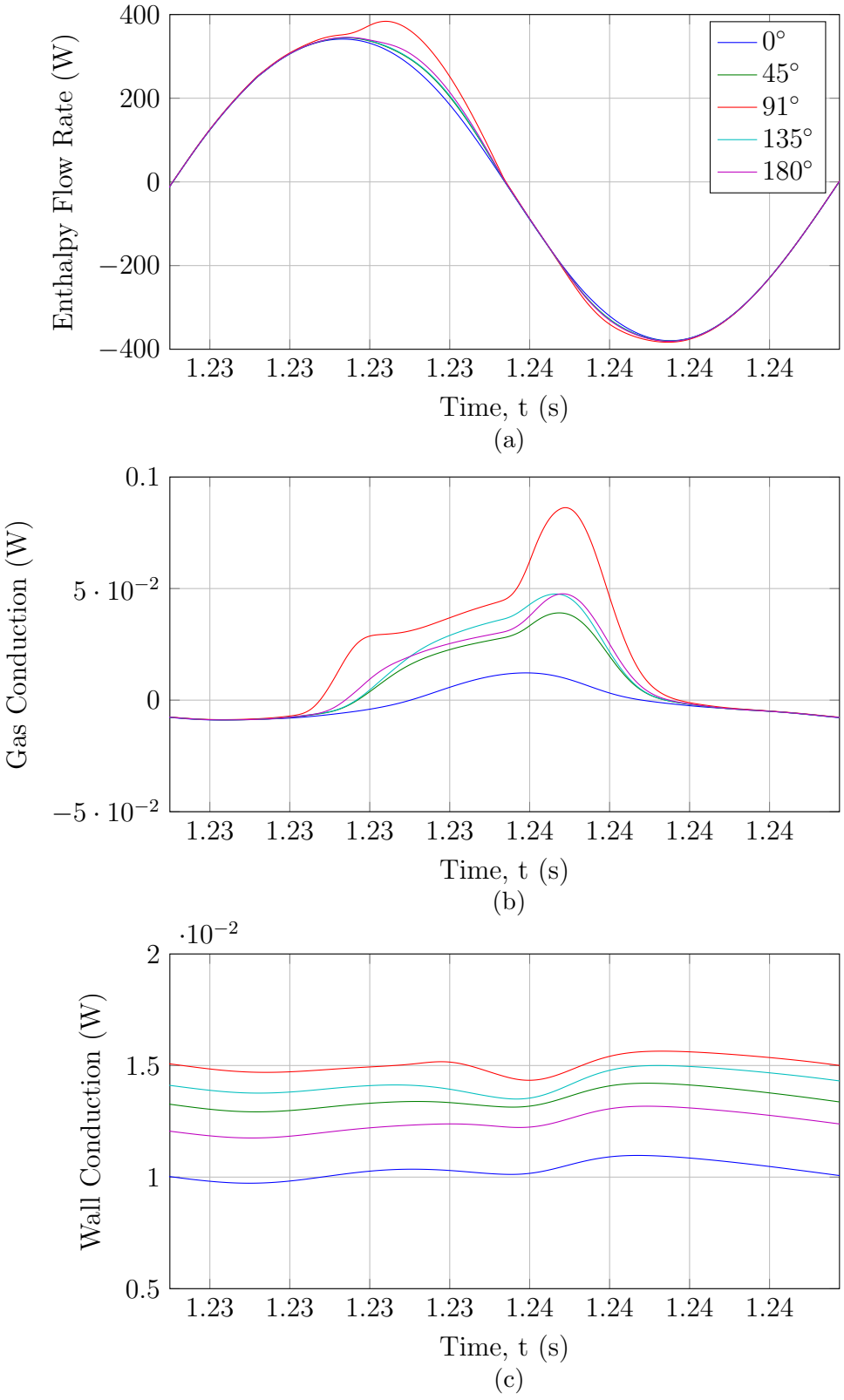

Figure 5.22: Comparison of simulated energy flows for an $L/D = 8$ pulse tube operating between 300 K and 60 K with mass flow amplitude of **1 g/s** as a function of orientation angle. Positive energy flow denotes parasitic flow from hot to cold. Note that the legend in (a) applies to (a)-(c).

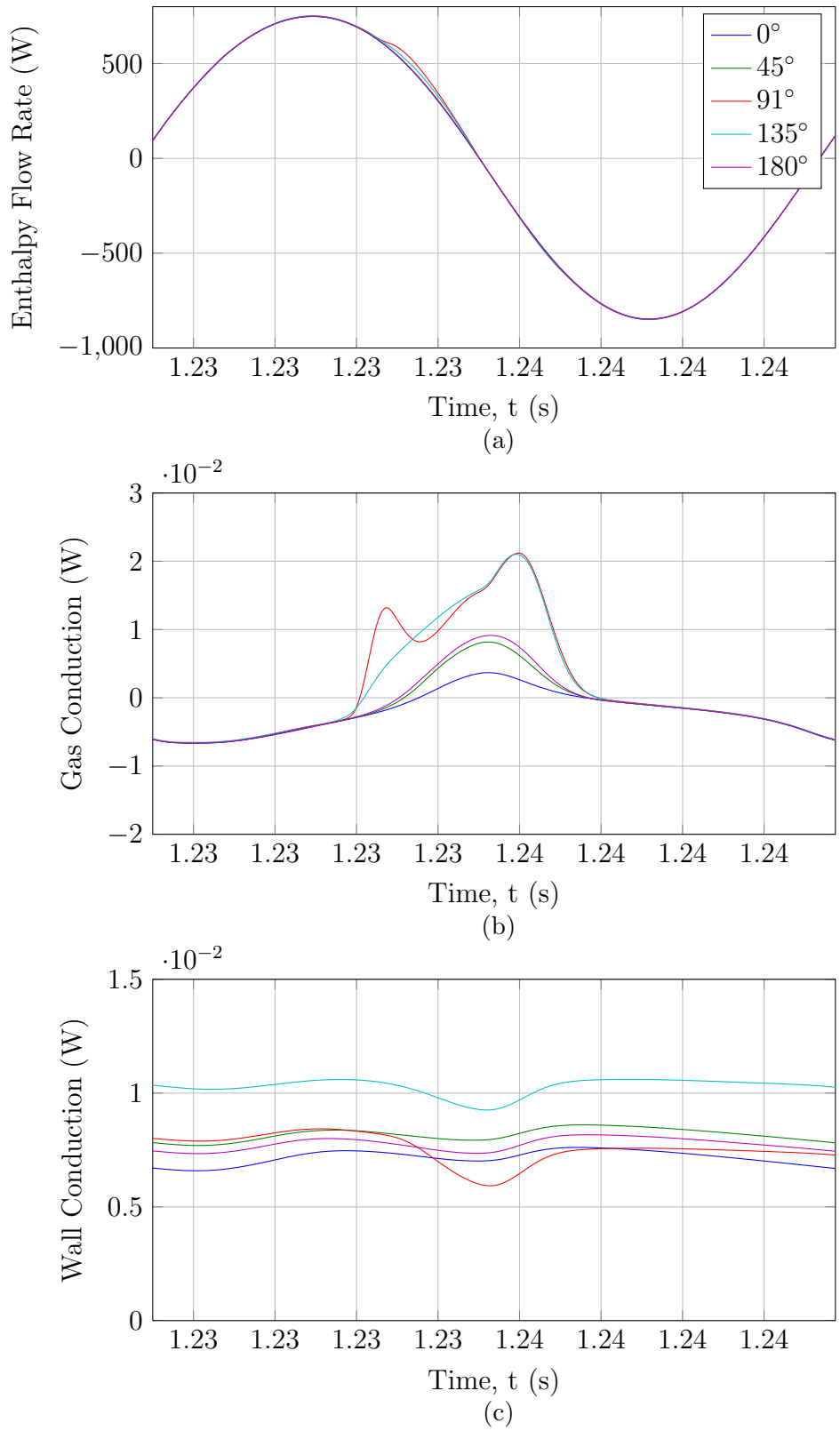

Figure 5.23: Comparison of simulated energy flows for an $L/D = 8$ pulse tube operating between 300 K and 60 K with mass flow amplitude of **2.5 g/s** as a function of orientation angle. Positive energy flow denotes parasitic flow from hot to cold. Note that the legend in (a) applies to (a)-(c).

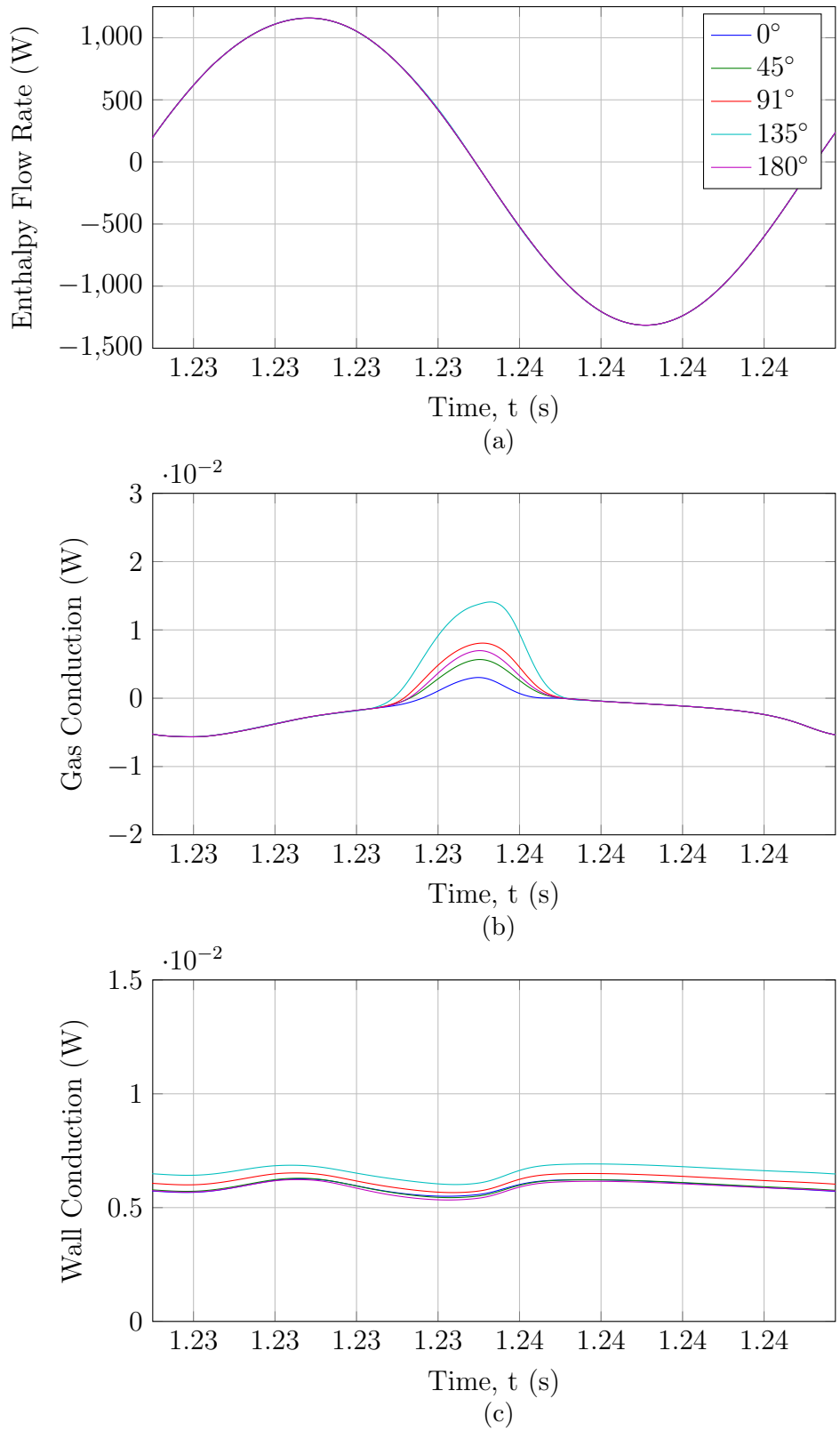

Figure 5.24: Comparison of simulated energy flows for an $L/D = 8$ pulse tube operating between 300 K and 60 K with mass flow amplitude of **4 g/s** as a function of orientation angle. Positive energy flow denotes parasitic flow from hot to cold. Note that the legend in (a) applies to (a)-(c).

There are few notable differences in the delineated energy terms for the two phase angles studied. Perhaps the most interesting observation is the behavior of the 91° traces for all three mass flow amplitudes, which varies significantly for 1 g/s and 2.5 g/s mass flow rates, and then is brought back under control as the mass flow is increased to 4 g/s. Another notable conclusion from the transient energy flow plots is that the gas conduction term is strongly influenced by the mass flow rate. The result is an order of magnitude reduction in the parasitic gas conduction energy flow as the flow rate increases from 1 g/s to 4 g/s.

Given the utility of the results presented in this section compared to the cases where mass flow leads pressure, the number of parametric branches explored here is significantly expanded, therefore the bulk of the data from the parametric study is presented in the following figures. The first set of data presented in Figures 5.25 and 5.26 identifies the cycle-averaged net energy flows for a pulse tube with aspect ratio L/D=8 operating at 60 Hz between 300 K and 60 K.

Inspection of Figures 5.25 and 5.26 shows a similar set of trends to those found in the directly comparable data set computed for $\varphi_{m-p} = +30°$ as shown in Figures 5.14 and 5.15. Previous research concluded based on elevated temperature experiments that orientation sensitivity was not a function of phase angle [3]. Although the trends are similar, the magnitude of the normalized loss is higher for $-30°$ than for $+30°$ cold end phase. In addition, the increase of Reynolds number has a smaller impact on the flow stability as evidenced by the two order of magnitude increase in the normalized loss compared to the previous cases at $+30°$ phase. This indicates that the conclusion that phase angle does not affect orientation sensitivity is not appropriate in all possible sets of operating parameters. Another interesting observation from Figures 5.25-5.26 is the shift in the maximum normalized loss from 91° towards 135° as mass flow increases from 1 g/s to 4 g/s. Most reported data sets from experimental coolers indicate that peak instability occurs at 135°.

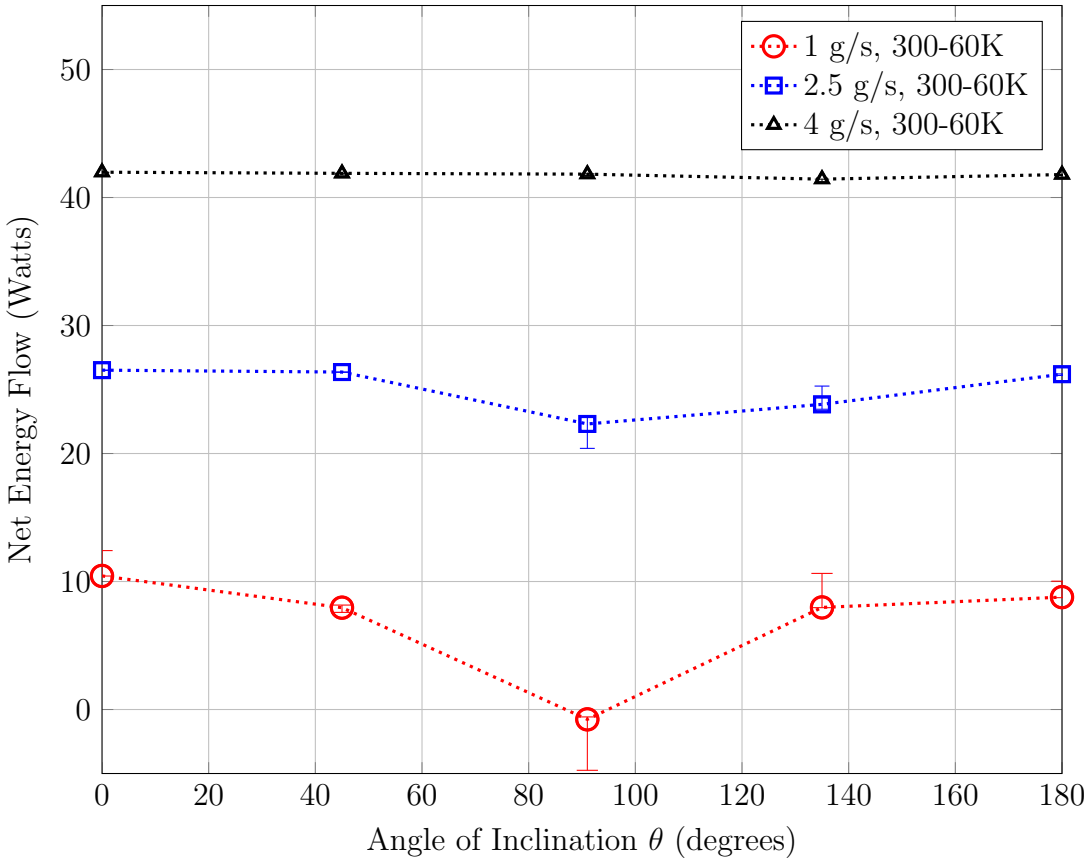

Figure 5.25: Net Cycle-averaged energy flow $\langle \dot{E} \rangle$ for 60 Hz simulations with 60 K cold end and 300 K warm end for an aspect ratio (L/D) of 8. The phase angle between mass flow and pressure is $\varphi_{m-p} = -30°$.

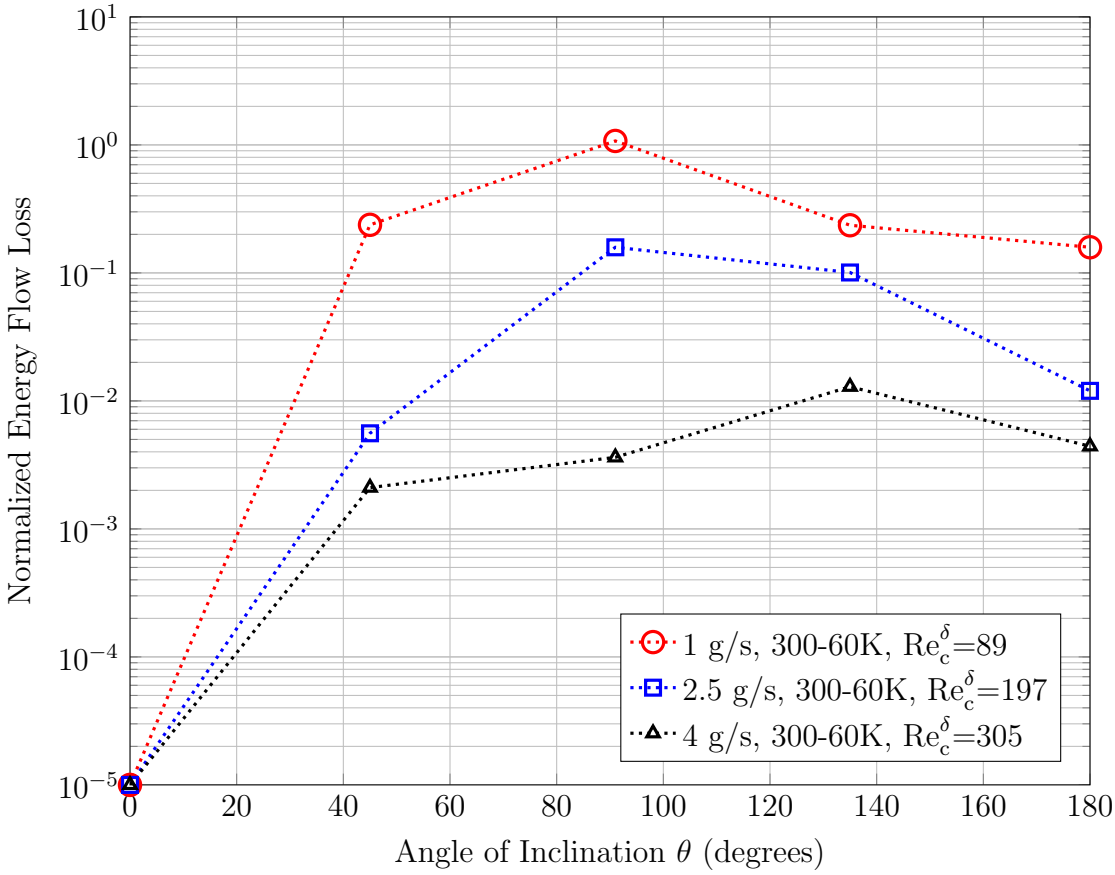

Figure 5.26: Normalized energy flow loss for 60 Hz simulations with 60 K cold end and 300 K warm end for an aspect ratio (L/D) of 8. The phase angle between mass flow and pressure is $\varphi_{m-p} = -30°$.

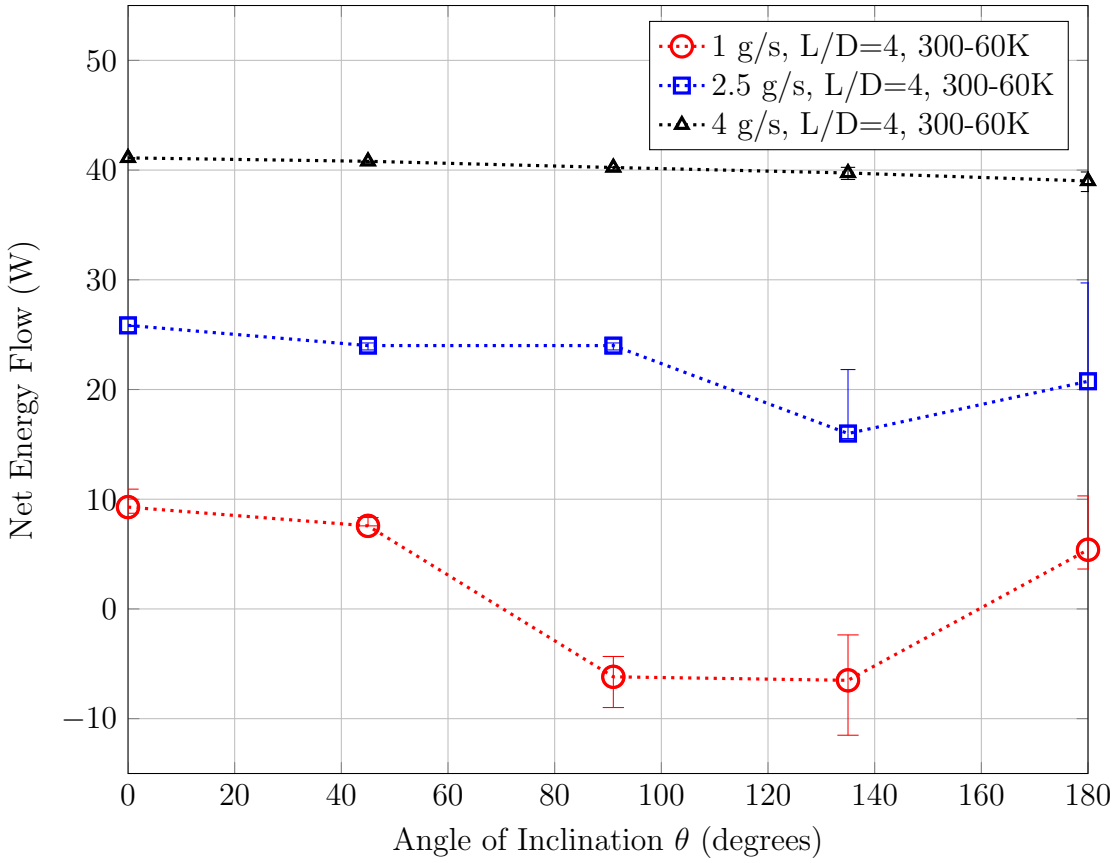

Figure 5.27: Net Cycle-averaged energy flow $\langle \dot{E} \rangle$ for 60 Hz simulations with 60 K cold end and 300 K warm end for an aspect ratio (L/D) of 4. The phase angle between mass flow and pressure is $\varphi_{m-p} = -30°$.

The next set of simulations addresses a design decision that is commonly experienced by pulse tube designers. It is common to compute an objective volume for the pulse tube based on cold end swept volume, but then to have a decision as to what length and diameter is appropriate for the conditions. This data set, shown in Figures 5.27 and 5.28 reports the computed losses for a pulse tube with operating conditions identical to the previous set (60 Hz, 300-60 K, -30° phase) for a pulse tube with identical volume but significantly reduced aspect ratio L/D=4.

The results reported in Figures 5.27 and 5.28 indicate the benefit to implementing the maximum pulse tube aspect ratio possible as it pertains to orientation sensitivity. Nonetheless, there are situations where mechanical design constrains the maximum

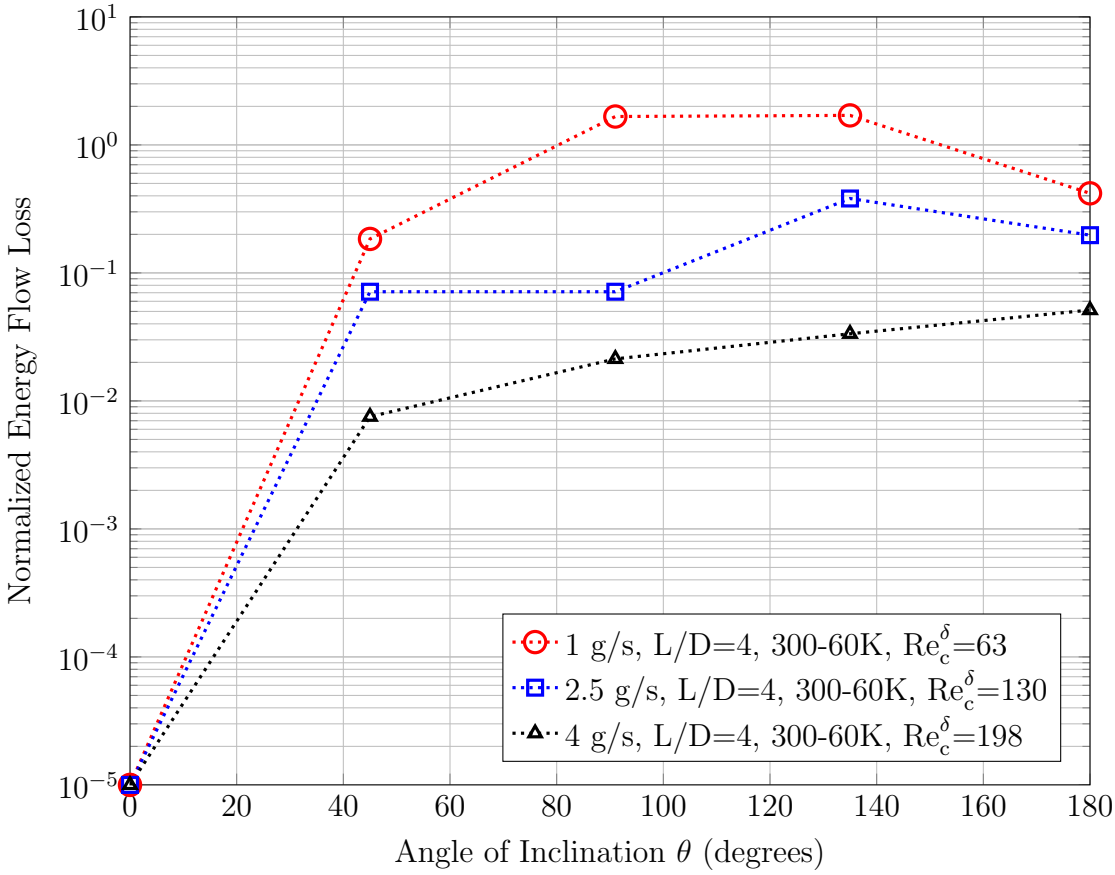

Figure 5.28: Normalized energy flow loss for 60 Hz simulations with 60 K cold end and 300 K warm end for an aspect ratio (L/D) of 4. The phase angle between mass flow and pressure is $\varphi_{m-p} = -30°$.

pulse tube length, therefore this set of data is a relevant reference for the orientation sensitivity that can be expected when implementing lower pulse tube aspect ratios. In all simulated cases, the larger pulse tube aspect ratio outperforms the smaller. This is an effect that cannot be captured with 1-D modeling codes.

The remaining cases address staged pulse tubes consistent with many cascaded PTR designs currently used to achieve temperatures lower than 4 K in a three stage design. The intermediate stage is commonly designed with end temperatures of 80 K and 20 K. Scoping studies in REGEN 3.3 have indicated that these are the global optima for staging temperatures to reach 4 K based on minimized exergy destruction. Figures 5.29 and 5.30 present the results of an L/D=8 pulse tube operating between 80 K and 20 K with a driving frequency of 45 Hz. This frequency was chosen as it is closer to the optimal drive frequency for this temperature range to maximize stage COP. Mass flow rates of 1 g/s to 4 g/s were chosen for consistency with the previously reported simulation sets.

The results of the energy flow computations presented in Figures 5.29 and 5.30 show significant deviation from the trends observed in higher temperature pulse tubes. One notable feature is the presence of large losses regardless of Reynolds number. The second notable observation is the size of the error bars, indicating the presence of significant instability in angles as low as 45° for 1 g/s. Four of the design points indicate a pulse tube that actually causes parasitic losses, resulting in a negative gross cooling capacity. This set of data demonstrates the strong influence of temperature range on the convective stability of the pulse tube design. Note that the end-to-end temperature difference is only 60 K compared to the 220 K - 240 K present in the upper stage models, though the density difference is higher for the low temperature case.

To illustrate the instability apparent in low temperature simulations, Figure 5.31 plots contours of temperature along with velocity vectors along the symmetry plane

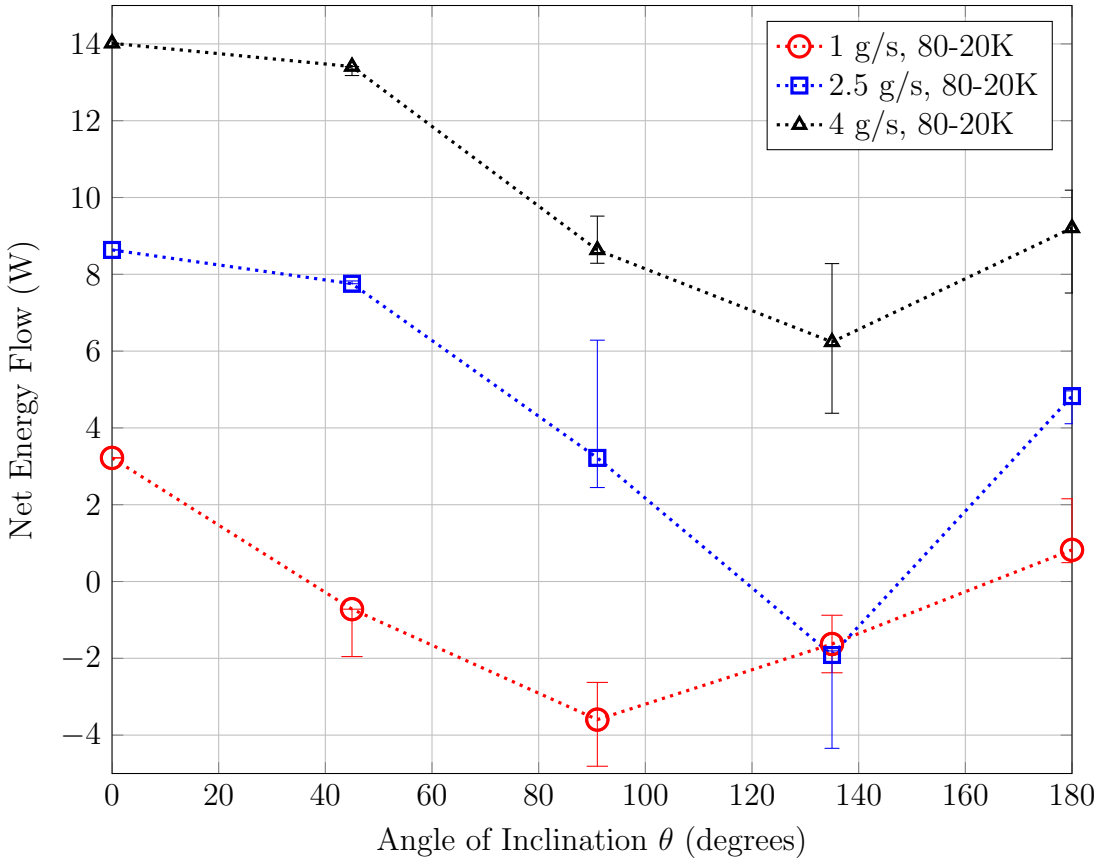

Figure 5.29: Net Cycle-averaged energy flow $\langle \dot{E} \rangle$ for 40 Hz simulations with 20 K cold end and 80 K warm end for an aspect ratio (L/D) of 8. The phase angle between mass flow and pressure is $\varphi_{m-p} = -30°$.

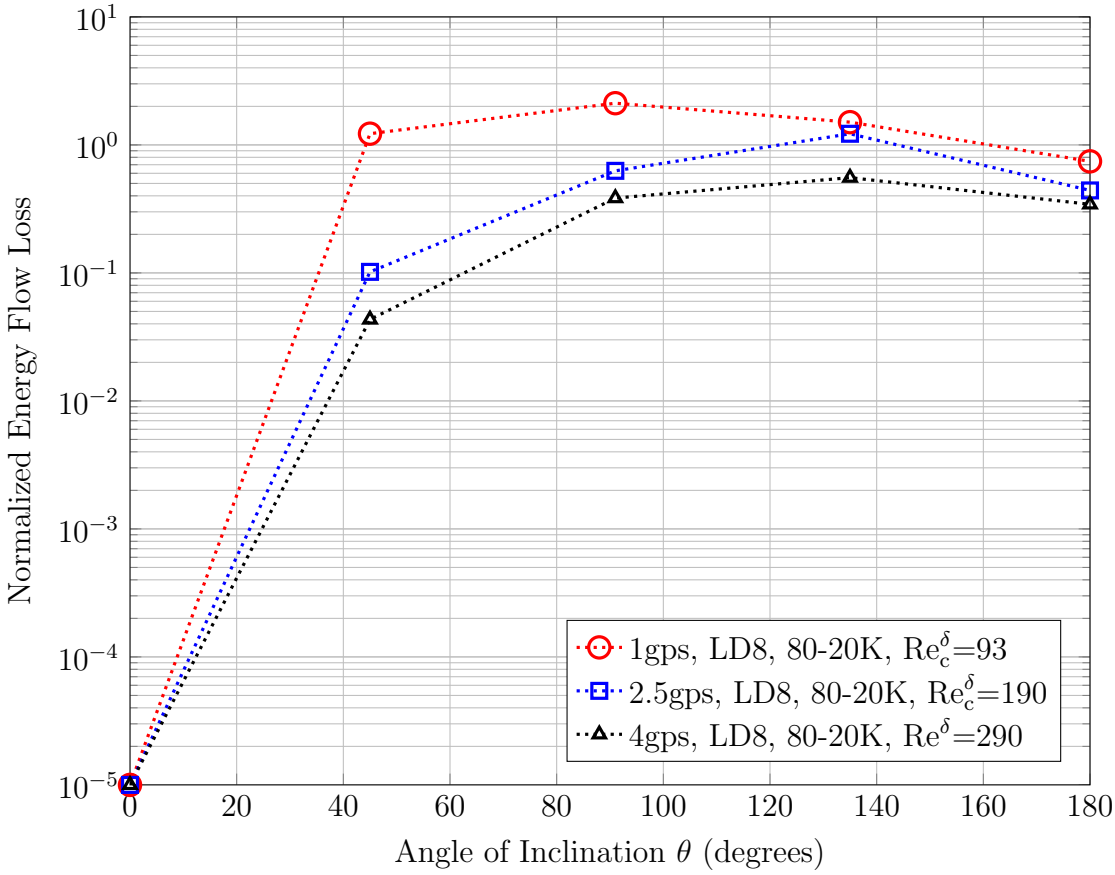

Figure 5.30: Normalized energy flow loss for 40 Hz simulations with 20 K cold end and 80 K warm end for an aspect ratio (L/D) of 8. The phase angle between mass flow and pressure is $\varphi_{m-p} = -30°$.

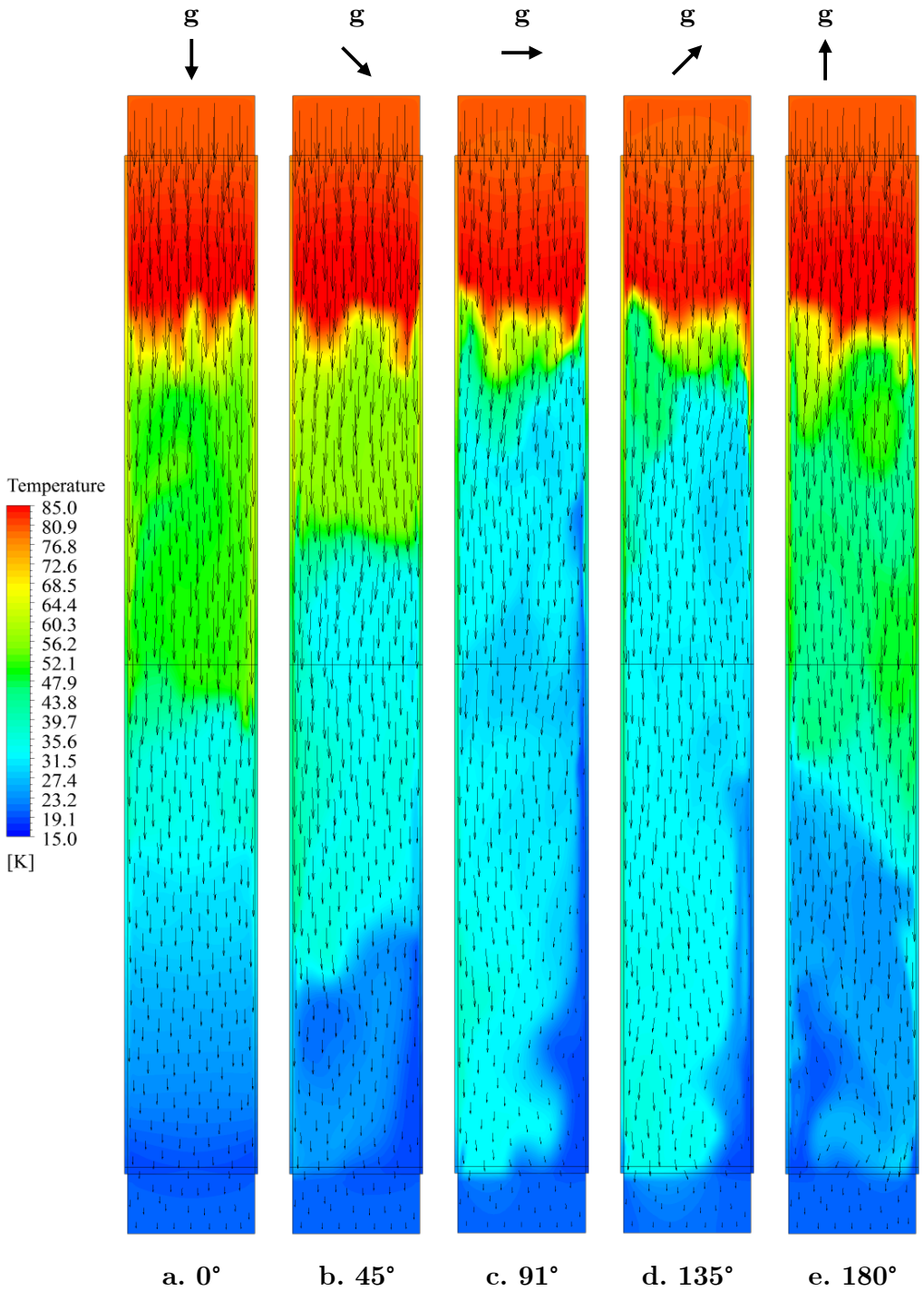

Figure 5.31: Contours of temperature and velocity vectors on the symmetry plane for an L/D=8, 80 K to 20 K pulse tube with 2.5 g/s mass flow amplitude.

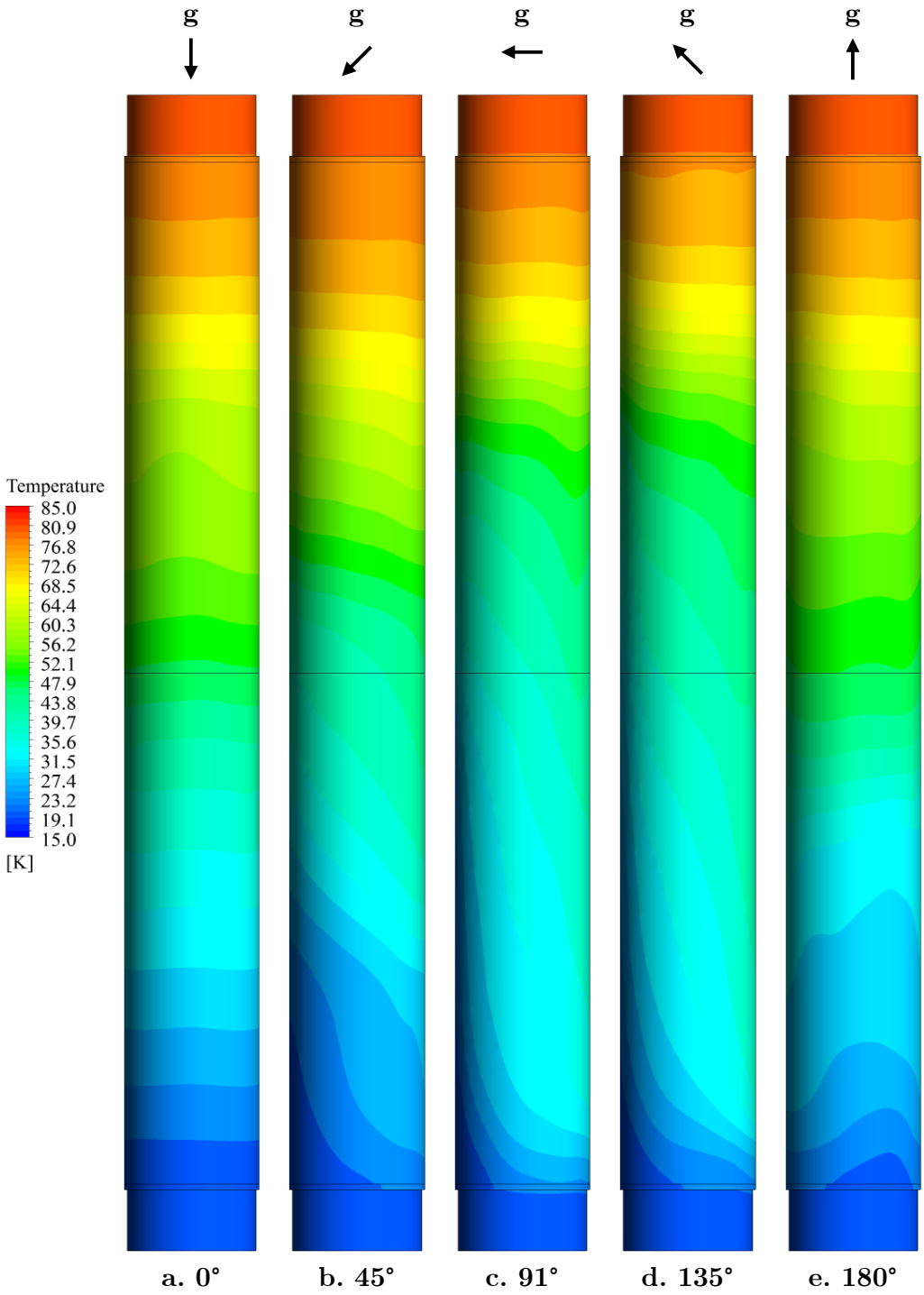

Figure 5.32: Contours of temperature on the pulse tube wall for an L/D=8, 80 K to 20 K pulse tube with 2.5 g/s mass flow amplitude.

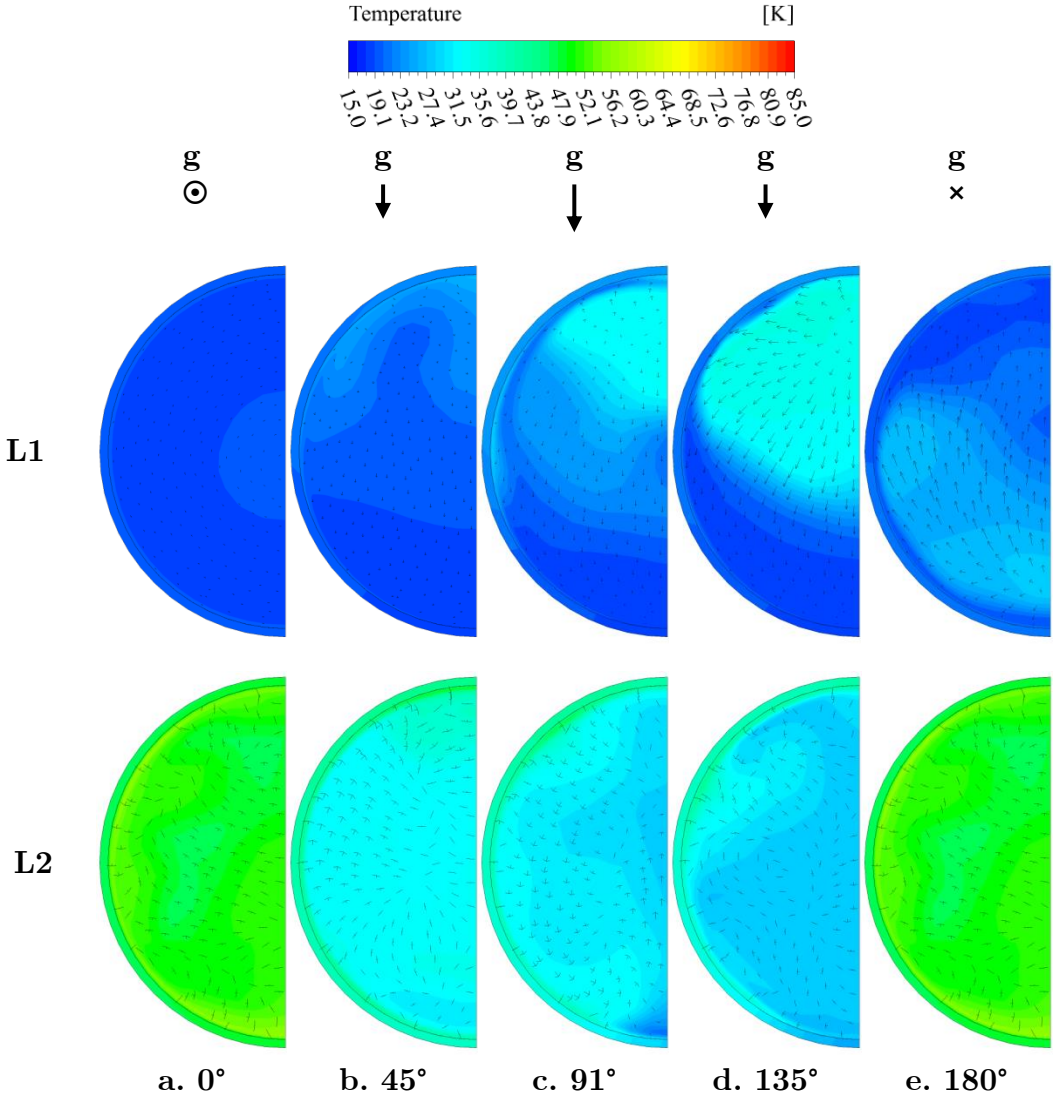

Figure 5.33: Contours of temperature and velocity vectors on radial slices at the cold end and center of the pulse tube for an L/D=8, 80 K to 20 K pulse tube with 2.5 g/s mass flow amplitude.

for all angles simulated, where the mass flow amplitude is 2.5 g/s. The temperature profiles at 91° and 135° indicate thorough mixing of the gas in the pulse tube, and therefore complete loss of temperature stratification. Observation of the corresponding data points in Figure 5.30 confirms that cooling power has completely deteriorated. In point of fact, the existence of any remaining temperature gradient is enforced solely by the isothermal wall conditions that must be satistified numerically. In practice, this mixing would result in a change in the cold end temperature.

Contours are additionally presented for slices perpendicular to the symmetry plane at locations L1 (the cold end) and L2 (the center of the pulse tube) in Figure 5.33, and on the walls of the domain in Figure 5.32. The temperature profile slices in Figure 5.33 illustrate the three-dimensionality of the flow field. The significant variation in the flow field as a function of angle and x-position indicates why an axisymmetric simulation would misrepresent the flow field. The asymmetric temperature profile on the walls also confirms the need for 3-D modeling techniques as well as confirming convergence of the model. The relatively high heat capacity of the walls causes the time constant to be much longer than the period of oscillation, therefore the propagation of thermal gradient from the cold end to the hot indicates that a sufficient flow time has passed to come into equilibrium.

The final data set simulated represents an optimized third stage pulse tube operating between 20 K and 4 K. The driving frequency is set to 25 Hz, indicative of the thermodynamic preference for frequency to decrease along with stage temperature. This data set was limited to 1 g/s and 2.5 g/s flow rates for the basic reason that 4 g/s flow rates are seldom encountered in stage 3 pulse tubes of the volume simulated as a result of the gas having to traverse three regenerator stages prior to entering the stage 3 pulse tube cold end.

The results for the 20 K to 4 K simulations bear resemblance to the trends observed for 80 K to 20 K results. Performance is entirely degraded for angles greater than

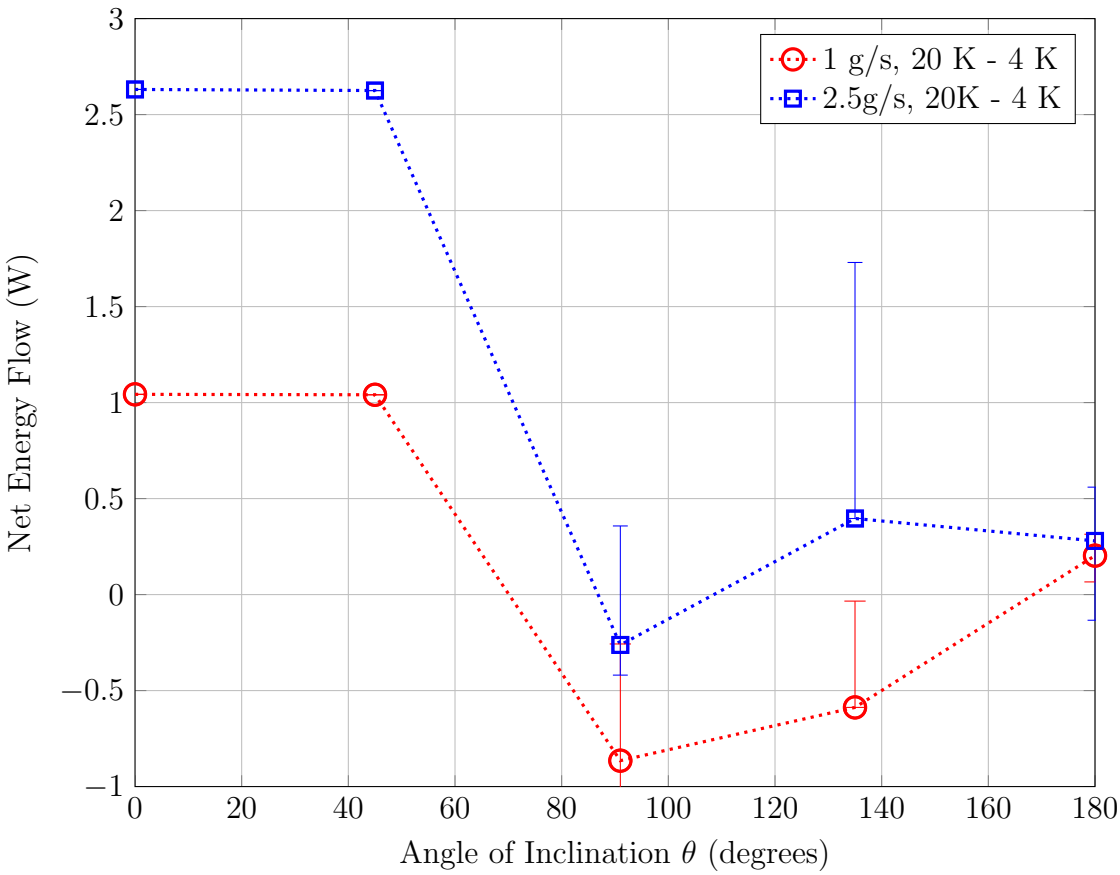

Figure 5.34: Net Cycle-averaged energy flow $\langle \dot{E} \rangle$ for 25 Hz simulations with 4 K cold end and 20 K warm end for an aspect ratio (L/D) of 8. The phase angle between mass flow and pressure is $\varphi_{m-p} = -30°$.

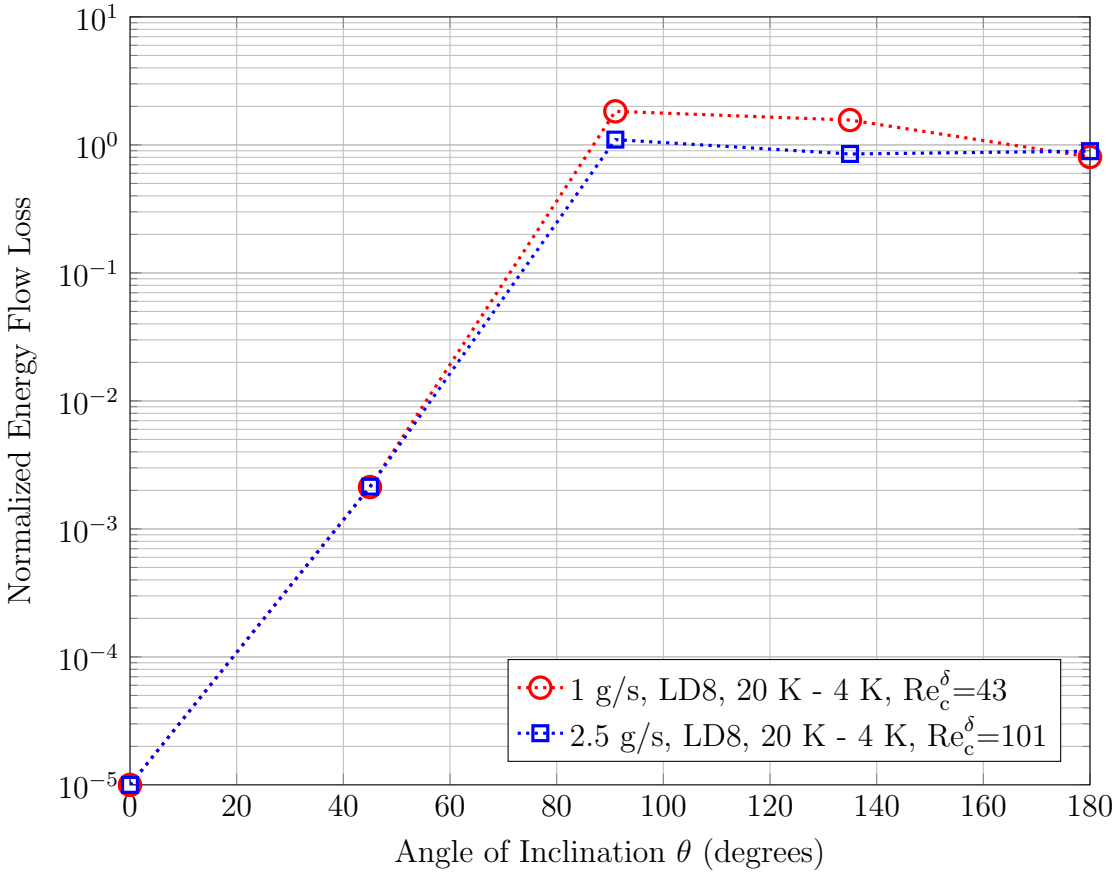

Figure 5.35: Normalized energy flow loss for 25 Hz simulations with 4 K cold end and 20 K warm end for an aspect ratio (L/D) of 8. The phase angle between mass flow and pressure is $\varphi_{m-p} = -30°$.

45°. The size of the error bars indicate very unstable solutions at large angles of inclination, but relatively stable performance below 45°. It should be noted that although the temperature difference is only 16 K across this pulse tube, the density imbalance is still larger than all of the preceding cases due to the nonlinearity of the temperature-dependent density illustrated in Figure 3.5.

In comparison to the 80 K to 20 K results, the Reynolds numbers have decreased by nearly a factor of two for identical flow rates, a result of the temperature dependence of the gas properties. In this case, the Reynolds number could feasibly be increased by decreasing the diameter of the pulse tube rather than increasing the mass flow rate. Aspect ratios of 10 or higher should be investigated for good orientation independence at 4 K. The results should not be taken to indicate that stable operation at off-axis orientation is not possible at 4 K. The instability reported here is a result of the combination of mass flow and cross-sectional area chosen for the design. The results do; however, indicate the need for very careful consideration of the design parameters at extremely low temperatures. Stability can likely be increased at 4 K by increasing the operating frequency as well, though thermodynamic performance is likely to decrease as a result. This trade may be worthwhile in the event that orientation insensitivity the critical design parameter at 4 K and efficiency can be slightly sacrificed in the cold end down orientation.

CHAPTER VI

MODEL VALIDATION AND ANALYSIS OF COMBINED RESULTS

6.1 Introduction

Computational Fluid Dynamics (CFD) studies are a cost-effective means of approaching thermal/fluid problems with solutions that would be difficult or impossible to derive with analytical methods. With reasonable user know-how, detailed results can be generated for nearly any problem of interest within computational limits. Although CFD codes never make calculation mistakes, there are underlying principles in the models that make assumptions about the flow, i.e., the theory behind the differential equations being numerically solved. Strict confidence in the results gleaned from CFD can only be inspired when the model has been properly validated and/or correlated. Validation can come in many forms, but always relies on either:

- An analytical solution to a limiting case for which the accuracy is known.
- Experimental data that can be directly compared with CFD results that brackets the range of model validity.

As indicated in Chapter 2, closed form analytical solutions to the problem of interest in this dissertation are not feasible. The task of validation is then left to comparison with experimentally measured data.

In order to validate the system-level and parametric results presented in Chapters 4 and 5, data sets were collected for three commercial space and tactical pulse tube cryocoolers in the vertical, cold end down configuration (0°) and horizontal (90°) orientations. In order to replicate these results using the CFD code developed in the

previous sections, the boundary conditions at the cold heat exchanger and warm heat exchanger were needed. The size of the flow passages, the thermal intercepts, and the generally high cost of the experimental (R&D) coolers precluded the possibility of incorporating mass flow and pressure sensors within the welded regions of the cold head. In order to gather these boundary conditions, a full system Sage model (See Section 3.1.2) was developed and correlated to the experimental data collected in the vertical position. When the model is capable of replicating the system-level performance over a wide range of operating conditions, it can be assumed with high confidence that the flow fields computed by the Sage model match the experimental values, within an error proportional to the accuracy of the model.

Primary validation was completed based on orientation testing results gathered from a commercial cryocooler manufacturer on a moderate capacity single stage coaxial pulse tube cryocooler (ITPTR) with no-load temperature of 41.3 K. The validation cooler was driven with an operating frequency of 60 Hz over a range of input electrical power to the pressure wave generator (PWG) spanning from 50 W to 160 W. Precise details regarding the experimental data collection on the validation cooler are given in the following section. A computational domain consisting of the CHX, pulse tube, pulse tube wall, and WHX was constructed in accordance with the method presented in Chapter 5. Slight modification to the domain was necessary as a result of the coaxial geometry of the reference PTR. The flow path into the cold heat exchanger from the regenerator is through an array of small radially drilled holes. In addition, the inertance tube makes a sharp 90° turn at the exit of the warm heat exchanger. These interesting flow boundaries warranted the use of a slightly extended computational domain including the features that deviate from the linear PTR configuration. A schematic representation of the coaxial cooler geometry and the modified computational domain are shown in Figure 6.1.

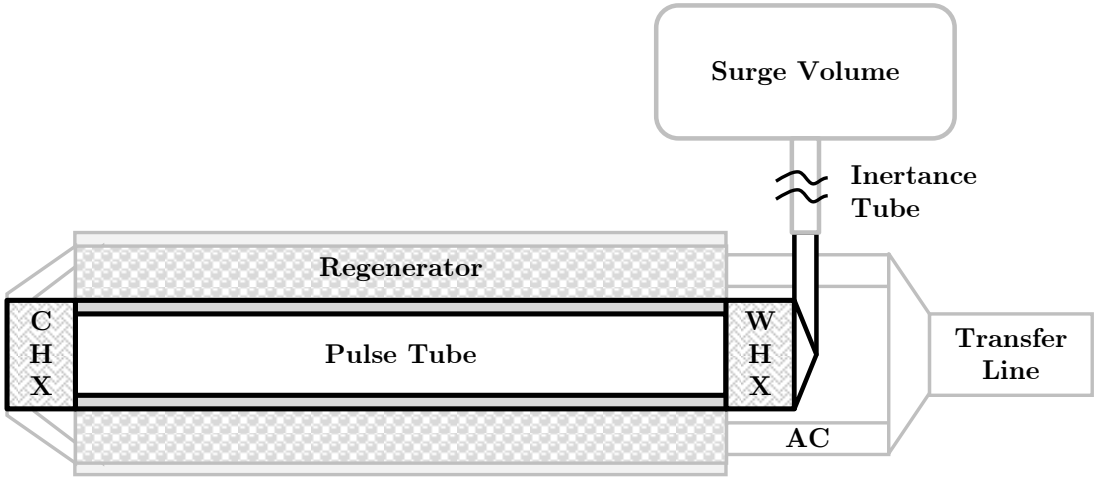

(a)

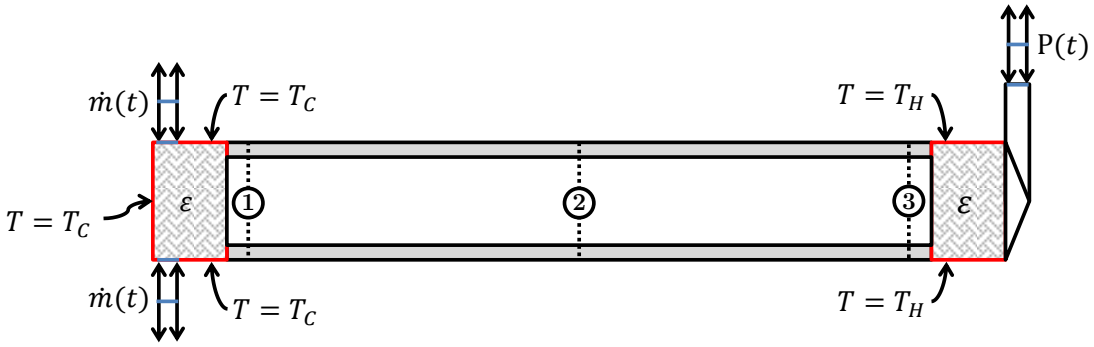

(b)

Figure 6.1: Schematic and computational domain representing the experimental coaxial cryocooler used for model validation.

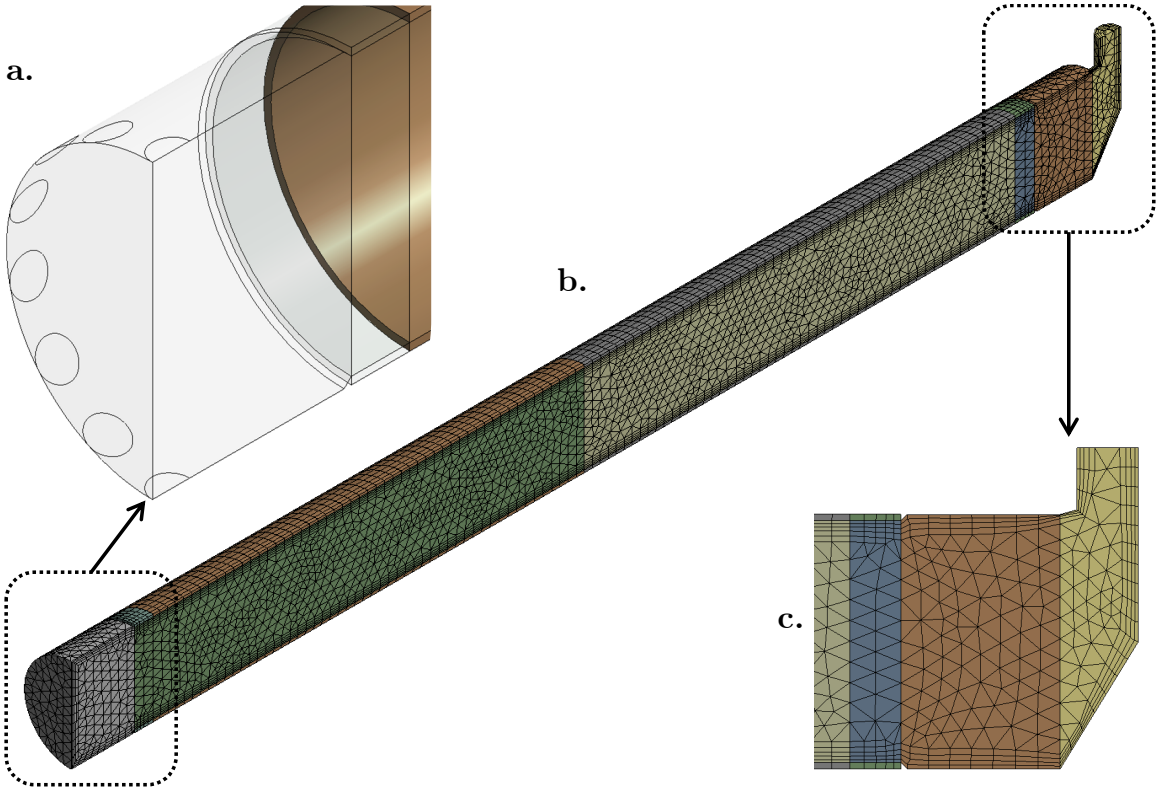

Figure 6.2: Computational mesh used to simulate the coaxial PTR for CFD model validation. **a.** Detail view of mass flow inlet holes applied to the cold heat exchanger. **b.** Overview of the entire grid. **c.** Detail view of the warm heat exchanger to inertance tube transition treatment.

In order to accommodate the complex geometries included in the transitions of the experimental PTR, the meshing methodology was slightly modified to incorporate tetrahedral elements. The conical features present cannot be approximated by purely prismatic cells without eliminating the boundary layer meshing critical to the model accuracy. The resulting mesh used to simulate the experimental coaxial cooler is shown in Figure 6.2 [93].

Oscillatory mass flow rate amplitudes at the cold heat exchanger are extracted from the correlated Sage model in the form of a four term Fourier series described by Equation 6.1.

$$\widetilde{\dot{m}}(t) = \sum_{n=1}^{4} \dot{M}_n \cos(\omega n t + \varphi_{mn}) \tag{6.1}$$

$$\widetilde{P}(t) = \sum_{n=1}^{4} P_{d,n} \cos(\omega n t + \varphi_{pn}) \tag{6.2}$$

The first harmonic $n = 1$ was stripped from the Sage solutions and implemented in a UDF to control the mass flow inlet and pressure outlet boundary conditions shown in Figure 6.1b. The remainder of the modeling methodology incuding solver settings, solution strategy, and convergence criteria is identical to that presented in Chapter 5.

6.2 Measurement Methodology

Orientation testing results were gathered from a commercial cryocooler manufacturer on a moderate capacity single stage coaxial pulse tube cryocooler (ITPTR) with no-load temperature of 41.3 K known as the Raytheon Dual Use Cooler (DUC). The Dual Use Cooler was designed for cross-functionality as both a space and tactical cryocooler with common thermodynamic design but different packaging based on application. Orientation sensitivity data and key geometry and operating parameters for a research and development brassboard (v4) DUC cooler were shared as part of an ongoing collaboration between Georgia Tech and Raytheon Space and Airborne Systems on the investigation of orientation dependence in pulse tubes. The validation cooler was driven with an operating frequency of 60 Hz [97, 98], using helium-4 (^{4}He) over a range of input electrical power to the pressure wave generator (PWG) spanning from 50 W to 160 W. The annular regenerator was packed with a proprietary high-performance advanced regenerator material composed of composite "pucks" which are used in place of traditional plain-weave stainless steel screens [99]. The Research and Development brassboard (v4) model DUC is depicted in Figure 6.3.

The manufacturer's safety protocol and quality control system limited the measurement of performance to 0° and 90° ± 0.1° where the assembly could be rigidly mounted to a surface. In order to maximize the scope over which the CFD model could be validated, three input power settings (corresponding to compressor stroke) were investigated. For each input power, the cold tip temperature was controlled in

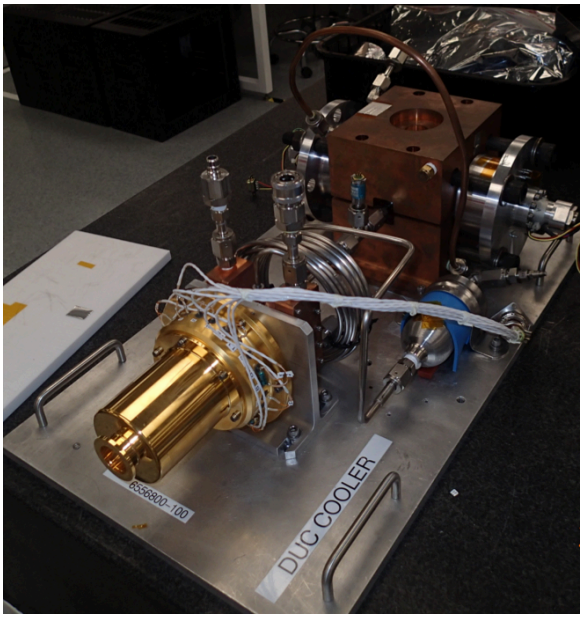

(a)

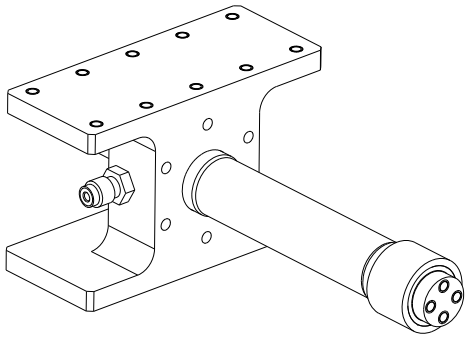

(b)

Figure 6.3: Images of the experimental coaxial cooler used to collect data for CFD model validation. **a.** Coaxial PTR in horizontal (90°) configuration. **b.** Isometric rendering of the experimental coaxial cold head

increments of 20 K, with additional tip temperatures measured in ranges of interest. Testing was performed in a vacuum jacket with a typical pressure of 1×10^{-5} to 1×10^{-6} torr to effectively eliminate convective and conductive thermal loading from the surroundings. All cold expander parts were gold plated and wrapped in multilayer insulation (MLI) in order to minimize thermal radiation loading.

Dynamic and static pressure measurements were recorded at the warm transitions of the cooler at the transfer tube (inlet to the aftercooler) and at the surge volume. Static pressure measurements were made using Paine Electronics Series 210-10 strain-gauge type pressure sensors amplified by an Omega DMD-465WB signal conditioner, resulting in an accuracy of ±6.8925 kPa within the pressure range of interest. Dynamic pressure measurements were made using PCB 101A05 miniature sensors which use a quartz piezoelectric sensing element capable of measuring dynamic amplitudes up to 689 kPa with resolution accuracy of ±14 Pa.

Temperature measurements were recorded at the warm block, the heat rejection

surface that houses both the aftercooler and warm heat exchanger, as well as on the cold tip housing the cold heat exchanger and flow transition. Warm temperature measurements were made using Type-E thermocouples with accuracy of ±0.88 K. Cooler heat rejection is accomplished using circulated chilled water controlled by a PID loop. The nominal rejection temperature of 293 K varied $+0.8/-0.2$ K throughout the course of testing. Cold tip temperatures were measured using two redundant Lake Shore Cryotronics DT-670 A-Band calibrated silicon diodes. Temperature measurements for the tolerance band A diodes fall within the manufacturer-stated accuracy of ±0.25 K for measurements in the 2 K to 100 K range, and have an accuracy of ±0.5 K from 100 K to 305 K.

Thermal load was applied to the cold heat exchanger using a Cryogenic Control Systems (Cryo-Con) Model 24 calibrated temperature controller applying PID-controlled voltage to a 1.000 Ω resistor with ±1% accuracy in order to fix the temperature at the desired set point. Temperatures were allowed to stabilize for approximately 15 minutes between set points, allowing the characteristic PID oscillations to fully decay before recording heat load data. Net cooling capacity at each temperature set point was measured by monitoring the voltage across the known resistance using a 4-wire measurement and applying Ohm's law to compute electrical input power. The voltage and current measurements were acquired through a calibrated National Instruments (NI) mainframe 16-bit analog-to-digital converter module with ± 10 V measurement range. The uncertainty in the voltage measurement as a result of quantization, noise, offset, non-linearity, and gain uncertainty in the ADC process is ± 4.61 mV in the voltage measurement range used in this study.

Input power to the pressure wave generator was measured separately for each of the driving coils by measuring RMS voltage. A calibrated LEM Norma 4000 power analyzer monitored input power to the drive motors using four-wire measurements (separate voltage and current leads), resulting in manufacturer-stated accuracy of

±0.1%. Input power uncertainty is stated in the legend for each measured curve.

6.3 Reference Cryocooler Data and Sage Model Correlation

Using the measurements obtained for the reference coaxial cooler as outlined in the previous section, a load map was generated for the PTR in the vertical cold end down orientation. These curves of net cooling capacity as a function of temperature and input power were then used to correlate a full system Sage model of the experimental PTR. Correlation was accomplished by comparing phasor pressures and temperatures in the Sage model to the measured net cooling capacity, thermal rejection temperatures, mean pressure, and oscillating pressures recorded at periodic steady-state. Adjustments were made to component thicknesses which represent conduction paths from the gas to the heat rejection surface. Adjustments were also made to the gas enthalpy and regenerator conduction adjustment factors provided in Sage for the purposes of correlation. The final correlated model includes the set of control parameters and correlation coefficients that minimize the simulated error (with respect to the net cooling capacity) over the entire range of measurement. The correlated Sage model predictions and the measured net cooling capacity are compared in Figure 6.4.

The measured loss in net cooling capacity, and therefore the change in net energy flow across the pulse tube, is determined from the experimental measurements based on the difference in cooling capacity between vertical and horizontal orientations. The resulting loss of cooling power (in Watts) is presented in Figure 6.5. Propagation of measurement uncertainty was computed according to the simplified variance formula for linear functions [100]:

$$\sigma(\dot{Q}_C) = \sqrt{\left(\frac{\partial \dot{Q}_C}{\partial V}\right)^2 \sigma_V^2 + \left(\frac{\partial \dot{Q}_C}{\partial R}\right)^2 \sigma_R^2} \tag{6.3}$$

where $\dot{Q}_C$ is the net cooling power at a given orientation and input compressor power

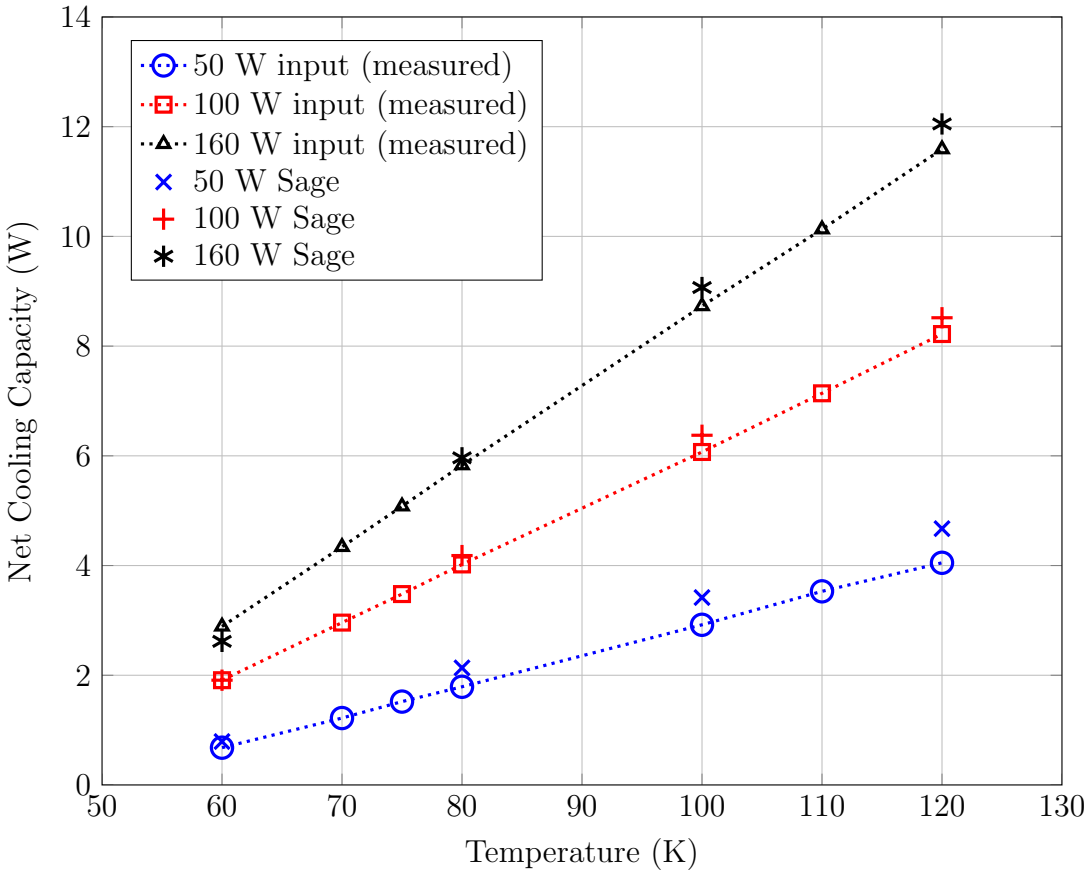

Figure 6.4: Comparison of measured net cooling capacity at 0° to the correlated Sage model of the experimental coaxial PTR.

given by Ohm's law for power:

$$\dot{Q}_C = \frac{V^2}{R} \tag{6.4}$$

Substituting the derived partial derivatives for Ohm's Law, with the pertinent measured variables being resistance R and voltage V:

$$\sigma(\dot{Q}_C) = \sqrt{\left(\frac{2V}{R}\right)^2 \sigma_V^2 + \left(-\frac{V^2}{R^2}\right)^2 \sigma_R^2} \tag{6.5}$$

The uncertainties for resistance and voltage measurements as stated in the previous section are then inserted in Equation 6.5. The cooling power at each orientation and input power were measured and recorded. The cooling loss as a function of orientation angle was then computed for each temperature and compressor input power according to:

$$\Delta\dot{Q}_C = \dot{Q}_C(0^\circ) - \dot{Q}_C(90^\circ) \tag{6.6}$$

The standard deviation in the cooling loss ($\Delta\dot{Q}_C$) computations is the sum of the propagated error in each of the cooling capacity measurements $\dot{Q}_C(0^\circ)$ and $\dot{Q}_C(90^\circ)$ necessary to obtain the resulting loss. Uncertainty in the cooling power loss is reported using vertical error bars in Figure 6.5. Horizontal error bars for temperature are not plotted since the error bars are contained within the size of the markers used.

Inspection of the resulting losses reveals the following trends: (1) the magnitude of the convective loss decreases as the PV power applied to the system is increased, and (2) the net convective energy flow is reduced by approximately a factor of 2 as the cold end temperature increases from 60 K to 120 K. The pulse tube convection number N_{PTC} introduced in Chapter 2 was calculated for all of the data points recorded for the DUC cooler. The pulse tube convection number was computed at the cold end of the pulse tube based on current best practices. The loss data was normalized by the net energy flow across the pulse tube to determine the normalized energy flow loss $|L|$ for the DUC data. The resulting plot of $|L|$ vs. N_{PTC} is shown in Figure 6.6. The exponential best fit line included in Figure 6.6 has an R^2 value

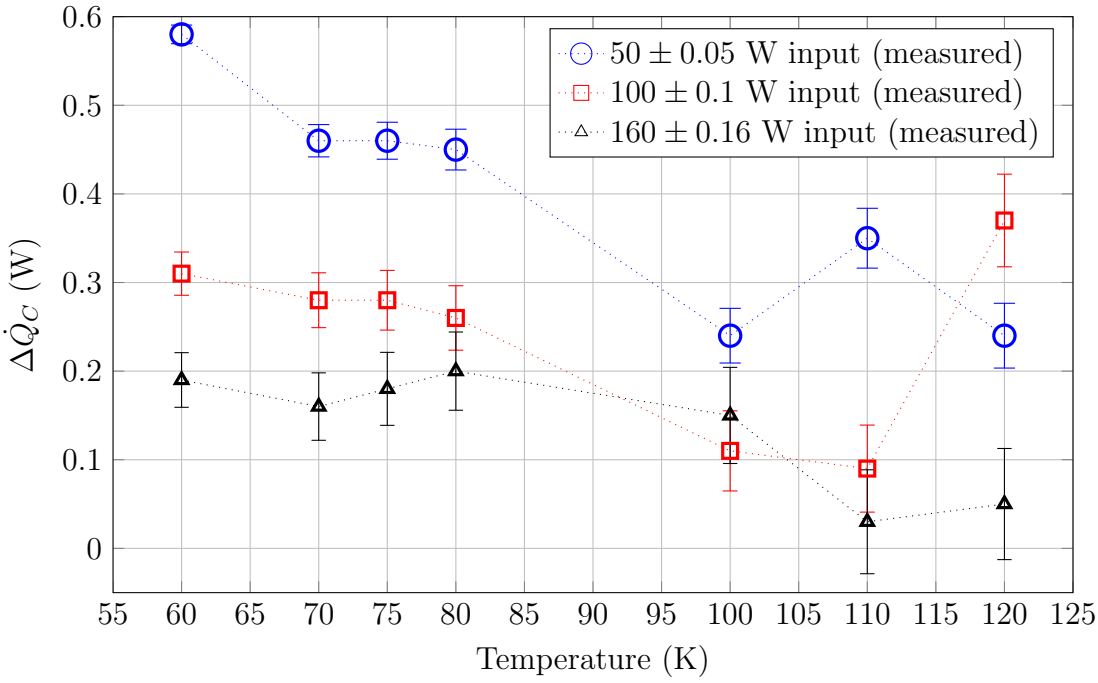

Figure 6.5: Measured loss in net cooling capacity between 0° and 90° for the Raytheon Dual Use Cooler.

of 0.7792, the best agreement achieved by any regression computed among linear, exponential, logarithmic, power, and polynomial types.

6.4 Data Comparison and Error Analysis

In order to validate the component level CFD model (cold heat exchanger, pulse tube, pulse tube wall, and warm heat exchanger), simulations of the experimental DUC domain were carried out at both orientations for which data was furnished, 0° and 90° for 12 operating conditions, requiring a total of 24 simulations to complete. Temperatures of 60 K, 80 K, 100 K, and 120 K were simulated for input power of 50 W, 100 W, and 160 W. This allows a direct comparison of the outputs of the ANSYS FLUENT 3-D CFD model to the corresponding net cooling loss $\Delta\dot{Q}_C$ in the experimental cooler. The results of this comparison are presented in Figure 6.7.

Comparison of the modeling results obtained using component-level 3-D CFD modeling of the pulse tubes, heat exchangers, and inertance tube transition to the

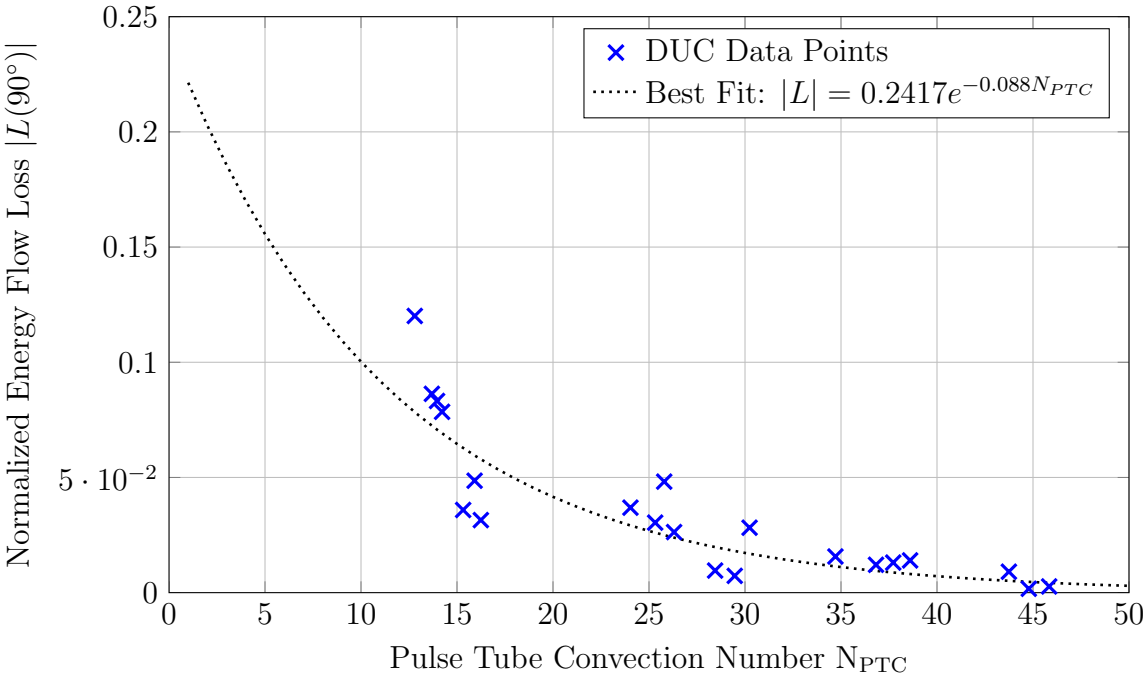

Figure 6.6: Normalized energy flow loss as a function of pulse tube convection number for experimental data recorded from the Raytheon Dual Use Cooler at 90° angle of inclination.

corresponding experimental measurements reveals some level of error imposed by the modeling assumptions; however, all but one operating point, 60 K with input power of 50 W, fall within the experimental uncertainty range. The estimates of cooling loss computed using CFD seem to overpredict the losses slightly in nearly all cases. The maximum percentage error in the CFD prediction of net energy flow is 8.2% and the average error is 3.67% of net energy flow. A portion of this error can be attributed to the lack of a regenerator in the model, as the system-level analysis revealed a regenerator contribution of approximately 6% to the overall loss in performance at elevated angles.

The errors in the CFD predictions compared to the measured data are a result of a compound error between measurement uncertainty, Sage error, and numerical modeling error. The largest percent errors in prediction occur when the net cooling capacity is very small, or when the actual tilt induced cooling losses are negligible.

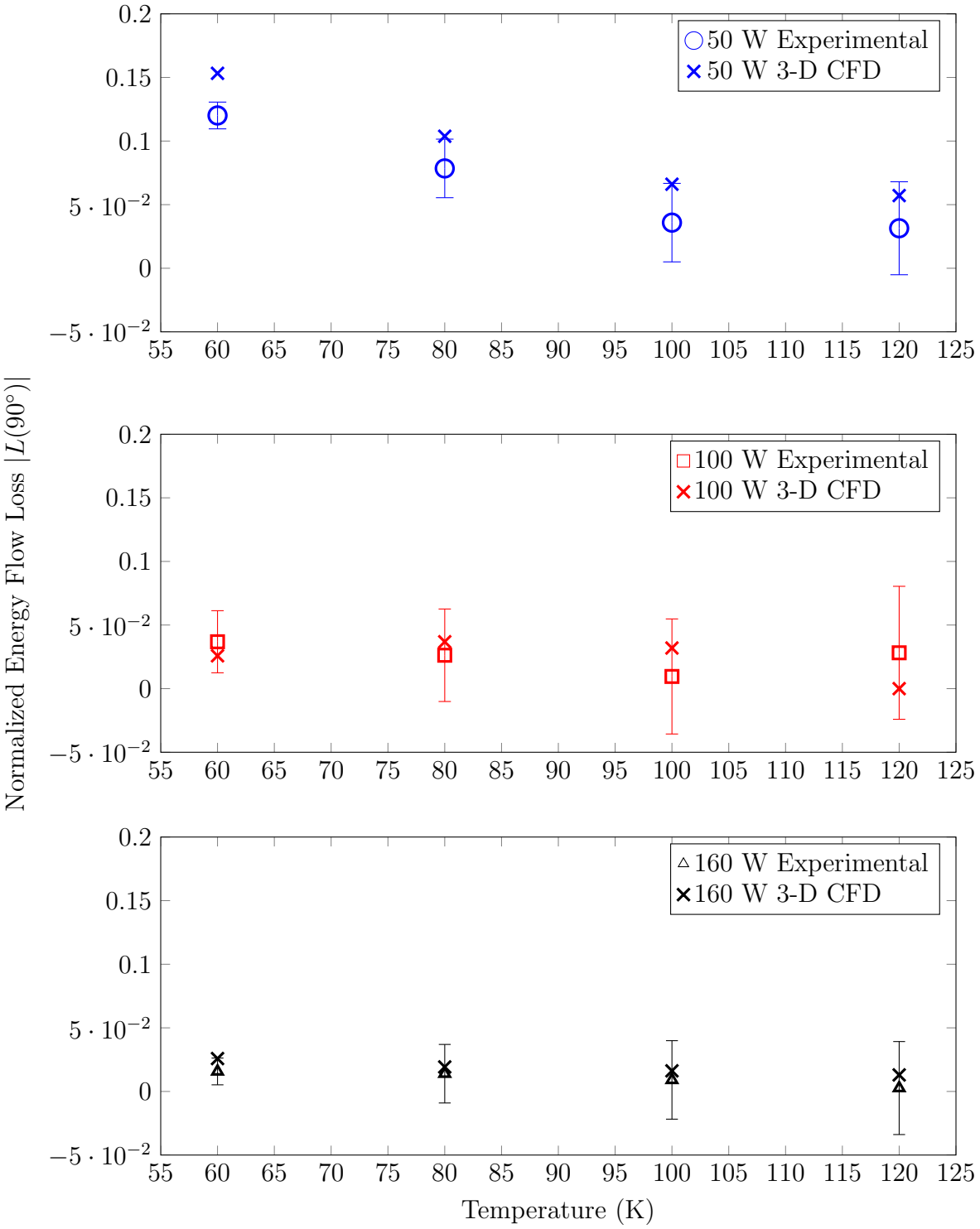

Figure 6.7: Comparison of normalized energy flow losses predicted by 3-D CFD compared to those measured experimentally. All but one point fits within the experimental error bars.

Given that energy is likely never to be fully conserved in a numerical analysis, errors on the order of 100 mW are quite small in comparison to the transient energy flows which can be on the order of 100 W, but yield a cycle-averaged flow in the mW range. Given the fidelity of the numerical models studied, it is unlikely that better accuracy can be achieved from CFD models. The models are therefore most suited to larger capacity cryocoolers where mW accuracy is not required. The modeling method is also well suited for relative comparison of various designs to determine orientation sensitivity.

6.5 Analysis of combined experimental and simulated results

In this section, the results of both investigation methods reported in Chapters 5 and 6 will be combined on common axes to develop an overall body of data from which to make conclusions. The hope in doing so is to develop a better understanding of the interplay between the variables that govern stability, as well as quantify cooling losses sustained in quasi-stable flows.

In addition to the Dual Use Cryocooler tilt data furnished by Raytheon to facilitate validation of the component-level CFD model discussed in the previous section, data was also provided on two additional internal R&D (IRAD) coolers operating over different temperature ranges [101]. The experimental refrigerators will simply be referred to as Cooler A and Cooler B as they are nameless development coolers. Cooler A is a two-stage 40 Hz cooler designed to provide 2-3 W of cooling 35 K with an intermediate temperature of 85 K for an input compressor power of approximately 500 W. Data was provided over a range of input powers in the horizontal orientation. This cooler exhibited excellent stability in the horizontal orientation with pulse tube convection numbers in the range of 1.04 to 1.22. The results of the Cooler A testing are shown in Figure 6.8. The exponential best fit reported for the DUC data previously presented is also plotted in Figure 6.8 and reveals some peculiar incongruity. The

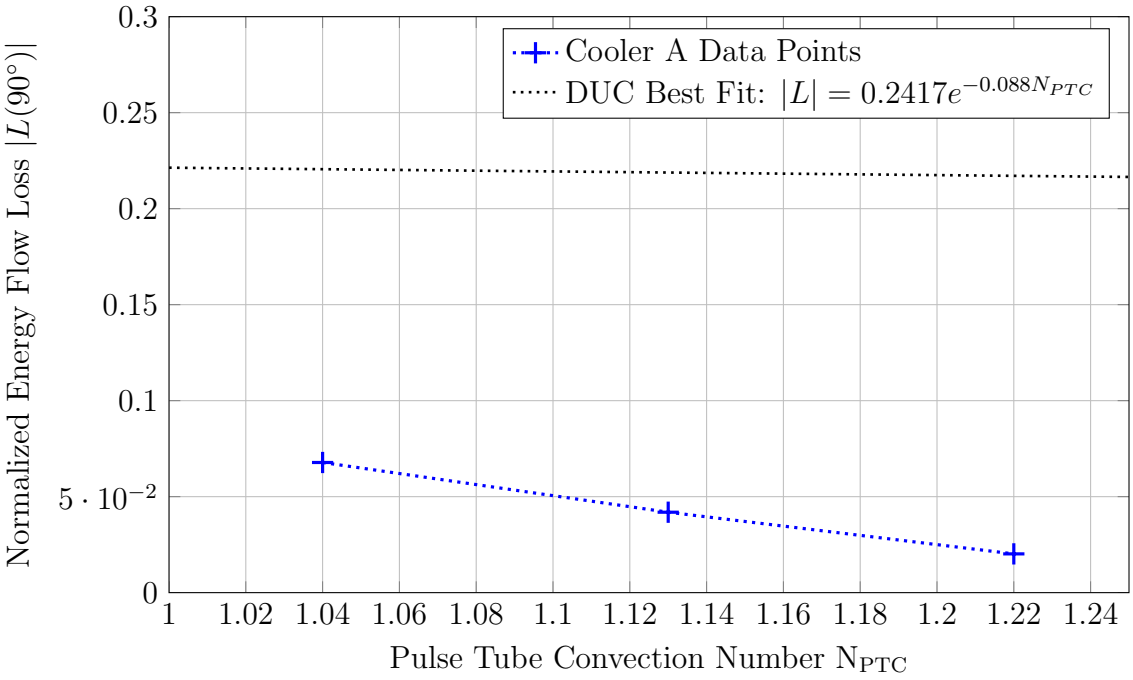

Figure 6.8: Normalized energy flow loss as a function of pulse tube convection number for experimental data recorded from Cooler A at 90° angle of inclination.

particularly low pulse tube convection numbers suggest that the convection should be fully suppressed, according to the originally reported critical pulse tube convection number of 1. This data seems to support the derived critical pulse tube convection number, in spite of the drastically different conclusion made for the DUC data.

Cooler B is also a two-stage operating at 26.5 Hz. This cooler was designed to provide 500 mW of cooling capacity at 10 K for an input power of approximately 550 W. Testing data was provided at a single compressor input power of 550 W and set temperature of 10 K for angles of 0°, 45°, 62.5°, 90°, and 180°. The interesting results accompanying this cooler concluded that catastrophic loss of cooling was present for pulse tube convection numbers as high as 4.7, which sharply contrasts the results of Cooler A, but agrees with the conclusions made for the DUC cooler. The complete convective instability at angles 90°, and 180° led to temperature instability as well, and therefore the 10 K objective temperature could not be held. The cooling capacity at these angles was reported as 0 W, indicating that there was no useful cooling

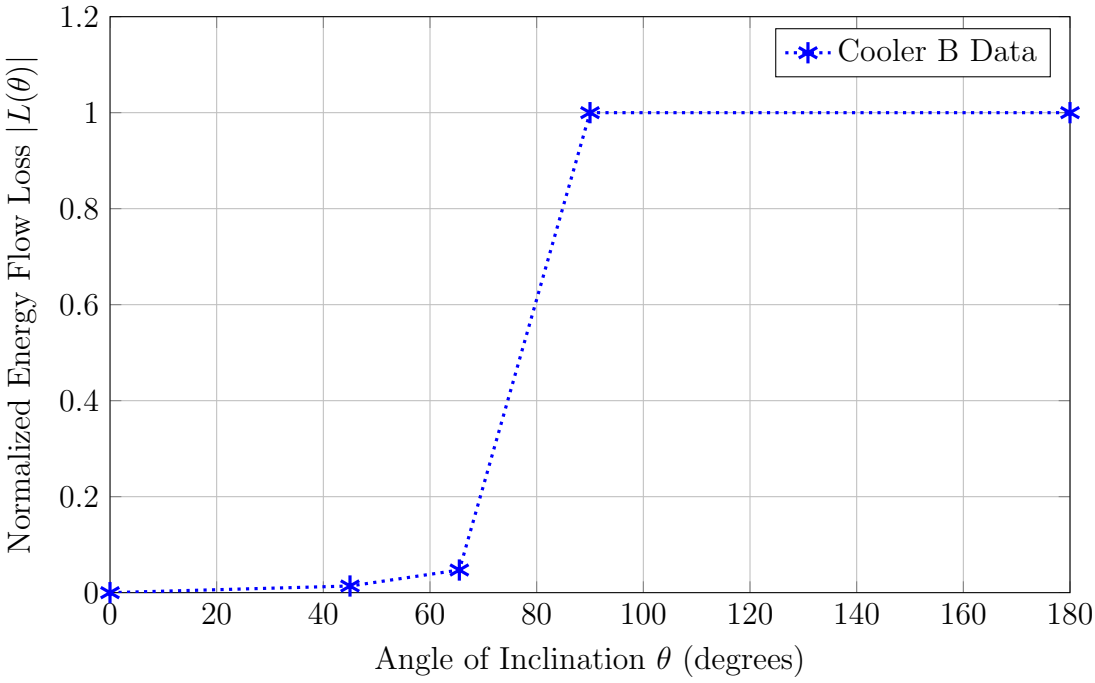

Figure 6.9: Normalized energy flow loss as a function of pulse tube convection number for experimental data recorded from Cooler B as a function of angle of inclination for a single compressor (PWG) input power.

produced. Evaluating the energy flow at 90°, and 180° in the framework of the analysis used in Chapter 5, the cooling capacity would in fact be negative, leading to the observed increase in temperature, and normalized loss greater than 1 would be reported.

The critical difference between Cooler A and Cooler B is the pulse tube temperature range, Cooler B being significantly lower (25 K colder). The results for the 20 K to 4 K pulse tube simulations from the parametric study in Chapter 5 indicated that at 90°, the convection was not stabilized regardless of Reynolds number. This data set therefore conforms with the simulated data conclusions as well. The orientation-dependent data set for Cooler B is presented in Figure 6.9. Note that the results are not reported in terms of N_{PTC} because angles less than 90° produce negative pulse tube convection numbers, despite the existence of instability as angles increase, a shortcoming of the current theory.

The compiled results from all data sources introduced in this study are presented in a common plot that compares dimensionless energy flow loss $|L(\theta)|$ and the cold end pulse tube convection number N_{PTC}. This result is presented on linear axes in Figure 6.10, and also on a logarithmic y-axis in Figure 6.11. Plotting on logarithmic axes helps clarify the apparently exponential decay in the normalized energy flow loss. The results presented in these plots include a frequency range of 25 Hz - 60 Hz, a cold end temperature range of 4 K to 120 K, aspect ratios from 4-10.2, and cold end mass/pressure phase relationships between $\varphi_{m-p} = -55°$ and $\varphi_{m-p} = +30°$ for orientation angles ranging from 0° to 180°.

The data collected from the commercial coolers was also normalized by pulse tube energy flow (as computed by Sage) and plotted according to their computed pulse tube convection number. By observing the relationship between normalized energy flow loss $|L|$ and the pulse tube convection number N_{PTC} it is obvious that there is significant variability in the low N_{PTC} range. Recall that the formal derivation of the pulse tube convection number places the critical at a value of $N_{PTC,cr} = 1$. Complete suppresion of convective instability would yield a value of $|L| = 0$, while a fully unstable system would be characterized by $|L| \geq 1$. Values exceeding 1 are permitted by the definition if the net energy flow reverses direction and the pulse tube in fact acts as a parasitic heat path from the warm heat exchanger. This would be categorized as catastrophic failure for a cryocooler and in practice the desired set temperature of the cooler could not be maintained.

Inspection of Figure 6.10 shows a reliable exponential decay of the normalized loss as a function of pulse tube convection number when plotted on linear axes. Plotting the data on a logarithmic y-axis in Figure 6.11 reveals the significant data scatter in the lower range of N_{PTC}. An attempt was made to reduce the scatter by applying a number of corrections to the pulse tube convection number formulation. First, the assumption that density and temperature are linearly related was removed, instead

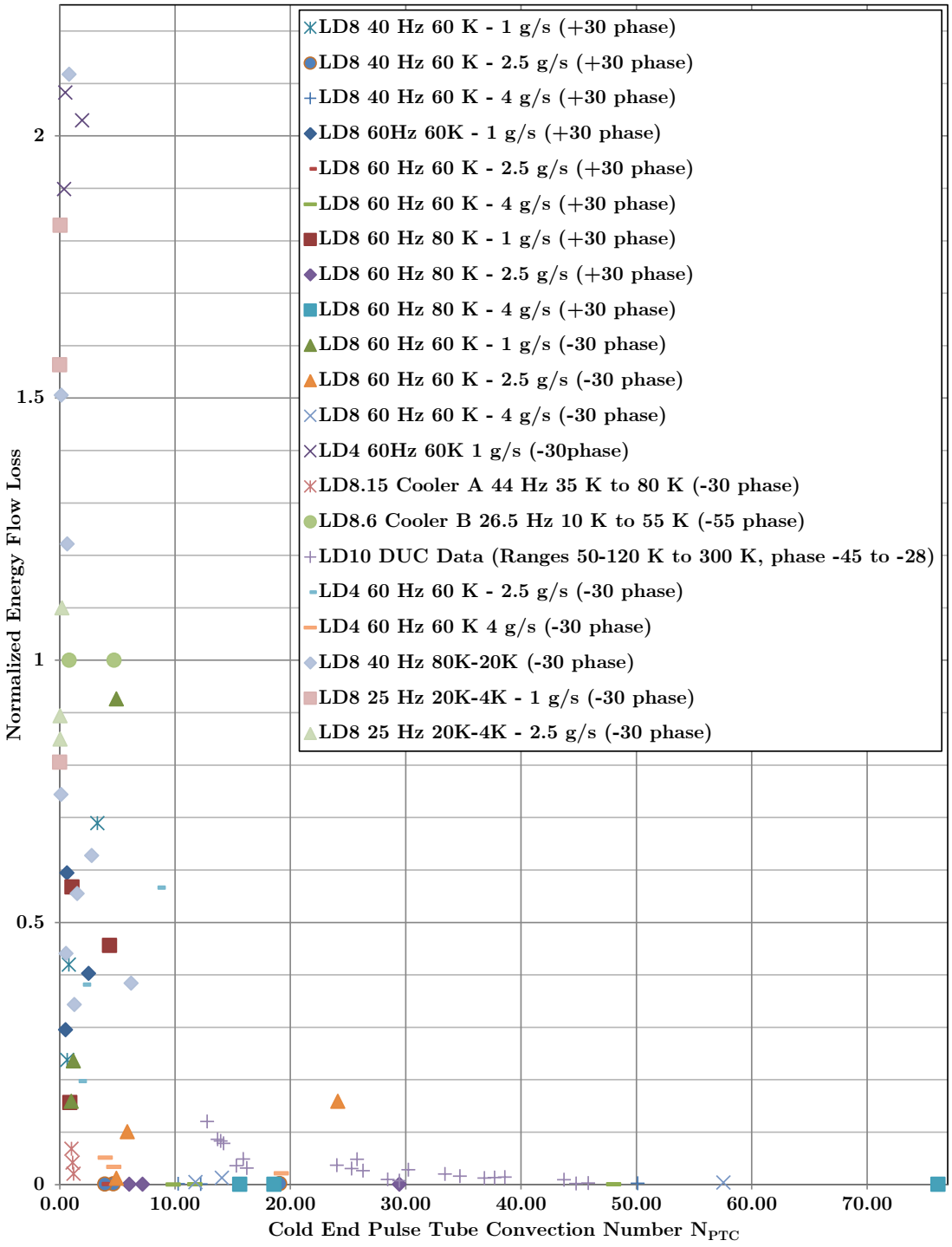

Figure 6.10: Plot of normalized energy flow loss as a function of cold end pulse tube convection number N_{PTC}.

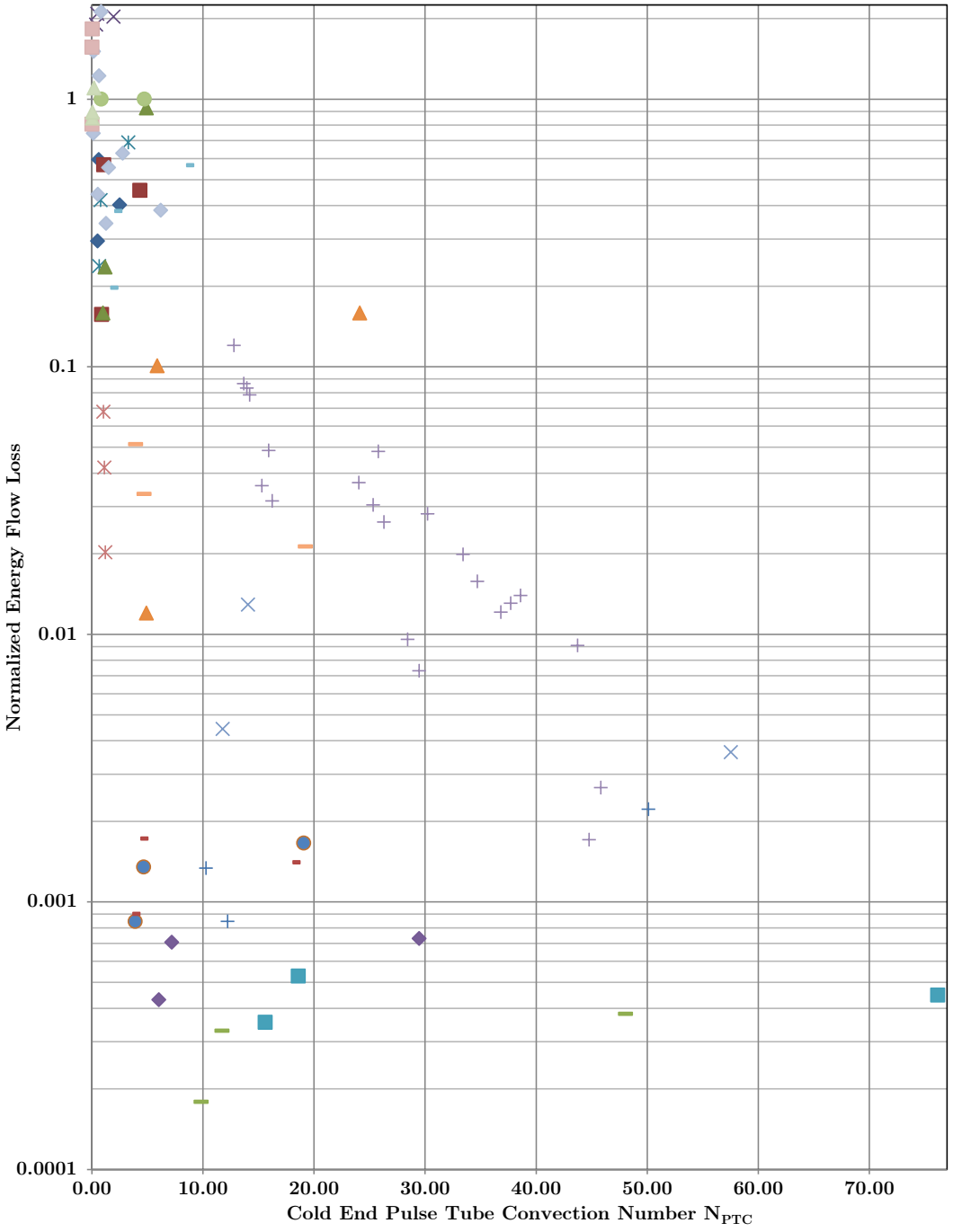

Figure 6.11: Logarithmic plot of normalized energy flow loss as a function of cold end pulse tube convection number N_{PTC}. The legend in Figure 6.10 applies to this plot as well and is not included for clarity.

using the real gas density values at the hot and cold end. The resulting equation was:

$$N_{PTC} = \frac{\omega^2 a^2}{g(\alpha_S D \sin\theta - L\cos\theta)} \sqrt{\left(\frac{\rho_C - \rho_H}{\rho_{avg}}\right)} \tag{6.7}$$

where $\alpha_S = 1.5$. After applying the correction, pulse tube convection numbers shifted only by an average 0.73% for cold end temperatures above 60 K, 0.31% for pulse tubes operating between 80 K and 20 K, and 8.66% for pulse tubes operating between 20 K and 4 K. This indicates that the need to incorporate real gas values is only important in the extreme low temperature range. Additionally, application of this correction did not improve scatter in the data for $N_{PTC} \leq 10$. Variation of the fitting parameter α_S yielded a similar effect to the inclusion of real gas density. All points were scaled, resulting in no scatter improvement.

An interesting observation of the overall trends is that the low frequency coolers ranging from 25 Hz to 40 Hz all experienced significant losses, with pulse tube convection numbers less than 10. The majority of these data points represent staged pulse tubes that operate entirely under cryogenic conditions. This emphasizes the importance of the gas properties as they pertain to convective instability.

The results plotted in Figure 6.10 and Figure 6.11 can be used as an approximation tool for estimating orientation sensitivity. With the exception of two data points, the results in Figure 6.11 indicate that less than 10% of pulse tube energy flow is likely to be lost for a design with a pulse tube convection number greater than 10. If the design requires extremely stable performance in all orientations, a minimum of $N_{PTC} = 40$ should be used as a design criterion. The results of course only bracket a range of possible losses, but give a reasonable estimate of the order of magnitude that one can expect as a function of pulse tube convection number.

6.6 Conclusion

Comparison of the results of the CFD modeling methods presented in this thesis with commercial cryocooler data reveals its suitability as a predictive tool for orientation

sensitivity. Although the accuracy of the model is only as accurate as the boundary conditions applied to the computational domain, the predictions are very useful for relative design comparison when optimizing a PTR design for minimized orientation sensitivity. The actual orientation sensitivity measured in practice may be a large percentage of the net cooling capacity for small capacity cryocoolers, where mW errors can cover the entire useful cooling range of the design. The model is better suited to higher power coolers where ± 0.1 W error is tolerable in a prediction.

What constitutes a reasonable level of convective supression is really a function of the tolerance afforded by the application. In order to put the results of Figure 6.10 into terms of net cooling capacity loss, the designer must be able to predict the regenerator losses associated with that particular design. To first order, it appears that the assertion by Berryhill and Spoor [50] that designers should avoid configurations yielding $N_{PTC} \leq 20 - 30$ is well founded. Unfortunately solutions yielding such high pulse tube convection numbers may be far from the most efficient design possible for vertical orientation.

CHAPTER VII

CONCLUSIONS AND FUTURE WORK

7.1 Summary

The goals of this dissertation study were to develop and validate a predictive methodology for convective cooling losses in modern pulse tube cryocoolers. The study was initiated by modeling a prototypical ITPTR system in 3-D half symmetry at various orientations and with two pulse tube aspect ratios. The results of that study concluded that for the packed screen regenerator configuration investigated, convective losses can be isolated to the pulse tube component and its impact on the adjacent heat exchangers.

A reduced 3-D component-level model was then developed to improve simulation time while maintaining predictive accuracy. The resulting methodology was then validated using data collected from a commercial cryocooler and found to yield energy flow predictions with a maximum error of 8.2%, while reducing simulation time from the 30 days required to simulate a full system using HPC resources to 6 days using standard 8-core workstations.

The experimentally validated component-level CFD code was then used to perform a small-scale parametric study to characterize losses over the range of 4 K to 80 K objective temperature. A parametric CFD study was carried out that investigated the contributions of frequency, Reynolds number, pulse tube aspect ratio, hot and cold temperatures, and mass flow - phase relationships. Results were reported in terms of a dimensionless loss $|L(\theta)|$ where the change in net pulse tube energy flow due to gravitational body force was isolated and normalized by the net energy flow in the untilted position with the cold end of the pulse tube pointed downward. Data sets

were incorporated from a corporate research partner on three commercially available pulse tube cryocoolers covering a range from 10 K to 120 K at various orientation angles. Correlated Sage system models were then used to compute the cold end pulse tube convection number and the magnitude of the pulse tube energy flow to enable the computation of $|L(\theta)|$ for the experimentally measured data.

Non-dimensionalized losses were then plotted as a function of the pulse tube convection number computed at the cold end of the pulse tube to evaluate a suitable value of the critical number $N_{PTC,cr}$. It was determined that a conservative critical value of $N_{PTC,cr} = 10$ would yield a design that reliably experiences energy flow losses less than 10% of the net pulse tube energy flow, with only a few exceptions. Designs with predicted pulse tube convection numbers less than 10 should be evaluated on an individual basis using the methods presented in this dissertation if orientation insensitivity is a critical feature of the design. If very little orientation sensitivity is required, a design incorporating $N_{PTC,cr} \geq 40$ is shown to maintain at least 99% of its pulse tube net energy flow regardless of orientation.

When using the pulse tube convection number as a design tool, the designer is urged to compute the predicted regenerator energy flows and take them into account when using the results in Figures 6.10 and 6.11 to bracket the possible range of normalized energy flow loss that is possible for a given pulse tube convection number. If the scatter in the possible losses is too large for the design tolerance, the designer should then proceed to a component-level CFD model as described here. A final measure to improve confidence in the model's prediction is to then perform a system-level model once all thermodynamic design is complete, in order to compare the results to the reduced component-level model. The benefit to utilizing the system-level modeling approach is the ability to directly predict the net cooling capacity as all parasitic energy flows are incorporated in the model. The negative to this approach, of course, is the time required for simulation of such domains. The level of accuracy required

for the design determines the complexity of the predictive methodology.

7.2 Contributions

The contributions of this study are of direct importance to the pulse tube cryocooler community. The methods presented in this work can be replicated by pulse tube designers in order to inform the design of more robust cryocoolers with respect to orientation sensitivity. Typical publications disclosing CFD methods in published research fail to list the important program settings and mesh features that allow the models to be reliably solved. The level of detail included in this disclosure allows any user familiar with the basic functionality of ANSYS FLUENT to be able to duplicate the results by copying and pasting the code included in Appendices B and C.

Appendix A introduces a secondary product of this research program where a cryogenic test facility with the ability to rotate was developed to facilitate cryocooler research down to 4 K in any orientation. The design was performed in such a way as to render the facility useful for experimentation on virtually any cryocooler or separate effects test currently envisioned, and will support the research needs of the next generation of researchers in the Georgia Tech Cryo Lab.

7.3 Future Work

7.3.1 Separate Effects Testing of Inclined Pulse Tubes

Investigation of convective losses in inclined and inverted pulse tubes has been underway for at least 15 years according to published records. The results of this dissertation do not close the book on the study, and further work is strongly suggested in order to continue the development of the PTR as a robust and efficient machine. The scope of the numerical study reported in this dissertation was severely limited by the computational resources required to produce the results. In order to make definitive statements regarding the functional relationships between driving variables, a significant body of data is needed covering a wider range of operating conditions.

Appendix A describes the development of a rotating cryogenic test facility at the Georgia Tech Cryo Lab that will support the next generation of investigation into gravitational sensitivity. The immediate need for future work is to continue the development of separate effects tests for static orientation sensitivity. Pulse tubes of varying aspect ratios should be tested over a wide range of temperatures, fill pressures, frequencies, pressure ratios, and phase angles in order to systematically isolate the variables of interest.

7.3.2 Exploration of Dynamic Gravitational Body Forces in Pulse Tubes

Another recent area of interest is in the study of dynamically applied gravitational body forces such as those that would be experienced during a rocking or pitching motion. Such a set of operating conditions might be experienced in terrestrial applications where a PTR is mounted on a moving platform such as a ship, aircraft, or military communications vehicle. Currently little is known about the effects of such envirnments on pulse tube cooler operation, therefore limiting its utilization in these applications.

A preliminary investigation during this research program identified that the CFD methodology presented in this dissertation is capable of modeling the dynamic orientation condition. By controlling the gravitational vector components as a function of time and pursuing a transient time marched solution, one could in fact capture the effects of dynamic tilt. The prohibiting factor involved in using CFD as a study tool for dynamic tilt is the disparity of time scales between the period of gas oscillation driven by the pressure wave generator, and the long period of oscillation of the dynamic tilting motion. Explained more clearly, the frequency associated with dynamic rocking is anticipated to be approximately 0.5 Hz, whereas the driving frequency of the cooler is in the range of 25-60 Hz. The simulated flow times involved in theses

static tilt studies reached quasi steady-state in approximately 1.25 seconds and required approximately a week to perform on the component level. The equivalent flow time was achieved on the system level in approximately one month. Assuming that a minimum of two rocking cycles would be required to capture dynamic tilt effects, the simulation time approaches 3.5 months for a single system-level run.

The rotating test facility described in Appendix A lends itself perfectly to an experimental study of dynamic tilt effects. By driving the rotation of the cooler with a stepper motor, the oscillation of the test section could easily be controlled with great precision.

APPENDIX A

DEVELOPMENT OF A ROTATING CRYOGENIC TEST FACILITY

The computational methods described in Chapters 4 and 5 require significant time and computational resources to complete. As such the results are limited to a small range of solutions that represent common configurations experienced in current modern pulse tube cryocoolers. In order to expand the scope of study on convective effects in pulse tubes, as well as other system components, an experimental cryogenic test facility has been designed, built, and characterized for future empirical studies. In this appendix, the process and methods for developing this facility are described in detail.

A.1 Experimental Setup Design and Development

Funding for an experimental facility, particularly the expensive instrumentation, was provided in large part by the Office of Naval Research (ONR) Defense University Research Instrumentation Program (DURIP). Integrating the equipment provided through that grant into a coherent unit mounted on a customized mount allowed the development of a world-class rotating cryogenic vacuum testing facility with testing temperatures down to 4 K. The facility integrates a 27 in. diameter stainless steel high vacuum dewar with 27 in. depth with an aluminum cover housing a 4 K G-M cryocooler, a 500 W (nominal) pressure wave generator, a turbomolecular vacuum pumping system, a calibrated thermal mounting system to measure heat flows to and from experimental sections, a calibrated oscillating mass flow meter, precision tempearature measurement and control loops, high sensitivity cryogenic pressure sensors,

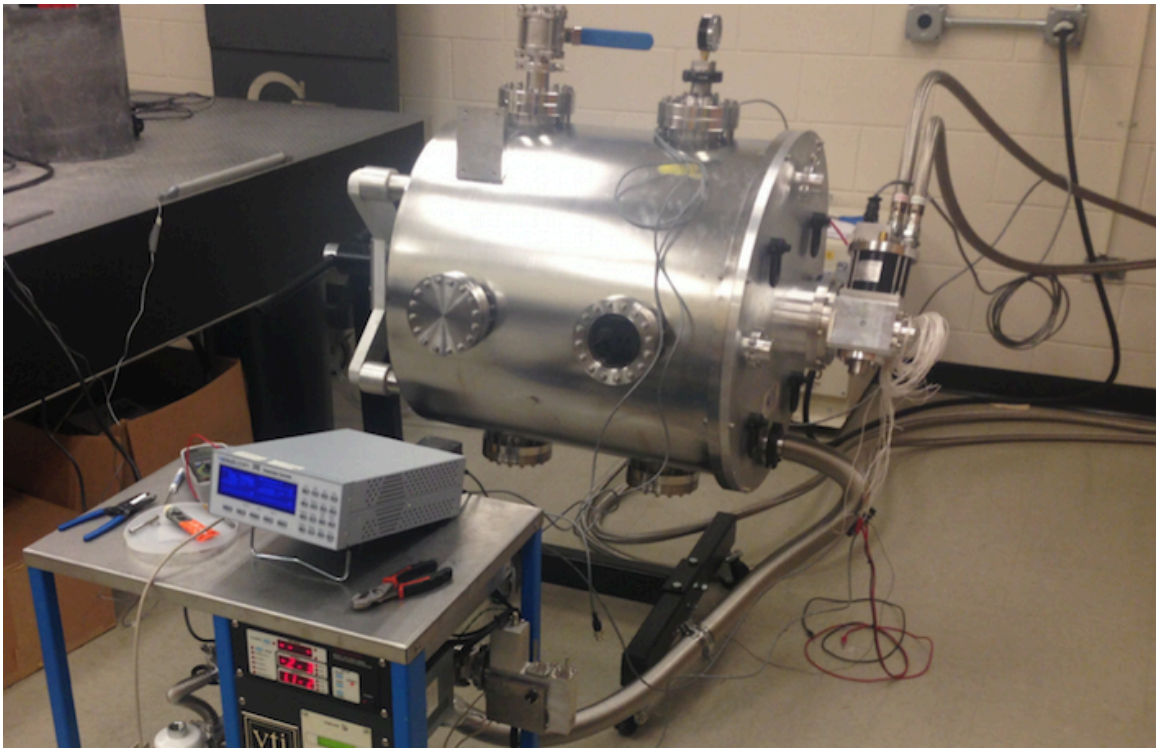

Figure A.1: Photograph of the GTCL rotating cryogenic test facility.

a subminiature thermal anemometry system, and a controlled cooling water loop. The design incorporates eight 6 in. access ports as well as six additional KF40 vacuum flanges to allow simple customization of the chamber. The result is a facility capable of rotating 360° with all instrumentation, cables, hoses and tubing fully attached while precisely measuring all relevant energy and hydraulic flow parameters of interest.

The completed experimental facility owned and housed by the Georgia Tech Cryo Lab (GTCL) is shown in Figure A.1. The completed test facility is the culmination of two years of development effort and system troubleshooting. The resulting setup is designed with interchangeability in mind in order to facilitate the next generation of GTCL projects. Components were designed with common flanges and bolt patterns whenever possible, and high quality adapters were designed and fabricated to customize non-conforming components.

In the following sections, the details of the components that have been developed and the calibration methodologies will be discussed. Following that discussion, a

description of a separate effects testing prototype design will be presented followed by commentary on improvements that can be made to the next design iteration to produce meaningful results that pertain to convective instability in inclined pulse tube refrigerators.

In order to render results obtained through experimental testing relevant, the primary operating conditions such as temperature, mass flow, heat flow, and pressure must be collected in a precise way. Cryogenic measurements represent significant challenges compared to room temperature testing. As a result of the pronounced effects that very small heat flows from contamination sources such as ambient environment, sensor excitation, and thermal conduction through leads, all of the components and sensors within the system are extremely sensitive and fragile. Extreme caution must be used when assembling experimental setups to avoid breakage of the tiny gauge leads as well as contamination of the experimental systems with dust, grease, and volatiles.

A.1.1 Vacuum Considerations

In order to achieve very low temperatures and to minimize the impact of varying environmental conditions on measurements, the experimental work must be contained within a high vacuum cryogenic vessel. High vacuum is defined between 1×10^{-3} torr (1 torr=133.32 Pa) and 1×10^{-9} torr. In a high vacuum environment, the mean free path of the residual gases within the chamber is larger than the vacuum enclosure and significantly larger than the test section being studied. The result is the effective elimination of convection and conduction between the cold apparatus and the walls of the chamber. The final remaining form of heat transfer to the surroundings then is radiation, which is minimized by surrounding the experimental apparatus with double-aluminized mylar sheets separated by low-conductivity skrim material. Up to 40 layers of this material are used, and the stack of material is known as MLI

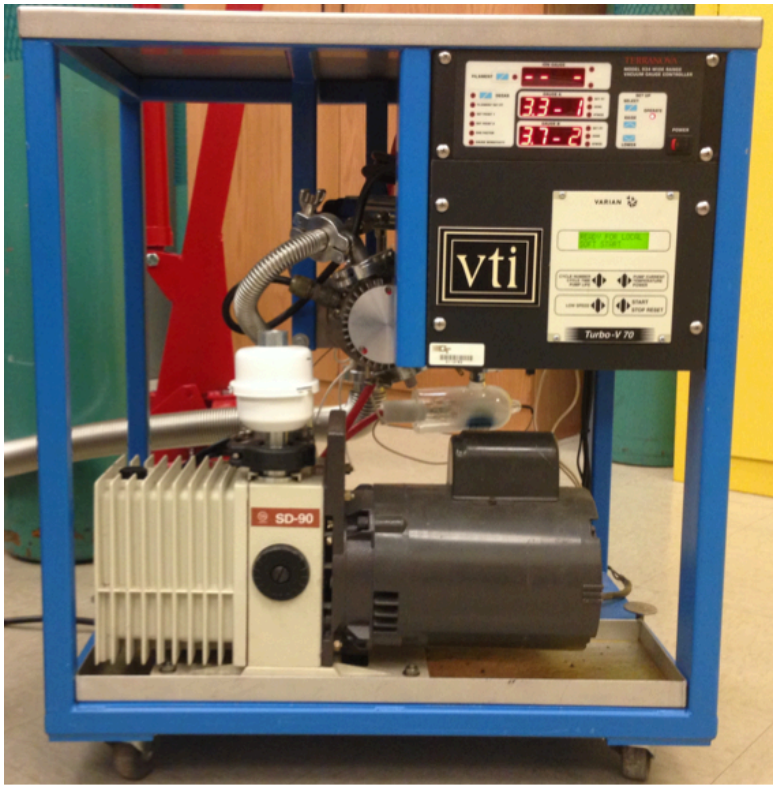

Figure A.2: Two-stage turbomolecular pump system used to provide insulating vacuum environment.

(multilayer insulation).

Vacuum levels are achieved through the use of a two-stage pumping system. The first roughing stage of the pumping system is a Varian SD90 rotary pump which initially brings the pressure in the chamber to approximately 1×10^{-3} torr. The seconary stage is a Varian V-70D Macro-Torr turbomolecular pump operating at a rotational speed of 75,000 RPM. The two-stage system is shown in Figure A.2. The combined system is capable of achieving pressures as low as 1×10^{-8} torr in a perfect hermetically sealed environment where only solid metal seals or weldments are used in construction and a vacuum proper bakeout procedure is followed. Additional pressure reduction is achieved as a side-effect of cryopumping that occurs as the cold test section cools the remaining gases in the chamber, reducing their partial pressure to a nearly negligible level. The experimental Dewar has been tested to 1×10^{-6} torr.

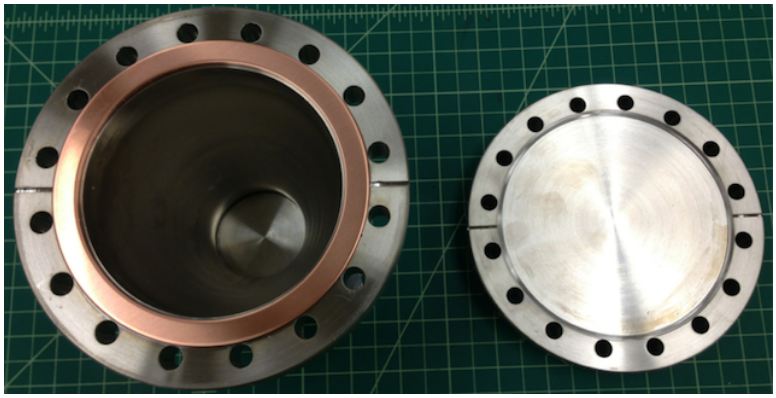

Figure A.3: Conflat all-metal seals used to seal infrequently accessed ports.

In order to maintain vacuum levels within the desired testing range of 1×10^{-5} to 1×10^{-6} torr, careful consideration must be made to the types of seals incorporated as well as the materials that will be housed within the chamber, ensuring that materials that outgas over time are properly treated before installation. Solid metal-to-metal seals provide the lowest rates of leakage, but are considered semi-permanent seals since they are not reusable once the seal has been disassembled, without incurring future leakage. 6 in. diameter stainless steel Conflat flanges are used to seal the eight access ports evenly spaced on the cylindrical body of the chamber. Four of the flanges incorporate glass-to-metal sealed optical access ports with 3.5 in. viewing diameter. Conflats utilize a patented flange design that incorporates a tapered knife-edge feature on both mating pieces. The knife-edge cuts into an annealed copper sealing ring that has been electropolished to ensure a scratch free mating surface. The cutting action permanently deforms the copper sealing material, filling any surface imperfections in the process and creating a hermetic seal. Images of the conflat seals used are shown in Figure A.3.

Seals that must be frequently accessed and remade are designed with Viton O-rings. O-rings are incorporated into traditional sealing grooves in order to seal the aluminum lid to the stainless steel chamber flange as well as to seal the Sumitomo RDK-408D2 Gifford-McMahon cryocooler to the chamber lid. KF40 (NW40) flanges

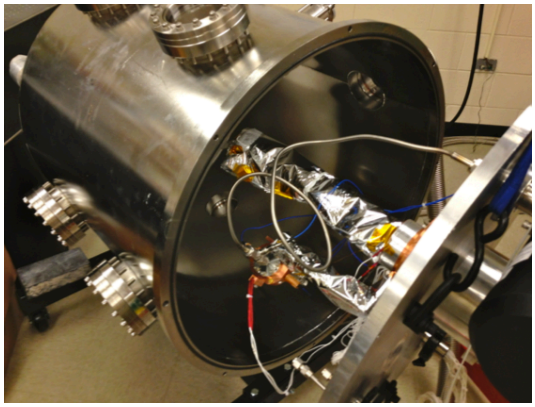

(a) Chamber lid O-ring seal.

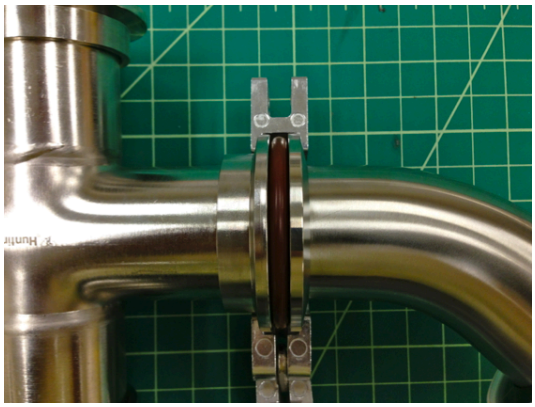

(b) KF40 seal joint

Figure A.4: O-ring sealing features in the GTCL test facility

are incorporated into all remaining components to facilitate interchangeability, a critically important feature for experimental flexibility. KF flanges incorporate a conical feature on each flange with matching features on a sealing clamp. a centering ring is placed between the two flanges with a Viton O-ring face seal. The O-ring is compressed as the sealing clamp is tightened and the two mating flanges are forced closer to one another. O-ring and KF flange features are shown in Figure A.4.

In order to pass power and sensor signals in and out of the chamber, hermetic feedthroughs are required. Since this is an experimental facility, generic unterminated wire feedthroughs are incorporated for connecting temperature sensors such as diodes and RTDs. Additionally, a custom feedthrough has been made to pass miniature shielded coaxial cables for obtaining pressure sensor measurements. These sealed wire feedthroughs are made by first drilling a hole in a KF40 blank large enough to pass the cables through, with slight clearance such that the wires do not touch each other or the edges. The cavity and wire surfaces are thoroughly degreased with cleaning solution and acetone (on the metal only) as adhesives will not bond permanently to contaminated surfaces. The void space is then filled with Stycast 2850-FT binary epoxy mixture with 1 hour working time. The epoxy is mixed, slightly heated to reduce the viscosity, then injected into the void spaces until the cavity is nearly full.

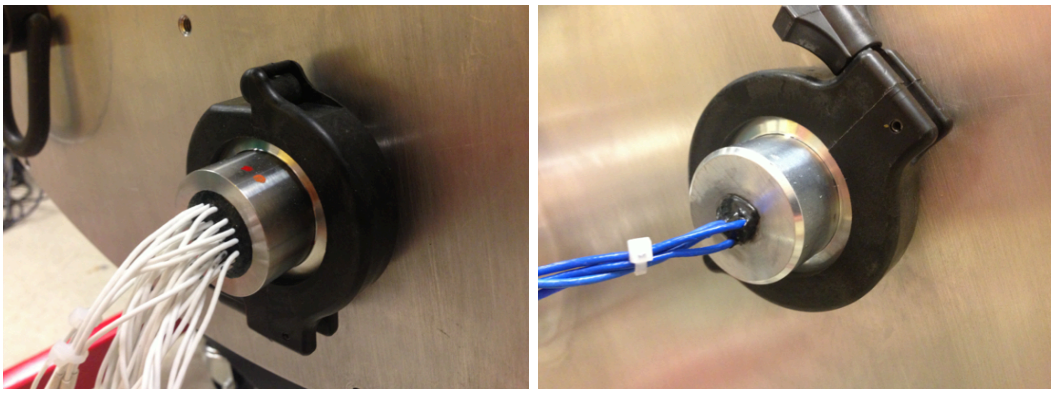

(a) Epoxy-sealed wire vacuum feedthroughs.

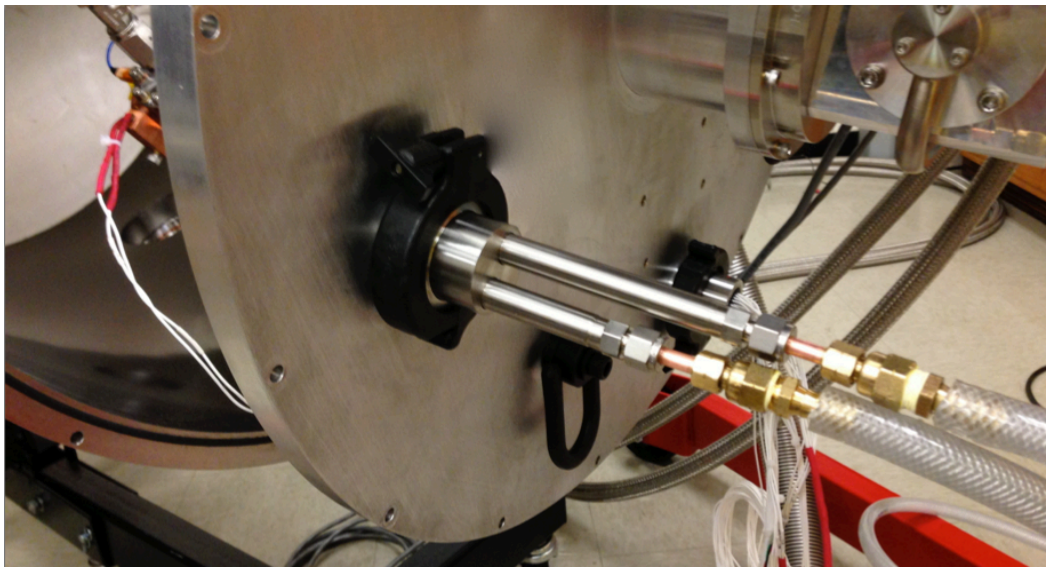

(b) Welded vacuum-jacketed liquid coolant feedthroughs

Figure A.5: Sensor and liquid coolant feedthroughs used in the rotating cryogenic vacuum test facility.

Slight vacuum is then pulsed on and off of the assembly, allowing trapped air within the epoxy to escape. The completed assembly is then cured for 24 hours while heated to approximately 40 °C. The cured assembly is the pressure tested, cleaned, and ready for use. The completed wire feedthroughs incorporated in the test facility are shown in Figure A.5a.

An alternative to this feedthrough method is to use glass-to-metal hermetic seal assemblies which surface mount with an O-ring face seal to the the vacuum vessel.

The negative consequences to that approach are increased expense as well as the introduction of additional terminations to the sensor wires, which creates an opportunity to introduce unwanted signal noise.

In order to pass cooling water or liquid nitrogen into an evacuated environment, welded vacuum-jacketed feedthroughs are used with a KF40 mounting flange. Feedthroughs are included with both 1/4" tube fitting ends as well as 1/4" Swagelock VCR fittings. These feedthroughs are also shown in Figure A.5b. These feedthroughs are incorporated to provide thermal rejection for experimental cold heads and test sections.

A.1.2 Cooling and Performance

Cooling of test sections is provided by a Sumitomo RDK-408D2 Gifford-McMahon cryocooler driven by a water-cooled F70L compressor requiring up to 9 kW of input electrical power. The two-stage refrigerator has a cooling capacity of 1 W at 4.2 K at the 2nd stage thermal intercept. The 1st stage intercept can also be used independently for large cooling loads at higher temperatures to provide cooling as low as 26 K and up to 80 W at 58 K. The sizing of this cooler is such that it should be able to handle most experimental cooling needs. The manufacturer's load map of the cooler is provided in Figure A.6 for reference.

Refrigerated and controlled circulated liquid coolant is also provided to cool test sections and experimental cold heads which require heat rejection at near ambient temperatures. A Julabo FL1201 chiller using a 50/50 mix of ethylene glycol and water provides thermal rejection over the controlled range of -20 to +40 °C with PID control accuracy of ±0.5 °C. The thermal rejection capacity is a maximum of 900 W at 20 °C with a circulation rate of up to 28 L/min.

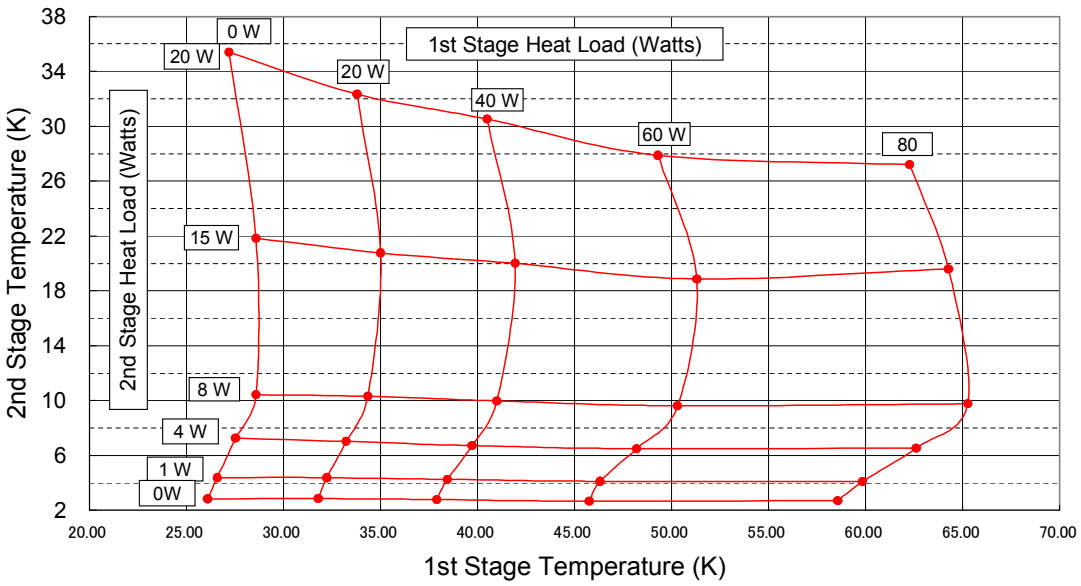

Figure A.6: Load map of Sumitomo RDK-408D2 2-stage G-M cooler incorporated in the test facility.

A.1.3 Thermometry and Heat Flow Measurement

Temperature measurements within the cryogenic testing dewar are made using a number of devices of varying precision. The least precise is a set of 32 small gauge Type-E thermocouples mounted in an epoxy-sealed KF40 feedthrough. The manufacturer specified tolerance on these devices is ±0.88 K at ambient temperatures. The second level of precision is a set of eight Cryogenic Control Systems (Cryo-Con) S900-A silicon diodes in an assortment of cap, bobbin, and SM packages. These sensors provide excellent sensitivity at low temperatures down to 4 K at a median price point. The accuracy of the A-band tolerance diode sensors is stated by the manufacturer as ±0.1 K at 1.5 - 30 K, ±0.5 K from 30 - 100 K, and ±1.0 K from 100 - 400 K. Reference temperature is provided by a 4L-calibrated Cernox CX-1070-CU thin-film resitance RTD from Lake Shore Cryotronics with calibrated accuracy of ±5 mK at 4.2 K up to ±40 mK at 300 K.

Temperature measurement is performed using a 4-channel Model 24C cryogenic temperature controller from Cryogenic Control Systems. Connections to the diodes

and RTD are made using 4-wire 36AWG phosphor-bronze ribbon cables thermally sunk to the cryocooler heat station. The combination of very fine gauge wire leads with small cross-section and the thermal sinking provides minimal heat leak to the sensors that could skew temperature measurements. 4-wire measurement is used to separately monitor voltage and provide excitation current, thus compensating for the resistance of the wire leads themselves.

The cooling power provided from the Sumitomo G-M cooler is not constant at a given temperature. The cooling power can depend on the temperature of the cooling water as well as the orientation of the device's cold head. Manufacturer testing has shown that the cold head performance is sensitive to tilt [102]. Independent lab testing at GT has shown that twist (about the centerline of the cooler) also affects performance slightly, presumably due to the 90° entry angle between the working gas lines and the cold head. For the purposes of collecting reliable and repeatable data, it is critical to gather information about the cooling load being removed by the G-M cooler in a more reliable way.

Publications by Taylor [31] and Taylor, Lewis, Bradley, and Radebaugh [103] describe the utility of a calibrated thermal bus bar that correlates temperature difference across the connection to the applied heat load. We have applied this methodology to the rotating experimental setup to measure heat flows. An oxygen-free electronic (OFE) copper bar was designed based on the maximum anticipated thermal load of the test sections of 50 W at 80 K. Using the load map shown in Figure A.6, the bus bar was designed using a coarse (10 element) finite difference model implemented in MATLAB based on 1-D conduction using Fourier's law as shown in Equation A.1, where the conductivity k_s is evaluated at the average temperature for each element.

$$Q = -k_s A_{x-sect} \frac{dT}{dx} \tag{A.1}$$

Cryogenic temperature-dependent conductivity of the bar stock base material was programmed using the 8th order logarithmic curve fits provided by NIST [88], and the

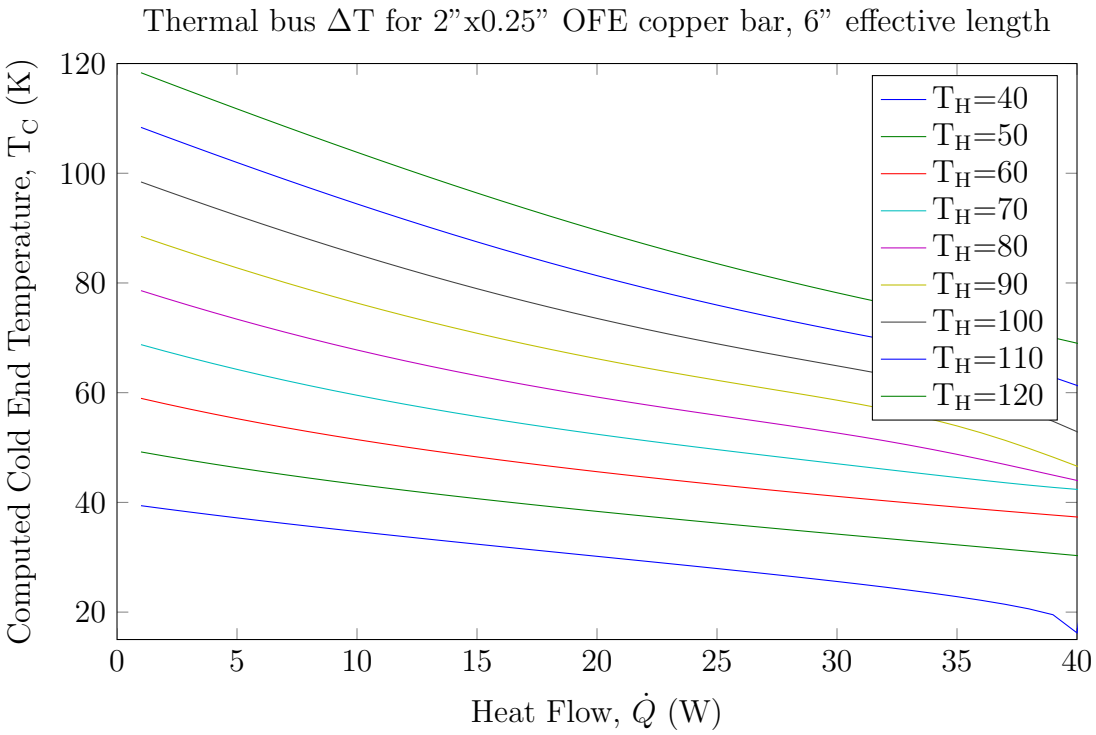

Figure A.7: Predicted bus bar temperature difference as a function of heat load and temperature. T_H is the temperature of the test section and T_C is the temperature of the G-M cooler interface.

solution was iterated until the values no longer changed. The predicted temperature difference as a function of experimental section temperature and heat rejection are shown in Figure A.7.

A 11.5 in. long bus bar with cross-section of 0.25 in. × 2 in. was fabricated incorporating mounting holes spaced 6 inches apart drilled to a depth of 0.125 inches, i.e. to the centerline of the bar. Cryo-Con S900-A-CP sensors were epoxy mounted into the holes using Stycast 2850-FT. Permanent mounting of the sensors ensures consistent thermal contact and location of the sensors such that the calibration does not change with time. The bar was bent 90° such that test sections are mounted perpendicular to the axis of the G-M cooler, inducing tilt as the chamber rotates. The bus bar was mounted to the stage 1 thermal intercept on the Sumitomo RDK-408D2 using 10-32 socket head cap screws with a thin layer of Apiezon-L grease between the

mating surfaces in order to create a good thermal interface.

Calibration of the thermal bus was performed by mounting one 50 Ω DC cartridge heater (Cryocon 3039-001) in a copper mounting block attached to the end of the bus bar as a fixed calibration load to simulate the applied load from the test section. Two additional 50 Ω 32AWG NiCr heater wires with Polyamide insulation were attached using aluminum tape to the 1st stage heat station of the G-M cooler as trim heaters. A smoothing tool was used to ensure that no air bubbles were trapped that could lead to virtual leaks in the vacuum chamber, thus limiting the vacuum level. One of the trim heaters was controlled using a PID loop on the temperature controller with the reference temperature being recorded at the opposing end of the bus bar where the experimental section would mount. As the temperature controller is only capable of PID controlling a 50 W heater load, the second G-M trim heater was powered with a variable DC laboratory power supply (Mastech HY3003). Once 50 W was reached using the temperature controller, saturating the PID control, the 50 W DC power supply was switched on providing the PID loop with overhead capacity to control.

The proportional (P), integral (I), and derivative (D) control settings were optimized using an autotune functionality of the controller, for which the temperature is first manually controlled near the desired temperature set point. Once temperature is manually stabilized, the controller performs a series of applied heat loads and measured the response to create a system model. The optimized control parameters are then generated automatically.

The measurement set point was set on the PID control which added trim heat until the temperature of the assembly stabilized. Power was then incrementally applied to the calibration heater to simulate experimental loads. Temperatures were allowed to restabilize according to the PID time constant. Actual power loads were computed using Ohm's law on the applied voltage measured using EZ DM-334 multimeter and

the known resistance of the heaters measured by the same device.

$$\dot{Q}_{applied} = \frac{V^2}{R_{heater}} \tag{A.2}$$

Calibration curves were collected for all anticipated temperature set points of the experimental section. Steady-state temperatures for each of the two bus bar sensors were recorded for each set point and the difference was computed. A calibration curve at each set temperature was generated as shown in Figure A.8.

A.1.4 Mass Flow Measurement

Mass flow measurement has been historically challenging at cryogenic temperatures. Measurements are even more challenging for the oscillatory flow present in pulse tube cryocoolers. The harsh working environment makes it difficult for most traditional flow sensor types such as hot wire anemometers to function reliably without breaking the sensitive wire element that makes it work. Additionally, as cryogenic temperatures are reached, the resistance of constant temperature anemometers decreases and the amount of power required to maintain probe temperature increases dramatically, introducing a non-negligible load in the experiments. It is also difficult to create probes sufficiently miniaturized to avoid disturbing the flow in the small cavities present.

In order to work around the difficulties associated with anemometers, a method of oscillatory flow measurement is utilized based on the pressure drop across a cold heat exchanger, thus the measurement can be performed using a component that would be present anyways. Differential pressure is recorded across a 19.05 mm diameter, 20 mm long pack of #100 mesh plain-weave copper screens used as the heat exchanger element within the CHX that interfaces with the G-M cooler, providing the cooling for experimental test sections. Cryogenic dynamic pressure sensors (PCB model 113B03 charge sensors with 422E51 inline charge capacitor) rated to approximately 20 K are incorporated in the heat exchanger design using 0.5 mm diameter holes drilled at a 45° angle such that the pressure tap intersects the corner of the heat exchanger,

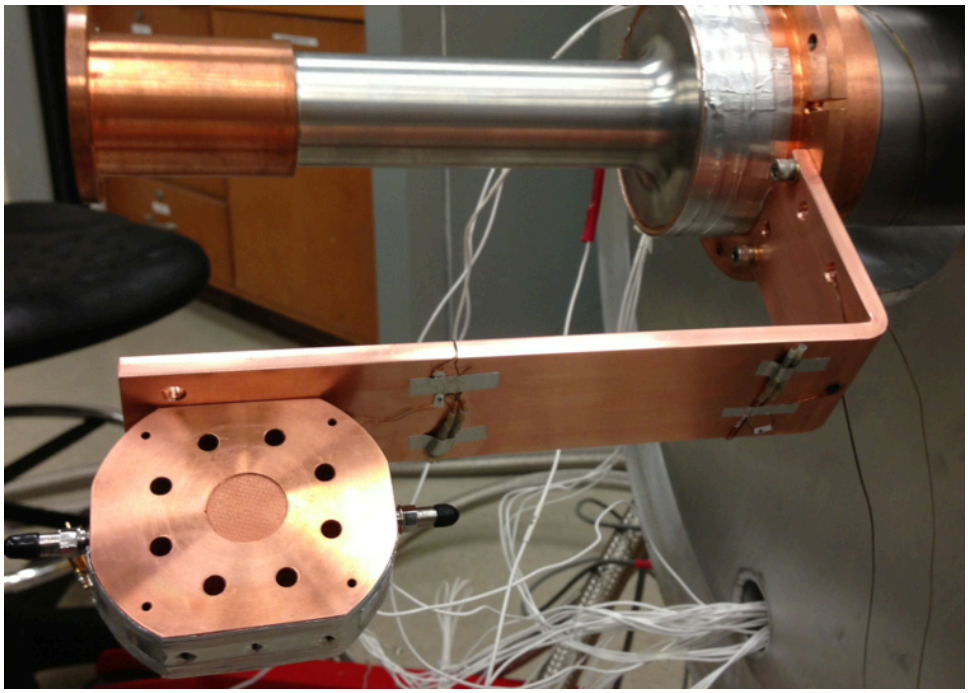

(a) Thermal bus apparatus

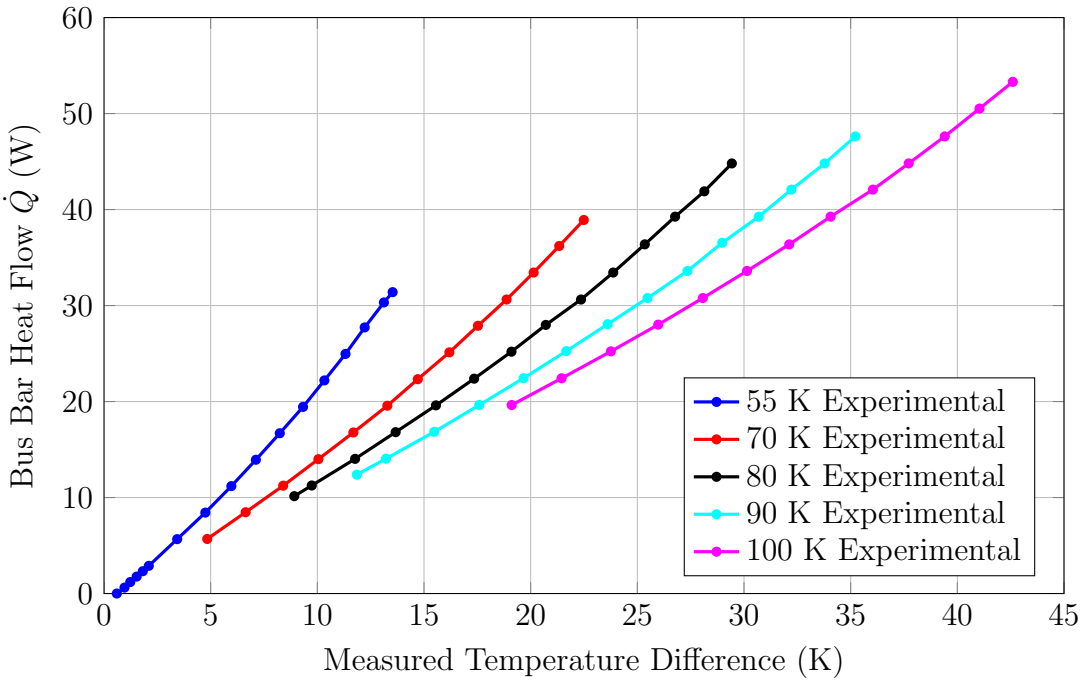

(b) Calibration curve

Figure A.8: Thermal bus apparatus and calibration curves showing steady-state temperature difference as a function of heat load and temperature. The reference temperature is at the end of the bus bar where the experimental load is applied.

introducing minimal dead volume. A rendered cross-section of the cold heat exchanger is shown in Figure A.9.

In order to calibrate the pressure difference across the heat exchanger to the oscillatory flow amplitude, a reference mass flow is needed. A calibration setup consisting of a pressure wave generator, the instrumented cold heat exchanger, and a nominally 50 cc calibration surge volume were connected, with indium wire seals between cryogenic components (more detail on the indium seals will be presented in Section A.2). Two PCB model 102A10 cryogenic pressure sensors were placed as reference sensors: one between the PWG and the CHX (upstream), the other in the surge volume. A number of assumptions are applied to relate the pressure in the surge volume to the mass flow exiting the cold heat exchanger. First, it is assumed that the helium behaves as an ideal gas such that the ideal gas law can be applied:

$$PV = mRT \tag{A.3}$$

where R is the gas constant for helium, V is the enclosed volume, P is the pressure, T is the gas temperature, and m is the enclosed mass of the gas. All properties are evaluated within the calibration surge volume. The ideal gas assumption is appropriate only if the gas temperature is in excess of about 60 K. Real gas correction can be applied using the compressibility factor Z for temperatures below 60 K. The gas is then assumed to experience adiabatic expansion and compression. This assumption holds due to the large diameter of the surge volume compared to the thermal penetration depth and the large thermal time constant of the wall material. Incorporating this assumption and rearranging leads to:

$$m = \frac{PV}{\gamma RT} \tag{A.4}$$

where γ is the ratio of specific heats. In the oscillatory flow scenario we must replace

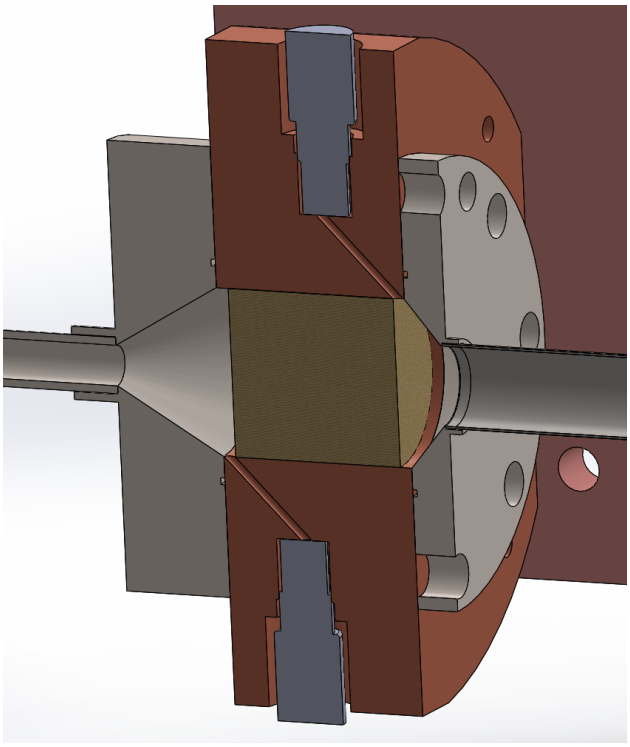

(a) Cross-section of cold heat exchanger. Gray inserts at top and bottom represent pressure sensors.

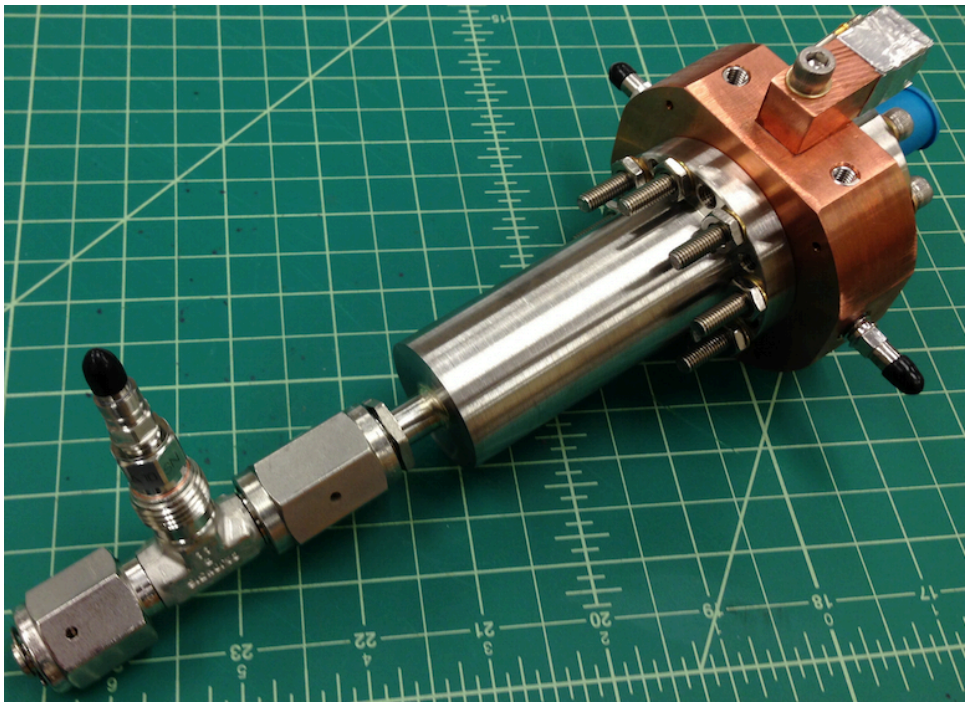

(b) Mass flow calibration setup. Left to right: SV pressure sensor, calibration SV, CHX (copper), transfer tube flange (behind CHX).

Figure A.9: Cross-section view of the experimental test section illustrating the cold heat exchanger configuration with pressure taps for mass flow and pressure ratio measurement and photos of the actual hardware.

mass m and pressure P with their harmonic representations:

$$P(t) = \widetilde{P} + \bar{P} = P_d \sin(\omega t + \varphi_p) + \bar{P} \tag{A.5a}$$

$$m(t) = \widetilde{m} + \bar{m} = m_d \sin(\omega t + \varphi_m) \tag{A.5b}$$

where the notations used are consistent with those presented in Chapter 2. In order to relate the adiabatic gas law relationship to measurable quantities, namely dynamic pressure and temperature, and obtain the mass flow rate we must substitute the harmonic pressure and mass in Equation A.4 and take the time derivative of both sides to obtain the rate form of the equation.

$$\left(\frac{dm(t)}{dt}\right) = \left(\frac{dP(t)}{dt}\right)\frac{V}{\gamma RT} \tag{A.6}$$

Computing the derivatives and isolating the magnitudes of the oscillating terms yields:

$$|\dot{m}| = (\omega P_d)\frac{V}{\gamma RT} \tag{A.7}$$

therefore, knowledge of the oscillating pressure amplitude in the surge volume, the temperature, and the precise volume of the surge volume allows the computation of the reference mass flow.

In order to determine the phase relationships between mass flow and pressure, the individual phases the pressure signals upstream (P1) and downstream (P2) must be measured. Pressure signals are simultaneously recorded using a NI-9234 high frequency dynamic signal acquisition card in a NI-cDAQ 9178 chassis at a sampling rate of 25.6 kHz. Although the signals being measured only contain frequency content less than 80 Hz, setting the Nyquist sampling criteria as low as 160 Hz, the high sampling rate used here is required to precisely isolate the amplitude and phase of the signals. The individual signal phases and amplitudes are computed using tone isolation modules in NI LabVIEW 2012's Sound & Vibration toolkit. The amplitudes and phases are computed and averaged over 2 seconds to minimize errors associated

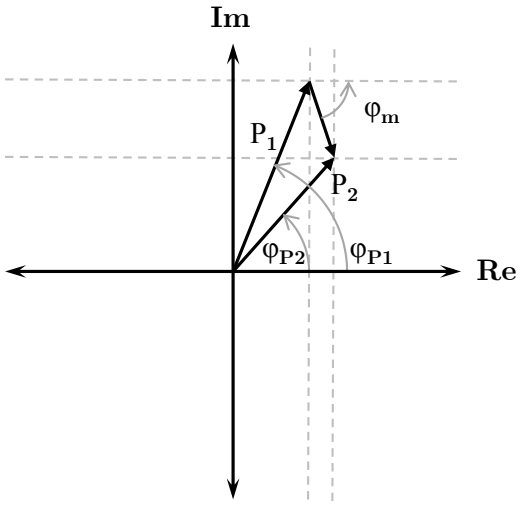

Figure A.10: Phasor diagram of the relationship between upstream pressure (P1), downstream pressure (P2), and the mass flow rate through the cold heat exchanger ($\dot{m}$).

with signal noise. The phases and amplitudes for signals P1 and P2 are applied to a phasor analysis relating the relevant properties as shown in Figure A.10.

The individual phase angles φ_{P1} and φ_{P1} and the computed dynamic amplitudes $P_{d,1}$ and $P_{d,2}$ were processed using trigonometric relationships to determine the mass flow phase angle:

$$\varphi_m = \tan^{-1}\left(\frac{P_{d,1}\sin\varphi_{P1} - P_{d,2}\sin\varphi_{P2}}{P_{d,2}\sin\varphi_{P2} - P_{d,1}\cos\varphi_{P1}}\right) \tag{A.8}$$

A rough initial calibration was performed at ambient temperatures. The results of this calibration are shown in Figure A.11. An order-of-magnitude validation of the resulting mass flow computation was performed by comparing the a measured pressure drop across the screen pack to the steady-flow pressure drop computed using the Forchheimer-extended version of Darcy's Law using the computed mass flow rate:

$$\Delta P_z = -\left(D_z\mu_g u_z L_{CHX} + \frac{\rho_g}{2}C_z u_z^2 L_{CHX}\right) \tag{A.9}$$

where the viscous and inertial coefficients are approximated for #100 mesh screens presented in Chapter 2. u_z is the superficial velocity (and therefore does not require scaling by porosity) related to mass flow via the cross-sectional area of the heat

exchanger and the gas density:

$$u_z = \frac{\dot{m}}{\rho A_{CHX}} \tag{A.10}$$

The theoretical pressure drop computed using the closed form steady-flow version of Darcy's law agreed with the measured pressure drop within 14.7%, which is excellent considering the uncertainty in the hydrodynamic parameters used in addition to the use of the steady flow computation in place of oscillatory flow. Calibration was limited to room temperature at the time of this dissertation due to the need to fabricate an aftercooler for the testing pressure wave generator (PWG). Without the aftercooler, testing can only be performed up to approximately 50 W input power before the intercept temperature reaches 120 K due to the acoustic power being entirely dissipated on the G-M cold head. As shown in Figure A.12, initial testing outside the vacuum chamber was performed to verify the functionality of the sensors at reduced temperatures. Calibration will be completed using this methodology within the vacuum chamber when the aftercooler is fabricated and installed.

A.1.5 Oscillatory Pressure Wave Excitation and Control

Oscillatory flow is excited in the system using a Chart/Q-Drive 2S132W resonant pressure wave generator (PWG) rated for 500 We continuous operation and a maximum of 600 W. The maximum working pressure is 3 MPa and the tested frequency range is 33-122 Hz, with a resonance (and therefore maximum PV power generation) around 60 Hz. The PWG is connected to the rotating test facility using a custom stainless steel KF40 flange adapter with O-ring face seal to the PWG. Adapters to 1/2 in. and 1/4 in. Swagelock VCR fittings were purchased to allow easy interchangeability with different-sized test sections. The PWG was purchased with an option set of pressure sensors (Endevco 8530B-500) that measure both static and dynamic pressure in the piston front and back volume, which can be calibrated approximately to the piston stroke. The PWG is controlled using an Allen-Bradley PowerFlex 700 drive

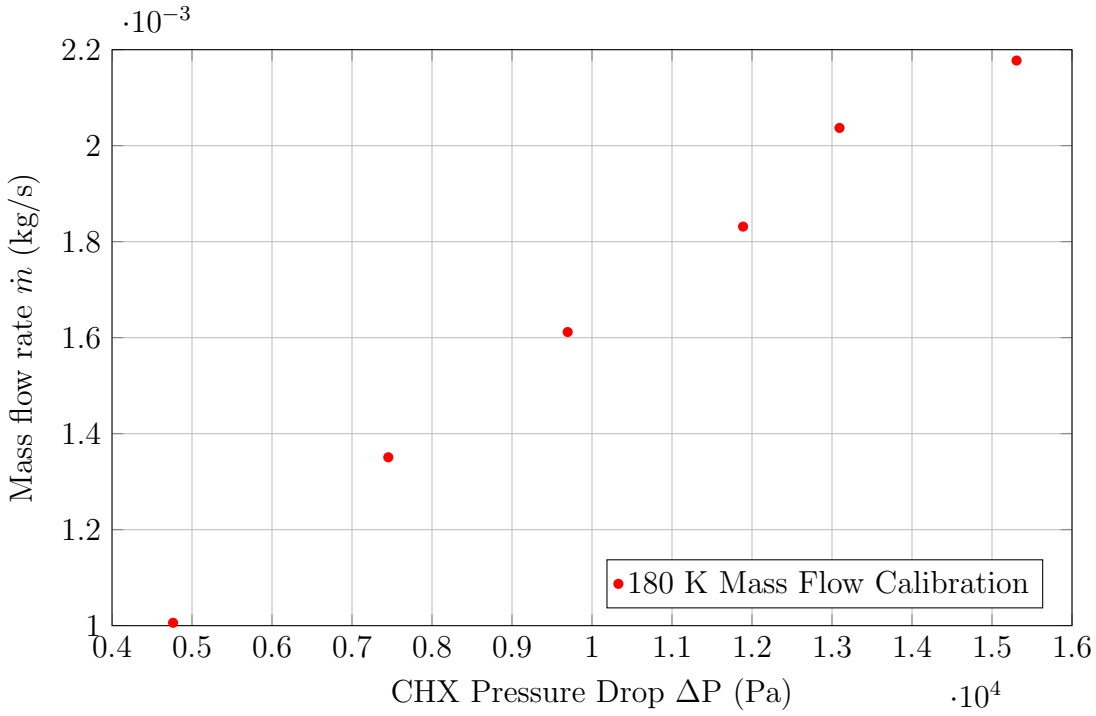

(a) Mass flow calibration curve

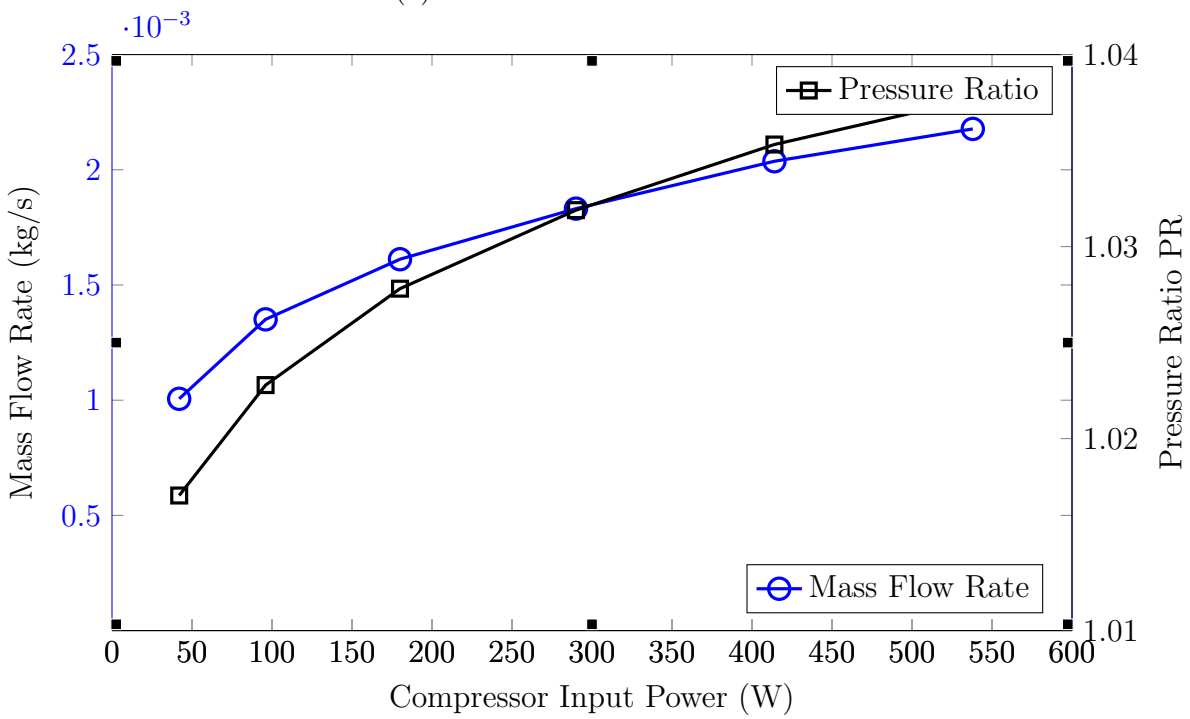

(b) Mass flow calibration curve

Figure A.11: Mass flow calibration curve for 180 K operation and mass flow and pressure ratio as a function of compressor input power.

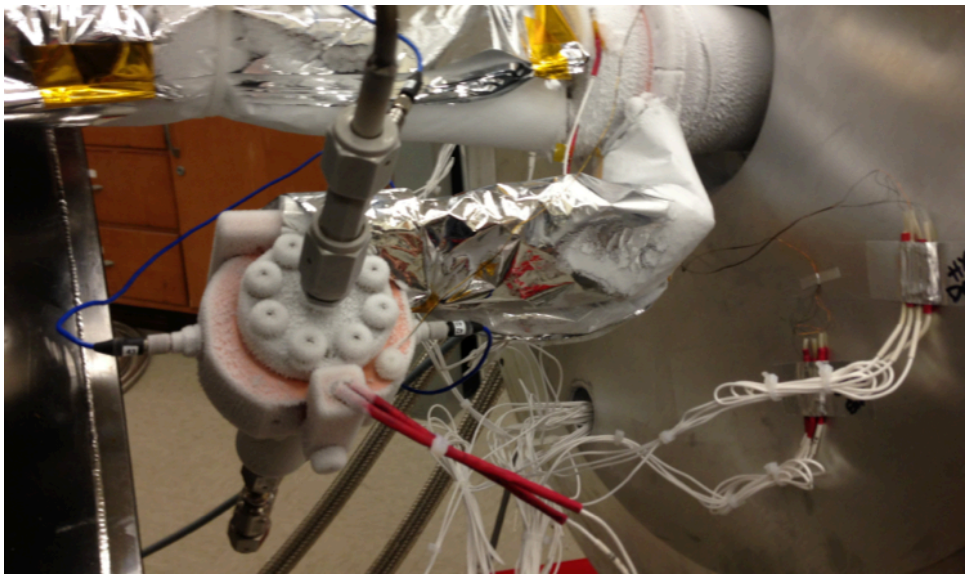

Figure A.12: Image of the mass flow calibration setup during ambient calibration testing at 180 K.

controller, allowing control of the frequency and voltage amplitude. The completed assembly mounted to the chamber lid is shown in Figure A.13.

A.2 Off-axis Pulse Tube Separate Effects Testing

A separate-effects testing setup for isolating energy flows in the pulse tube has been developed. A set of experimental 304 stainless steel pulse tubes with common volume but varying aspect ratio and a necessary warm heat exchanger were designed and fabricated. A schematic of the experimental test section is shown in Figure A.14. The completed experimental pulse tubes are shown in Figure A.15. 30-35° (included angle) conical tapers were included in the cold end flanges of each pulse tube to match the 19.05 mm (3/4 in.) cold heat exchanger diameter.

A warm heat exchanger was designed and fabricated consting of an OFHC copper housing filled with #100 copper mesh screens packed tightly using a machined tight-fitting ramrod of G10/FR4 fiberglass-epoxy resin. A 30° conical taper was included in the design to transition to the 4 mm I.D. inertance tube. Heat rejection occurs by passing temperature-controlled Glycol-water mixture through a helical coil of 0.25

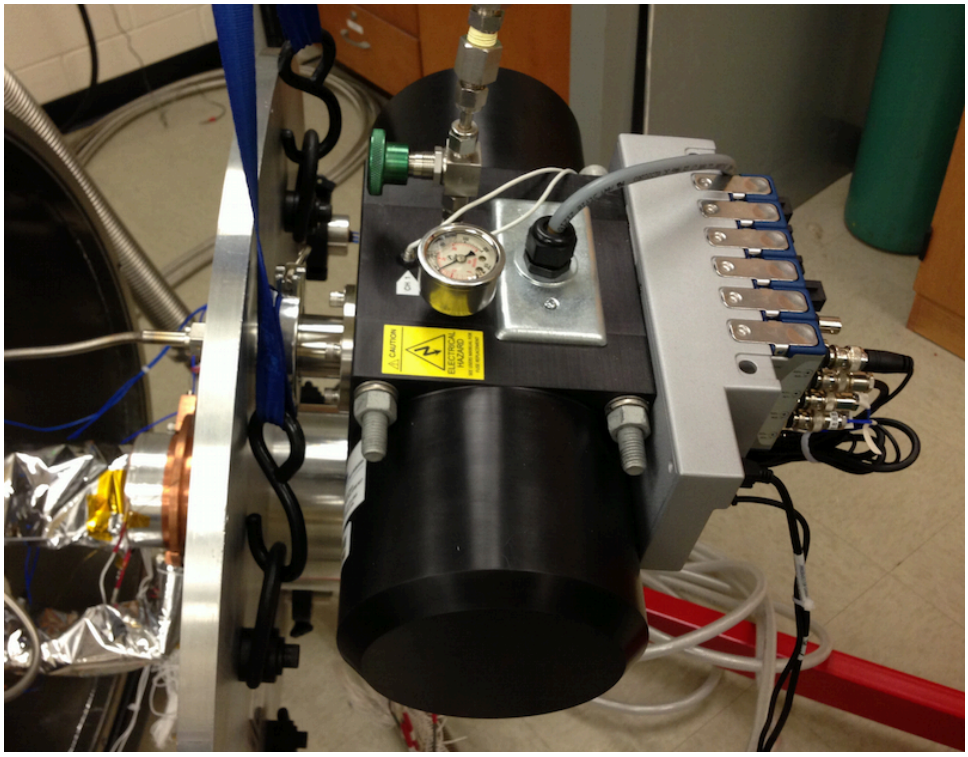

Figure A.13: Chart/Qdrive PWG mounted to the Dewar lid with custom stainless steel KF40 adapter.

in. O.D. copper tubing soldered to the circumference of the WHX housing. The completed WHX assembly is shown in Figure A.16.

A 4 mm I.D. stainless steel inertance tube 0.92 m long is connected to the warm heat exchanger with a 1/4 in. VCR fitting using an annealed copper gasket. A 50 cc surge volume is attached to the opposing end. The combined inertance tube and surge volume network were designed to produce a desired $-30°$ phase shift between mass flow and pressure at the cold end of the pulse tube sections; however, the actual phase shift is likely to vary for each of the three pulse tube designs.

On overview of the dimensions of the components designed and built for the separate effects test section is given in Table A.1

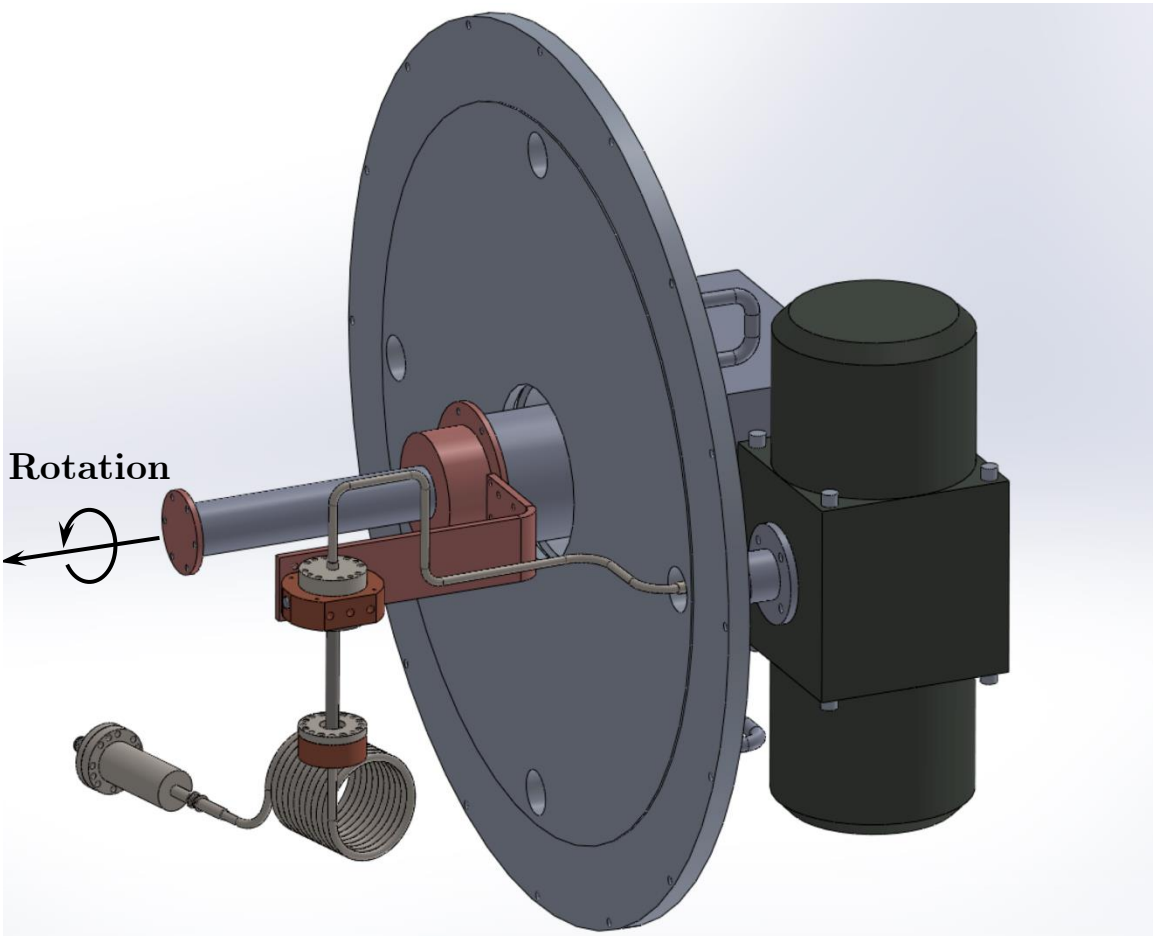

(a) Overview of pulse tube tilt test section.

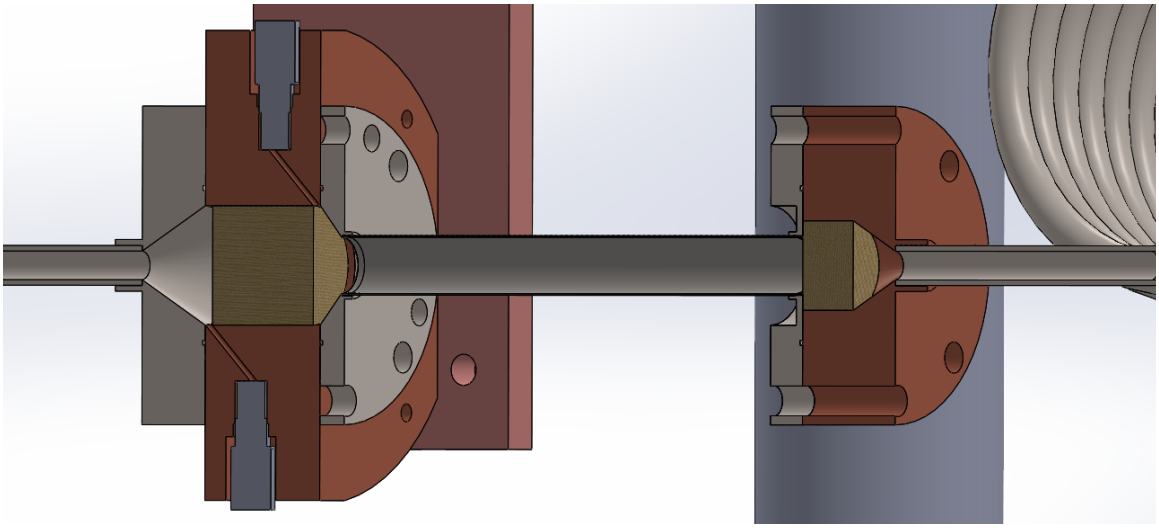

(b) Cross-section of the experimental pulse tube testing design.Parts from left to right: transfer tube, CHX, pulse tube, WHX, inertance tube.

Figure A.14: Schematic renderings of the pulse tube tilt test section assembly.

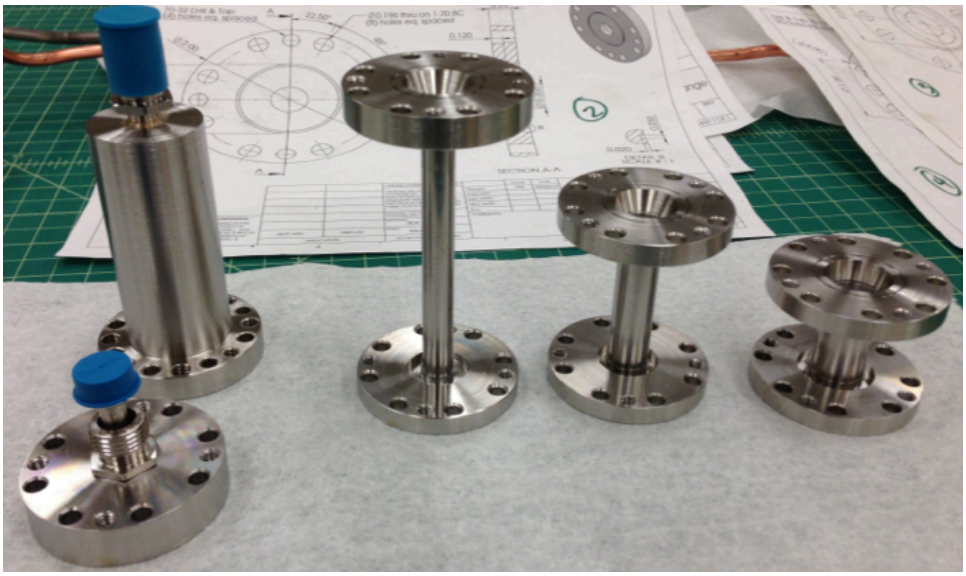

Figure A.15: Experimental pulse tubes.

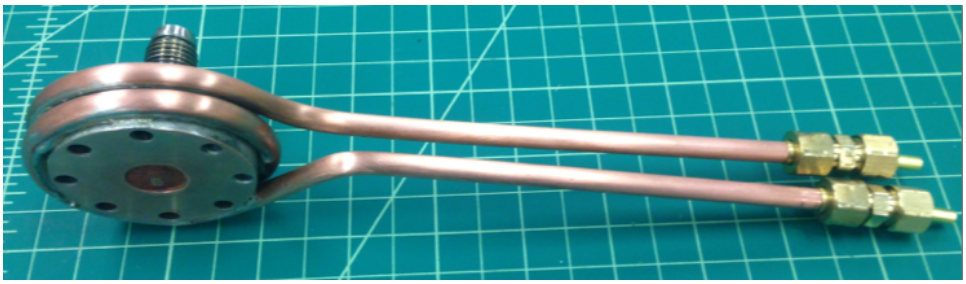

Figure A.16: OFHC copper warm heat exchanger (WHX) with liquid coolant loop.

Table A.1: Separate effects component dimensions relevant to flow.

Component	**Inside Diameter**	**Wall Thickness**	**Length**
Transfer Tube	4 mm	1.59 mm	-
Cold Heat Exchanger	19.05 mm	-	20 mm
L/D=10 Pulse Tube	9.017 mm	0.254 mm	90.17 mm
L/D=4.6 Pulse Tube	11.68 mm	0.508 mm	53.7 mm
L/D=2.235 Pulse Tube	14.86 mm	0.508 mm	33.2 mm
Warm Heat Exchanger	14.3 mm	-	10 mm
Inertance Tube	4 mm	1.59 mm	0.914 m
Surge Volume	29.21 mm	1.27 mm	74.68 mm

A.2.1 Fabrication, Cryogenic Seals, and Assembly Methods

A.2.1.1 Cryogenic Sealing

The pulse tubes mate to the previously described cold heat exchanger. High pressure seals at cryogenic temperatures are not straightforward as most compressible sealing materials become brittle upon cooling. The solution to this problem is to incorporate indium wire O-rings in precision machined grooves. The mating face is machined and polished to a surface finish of 32μin. or better to allow effective mating of the surfaces. Surfaces are prepared by ultrasonic cleaning in a degreasing solution, followed by thorough wipe down with acetone. The 0.030 inch diameter indium wire is then gently pressed into the O-ring groove and the ends of the wire are beveled using a razorblade such that they overlap one another and lightly pressed together to terminate the seal. Indium is a semi-precious metal that is extremely soft and remains ductile at temperatures approaching absolute zero. The metal also has the interesting attribute of being able to cold weld to dissimilar metals and to itself at room temperature, provided that the surfaces are free of contaminants and oxidation. The mating surfaces are guided together and torqued in a star pattern. Once the seal is made, it is set aside for an hour to allow the material to creep, then subsequently retightened before pressurizing. A properly prepared indium O-ring seal ready for mate-up is shown in Figure A.17.

Joints that need to be permanently made can be accomplished through a number of options depending on the materials to be joined. Materials common to this setup are oxygen-free high conductivity (OFHC) copper and AISI 304 stainless steel. Copper can easily be soldered to itself at low temperatures using 96%Pb-4% Staybrite^{TM} solder using rosin flux applied with a clean brush. Soft silver soldering can be done on a laboratory hot plate using a graphite heat spreader that will not mar polished copper surfaces. Stainless is a more difficult material to join due to a tough oxide

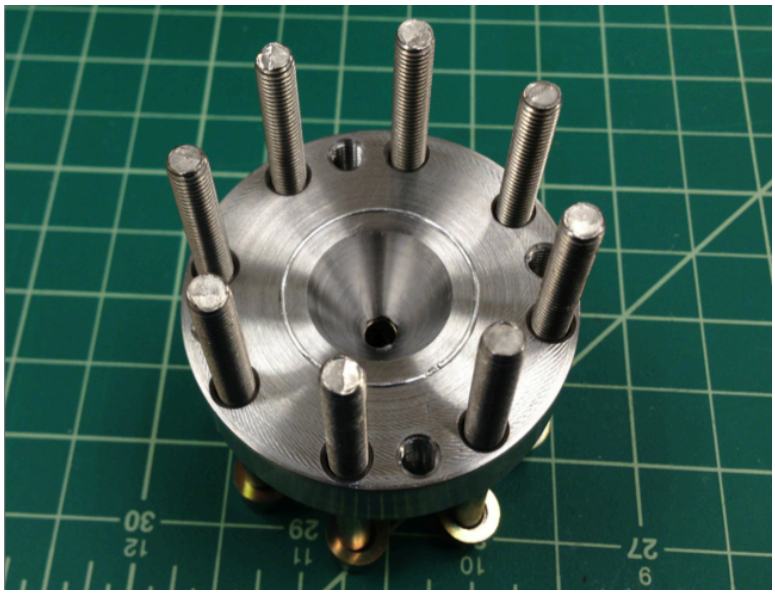

Figure A.17: Indium seal in an O-ring groove on the transfer tube flange prepared for assembly.

layer that will not dissolve below 950 °C that makes it impossible to wet at low temperatures. High temperature brazing is used instead to join stainless to stainless, or stainless to copper. The filler braze must be high purity silver, or a gold/copper alloy to properly wet the joint. For the pulse tubes built for this apparatus, braze material consisting of 50%Ag/15.5%Cu/15.5%Zn/16%Cd/3%Ni was used with Superior No. 601 silver braze paste flux. The joints were designed according to best practices for double scarf joints, with a 0.003" nominal gap between concentric parts. Heating was done using a Oxygen/MAP gas torch. Special care was taken to thoroughly heat copper parts prior to heating the stainless to avoid burning, as the high conductivity of the copper draws the heat away from the joint quickly, while the low conductivity stainless quickly overheats and oxidizes. For additional information on cryogenic joint design and techniques, please see Ref. [104].

A.2.2 Experimental Procedures

A.2.2.1 Evacuating and Pressurizing the Test Section

Volatile contamination can cause instability during cryogenic measurements. Gases remaining in the test section can be trapped within the porous sections and adsorbed within the surface of the metal wall materials. Volatile contamination occurs when trapped gases are cooled below their freezing point, solidifying on the walls and within the porous materials. As the frozen gas fills the matrix materials, the passages are occluded and the flow is restricted. In a cryocooler, this then causes the temperature to rise until the contaminant evaporates and flow is restored. This occurs in a cyclical pattern and makes repeatable measurements extremely challenging.

In order to avoid this contamination issue, proper preparation is required. The first step required is to thoroughly clean the passages of the test section using an ultrasonic cleaner with degreasing solution, followed by acetone cleaning. Once the assembly is sealed, it should be placed under high vacuum for a minimum of 24 hours to allow all volatiles to be evacuated. A residual pressure of approximately 1×10^{-6} torr or lower is desireable. Elevated temperature bakeout at approximately 320-340 K can be used to improve the efficacy and speed of the purging procedure using heaters installed on the test section. Leak testing using a mass spectrometer can help to identify any leak points that may exist in the test section. Once the section is fully evacuated and leak tested, it can be filled with helium. Pressure should be applied gradually to the system due to the presence of sensitive pressure sensors. Research grade helium with a minimum purity of 99.9999% should then be applied to the test section at the desired pressure.

A.3 Anticipated Applications and Suggestions for Future Use

A.3.1 Regenerator Performance Testing

The developed setup lends itself well to performance testing of regenerators down to temperatures of approximately 20 K (limited by the pressure sensor range). The calibrated mass flow meter and cryogenic pressure sensors can be applied to either side of a regenerator test section to determine the pressure drop in order to measure hydrodynamic parameters at cryogenic temperatures. This data would be immensely useful to cryocooler designers, as the room temperature data currently available may not represent the properties correctly at cryogenic temperatures.

A.3.2 Pulse Tube Static Orientation Testing

The scope and quantity of data that were able to be generated with computational methods were limited by the immense time and resources required to simulate cryogenic pulse tube refrigerators. The development of this facility will allow for the characterization of pulse tubes over a wide range of temperatures, fill pressures, mass flows, and frequencies in any orientation. Budget permitting, incorporation of a regenerator would complete the assembly in order to obtain a fully modular instrumented experimental cold head. The cryocooler intercept could then be used to precool instead of setting the cold temperature, allowing for the measurement of staged pulse tubes where the temperature of both pulse tube ends can be set. The calibrated thermal bus bar could then be used to measure heat rejection from the test section.

A.3.3 Pulse Tube Dynamic Orientation Testing

As mentioned in the Future Work section, dynamic tilt testing has become an interesting topic for future pulse tube research. The design of this experimental facility can be quickly and easily modified to incorporate a DC stepper motor to control the

rotational orientation of the chamber in real time. Virtually any SDOF rocking motion can be generated. Modification to the mount would include replacing the current mounting tube/bushing assembly with a solid shaft rotating on ball bearings. The stepper motor and drive assembly would then need to be mounted to the stand as well to drive the rocking motion.

APPENDIX B

FLUENT CODE

This appendix contains the codes used to define and execute FLUENT simulations within a Linux HPC (cluster computing) environment. The codes included are simply samples and vary according to the various models they control. For instance, turbulence models are applied subsequent to the initial model run and then runs are resumed manually, therefore the commands are not present in the text command samples.

Sample job scripts are also included for reference to future students who may wish to leverage supercomputing resources such as those provided by PACE at Georgia Tech.

B.1 System-Level Journal File

SLjournal.jou

```
rc mesh.msh
grid/reorder/reorder-domain
define/models/energy/y n n y y
define/models/unsteady-2nd-order/y
define/operating-conditions/operating-pressure/2.0e+6
define/operating-conditions/gravity y 0 -6.9367 -6.9367
define/operating-conditions/operating-density y 0
;
;--------Read in UDF Files----------------------;
;
/define/user-defined/compiled-functions/compile libudf yes ...
    moving_walls.c "" ""
/define/user-defined/compiled-functions/load/libudf
;
;-------- Access and read in material props-----;
;
define/materials/data-base/database-type/user-defined ...
    "cryomaterials.scm"
define/materials/copy/s/ofhc-cu-hot
define/materials/copy/s/ofhc-cu-cold
define/materials/copy/s/inco-c267
define/materials/copy/s/ss304
;
;--------Define Porous Media Conditions---------;
;
define/boundary-conditions/fluid chx n n n n n 0 n 0 n 0 n 0 n 1 ...
    n 1 n n y n n 1 n 0 n 0 n 0 n 1 n 0 y n 2.9e+10 n 2.9e+10 n ...
    1.7e+10 n n 50000 n 50000 n 50000 0 0 n 0.634 y y ofhc-cu-cold
```

```
define/boundary-conditions/fluid whx n n n n n 0 n 0 n 0 n 0 n 1 ...
    n 1 n n y n n 1 n 0 n 0 n 0 n 1 n 0 y n 2.9e+10 n 2.9e+10 n ...
    1.7e+10 n n 50000 n 50000 n 50000 0 0 n 0.634 y y ofhc-cu-hot
define/boundary-conditions/fluid regen n n n n n 0 n 0 n 0 n 0 n ...
    1 n 1 n n y n n 1 n 0 n 0 n 0 n 1 n 0 y n 2.85e+10 n 2.85e+10 ...
    n 1.7e+10 n n 58000 n 58000 n 27500 0 0 n 0.6738 y y ss304
define/boundary-conditions/fluid ac n n n n n 0 n 0 n 0 n 0 n 1 n ...
    1 n n y n n 1 n 0 n 0 n 0 n 1 n 0 y n 2.9e+10 n 2.9e+10 n ...
    1.7e+10 n n 50000 n 50000 n 50000 0 0 n 0.634 y y ofhc-cu-hot
define/boundary-conditions/solid ptwall y inco-c267 n n n n 0 n 0 ...
    n 0 n 0 n 0 n 1 n n
define/boundary-conditions/solid chxsolid y ofhc-cu-cold n n n n ...
    0 n 0 n 0 n 0 n 0 n 1 n n
define/boundary-conditions/solid whxsolid y ofhc-cu-hot n n n n 0 ...
    n 0 n 0 n 0 n 0 n 1 n n
;
;--------Set thermal boundary conditions------;
;
define/boundary-conditions/wall chxwall 0 n 0 y ofhc-cu y ...
    temperature n 60 n n n n 1
define/boundary-conditions/wall whxwall 0 n 0 y ofhc-cu y ...
    temperature n 300.0 n n n n 1
define/boundary-conditions/wall acwall 0 n 0 y ofhc-cu y ...
    temperature n 300.0 n n n n 1
;
;
;--------Define Dynamic Meshing Zone Motion---;
define/dynamic-mesh/dynamic-mesh? y n n n n
define/dynamic-mesh/controls/layering? y y
define/dynamic-mesh/controls/smoothing? n
define/dynamic-mesh/controls/layering-parameters/constant-height? n
define/dynamic-mesh/controls/layering-parameters/collapse-factor 0.04
```

```
45 define/dynamic-mesh/controls/layering-parameters/split-factor 0.4
46 define/dynamic-mesh/zones/create pistonface rigid-body ...
       "inlet_motion::libudf" n 0 0 0 0 0 0 piston constant 0.005 n
47 ;
48 ;--------Set solver parameters---------------;
49 ;
50 solve/set/gradient-scheme n n
51 solve/set/discretization-scheme/mom/1
52 solve/set/discretization-scheme/pressure/14
53 solve/set/discretization-scheme/temperature/1
54 solve/set/p-v-coupling/24
55 ;
56 ;
57 solve/set/p-v-controls 5 0.75 0.75
58 solve/set/under-relaxation mom 0.75
59 solve/set/under-relaxation density 0.75
60 solve/set/under-relaxation body 0.75
61 ;
62 ;
63 ;--------Set convergence criteria----;
64 ;
65 solve/monitors/residual convergence-criteria 1e-6 1e-6 1e-6 1e-6 1e-8
66 ;
67 ;--------Set gas props------;
68 ;
69 define/user-defined/real-gas/nist-real-gas y "helium.fld"
70 ;
71 ;--------Initialize Solution----------;
72 ;
73 define/custom-field-functions/define "pt-temp-grad" ...
       60.0*(300.0/60)^((-z_coordinate-0.095)/0.084864)
```

```
define/custom-field-functions/define "regen-temp-grad" ...
    (60.0-300.0)/(0.08)*(-z_coordinate-0.010)+300.0
;
solve/initialize/set-defaults/x-velocity 0.001
solve/initialize/set-defaults/y-velocity 0.001
solve/initialize/set-defaults/z-velocity 0.1
solve/initialize/initialize-flow
solve/patch whx whxsolid ac it sv piston () temperature n 300
solve/patch chx chxsolid () temperature n 60
solve/patch pt ptwall () temperature y pt-temp-grad
solve/patch regen () temperature y regen-temp-grad
;
;--------Set Auto-Save functions to recover cases in event of crash-;
file/write-case-data "base.cas"
file/auto-save/root-name ./results
file/auto-save/data-frequency 50
file/auto-save/case-frequency if-case-is-modified
file/auto-save/retain-most-recent-files y
file/auto-save/append-file-name-with time-step 10
;
;--------Set solution parameters & Iterate--------;
;
solve/set/timestep/4.1666668e-5
solve/dual-time-iterate 1 500
;
;--------Set Pulse Tube Surface Monitors---------;
;
solve/set/expert n n y n
solve/monitors/surface/set mdot1 "Mass Flow Rate" p1 () n n y ...
    "m1.out" 1 y flow-time
solve/monitors/surface/set mdot2 "Mass Flow Rate" p2 () n n y ...
    "m2.out" 1 y flow-time
```

```
103 solve/monitors/surface/set mdot3 "Mass Flow Rate" p3 () n n y ...
       "m3.out" 1 y flow-time
104 solve/monitors/surface/set mdot4 "Mass Flow Rate" p4 () n n y ...
       "m4.out" 1 y flow-time
105 solve/monitors/surface/set mdot4 "Mass Flow Rate" p4 () n n y ...
       "m5.out" 1 y flow-time
106 solve/monitors/surface/set v1 "Volume Flow Rate" p1 () n n y ...
       "v1.out" 1 y flow-time
107 solve/monitors/surface/set v2 "Volume Flow Rate" p2 () n n y ...
       "v2.out" 1 y flow-time
108 solve/monitors/surface/set v3 "Volume Flow Rate" p3 () n n y ...
       "v3.out" 1 y flow-time
109 solve/monitors/surface/set vdot4 "Volume Flow Rate" p4 () n n y ...
       "v4.out" 1 y flow-time
110 solve/monitors/surface/set vdot4 "Volume Flow Rate" p4 () n n y ...
       "v5.out" 1 y flow-time
111 solve/monitors/surface/set p1 "Area-Weighted Average" pressure p1 ...
       () n n y "p1.out" 1 y flow-time
112 solve/monitors/surface/set p2 "Area-Weighted Average" pressure p2 ...
       () n n y "p2.out" 1 y flow-time
113 solve/monitors/surface/set p3 "Area-Weighted Average" pressure p3 ...
       () n n y "p3.out" 1 y flow-time
114 solve/monitors/surface/set p4 "Area-Weighted Average" pressure p4 ...
       () n n y "p4.out" 1 y flow-time
115 solve/monitors/surface/set p5 "Area-Weighted Average" pressure p5 ...
       () n n y "p5.out" 1 y flow-time
116 solve/monitors/surface/set h1 "Flow Rate" enthalpy p1 () n n y ...
       "h1.out" 1 y flow-time
117 solve/monitors/surface/set h2 "Flow Rate" enthalpy p2 () n n y ...
       "h2.out" 1 y flow-time
118 solve/monitors/surface/set h3 "Flow Rate" enthalpy p3 () n n y ...
       "h3.out" 1 y flow-time
```

```
119 solve/monitors/surface/set h4 "Flow Rate" enthalpy p4 () n n y ...
       "h4.out" 1 y flow-time
120 solve/monitors/surface/set h4 "Flow Rate" enthalpy p5 () n n y ...
       "h5.out" 1 y flow-time
121 solve/monitors/surface/set qin "Integral" heat-flux chxwall () n ...
       n y "qin.out" 1 y flow-time
122 solve/monitors/surface/set qout "Integral" heat-flux whxwall () n ...
       n y "qout.out" 1 y flow-time
123 solve/monitors/surface/set qrej "Integral" heat-flux acwall () n ...
       n y "qacout.out" 1 y flow-time
124 solve/monitors/surface/set q1 "Integral" heat-flux p1wall () n n ...
       y "q1.out" 1 y flow-time
125 solve/monitors/surface/set q2 "Integral" heat-flux p2wall () n n ...
       y "q2.out" 1 y flow-time
126 solve/monitors/surface/set q3 "Integral" heat-flux p3wall () n n ...
       y "q3.out" 1 y flow-time
127 solve/monitors/surface/set q4 "Integral" heat-flux p4wall () n n ...
       y "q4.out" 1 y flow-time
128 solve/monitors/surface/set q5 "Integral" heat-flux p4wall () n n ...
       y "q5.out" 1 y flow-time
129 solve/monitors/surface/set dtdz1 "Area-Weighted Average" dt-dz p1 ...
       () n n y "dtdz1.out" 1 y flow-time
130 solve/monitors/surface/set dtdz2 "Area-Weighted Average" dt-dz p2 ...
       () n n y "dtdz2.out" 1 y flow-time
131 solve/monitors/surface/set dtdz3 "Area-Weighted Average" dt-dz p3 ...
       () n n y "dtdz3.out" 1 y flow-time
132 solve/monitors/surface/set dtdz4 "Area-Weighted Average" dt-dz p4 ...
       () n n y "dtdz4.out" 1 y flow-time
133 solve/monitors/surface/set dtdz5 "Area-Weighted Average" dt-dz p5 ...
       () n n y "dtdz5.out" 1 y flow-time
134 solve/monitors/surface/set k1 "Area-Weighted Average" ...
       thermal-conductivity-lam p1 () n n y "k1.out" 1 y flow-time
```

```
135 solve/monitors/surface/set k2 "Area-Weighted Average" ...
       thermal-conductivity-lam p2 () n n y "k2.out" 1 y flow-time
136 solve/monitors/surface/set k3 "Area-Weighted Average" ...
       thermal-conductivity-lam p3 () n n y "k3.out" 1 y flow-time
137 solve/monitors/surface/set k4 "Area-Weighted Average" ...
       thermal-conductivity-lam p4 () n n y "k4.out" 1 y flow-time
138 solve/monitors/surface/set k5 "Area-Weighted Average" ...
       thermal-conductivity-lam p5 () n n y "k5.out" 1 y flow-time
139 ;
140 ;--------Set System-level Specific Surface Monitors---------;
141 ;
142 solve/monitors/surface/set mregen1 "Mass Flow Rate" regenhot () n ...
       n y "mregen1.out" 1 y flow-time
143 solve/monitors/surface/set mregen2 "Mass Flow Rate" regencold () ...
       n n y "mregen2.out" 1 y flow-time
144 solve/monitors/surface/set vregen1 "Volume Flow Rate" regenhot () ...
       n n y "vregen1.out" 1 y flow-time
145 solve/monitors/surface/set vregen2 "Volume Flow Rate" regencold ...
       () n n y "vregen2.out" 1 y flow-time
146 solve/monitors/surface/set pregen1 "Area-Weighted Average" ...
       pressure regenhot () n n y "pregen1.out" 1 y flow-time
147 solve/monitors/surface/set pregen2 "Area-Weighted Average" ...
       pressure regencold () n n y "pregen2.out" 1 y flow-time
148 solve/monitors/surface/set hregen1 "Flow Rate" enthalpy regenhot ...
       () n n y "hregen1.out" 1 y flow-time
149 solve/monitors/surface/set hregen2 "Flow Rate" enthalpy regencold ...
       () n n y "hregen2.out" 1 y flow-time
150 solve/monitors/surface/set dtdzregen1 "Area-Weighted Average" ...
       dt-dz regenhot () n n y "dtdzregen1.out" 1 y flow-time
151 solve/monitors/surface/set dtdzregen2 "Area-Weighted Average" ...
       dt-dz regencold () n n y "dtdzregen2.out" 1 y flow-time
```

```
152 solve/monitors/surface/set kregen1 "Area-Weighted Average" ...
       thermal-conductivity-lam regenhot () n n y "kregen1.out" 1 y ...
       flow-time
153 solve/monitors/surface/set kregen2 "Area-Weighted Average" ...
       thermal-conductivity-lam regencold () n n y "kregen2.out" 1 y ...
       flow-time
154 solve/monitors/surface/set mregen1 "Mass Flow Rate" regenhot () n ...
       n y "mregen1.out" 1 y flow-time
155 ;
156 ;solve/dual-time-iterate 29999 120
```

B.2 Component-Level Journal File

CLjournal.jou

```
rc 77K.msh
grid/reorder/reorder-domain
define/models/energy/y n n y y
define/models/unsteady-2nd-order/y
define/operating-conditions/operating-pressure/2.0e+6
define/operating-conditions/gravity y 0 -9.8085 -0.1712
define/operating-conditions/operating-density y 0
;
;--------Read in UDF Files----------;
;
/define/user-defined/compiled-functions/compile libudf yes ...
    mdotin_Pout.c "" ""
/define/user-defined/compiled-functions/load/libudf
;
;-------- Access and read in material props--------;
;
define/materials/data-base/database-type/user-defined ...
    "cryomaterials.scm"
define/materials/copy/s/ofhc-cu-hot
define/materials/copy/s/ofhc-cu-cold
define/materials/copy/s/inco-c267
;
;--------Define Porous Media Conditions----------;
;
define/boundary-conditions/fluid part-chx1 n n n n n 0 n 0 n 0 n ...
    0 n 1 n 1 n n y n n 1 n 0 n 0 n 0 n 1 n 0 y n 2.9e+10 n ...
    2.9e+10 n 1.7e+10 n n 50000 n 50000 n 50000 0 0 n 0.634 y y ...
    ofhc-cu-cold
```

```
define/boundary-conditions/fluid part-whx1 n n n n n 0 n 0 n 0 n ...
    0 n 1 n 1 n n y n n 1 n 0 n 0 n 0 n 1 n 0 y n 2.9e+10 n ...
    2.9e+10 n 1.7e+10 n n 50000 n 50000 n 50000 0 0 n 0.634 y y ...
    ofhc-cu-hot
define/boundary-conditions/solid part-pt1-wall y inco-c267 n n n ...
    n 0 n 0 n 0 n 0 n 0 n 1 n n
define/boundary-conditions/solid part-pt2-wall y inco-c267 n n n ...
    n 0 n 0 n 0 n 0 n 0 n 1 n n
define/boundary-conditions/solid part-pt3-wall y inco-c267 n n n ...
    n 0 n 0 n 0 n 0 n 0 n 1 n n
define/boundary-conditions/solid part-pt4-wall y inco-c267 n n n ...
    n 0 n 0 n 0 n 0 n 0 n 1 n n
;
;--------Set flow boundary conditions------;
;
define/boundary-conditions/mass-flow-inlet mass-flow-inlet y y y ...
    y "udf" "mdot_inlet::libudf" n 4.0 n 0 n y
define/boundary-conditions/pressure-outlet pressure-outlet y y ...
    "udf" "p_outlet::libudf" n 20.0 n y n n n
;
;
;--------Set thermal boundary conditions---------;
;
define/boundary-conditions/wall chx-wall 0 n 0 y ofhc-cu y ...
    temperature n 4.0 n n n n 1
define/boundary-conditions/wall whx-wall 0 n 0 y ofhc-cu y ...
    temperature n 20.0 n n n n 1
;
;
;--------Set solver parameters-----------;
;
solve/set/gradient-scheme n n
```

```
45 solve/set/discretization-scheme/mom/1
46 solve/set/discretization-scheme/pressure/14
47 solve/set/discretization-scheme/temperature/1
48 solve/set/p-v-coupling/24
49 ;
50 ;
51 solve/set/p-v-controls 5 0.75 0.75
52 solve/set/under-relaxation mom 0.75
53 solve/set/under-relaxation density 0.75
54 solve/set/under-relaxation body 0.75
55 ;
56 ;
57 ;--------Set convergence criteria----------;
58 ;
59 solve/monitors/residual convergence-criteria 1e-6 1e-6 1e-6 1e-6 1e-8
60 ;
61 ;--------Set gas props--------------------;
62 ;
63 define/user-defined/real-gas/nist-real-gas y "helium.fld"
64 ;
65 ;--------Initialize Solution--------------;
66 ;
67 define/custom-field-functions/define "temp-grad" ...
       4.0*(20.0/4.0)^((-z_coordinate-0.005)/0.08486)
68 solve/initialize/hyb-initialization
69 solve/patch part-whx1 () temperature n 20.0
70 solve/patch part-chx1 () temperature n 4.0
71 solve/patch part-pt1-wall part-pt1 part-pt2-wall part-pt2 ...
       part-pt3 part-pt3-wall part-pt4-wall part-pt4 () temperature y ...
       temp-grad
72 ;
73 ;---Set Auto-Save functions to recover cases in event of crash----;
```

```
file/write-case-data "base.cas"
file/auto-save/root-name ./results
file/auto-save/data-frequency 50
file/auto-save/case-frequency if-case-is-modified
file/auto-save/retain-most-recent-files y
file/auto-save/append-file-name-with time-step 9
file/auto-save/max-files 9
;
;--------Set solution parameters & Iterate -------;
;
solve/set/timestep/1e-4
solve/dual-time-iterate 1 500
;
;--------Set surface monitors--------;
;
solve/set/expert n n y n
solve/monitors/surface/set mdotin "Mass Flow Rate" chx-pt () n n ...
    y "mdotin.out" 1 y flow-time
solve/monitors/surface/set mdot1 "Mass Flow Rate" p1 () n n y ...
    "m1.out" 1 y flow-time
solve/monitors/surface/set mdot2 "Mass Flow Rate" p2 () n n y ...
    "m2.out" 1 y flow-time
solve/monitors/surface/set mdot3 "Mass Flow Rate" p3 () n n y ...
    "m3.out" 1 y flow-time
solve/monitors/surface/set mdotout "Mass Flow Rate" pt-whx () n n ...
    y "mdotout.out" 1 y flow-time
solve/monitors/surface/set vdotin "Volume Flow Rate" chx-pt () n ...
    n y "vdotin.out" 1 y flow-time
solve/monitors/surface/set v1 "Volume Flow Rate" p1 () n n y ...
    "v1.out" 1 y flow-time
solve/monitors/surface/set v2 "Volume Flow Rate" p2 () n n y ...
    "v2.out" 1 y flow-time
```

```
98 solve/monitors/surface/set v3 "Volume Flow Rate" p3 () n n y ...
       "v3.out" 1 y flow-time
99 solve/monitors/surface/set vdotout "Volume Flow Rate" pt-whx () n ...
       n y "vdotout.out" 1 y flow-time
100 solve/monitors/surface/set pin "Area-Weighted Average" pressure ...
       chx-pt () n n y "pin.out" 1 y flow-time
101 solve/monitors/surface/set p1 "Area-Weighted Average" pressure p1 ...
       () n n y "p1.out" 1 y flow-time
102 solve/monitors/surface/set p2 "Area-Weighted Average" pressure p2 ...
       () n n y "p2.out" 1 y flow-time
103 solve/monitors/surface/set p3 "Area-Weighted Average" pressure p3 ...
       () n n y "p3.out" 1 y flow-time
104 solve/monitors/surface/set pout "Area-Weighted Average" pressure ...
       pt-whx () n n y "pout.out" 1 y flow-time
105 solve/monitors/surface/set hin "Flow Rate" enthalpy chx-pt () n n ...
       y "hin.out" 1 y flow-time
106 solve/monitors/surface/set h1 "Flow Rate" enthalpy p1 () n n y ...
       "h1.out" 1 y flow-time
107 solve/monitors/surface/set h2 "Flow Rate" enthalpy p2 () n n y ...
       "h2.out" 1 y flow-time
108 solve/monitors/surface/set h3 "Flow Rate" enthalpy p3 () n n y ...
       "h3.out" 1 y flow-time
109 solve/monitors/surface/set hout "Flow Rate" enthalpy pt-whx () n ...
       n y "hout.out" 1 y flow-time
110 solve/monitors/surface/set qin "Integral" heat-flux chx-wall () n ...
       n y "qin.out" 1 y flow-time
111 solve/monitors/surface/set qout "Integral" heat-flux whx-wall () ...
       n n y "qout.out" 1 y flow-time
112 solve/monitors/surface/set q1 "Integral" heat-flux p1-wall () n n ...
       y "q1.out" 1 y flow-time
113 solve/monitors/surface/set q2 "Integral" heat-flux p2-wall () n n ...
       y "q2.out" 1 y flow-time
```

```
114 solve/monitors/surface/set q3 "Integral" heat-flux p3-wall () n n ...
      y "q3.out" 1 y flow-time
115 solve/monitors/surface/set dtdzin "Area-Weighted Average" dt-dz ...
      chx-pt () n n y "dtdzin.out" 1 y flow-time
116 solve/monitors/surface/set dtdz1 "Area-Weighted Average" dt-dz P1 ...
      () n n y "dtdz1.out" 1 y flow-time
117 solve/monitors/surface/set dtdz2 "Area-Weighted Average" dt-dz P2 ...
      () n n y "dtdz2.out" 1 y flow-time
118 solve/monitors/surface/set dtdz3 "Area-Weighted Average" dt-dz P3 ...
      () n n y "dtdz3.out" 1 y flow-time
119 solve/monitors/surface/set dtdzout "Area-Weighted Average" dt-dz ...
      pt-whx () n n y "dtdzout.out" 1 y flow-time
120 solve/monitors/surface/set kin "Area-Weighted Average" ...
      thermal-conductivity-lam chx-pt () n n y "kin.out" 1 y flow-time
121 solve/monitors/surface/set k1 "Area-Weighted Average" ...
      thermal-conductivity-lam p1 () n n y "k1.out" 1 y flow-time
122 solve/monitors/surface/set k2 "Area-Weighted Average" ...
      thermal-conductivity-lam p2 () n n y "k2.out" 1 y flow-time
123 solve/monitors/surface/set k3 "Area-Weighted Average" ...
      thermal-conductivity-lam p3 () n n y "k3.out" 1 y flow-time
124 solve/monitors/surface/set kout "Area-Weighted Average" ...
      thermal-conductivity-lam pt-whx () n n y "kout.out" 1 y flow-time
125 ;
126 solve/dual-time-iterate 29999 100
```

B.3 Moving Piston Wall User-Defined Functions

moving_walls.c

```
#include "udf.h"

DEFINE_CG_MOTION(inlet_motion, dt, vel, omega, time, dtime)
{
  real freq = 60.0;
  real w = 2.0*M_PI*freq;
  real Uamp = 3.41;
  real phase = M_PI;

  /* reset velocities */
  NV_S (vel, =, 0.0);
  NV_S (omega, =, 0.0);

  vel[2] = Uamp*sin(w*time + phase);
}
```

B.4 Oscillating Mass Flow Inlet and Pressure Outlet User-Defined Functions

mdotin_Pout.c

```
#include "udf.h"

#define freq 40
#define M1 0.004
#define M1_phi 30.0
#define P1 400000
#define P1_phi 0.0

DEFINE_PROFILE(mdot_inlet, thread, position)
{
 face_t f;
 real t = CURRENT_TIME;
  real omega  = 2*M_PI*freq;
 begin_f_loop(f, thread)
  {
  F_PROFILE(f, thread, position) = ...
      (M1/2*sin(1*omega*t-M1_phi*M_PI/180));
  }
 end_f_loop(f,thread)
}

DEFINE_PROFILE(p_outlet, thread, position)
{
 face_t f;
 real t = CURRENT_TIME;
  real omega  = 2*M_PI*freq;
 begin_f_loop(f, thread)
  {
```

```
28    F_PROFILE(f, thread, position) = ...
          (P1*sin(1*omega*t+P1_phi*M_PI/180));
29    }
30   end_f_loop(f,thread)
31  }
```

B.5 Sample Cluster Job Script

pace-job-script.pbs

```
#PBS -N LD4_System-level_91     %<Job ID>
#PBS -l nodes=1:ppn=64      %<#nodes>:<#CPUs>
#PBS -l mem=16gb        %<Memory Requested>
#PBS -l walltime=120:00:00  %<Wall Clock Length of Run> estimate, ...
    up to max allowed
#PBS -q prometforce-6       %<queue-name>
#PBS -k oe          %request output logs
#PBS -m abe
#PBS -M tom.mulcahey@gatech.edu %<Email address for output logs>

cd $PBS_O_WORKDIR       %sets current folder as work directory
%Following lines are headers for the log files and email ...
    notifications
echo "Started on `/bin/hostname`"
echo "Nodes chosen are:"
cat $PBS_NODEFILE

module load ansys/14.5.7    %Choose current version of ANSYS, NOT ...
    14.5.0

fluent 3ddp -pshmem -alnamd64 -r14.5.7 -t62 -ssh -pinfiniband ...
    -mpi=pcmpi -path/usr/local/packages/ansys/14.5.7/v145/fluent ...
    -g < journal.jou

%fluent <3-D or 2-D> -<allow shared memory> -<64-bit OS> -<Ansys ...
    version to match loaded> -t<# parallel processes> -<launch ...
    remotely via SSH> -<select interconnect type> -<select MPI ...
    method> -<path where Ansys lives> -g<run without GUI> < ...
    <Journal file to use instead of GUI>
```

APPENDIX C

MATLAB PROCESSING CODES

C.1 System-Level Post-Processing Code

FOMSL.m

```
1
2  %%This Matlab code reads Fluent data files and calculates the ...
       pulse tube
3  %%efficiency based on cycle-averaged quantities during the final ...
       cycle.
4
5  DELIMITER = ' ';
6  %Request location of data files from user
7  [fname, file]=uigetfile('*.*','1');
8
9  %User inputs (case-dependent)
10 d_in=input('pulse tube diameter');
11 A=pi/8*d_in^2;                              %x-sect area of PT, ...
       divided by 2 for half-symmetry (fixed 11-13)
12 f=input('Operating Frequency (Hz)');      %Cooler operating frequency
13 n=input('Samples per time cycle');        %number of time steps ...
       per cycle
14 epsHX=0.634;                             %Porosity of Heat ...
       exchangers (#140 twill)
15 kHXc=(1-epsHX)*670;                      %Effective HX conductivity
16 kHXh=(1-epsHX)*300;                      %Effective HX conductivity
17 epsREGEN=0.6425;                         %Porosity of Regenerator ...
       Screens (#325 mesh)
```

```
kREGEN=(1-epsREGEN)*670;                %Effective Regenerator ...
    conductivity
AREGEN=pi*0.018^2/4;                    %Regenerator X-sect flow area
Pcharge=2e+6;                           %System charge (fill) ...
    pressure, Pa

%-------------------------------------------------------------------------%
%Read data files at Location 1 (CHX-PT transition)
%-------------------------------------------------------------------------%
p1=dlmread(strcat(file,'p1.out'),DELIMITER,2,0);
h1=dlmread(strcat(file,'h1.out'),DELIMITER,2,0);
q1=dlmread(strcat(file,'q1.out'),DELIMITER,2,0);
V1=dlmread(strcat(file,'v1.out'),DELIMITER,2,0);
k1=dlmread(strcat(file,'k1.out'),DELIMITER,2,0);
dtdz1=dlmread(strcat(file,'dtdz1.out'),DELIMITER,2,0);
m1=dlmread(strcat(file,'m1.out'),DELIMITER,2,0);

%Clean up extra data points from run restarts
p1=cleanmyoutfile(p1);
h1=cleanmyoutfile(h1);
q1=cleanmyoutfile(q1);
V1=cleanmyoutfile(V1);
k1=cleanmyoutfile(k1);
dtdz1=cleanmyoutfile(dtdz1);
m1=cleanmyoutfile(m1);

%Calculate real-time PV power
PV1=[p1(:,1) p1(:,2).*V1(:,2)];

%compute corrections for porous HX interface
hg1=[h1(:,1) epsHX.*h1(:,2)];
%Gas Conduction
```

```
Qg1=[k1(:,1) -k1(:,2).*(A*epsHX).*dtdz1(:,2)];
%Matrix Conduction
Qm1=[dtdz1(:,1) -kHXc.*A.*(1-epsHX).*dtdz1(:,2)];

%Compute last cycle averages (LCA)
hLCA1=LCA(hg1,n,f);
qwallLCA1=LCA(q1,n,f);
QgLCA1=LCA(Qg1,n,f);
QmLCA1=LCA(Qm1,n,f);
PVLCA1=LCA(PV1,n,f);

%Compute cycle-avg net energy flow
edotLCA1=hLCA1+qwallLCA1+QgLCA1+QmLCA1
FOM1=edotLCA1/PVLCA1;

%Compute real-time energy flow and perform moving cycle-avg
e1=[hg1(:,1) hg1(:,2)+q1(:,2)+Qg1(:,2)+Qm1(:,2)];

win=n;
CA_e1=zeros(size(e1));
for i=(win+1):(length(e1))
    CA_e1(i,1)=e1(i,1);
    CA_e1(i,2)=f*trapz(e1((i-win):i,1),e1((i-win):i,2));
end
%Compute real-time PV Power and perform moving cycle-avg
CA_PV1=zeros(size(PV1));
for i=(win+1):(length(PV1))
    CA_PV1(i,1)=PV1(i,1);
    CA_PV1(i,2)=f*trapz(PV1((i-win):i,1),PV1((i-win):i,2));
end
FOMt1=CA_e1(:,2)./CA_PV1(:,2);
t=CA_e1(:,1);
```

```
80
81 %------------------------------------------------------------------------%
82 % Repeat full process for Point 2 (0.5mm from PT Cold end)
83 %------------------------------------------------------------------------%
84
85 p2=dlmread(strcat(file,'p2.out'),DELIMITER,2,0);
86 h2=dlmread(strcat(file,'h2.out'),DELIMITER,2,0);
87 q2=dlmread(strcat(file,'q2.out'),DELIMITER,2,0);
88 V2=dlmread(strcat(file,'v2.out'),DELIMITER,2,0);
89 k2=dlmread(strcat(file,'k2.out'),DELIMITER,2,0);
90 dtdz2=dlmread(strcat(file,'dtdz2.out'),DELIMITER,2,0);
91 m2=dlmread(strcat(file,'m2.out'),DELIMITER,2,0);
92
93 p2=cleanmyoutfile(p2);
94 h2=cleanmyoutfile(h2);
95 q2=cleanmyoutfile(q2);
96 V2=cleanmyoutfile(V2);
97 k2=cleanmyoutfile(k2);
98 dtdz2=cleanmyoutfile(dtdz2);
99 m2=cleanmyoutfile(m2);
100
101 %Compute velocity amplitude for N_ptc calculations
102 VcMAX=max(V1(length(V1)-n:length(V1),2));
103 VcMIN=min(V1(length(V1)-n:length(V1),2));
104 VcAMP=(VcMAX-VcMIN)/2;
105 Ucold=VcAMP/A
106
107 %Compute gas conduction and PV power
108 Qg2=[k2(:,1) -k2(:,2).*A.*dtdz2(:,2)];
109 PV2=[p2(:,1) p2(:,2).*V2(:,2)];
110
111 hLCA2=LCA(h2,n,f);
```

```
112 qwallLCA2=LCA(q2,n,f);
113 QgLCA2=LCA(Qg2,n,f);
114
115 PVLCA2=LCA(PV2,n,f);
116 edotLCA2=hLCA2+qwallLCA2+QgLCA2
117 FOM2=edotLCA2/PVLCA2;
118
119 e2=[h2(:,1) h2(:,2)+q2(:,2)+Qg2(:,2)];
120 CA_e2=zeros(size(e2));
121 for i=(win+1):(length(e2))
122     CA_e2(i,1)=e2(i,1);
123     CA_e2(i,2)=f*trapz(e2((i-win):i,1),e2((i-win):i,2));
124 end
125 CA_PV2=zeros(size(PV2));
126 for i=(win+1):(length(PV2))
127     CA_PV2(i,1)=PV2(i,1);
128     CA_PV2(i,2)=f*trapz(PV2((i-win):i,1),PV2((i-win):i,2));
129 end
130 FOMt2=CA_e2(:,2)./CA_PV2(:,2);
131
132 %-------------------------------------------------------------------------%
133 %Repeat entire process for Point 3 (Center of PT)
134 %-------------------------------------------------------------------------%
135
136 p3=dlmread(strcat(file,'p3.out'),DELIMITER,2,0);
137 h3=dlmread(strcat(file,'h3.out'),DELIMITER,2,0);
138 q3=dlmread(strcat(file,'q3.out'),DELIMITER,2,0);
139 V3=dlmread(strcat(file,'v3.out'),DELIMITER,2,0);
140 k3=dlmread(strcat(file,'k3.out'),DELIMITER,2,0);
141 dtdz3=dlmread(strcat(file,'dtdz3.out'),DELIMITER,2,0);
142 m3=dlmread(strcat(file,'m3.out'),DELIMITER,2,0);
143
```

```
144 p3=cleanmyoutfile(p3);
145 h3=cleanmyoutfile(h3);
146 q3=cleanmyoutfile(q3);
147 V3=cleanmyoutfile(V3);
148 k3=cleanmyoutfile(k3);
149 dtdz3=cleanmyoutfile(dtdz3);
150 m3=cleanmyoutfile(m3);
151
152 Qg3=[k3(:,1) -k3(:,2).*A.*dtdz3(:,2)];
153 PV3=[p3(:,1) p3(:,2).*V3(:,2)];
154
155 hLCA3=LCA(h3,n,f);
156 qwallLCA3=LCA(q3,n,f);
157 QgLCA3=LCA(Qg3,n,f);
158
159 PVLCA3=LCA(PV3,n,f);
160 edotLCA3=hLCA3+qwallLCA3+QgLCA3
161 FOM3=edotLCA3/PVLCA3;
162
163 e3=[h3(:,1) h3(:,2)+q3(:,2)+Qg3(:,2)];
164 CA_e3=zeros(size(e3));
165 for i=(win+1):(length(e3))
166     CA_e3(i,1)=e3(i,1);
167     CA_e3(i,2)=f*trapz(e3((i-win):i,1),e3((i-win):i,2));
168 end
169 CA_PV3=zeros(size(PV3));
170 for i=(win+1):(length(PV3))
171     CA_PV3(i,1)=PV3(i,1);
172     CA_PV3(i,2)=f*trapz(PV3((i-win):i,1),PV3((i-win):i,2));
173 end
174 FOMt3=CA_e3(:,2)./CA_PV3(:,2);
175
```

```
176 ------------------------------------------------------------------------%
177 Repeat entire process for Point 4 (0.5mm from PT warm end)
178 ------------------------------------------------------------------------%
179
180 p4=dlmread(strcat(file,'p4.out'),DELIMITER,2,0);
181 h4=dlmread(strcat(file,'h4.out'),DELIMITER,2,0);
182 q4=dlmread(strcat(file,'q4.out'),DELIMITER,2,0);
183 V4=dlmread(strcat(file,'V4.out'),DELIMITER,2,0);
184 k4=dlmread(strcat(file,'k4.out'),DELIMITER,2,0);
185 dtdz4=dlmread(strcat(file,'dtdz4.out'),DELIMITER,2,0);
186 m4=dlmread(strcat(file,'m4.out'),DELIMITER,2,0);%
187
188 p4=cleanmyoutfile(p4);
189 h4=cleanmyoutfile(h4);
190 q4=cleanmyoutfile(q4);
191 V4=cleanmyoutfile(V4);
192 k4=cleanmyoutfile(k4);
193 dtdz4=cleanmyoutfile(dtdz4);
194 m4=cleanmyoutfile(m4);
195
196 Compute hot end velocity
197 VhMAX=max(V4(length(V4)-n:length(V4),2));
198 VhMIN=min(V4(length(V4)-n:length(V4),2));
199 VhAMP=(VhMAX-VhMIN)/2;
200 Uhot=VhAMP/A
201
202 Qg4=[k4(:,1) -k4(:,2).*A.*dtdz4(:,2)];
203 PV4=[p4(:,1) p4(:,2).*V4(:,2)];
204
205 hLCA4=LCA(h4,n,f);
206 qwallLCA4=LCA(q4,n,f);
207 QgLCA4=LCA(Qg4,n,f);
```

```
208
209 PVLCA4=LCA(PV4,n,f);
210 edotLCA4=hLCA4+qwallLCA4+QgLCA4
211 FOM4=edotLCA4/PVLCA4;
212
213 e4=[h4(:,1) h4(:,2)+q4(:,2)+Qg4(:,2)];
214 CA_e4=zeros(size(e4));
215 for i=(win+1):(length(e4))
216    CA_e4(i,1)=e4(i,1);
217    CA_e4(i,2)=f*trapz(e4((i-win):i,1),e4((i-win):i,2));
218 end
219 CA_PV4=zeros(size(PV4));
220 for i=(win+1):(length(PV4))
221    CA_PV4(i,1)=PV4(i,1);
222    CA_PV4(i,2)=f*trapz(PV4((i-win):i,1),PV4((i-win):i,2));
223 end
224 FOMt4=CA_e4(:,2)./CA_PV4(:,2);
225
226 %-------------------------------------------------------------------------%
227 %Repeat entire process for Point 5 (0.5mm from PT warm end)
228 %-------------------------------------------------------------------------%
229
230 p5=dlmread(strcat(file,'p5.out'),DELIMITER,2,0);
231 h5=dlmread(strcat(file,'h5.out'),DELIMITER,2,0);
232 q5=dlmread(strcat(file,'q5.out'),DELIMITER,2,0);
233 V5=dlmread(strcat(file,'V5.out'),DELIMITER,2,0);
234 k5=dlmread(strcat(file,'k5.out'),DELIMITER,2,0);
235 dtdz5=dlmread(strcat(file,'dtdz5.out'),DELIMITER,2,0);
236 m5=dlmread(strcat(file,'m5.out'),DELIMITER,2,0);
237
238 p5=cleanmyoutfile(p5);
239 h5=cleanmyoutfile(h5);
```

```
240 q5=cleanmyoutfile(q5);
241 V5=cleanmyoutfile(V5);
242 k5=cleanmyoutfile(k5);
243 dtdz5=cleanmyoutfile(dtdz5);
244 m5=cleanmyoutfile(m5);
245
246 %Calculate real-time PV power
247 PV5=[p5(:,1) p5(:,2).*V5(:,2)];
248
249 %compute corrections for porous HX interface
250 hg5=[h5(:,1) epsHX.*h5(:,2)];
251 %Gas Conduction
252 Qg5=[k5(:,1) -k5(:,2).*(A*epsHX).*dtdz5(:,2)];
253 %Matrix Conduction
254 Qm5=[dtdz5(:,1) -kHXh.*A.*(1-epsHX).*dtdz5(:,2)];
255
256 %Compute last cycle averages (LCA)
257 hLCA5=LCA(hg5,n,f);
258 qwallLCA5=LCA(q5,n,f);
259 QgLCA5=LCA(Qg5,n,f);
260 QmLCA5=LCA(Qm5,n,f);
261 PVLCA5=LCA(PV5,n,f);
262
263 %Compute cycle-avg net energy flow
264 edotLCA5=hLCA5+qwallLCA5+QgLCA5+QmLCA5
265 FOM5=edotLCA5/PVLCA5;
266
267 %Compute real-time energy flow and perform moving cycle-avg
268 e5=[hg5(:,1) hg5(:,2)+q5(:,2)+Qg5(:,2)+Qm5(:,2)];
269 CA_e5=zeros(size(e5));
270 for i=(win+1):(length(e5))
271     CA_e5(i,1)=e5(i,1);
```

```
272     CA_e5(i,2)=f*trapz(e5((i-win):i,1),e5((i-win):i,2));
273 end
274 CA_PV5=zeros(size(PV5));
275 for i=(win+1):(length(PV5))
276     CA_PV5(i,1)=PV5(i,1);
277     CA_PV5(i,2)=f*trapz(PV5((i-win):i,1),PV5((i-win):i,2));
278 end
279 FOMt5=CA_e5(:,2)./CA_PV5(:,2);
280
281 %-------------------------------------------------------------------------%
282 %Plotting functions - for user inspection of convergence and ...
      stability
283 %-------------------------------------------------------------------------%
284 figure
285 plot(t,FOMt1.*100,t,FOMt2.*100,t,FOMt3.*100,t,FOMt5.*100)
286 xlabel('Time (s)')
287 ylabel('FOM (%)')
288 legend('Location 1','Location 2','Location 3','Location 5')
289
290 %-------------------------------------------------------------------------%
291 %Compute energy terms in the regenerator matrix
292 %-------------------------------------------------------------------------%
293
294 %pressure ratio:
295 pregenhot=dlmread(strcat(file,'pregen1.out'),DELIMITER,2,0);
296 pramph=sinamp(pregenhot,f,n);
297 PRrh=(pramph+Pcharge)/Pcharge;
298 sprintf('The regen warm end pressure ratio is %E',PRrh)
299
300 pregencold=dlmread(strcat(file,'pregen2.out'),DELIMITER,2,0);
301 prampc=sinamp(pregencold,f,n);
302 PRrc=(prampc+Pcharge)/Pcharge;
```

```
303 sprintf('The regen cold end pressure ratio is %E',PRrc)
304
305 %Enthalpy flow rates:
306 hregen1=dlmread(strcat(file,'hregen1.out'),DELIMITER,2,0);
307 hregen1LCA=LCA(hregen1,n,f)
308
309 hregen2=dlmread(strcat(file,'hregen2.out'),DELIMITER,2,0);
310 hregen2LCA=LCA(hregen2,n,f);
311
312 %-------------------------------------------------------------------------%
313 %Compute cyc-avg heat flow through isothermal walls (net cooling ...
      capacity)
314 %-------------------------------------------------------------------------%
315 %Cold Heat Exchanger
316 Qchx=dlmread(strcat(file,'qin.out'),DELIMITER,2,0);
317 Qnet=LCA(Qchx,n,f)
318
319 %Aftercooler
320 Qac=dlmread(strcat(file,'qacout.out'),DELIMITER,2,0);
321 Qrej1=LCA(Qac,n,f)
322
323 %Warm Heat Exchanger
324 Qwhx=dlmread(strcat(file,'qout.out'),DELIMITER,2,0);
325 Qrej2=LCA(Qwhx,n,f)
326
327
328 %-------------------------------------------------------------------------%
329 %Clear extra process variables
330 %-------------------------------------------------------------------------%
331 %clear A DELIMITER d_in f file fname i n win VcAMP VcMAX VcMIN ...
      VhAMP VhMAX VhMIN
```

C.2 Component-Level Post-Processing Code

FOMall.m

```
%%This Matlab code reads Fluent data files and calculates the ...
    pulse tube
%%efficiency based on cycle-averaged quantities during the final ...
    cycle.

DELIMITER = ' ';
%Request location of data files from user
[fname, file]=uigetfile('*.*','1');

%User inputs (case-dependent)
d_in=input('pulse tube diameter');
A=pi/8*d_in^2;                          %x-sect area of PT, ...
    divided by 2 for half-symmetry (fixed 11-13)
f=input('Operating Frequency (Hz)');    %Cooler operating frequency
n=input('Samples per time cycle');      %number of time steps ...
    per cycle

%Read data files at Location 1
p1=dlmread(strcat(file,'p1.out'),DELIMITER,2,0);
h1=dlmread(strcat(file,'h1.out'),DELIMITER,2,0);
q1=dlmread(strcat(file,'q1.out'),DELIMITER,2,0);
V1=dlmread(strcat(file,'v1.out'),DELIMITER,2,0);
k1=dlmread(strcat(file,'k1.out'),DELIMITER,2,0);
dtdz1=dlmread(strcat(file,'dtdz1.out'),DELIMITER,2,0);
m1=dlmread(strcat(file,'m1.out'),DELIMITER,2,0);

%Clean up extra data points from run restarts
p1=cleanmyoutfile(p1);
h1=cleanmyoutfile(h1);
```

```
q1=cleanmyoutfile(q1);
V1=cleanmyoutfile(V1);
k1=cleanmyoutfile(k1);
dtdz1=cleanmyoutfile(dtdz1);
m1=cleanmyoutfile(m1);

%Compute velocity amplitude for N_ptc calculations
VcMAX=max(V1(length(V1)-n:length(V1),2));
VcMIN=min(V1(length(V1)-n:length(V1),2));
VcAMP=(VcMAX-VcMIN)/2;
Ucold=VcAMP/A

%Calculate gas conduction from Fourier's Law (1-D)
Qg1=[k1(:,1) -k1(:,2).*A.*dtdz1(:,2)];
%Calculate real-time PV power
PV1=[p1(:,1) p1(:,2).*V1(:,2)];
%Compute last cycle averages (LCA)
hLCA1=LCA(h1,n,f);
qwallLCA1=LCA(q1,n,f);
QgLCA1=LCA(Qg1,n,f);

PVLCA1=LCA(PV1,n,f);
%Compute cycle-avg net energy flow
edotLCA1=hLCA1+qwallLCA1+QgLCA1
FOM1=edotLCA1/PVLCA1

%Compute real-time energy flow and perform moving cycle-avg
e1=[h1(:,1) h1(:,2)+q1(:,2)+Qg1(:,2)];
win=n;
CA_e1=zeros(size(e1));
for i=(win+1):(length(e1))
    CA_e1(i,1)=e1(i,1);
```

```
58      CA_e1(i,2)=f*trapz(e1((i-win):i,1),e1((i-win):i,2));
59  end
60  %Compute real-time PV Power and perform moving cycle-avg
61  CA_PV1=zeros(size(PV1));
62  for i=(win+1):(length(PV1))
63      CA_PV1(i,1)=PV1(i,1);
64      CA_PV1(i,2)=f*trapz(PV1((i-win):i,1),PV1((i-win):i,2));
65  end
66  FOMt1=CA_e1(:,2)./CA_PV1(:,2);
67  t=CA_e1(:,1);
68
69  % Repeat full process for Point 2
70
71  p2=dlmread(strcat(file,'p2.out'),DELIMITER,2,0);
72  h2=dlmread(strcat(file,'h2.out'),DELIMITER,2,0);
73  q2=dlmread(strcat(file,'q2.out'),DELIMITER,2,0);
74  V2=dlmread(strcat(file,'v2.out'),DELIMITER,2,0);
75  k2=dlmread(strcat(file,'k2.out'),DELIMITER,2,0);
76  dtdz2=dlmread(strcat(file,'dtdz2.out'),DELIMITER,2,0);
77  m2=dlmread(strcat(file,'m2.out'),DELIMITER,2,0);
78
79  p2=cleanmyoutfile(p2);
80  h2=cleanmyoutfile(h2);
81  q2=cleanmyoutfile(q2);
82  V2=cleanmyoutfile(V2);
83  %V2(:,2)=-V2(:,2);
84  k2=cleanmyoutfile(k2);
85  dtdz2=cleanmyoutfile(dtdz2);
86  m2=cleanmyoutfile(m2);
87
88  Qg2=[k2(:,1) -k2(:,2).*A.*dtdz2(:,2)];
89  PV2=[p2(:,1) p2(:,2).*V2(:,2)];
```

```
90
91  hLCA2=LCA(h2,n,f);
92  qwallLCA2=LCA(q2,n,f);
93  QgLCA2=LCA(Qg2,n,f);
94
95  PVLCA2=LCA(PV2,n,f);
96  edotLCA2=hLCA2+qwallLCA2+QgLCA2
97  FOM2=edotLCA2/PVLCA2
98
99  e2=[h2(:,1) h2(:,2)+q2(:,2)+Qg2(:,2)];
100 CA_e2=zeros(size(e2));
101 for i=(win+1):(length(e2))
102     CA_e2(i,1)=e2(i,1);
103     CA_e2(i,2)=f*trapz(e2((i-win):i,1),e2((i-win):i,2));
104 end
105 CA_PV2=zeros(size(PV2));
106 for i=(win+1):(length(PV2))
107     CA_PV2(i,1)=PV2(i,1);
108     CA_PV2(i,2)=f*trapz(PV2((i-win):i,1),PV2((i-win):i,2));
109 end
110 FOMt2=CA_e2(:,2)./CA_PV2(:,2);
111
112 %Repeat entire process for Point 3
113
114 p3=dlmread(strcat(file,'p3.out'),DELIMITER,2,0);
115 h3=dlmread(strcat(file,'h3.out'),DELIMITER,2,0);
116 q3=dlmread(strcat(file,'q3.out'),DELIMITER,2,0);
117 V3=dlmread(strcat(file,'v3.out'),DELIMITER,2,0);
118 k3=dlmread(strcat(file,'k3.out'),DELIMITER,2,0);
119 dtdz3=dlmread(strcat(file,'dtdz3.out'),DELIMITER,2,0);
120 m3=dlmread(strcat(file,'m3.out'),DELIMITER,2,0);
121
```

```
p3=cleanmyoutfile(p3);
h3=cleanmyoutfile(h3);
q3=cleanmyoutfile(q3);
V3=cleanmyoutfile(V3);
k3=cleanmyoutfile(k3);
dtdz3=cleanmyoutfile(dtdz3);
m3=cleanmyoutfile(m3);

%Compute hot end velocity
VhMAX=max(V3(length(V3)-n:length(V3),2));
VhMIN=min(V3(length(V3)-n:length(V3),2));
VhAMP=(VhMAX-VhMIN)/2;
Uhot=VhAMP/A

Qg3=[k3(:,1) -k3(:,2).*A.*dtdz3(:,2)];
PV3=[p3(:,1) p3(:,2).*V3(:,2)];

hLCA3=LCA(h3,n,f);
qwallLCA3=LCA(q3,n,f);
QgLCA3=LCA(Qg3,n,f);

PVLCA3=LCA(PV3,n,f);
edotLCA3=hLCA3+qwallLCA3+QgLCA3
FOM3=edotLCA3/PVLCA3

e3=[h3(:,1) h3(:,2)+q3(:,2)+Qg3(:,2)];
CA_e3=zeros(size(e3));
for i=(win+1):(length(e3))
    CA_e3(i,1)=e3(i,1);
    CA_e3(i,2)=f*trapz(e3((i-win):i,1),e3((i-win):i,2));
end
CA_PV3=zeros(size(PV3));
```

```
for i=(win+1):(length(PV3))
    CA_PV3(i,1)=PV3(i,1);
    CA_PV3(i,2)=f*trapz(PV3((i-win):i,1),PV3((i-win):i,2));
end
FOMt3=CA_e3(:,2)./CA_PV3(:,2);

%Plotting functions - for user inspection of convergence and ...
    stability
figure
plot(t,FOMt1.*100,t,FOMt2.*100,t,FOMt3.*100)
xlabel('Time (s)')
ylabel('FOM (%)')
legend('Location 1','Location 2','Location 3')

clear A DELIMITER d_in f file fname i n win VcAMP VcMAX VcMIN ...
    VhAMP VhMAX VhMIN
```

C.3 Cycle-averaging Routine

LCA.m

```
function [ avg ] = LCA( data,win,opfrequency )
%LCA This function computes the final cycle average for any 2 ...
    column vector
%containing time in the 1st column, harmonic data in the 2nd. win ...
    is the cycle
%discretization (# samples/cycle) and opfrequency is the ...
    frequency of oscillation (Hz).

avg=opfrequency*trapz(data(length(data)-win:length(data),1),...
    ..data(length(data)-win:length(data),2));

end
```

REFERENCES

[1] Radebaugh, R., "Development of the pulse tube refrigerator as an efficient and reliable cryocooler," *Proc. Institute of Refrigeration*, 2000.

[2] Getling, A. V., *Rayleigh-Bénard Convection: Structures and Dynamics*, vol. 11 of *Advanced Series in Nonlinear Dynamics*. River Edge, NJ: World Scientific Publishing Co., 1998.

[3] Swift, G. W. and Backhaus, S., "The pulse tube and the pendulum," *Journal of the Acoustical Society of America*, vol. 126, no. 5, pp. 2273–2284, 2009.

[4] Çengel, Y. A. and Boles, M. A., *Thermodynamics: An Engineering Approach*. 1221 Avenue of the Americas, New York, NY 10020: McGraw-Hill, 5 ed., 2006.

[5] Herschel, J., *The Athenaeum*. 1834.

[6] Kirk, A., "On the mechanical production of cold," *Proceedings of the Institute of Civil Engineering (London)*, vol. 37, pp. 244–315, 1874.

[7] Köhler, J. W. L. and Jonkers, C. O., "Fundamentals of the gas refrigeration machine," *Philips Technology Review*, vol. 16, no. 3, pp. 69–78, 1954.

[8] Organ, A. J., *Thermodynamics & Gas Dynamics of the Stirling Cycle Machine*. Cambridge University Press, 1992.

[9] Gifford, W. E. and Longsworth, R. C., "Pulse tube refrigeration," *Transactions of the ASME Journal of Engineering for Industry*, 1964.

[10] Gifford, W. E. and Longsworth, R. C., "Pulse tube refrigeration progress," *Advances in Cryogenic Engineering*, vol. 10, p. 69, 1965.

[11] Longsworth, R. C., "An experimental investigation of pulse tube refrigeration heat pumping rates," *Advances in Cryogenic Engineering*, vol. 12, p. 608, 1967.

[12] Mikulin, E. I., Tarasov, A. A., and Shkrbyonock, M. P., "Low temperature expansion pulse tubes," *Advances in Cryogenic Engineering*, vol. 29, pp. 629–637, 1984.

[13] Radebaugh, R., Zimmerman, J., Smith, D. R., and Louie, B., "A comparison of three types of pulse tube refrigerators: New methods for reaching 60 K," *Advances in Cryogenic Engineering*, vol. 31, p. 779, 1986.

[14] Zhu, S., Wu, P., and Chen, Z., "Double inlet pulse tube refrigerators: An important improvement," *Cryogenics*, vol. 30, pp. 514–520, 1990.

[15] Gedeon, D., "DC gas flows in Stirling and pulse tube refrigerators," *Cryocoolers*, vol. 9, pp. 385–392, 1997.

[16] Olsen, J. R. and Swift, G. W., "Acoustic streaming in pulse tube refrigerators: Tapered pulse tubes," *Cryogenics*, vol. 37, pp. 769–776, December 1997.

[17] Radebaugh, R., "Pulse tube cryocoolers for cooling infrared sensors," in *Proceedings of SPIE: Infrared Technologies & Applications*, vol. 4130, pp. 363–379, 2000.

[18] Godshalk, K. M., Jin, C., Kwong, Y. K., Herchberg, E. L., Swift, G. W., and Radebaugh, R., "Characterization of 350 Hz thermoacoustically drive orifice pulse tube refrigerator with measurements of the phase of the mass flow and pressure," *Advances in Cryogenic Engineering*, vol. 41, pp. 1411–1418, 1996.

[19] Zhu, S. W., Zhou, S. L., Yoshimura, N., and Matsubara, Y., "Phase shift effect of the long neck tube for the pulse tube refrigerator," *Cryocoolers*, vol. 9, pp. 269–278, 1997.

[20] Gardner, D. L. and Swift, G. W., "Use of inertance in orifice pulse tube refrigerators," *Cryogenics*, vol. 37, pp. 117–121, 1997.

[21] Garaway, I. and Grossman, G., "A study of a high frequency miniature reservoir-less pulse tube," *Advances in Cryogenic Engineering*, vol. 53, pp. 1547–1554, 2008.

[22] Conrad, T. J., *Miniaturized Pulse Tube Refrigerators*. PhD thesis, Georgia Institute of Technology, Atlanta, GA, August 2011.

[23] Conrad, T. J., Landrum, E. C., Ghiaasiaan, S. M., Kirkconnell, C. S., Crittenden, T., and Yorish, S., "CFD modeling of meso-scale and micro-scale pulse tube refrigerators," *Cryocoolers 15*, 2008.

[24] Swift, G. W., *Thermoacoustics: A Unifying Perspective for Some Engines and Refrigerators*. 2 Huntington Quadrangle, Melville, NY 11747: Acoustical Society of America, 2002.

[25] Garaway, I., Gan, Z. H., Bradley, P. E., Veprik, A., and Radebaugh, R., "Development of a miniature 150 Hz pulse tube cryocooler," in *Cryocoolers 15* (Miller, S. D. and R. G. Ross, J., eds.), pp. 105–113, 2008.

[26] Schaefer, B. R., Bellis, L. A., Ellis, M. J., and Conrad, T. J., "Raytheon low temperature RSP2 cryocooler performance," *Cryocoolers 17*, pp. 9–15, 2012.

[27] Kittel, P., "Enthalpy, entropy, and exergy flows in ideal pulse tube cryocoolers," *Cryocoolers 17*, pp. 333–341, 2004.

[28] Kittel, P., Kashani, A., Lee, J. M., and Roach, P. R., "General pulse tube theory," *Cryogenics*, vol. 36, p. 849, 1996.

[29] de Waele, A. T. A. M., Steijaert, P. P., and Gijzen, P., "Thermodynamic aspects of pulse tube cryocoolers," *Cryogenics*, vol. 37, p. 313, 1997.

[30] Storch, P. J. and Radebaugh, R., "Development and experimental test of an analytical model of the orifice pulse tube refrigerator," *Advances in Cryogenic Engineering*, vol. 33, no. 851, 1988.

[31] Taylor, R. P., *Development and Experimental Validation of a Pulse-Tube Design Tool Using Computational Fluid Dynamics*. PhD thesis, The University of Wisconsin-Madison, 2009.

[32] Rott, N., "The influence of heat conduction on acoustic streaming," *Z. Agnew. Math. Phys.*, vol. 25, no. 417, 1974.

[33] Brereton, G. J. and Mankbadi, R. R., "Review of recent advances in the study of unsteady turbulent internal flows," *ASME Appl. Mech. Rev.*, vol. 48, no. 4, pp. 189–212, 1995.

[34] Ohmi, M., Iguchi, M., Kakehashi, K., and Masuda, T., "Transition to turbulence and velocity distribution in an oscillating pipe flow," *Bulletin of the JSME*, vol. 25, pp. 365–371, February 1982.

[35] Pfotenhauer, J. M., Gan, Z. H., and Radebaugh, R., "Approximate design method for single stage pulse tube refrigerators," *Advances in Cryogenic Engineering: Transactions of the Cryogenic Engineering Conference - CEC*, vol. 53, pp. 1437–1444, 2008.

[36] Akhavan, R., Kamm, R. D., and Shapiro, A. H., "An investigation of transition to turbulence in bounded oscillatory stokes flows part 1. experiments," *J. Fluid Mechanics*, vol. 225, pp. 395–422, 1991.

[37] Akhavan, R., Kamm, R. D., and Shapiro, A. H., "An investigation of transition to turbulence in bounded oscillatory stokes flows part 2. numerical simulations," *J. Fluid Mechanics*, vol. 225, pp. 423–444, 1991.

[38] VanDyke, M., *An album of Fluid Motion*. Palo Alto, CA: Parabolic Press, 1982.

[39] Swift, G. W. and Backhaus, S., "Why high-frequency pulse tubes can be tipped," in *Cryocoolers 16* (R. G. Ross, J., ed.), 2008.

[40] Scurlock, R. G. and Beduz, C., "Reduction of the effects of asymmetrical convection in tilted pulse-tube refrigerators," *Cryogenics*, vol. 38, pp. 359–360, 1998.

[41] Thummes, G., Schreiber, M., Landgraf, R., and Heiden, C., "Convective heat losses in pulse tube coolers: effect of pulse tube inclination," *Cryocoolers*, vol. 9, pp. 393–402, 1997.

[42] Yang, L. W. and Thummes, G., "High frequency two-stage pulse tube cryocooler with base temperature below 20 K," *Cryogenics*, vol. 45, pp. 155–159, 2005.

[43] Wang, C. and Gifford, P. E., "Development of 4 K pulse tube cryorefrigerators at Cryomech," *Advances in Cryogenic Engineering: Proceedings of the Cryogenic Engineering Conference - CEC*, vol. 47, pp. 641–648, 2002.

[44] R. G. Ross, J. and Johnson, D. L., "Effect of gravity orientation on the thermal performance of Stirling-type pulse tube cryocoolers," *Cryogenics*, vol. 44, pp. 403–408, 2004.

[45] Kasthurirengan, S., "Experimental studies of convection in a single stage pulse tube refrigerator," *Advances in Cryogenic Engineering: Proceedings of the Cryogenic Engineering Conference - CEC*, vol. 49B, pp. 1474–1481, 2004.

[46] Kasthurirengan, S., "Elliptical and circular pulse tubes: A comparative experimental study," *Proceedings of the Eighteenth International Cryogenic Engineering Conference*, vol. 547-550, pp. 547–550, 2000.

[47] Trollier, T., Ravex, A., Charles, I., Duband, L., Mullie, J., Bruins, P., Benschop, T., and Linder, M., "Performance test results of a miniature 50 to 80 K pulse tube cooler," in *Cryocoolers 13* (R. G. Ross, J., ed.), (New York), Springer Science + Business Media, Inc., 2004.

[48] Hou, X. F., Yang, L. W., and Liang, J. T., "Gravity effect in high frequency coaxial pulse tube cryocoolers," in *Cryocoolers 14* (Miller, S. D. and R. G. Ross, J., eds.), pp. 241–247, 2007.

[49] James, E. R., Corey, J. A., and Spoor, P. S., "Performance and orientation independence of two production model desktop acoustic Stirling cryocoolers," in *AIP Conference Proceedings*, vol. 823, pp. 1703–1710, 2006.

[50] Berryhill, A. and Spoor, P. S., "High-frequency pulse tubes can't always be tipped," in *Advances in Cryogenic Engineering*, vol. 1434, pp. 1593–1599, 2012.

[51] Shiraishi, M., Murakami, M., Nakano, A., and Iida, T., "Visualization of secondary flow in an inclined double-inlet pulse tube refrigerator," in *Cryocoolers 14* (Miller, S. D. and R. G. Ross, J., eds.), pp. 277–284, 2007.

[52] Shiraishi, M., Takamatsu, K., Murakami, M., and Nakano, A., "Dependence of convective secondary flow on inclination angle in an inclined pulse tube refrigerator revealed by visualization," *Cryogenics*, vol. 44, pp. 101–107, 2004.

[53] Zhang, L. M., Hu, J. Y., Luo, E. C., and Dai, W., "A novel effective suppression of natural convection in pulse tube coolers," *Cryogenics*, vol. 51, pp. 85–89, 2011.

[54] Matsumoto, N., Yasukawa, Y., and Ohshima, K., "Development of the miniature pulse tube cryocooler," in *Advances in Cryogenic Engineering: Proceedings of the Cryogenic Engineering Conference - CEC*, vol. 710, pp. 1339–1346, American Institute of Physics, 2004.

[55] Kirkconnell, C. S., *Numerical Analysis of the Mass Flow and Thermal Behavior in High-frequency Pulse Tubes*. PhD thesis, Georgia Institute of Technology, Atlanta, GA 30332, 1995.

[56] Kirkconnell, C. S. and Colwell, G. T., "Parametric studies on numerical, nonlinear pulse tube flow," *Journal of Fluids Engineering*, vol. 119, pp. 831–838, 1998.

[57] Cha, J. S., *Hydrodynamic Parameters of Micro Porous Media for Steady and Oscillatory Flow: Application to Cryocooler Regenerators*. PhD thesis, Georgia Institute of Technology, Atlanta, GA 30332, August 2007.

[58] Cha, J. S., Ghiaasiaan, S. M., Desai, P. V., Harvey, J. P., and Kirkconnell, C. S., "Multi-dimensional flow effects in pulse tube refrigerators," *Cryogenics*, vol. 46, pp. 658–665, 2006.

[59] Kim, S. M., "Numerical investigation on laminar pulsating flow through porous media," Master's thesis, Georgia Institute of Technology, Atlanta, GA 30332, 2008.

[60] Pathak, M. G., "Thermal dispersion and convective heat transfer during laminar pulsating flow in porous media," Master's thesis, Georgia Institute of Technology, Atlanta, GA 30332, 2010.

[61] Pathak, M. G. and Ghiaasiaan, S. M., "Convective heat transfer and thermal dispersion during laminar pulsating flow in porous media," *Int. J. Thermal Sciences*, vol. 50, pp. 440–448, 2011.

[62] Mulcahey, T. I., Pathak, M. G., and Ghiaasiaan, S. M., "Drag coefficient and nusselt number for laminar pulsating flow in porous media," in *Cryocoolers 17* (Miller, S. D. and R. G. Ross, J., eds.), pp. 315–322, 2012.

[63] Mulcahey, T. I., Pathak, M. G., and Ghiaasiaan, S. M., "The effect of flow pulsation on drag and heat transfer in an array of heated square cylinders," *Int. J. Thermal Sciences*, vol. 64, pp. 105–120, February 2013.

[64] Taylor, R. P., Nellis, G. F., and Klein, S. A., "Optimal pulse tube design using computational fluid dynamics," in *Advances in Cryogenic Engineering* (J. G. Weisand, I., ed.), vol. 53B, pp. 1445–1451, American Institute of Physics, 2007.

[65] Liang, W. and de Waele, A., "A new type of streaming in pulse tubes," in *Cryocoolers 14* (Miller, S. D. and R. G. Ross, J., eds.), pp. 271–276, 2007.

[66] Hozumi, Y., Shiraishi, M., and Murakami, M., "Simulation of thermodynamics aspects about pulse tube refrigerator," in *Advances in Cryogenic Engineering: Transactions of the Cryogenic Engineering Conference - CEC*, vol. 49, pp. 1500–1507, 2004.

[67] Carbo, R. M., *Dynamic Stabilization of the Rayleigh-Bènard Instability in Rectangular Enclosures: a Computational Approach*. PhD thesis, The Pennsylvanua State University, 2012.

[68] Kasthurirengan, S., "Reduction of convective heat loss in low frequency pulse tube cooler with mesh inserts,," *Advances in Cryogenic Engineering: Proceedings of the Cryogenic Engineering Conference - CEC*, vol. 45B, pp. 135–142, 2000.

[69] Gary, J. and O'Gallagher, A., *REGEN 3.3: User Manual*. National Institute of Standards and Technology, 325 Broadway, Boulder, CO 80303, April 2008.

[70] Gedeon, D., *Sage User's Guide*. Gedeon Associates, 16922 South Canaan Rd. Athens, OH 45701, v8 ed., August 2011.

[71] Lemmon, E. W. and Huber, M. L., *REFPROP: NIST Materials Reference Properties Database: Version 9.1*. NIST, 2013.

[72] Ward, B., Clark, J., and Swift, G. W., *Design Environment for Low-amplitude Thermoacoustic Energy Conversion: DeltaEC*. Los Alamos National Laboratory, Los Alamos, NM, 6.3b11 ed., February 2012.

[73] ANSYS, *ANSYS FLUENT User's Guide*. No. Release 14.5, Canonsburg, PA 15317: Southpointe, 2012.

[74] ANSYS, *ANSYS FLUENT Theory Guide*. No. Release 14.5, Canonsburg, PA 15317: Southpointe, 2012.

[75] Landrum, E. C., Conrad, T. J., Ghiaasiaan, S. M., and Kirkconnell, C. S., "Hydrodynamic parameters of mesh fillers relevant to miniature regenerative cryocoolers," *Cryogenics*, vol. 50, pp. 373–380, 2009.

[76] Landrum, E. C., "Anisotropic parameters of mesh fillers relevant to miniature cryocoolers," Master's thesis, Georgia Institute of Technology, Atlanta, GA 30332, May 2009.

[77] Cha, J. S., Ghiaasiaan, S. M., and Kirkconnell, C. S., "Oscillatory flow in microporous media applied in pulse-tube and Stirling-cycle cryocooler regenerators," *Exp. Thermal and Fluid Science*, vol. 32, pp. 1264–1278, 2008.

[78] Cha, J. S., Ghiaasiaan, S. M., and Kirkconnell, C. S., "Measurement of anisotropic hydrodynamic parameters of pulse tube or Stirling cryocooler regenerators," *Advances in Cryogenic Engineering*, p. 1911, 2006.

[79] Clearman, W. M., "Measurement and correlation of directional permeability and forchheimer's inertial coefficient of micro porous structures used in pulse-tube cryocoolers," Master's thesis, Georgia Institute of Technology, Atlanta, GA 30332, 2007.

[80] Clearman, W. M., Cha, J. S., Ghiaasiaan, S. M., and Kirkconnell, C. S., "Anisotropic steady-flow hydrodynamic parameters of microporous media applied to pulse tube and stirling cryocooler regenerators," *Cryogenics*, vol. 48, pp. 112–121, 2008.

[81] Harvey, J. P., *Oscillatory Compressible Flow and Heat Transfer in Porous Media - Application to Cryocooler Regenerators*. PhD thesis, Georgia Institute of Technology, Atlanta, GA 30332, 2003.

[82] Ergun, S., "Fluid flow through packed columns," *Chem. Eng. Prog.*, vol. 48, no. 2, pp. 89–94, 1952.

[83] Pathak, M. G., Patel, V. C., Helvensteign, B. P., Mulcahey, T. I., Ghiaasiaan, S. M., Kashani, A., and Feller, J. R., "Hydrodynamic resistance parameters for erpr rare-earth regenerator material under steady and periodic flow conditions," in *Advances in Cryogenic Engineering* (II, J. G. W., ed.), vol. 59, (Melville, NY), American Institute of Physics, 2013.

[84] Pathak, M. G., Patel, V. C., Ghiaasiaan, S. M., Mulcahey, T. I., Helvensteijn, B. P., Kashani, A., and Feller, J. R., "Hydrodynamic parameters for ErPr cryocooler regenerator fillers under steady and periodic flow conditions," *Cryogenics*, vol. 58, pp. 68–77, 2013.

[85] Pathak, M. G., *Periodic Flow Physics in Porous Media of Regenerative Cryocoolers*. PhD thesis, Georgia Institute of Technology, Atlanta, GA 30332, August 2013.

[86] Cheadle, M. J., Nellis, G. F., and Klein, S. A., "Regenerator friction factor and nusselt number information derived from CFD analysis," in *Cryocoolers* (Miller, S. D. and R. G. Ross, J., eds.), vol. 16, pp. 397–404, 2011.

[87] Pathak, M. G., Mulcahey, T. I., and Ghiaasiaan, S. M., "Conjugate heat transfer during oscillatory laminar flow in porous media," *Int. J. Heat and Mass Transfer*, vol. 66, pp. 23–30, November 2013.

[88] Marquardt, E. D., Le, J. P., and Radebaugh, R., "Cryogenic material properties database," in *Cryocoolers 11* (R. G. Ross, J., ed.), pp. 681–687, 2002.

[89] "Newark wire cloth company, woven wire cloth." `http://www.newarkwire.com/wwc.html#weaves`, December 2013.

[90] Yuan, Y. and Zhi, X., "CFD simulation for the optimal pulse tube volume for 120 Hz pulse tube cryocooler," in *Cryocoolers 17* (R. G. Ross, J., ed.), pp. 151–159, 2012.

[91] Radebaugh, R., Lewis, M., Luo, E., Pfotenhauer, J. M., and Nellis, G. F., "Inertance tube optimization for pulse tube refrigerators," *AIP Conference Proceedings*, vol. 823, no. 59, pp. 59–67, 2006.

[92] Radebaugh, R. and Arp, V., "Isothermal heat exchanger (ISOHX)." Program not commercially available, 2013.

[93] Mulcahey, T. I., Conrad, T. J., Ghiaasiaan, S. M., and Pathak, M. G., "Investigation of gravitational effects in pulse tube cryocoolers using 3-D CFD," in *Advances in Cryogenic Engineering: Transactions of the Cryogenic Engineering Conference - CEC* (II, J. G. W., ed.), vol. 59, 2013.

[94] Celik, I., Chen, C. J., Roache, P. J., and Sheurer, G., "Quantification of uncertainty in computational fluid dynamics," in *ASME Fluids Engineering Division Summer Meeting*, vol. 158, ASME, June 1993.

[95] Richardson, L. F., "The approximate arithmetical solution by finite differences of physical problems involving differential equations, with an application to the stresses in a masonry dam," *Transactions of the Royal Society of London, Ser. A*, vol. 210, pp. 307–357, 1910.

[96] Hofman, A. and Pan, H., "Phase shifting in pulse tube refrigerators," *Cryogenics*, vol. 39, no. 6, pp. 529–537, 1999.

[97] Hon, R. C. and Kirkconnell, C. S., "Raytheon dual-use long life cryocooler development," in *Infrared Technology and Applications XXXIII* (Andreson, B. F., Fulop, G. F., and Norton, P. R., eds.), vol. 6542, 2007.

[98] Hon, R. C., Kirkconnell, C. S., and Roberts, T., "Raytheon dual-use cryocooler system development," in *Advances in Cryogenic Engineering: Transactions of the Cryogenic Engineering Conference - CEC* (II, J. G. W., ed.), vol. 53, pp. 538–545, 2008.

[99] Schaefer, B. R., Bellis, L. A., Ellis, M. J., and Conrad, T. J., "Advanced regenerator testing in the Raytheon dual-use cryocooler," in *Cryogenic Optical Systems and Instruments* (Heaney, J. B. and Kvamme, E. T., eds.), vol. 8863, Proc. SPIE, 2013.

[100] Ku, H. H., "Notes on the use of propagation of error formulas," *Journal of Research of the National Bureau of Standards*, vol. 70C, no. 4, pp. 263–273, 1966.

[101] Mulcahey, T. I., Conrad, T. J., and Ghiaasiaan, S. M., "CFD modeling of tilt induced cooling losses in inertance tube pulse tube cryocoolers," in *Cryocoolers 17* (Miller, S. D. and R. G. Ross, J., eds.), pp. 143–150, 2012.

[102] Morie, T. and Xu, M. Y., "Experimental investigation of high-efficiency 4K GM cryocoolers," in *Cryocoolers 17* (Miller, S. D. and R. G. Ross, J., eds.), pp. 247–259, 2012.

[103] Taylor, R., Lewis, M., Bradley, P., and Radebaugh, R., "Development of a 4 K regenerator and pulse tube test facility," in *Cryocoolers 17* (Miller, S. D. and R. G. Ross, J., eds.), pp. 219–228, 2012.

[104] Ekin, J. W., *Experimental Techniques for Low-Temperature Measurements*. Oxford University Press, 2006.

VITA

Thomas Ian Mulcahey was born in Columbia, MD on February 4, 1985 to Debra and Michael Mulcahey. He was drawn to physics early on, and would regularly watch "The Joy of Physics," an educational program hosted by Dr. Juluis Sumner Miller. He recalls one of his favorite episodes being a primer on low-temperature physics, where a number of objects including a balloon were shattered after soaking in liquid nitrogen. At the age of six his family moved to Southbury, CT where he lived until he graduated from Pomperaug Regional High School. In middle school he became intensely interested in music, first as a percussionist for three years, then switching to the guitar at the age of 12. The guitar has become a lifelong passion.

Mulcahey completed a B.S. in Mechanical Engineering at Western New England University (formerly Western New England College) in Springfield, MA under the guidance of Dr. Bart Lipkens. Directly following graduation, he spent one year working as an engineer at Alstom Power, Inc. in Windsor, CT designing pulverizers for coal-fired power plants. In Fall 2008 he enrolled in the M.S. program at the George W. Woodruff School of Mechanical Engineering at the Georgia Institute of Technology.

The first two years at Georgia Tech were spent in the Acoustics & Dynamics research group, investigating sound and vibration measurement and localization methods. Upon completion of the M.S.M.E. in 2010, Mulcahey joined the Georgia Tech Cryo Lab under Prof. S. Mostafa Ghiaasiaan to complete the Doctor of Philosophy degree. Mulcahey was a researcher in the Cryo Lab group from 2010 through 2013, defending his dissertation the first week of January 2014.